

Spatial and Morphological Control of Cyanine Dye Thin Films

THÈSE N° 8791 (2018)

PRÉSENTÉE LE 24 AOÛT 2018

À LA FACULTÉ DES SCIENCES ET TECHNIQUES DE L'INGÉNIEUR
UNITÉ DE RATTACHEMENT POUR SCIENTIFIQUES IMX
PROGRAMME DOCTORAL EN SCIENCE ET GÉNIE DES MATÉRIAUX

ÉCOLE POLYTECHNIQUE FÉDÉRALE DE LAUSANNE

POUR L'OBTENTION DU GRADE DE DOCTEUR ÈS SCIENCES

PAR

Nicolas Alexandre Serge LECLAIRE

acceptée sur proposition du jury:

Prof. A. Fontcuberta i Morral, présidente du jury
Prof. F. Nüesch, Dr J. Heier, directeurs de thèse
Prof. G. Reiter, rapporteur
Dr O. Enger, rapporteur
Prof. K. Sivula, rapporteur



ÉCOLE POLYTECHNIQUE
FÉDÉRALE DE LAUSANNE

Suisse
2018

*Ring the bells that still can ring
Forget your perfect offering
There is a crack in everything
That's how the light gets in*

— Leonard Cohen



Acknowledgements

When I started this PhD four years ago, I suppose I was not exactly sure what kind of adventure I was embarking on. Now a few years later, I have almost reached the opposite shore and I can start looking back on this journey with a certain satisfaction. Sailing has not always been smooth and there have been a few storms, but there were blissful moments too. There are a number of people I would like to thank here for having taken part in this journey by my side.

First, I would like to thank my supervisor Frank Nüesch, for giving me the opportunity to conduct my PhD thesis in his group, for always letting his door (and his mind) open for discussion as well as for his infallible optimism. I also have to acknowledge my co-supervisor Jakob Heier for the numerous discussions and the time he has devoted to this work.

For "passing the hot potato" to me with enthusiasm but honesty and also for the nice hikes we did together, I would like to thank Jean-Nicolas Tisserant.

There are a number of people at EMPA I would like to thank for their contributions and help with this work. I am grateful to Florent Boudoire for his help with FDTD simulations and his coding skills which have been very useful for the first part of this thesis. I thank Erwin Hack, for his expertise in optics and the efficient collaboration we had. I would like to thank Ivan Shorubalko, for his assistance with various optical and spectroscopic equipments I have had the occasion to use during these four years of research work. His commitment and professionalism were greatly appreciated. I thank Ulrich Müller for introducing me to atomic force microscopy and for his assistance with the equipment. For her expertise in single crystal X-ray diffraction I would like to thank Antonia Neels. I would also like to express my gratitude to Arndt Remhof and Elsa Roedern for their help with other X-ray diffraction experiments. I also want to thank Kerda Keevend for spending the time trying to measure confocal fluorescence microscopy with me.

Acknowledgements

A few people from other academic horizons have also contributed to this PhD work and I want to take this opportunity to thank them too. Especially, I want to thank Olivier Martin for fruitful discussions early in this work, about optical phenomena and for hosting me to perform a few experiments in his laboratory at EPFL. I would also like to thank Jeffrey R. Reimers and Li Musen from the International Center for Quantum and Molecular Structures at the University of Shanghai for the interest they took in this work and the time and effort they have devoted to trying understand the optical properties of the cyanine crystals.

I would like to thank my fellow students, past and present, from the "Functional Polymers" group with whom I have shared parts of this journey: Sandra Jenatsch, Simon Dünki, Yee Song Ko, Philip Caspari, Wang Lei, Donatas Gesevičius, José Quinsaat, Surendra Anantharaman, Zhang Hui, Paolo Gelato, Silvia Fernandes, Philippe Schwaller, Matia Bulloni, Adrian Kaiser, Elena Perju, Mihaela Alexandru, Matteo de Donato, Karen Strassel, Matthias Diethelm, Mohammed Makha, Yauhen Sheima, Quirin Grossman, Micha Bajc, Thibault Fleurieau-Lintz, Nicole Pfeiffer, Rian Aderne and Tym De Wild.

I want to express all my gratitude to Anna Véron for her constant support during these four years. Her friendship helped me going through the most difficult times and contributed to making this adventure so special and memorable.

Many thanks to the other Functional Polymers group members for being part of my everyday life during the last four years: Roland Hany, Beatrice Fischer, Isabella Gartmann, Dorina Opris, Christian Walder, René Schneider and Roland Steim. I would like to thank Daniel Rentsch, for his friendship and the relaxing breaks we shared.

I would like thank Sara Vigne, who has been a wonderful host every time I had to stay in Lausanne.

Finally, I would like to thank my parents Jacques and Bayesté and my sister Clara who never doubted in my capacity to go through this challenging enterprise.

For her love, her faith in me, her unconditional support and her unfailing patience, I am deeply grateful to Brigitte Greenwood.

Dübendorf, June 13, 2018

N. L.



Abstract

Cyanine dyes are organic semiconductor compounds with light absorption and emission properties useful for emerging technologies such as solar cells and light-emitting devices. The characteristics of these materials in the solid state depend on their organization of the constituting building blocks. This thesis focuses on controlling the morphology of cyanine dye thin films at different length scales and clarifying the resulting properties.

When microstructures present features whose size matches visible light wavelengths, new properties may arise from light-matter interactions. Here the properties resulting from the light-matter interactions of cyanine droplet films cast from solution are studied. Based on experimental evidence, it is shown that dye droplet ensembles scatter light with different efficiencies and wavelength ranges depending on their dimensions. FDTD simulations are used to show that this effect results from scattering enhancement at the absorption edge of the dye where the refractive index varies considerably. Simulations also provide a better understanding of individual droplets' interaction with light. While earlier work had hypothesized that the observed scattering phenomenon were due to crystalline clusters within the droplets, this work highlights the contribution of the dye film morphology.

Cyanines also form single crystals whose fabrication induces molecular-scale order in the material. Previous work demonstrated that thin single crystals could be grown by solvent vapor annealing of dye droplets. Here it is shown that in uncontrolled conditions, cyanine single crystals destabilize to form dendritic crystals. *In-situ* microscopy observations highlight the solute reservoir role of the droplet distribution surrounding a growing crystal; when the distance between droplets and the crystal front is large, the solute supply is diffusion-limited. Moreover variations in local pressure equilibrium between the droplets and crystal front lead to advection fluxes which perturb the crystal growth. These observations help design configurations to either prevent crystal destabilization or take advantage of the dendritic growth in a

Abstract

controlled manner.

In addition, the patterning of crystals on a substrate is relevant for their application in devices. A practical challenge is to induce single crystal growth at specific locations. Here, surfaces patterned with SAMs of hydrophilic and hydrophobic thiols are used to create dye droplet arrays from which crystals can be grown. This method is shown to yield local crystallization of the dye and to prevent crystal destabilization through better control of the droplet distribution. By varying the dye solution concentration, partial control over crystal density is achieved, however it proved difficult to control the number of nuclei per droplet. A more controlled evaporation and solvent vapor annealing system might be necessary to master the nucleation process.

Finally the structure and optical properties of cyanine single crystals are addressed. The crystal structure was determined by X-ray diffraction. Structural aspects are shown to lead to excitonic couplings, which are evidenced by orientation-dependent spectroscopic measurements of single crystals. Although further investigation of the absorption band structure is necessary, the results are promising for photovoltaic devices as they might improve exciton transport compared to amorphous layers.

Key words: Organic semiconductors, cyanine dyes, morphology, molecular crystals, thin films

Résumé

Les cyanines sont des molécules organiques semiconductrices possédant des propriétés d'absorption et d'émission de la lumière intéressantes pour nombre de technologies émergentes telles que les cellules solaires ou les dispositifs d'émission de lumière. Les propriétés de ces matériaux à l'état solide dépendent de l'organisation des composants qui les constituent. Cette thèse s'intéresse à contrôler la morphologie de couches minces de cyanine à plusieurs échelles et examine les propriétés qui en résultent.

Si la microstructure d'un solide comprend des éléments dont la dimension correspond à celle de la longueur d'onde de la lumière, de nouvelles propriétés peuvent émerger. Ce travail examine les propriétés résultant de l'interaction entre la lumière et des films de gouttelettes de cyanine déposées par voie liquide. Des observations expérimentales montrent que la diffusion de la lumière par les films de gouttelettes est plus ou moins efficace selon leurs dimensions. Des simulations FDTD démontrent que la diffusion est particulièrement importante au bord d'absorption de la cyanine, où l'indice de réfraction varie considérablement. Alors qu'une précédente étude attribuait ce phénomène à la présence d'aggrégats cristallins dans les gouttelettes, ce travail montre qu'il peut être expliqué par la morphologie des films.

Les cyanines peuvent aussi former des cristaux dont la fabrication permet d'ordonner le matériaux à l'échelle moléculaire. Un précédent travail a montré la possibilité de croître des monocristaux de cyanine par recuit en vapeur de solvant. Ici, on montre que sous des conditions incontrôlées, la croissance est instable et devient dendritique. Des observations *in-situ* soulignent le rôle des gouttelettes entourant un cristal en croissance. Lorsque la distance entre gouttelettes et front de croissance est grande, l'apport en soluté est limité par diffusion. De plus, des fluctuations dans l'équilibre des pressions dans le films de gouttelettes créé des flux d'advection qui perturbent la pousse des cristaux. Ces observations permettent de créer un meilleur système de croissance pour empêcher la déstabilisation des cristaux.

Résumé

Outre la fabrication de cristaux, leur structuration est importante pour leur intégration dans des systèmes. Un défi est d'induire la croissance à des positions définies sur un substrat. Ici, les gouttelettes sont disposées sur des surfaces fonctionnalisées avec des monocouches auto-assemblées de thiols hydrophobes et hydrophiles, permettant de croître des cristaux aux positions ainsi définies. Cette méthode permet aussi d'éviter la déstabilisation des monocristaux par un meilleur contrôle de la distribution des gouttelettes. Varier la concentration de la solution de cyanine permet un contrôle partiel du degré de cristallisation. Cependant, le contrôle du nombre de cristaux par gouttelettes est difficile. Une meilleure maîtrise du processus d'évaporation et de recuit permettrait sûrement de mieux contrôler la nucléation. Enfin, la structure cristalline et les propriétés optiques des monocristaux de cyanine sont étudiés. La structure cristalline, résolue par diffraction de rayons X, donne lieu à des couplages excitoniques révélés par spectrophotométrie sous lumière polarisée. Quoiqu'une étude plus approfondie des propriétés optiques est nécessaire, ces résultats sont prometteurs pour les dispositifs photovoltaïques puisqu'ils permettraient d'améliorer le transport d'excitons dans les films de cyanine.

Mots clefs : Semiconducteurs organiques, cyanine, morphologie, cristaux moléculaires, couches minces



Contents

Acknowledgements	i
Abstract/Résumé	iii
List of figures	xi
List of tables	xv
List of schemes	xvii
Context and structure of the thesis	1
1 General introduction	5
1.1 Organic semiconductors for optoelectronic applications	5
1.1.1 General characteristics of organic semiconductors	5
1.1.2 Organic semiconductor materials	7
1.2 On the importance of OSC thin film morphology	12
1.2.1 Molecular solids	13
1.2.2 Spectroscopic properties of molecular crystals	14
1.3 Fabrication and patterning of thin-film molecular crystals	20
1.3.1 Vapor growth	21
1.3.2 Solution growth	22
1.3.3 Patterning of functional material	28
2 Structuring amorphous thin films of cyanine dyes	41
2.1 Introduction and aims	42
2.2 Results and discussion	44
	vii

Contents

2.2.1	Droplet film formation	44
2.2.2	Diffraction from droplet films	46
2.2.3	Extinction and contribution of scattering	46
2.2.4	Array of scatterers in a diffraction plane	49
2.2.5	Anomalous dispersion effect	52
2.2.6	Droplet height and size distribution	54
2.2.7	Non-resonant Mie scattering	55
2.2.8	Towards sensor applications	57
2.3	Conclusion	58
2.4	Experimental details	59
2.5	Supporting Information	61
3	Dye crystal stability	75
3.1	Introduction and aims	75
3.2	Results and discussion	81
3.2.1	Cyanine crystal morphology evolution: from polyhedral to hopper to dendritic crystals	81
3.2.2	Growth conditions	83
3.2.3	Stable growth of polyhedral crystals	85
3.2.4	Transition from stable growth to polyhedral instability	87
3.2.5	Dendritic branching	90
3.3	Conclusion	92
3.4	Experimental details	94
3.5	Supporting Information	94
4	Local droplet deposition, nucleation and growth of cyanine thin film crystals	103
4.1	Introduction and aims	103
4.2	Results and discussion	109
4.2.1	Droplets deposition and dimensions	109
4.2.2	Nucleation mechanism	114
4.2.3	Influence of solution concentration on crystal mass	121
4.3	Conclusion	122

4.4	Experimental details	123
4.5	Supporting Information	125
5	Structure and optical properties of cyanine thin film single crystals	131
5.1	Introduction and aims	131
5.2	Results and discussion	132
5.2.1	Crystal morphology and structure	132
5.2.2	Out-of-plane orientation of the thin film crystal	135
5.2.3	Optical transmission of CyC platelet crystals	136
5.3	Conclusion	141
5.4	Experimental details	142
5.5	Supporting Information	144
6	Conclusions and outlook	173
	Curriculum Vitae	177

List of Figures

1.1	Diagram of electronic coupling between two identical molecules and limiting case of allowed transition depending on the molecules' orientation	15
1.2	Absorption spectra of PIC in its non-aggregated and aggregated forms	17
1.3	Schematic representation of the extended dipole model	18
1.4	Schematic representation of energy levels resulting from electronic coupling in a molecular crystal	19
2.1	Morphogy of CyC droplets spin-cast at different velocities	45
2.2	Angular diffraction intensity from CyC droplet samples	47
2.3	Extinction spectra, absorbance spectra and optical constants of CyC droplet films	48
2.4	Simulated diffraction efficiencies for the three droplet scattering regimes	52
2.5	Simulated extinction spectra of droplets of different dimensions	53
2.6	Simulated extinction spectra of hemispherical droplets with fixed optical constants	54
2.7	Simulated near-field intensity within CyC droplets	55
2.8	Experimental and simulated changes in extinction spectra of CyC droplet structures with different environmental refractive index	57
S2.1	CyC droplets height and radius distributions as a function of spin-coating velocities	61
S2.2	Height and radius of droplets from droplet samples	61
S2.3	Arrangement of droplets used in the FDTD simulations	62
S2.4	FDTD simulations of extinction spectra of different droplet ensembles	63
S2.5	Simple geometric argument to explain the origin of diffraction orders	66
S2.6	Scattering elements distribution and calculated diffraction pattern	69
3.1	Normal growth rate as a function of the driving force for crystal growth	79

List of Figures

3.2	Schematic representation of the concentration distribution along a crystal face under diffusion limitations.	81
3.3	SEM images of crystals illustrating the observed stages of morphological transformation.	82
3.4	Configuration of crystal growth conditions.	83
3.5	Evolution of droplet number and area during crystal growth.	85
3.6	Growth kinetics of a CyC single crystal during SVA	86
3.7	Droplets distribution around a growing CyC crystal over time.	88
3.8	AFM topographic image of CyC crystal unstable face	90
3.9	Optical micrograph of a large dendritic crystal and evolution of fractal dimension with crystal size	91
S3.1	<i>In-situ</i> microscopy time lapse of droplets size evolution	95
S3.2	Binary images of <i>in-situ</i> time-lapse	96
S3.3	AFM topographic image of a CyC hopper crystal	97
S3.4	<i>In-situ</i> time-lapse of crystal growth	98
4.1	Excess Gibbs free energy as a function of cluster size	106
4.2	Schematic solubility-supersolubility phase diagram	108
4.3	CyC droplet deposited on substrates patterned with SAMs	110
4.4	Droplet dimensions after deposition on pattern substrates as a function of dye solution concentration	111
4.5	Array of annealed CyC droplets observed under optical microscope	115
4.6	AFM topography images of CyC droplets after solvent vapor annealing	116
4.7	Optical microscopy images of droplets cast from different concentrations, after solvent vapor annealing	117
4.8	Crystal density as a function of droplet volume	120
4.9	Crystal mass and droplet mass as a function of CyC solution concentration	121
5.1	AFM topographic image of a CyC single crystal	133
5.2	CyC crystal asymmetric unit and packing	134
5.3	Comparison between experimental crystal morphology and BFDH model	136

5.4 The comparison between θ - 2θ diffractograms of platelet crystals and calculated from single crystal analysis	137
5.5 Absorbance spectra of CyC in solution, as a thin film and a single crystal	138
5.6 Absorption spectra of CyC crystal under linearly polarized light	140
S5.1 Full BFDH morphology prediction of CyC crystal	144
S5.2 Photoluminescence and excitation spectra of CyC platelet crystals	145
S5.3 Calculated absorption spectra of CyC crystal neglecting excitonic couplings	146
S5.4 Identification of exciton coupling terms within the crystal structure	148
S5.5 Sketch of the micro-spectrometer setup	150
S5.6 Spatially resolved absorption spectra of a CyC single crystal	151
S5.7 Additional polarized transmission spectra of CyC platelet crystal	152
S5.8 Estimated reflection from a 50 nm CyC film	153



List of Tables

S4.1 Values measured for CyC amorphous film density evaluation	126
S4.2 Physical values used for calculations of the Péclet number	126
5.1 Calculated equilibrium BFDH morphology of CyC crystals	135
S5.1 Excitonic couplings between pairs of chromophores in the CyC crystal structure	147



List of Schemes

1.1	General structure of cyanine dyes and mesomeric resonance structure of poly-methines	11
1.2	Chemical structure of CyC	12



Context and structure of the thesis

The gloomy perspective of an imminent shortage of fossil fuels as well as the manifest impact of human energy consumption on the environment is driving the development of more sustainable and cost effective ways of harvesting energy from renewable sources, such as wind, biomass, geothermal, hydropower, ocean waves or solar power. On the other hand, the ever growing demand for consumer technology products necessitates the development of ever smaller and ever lighter electronic components and devices. These two factors have led to the development of new devices that have taken on a major importance from technological and economical points of view. These devices include thin film transistors, photovoltaic solar cells, light-emitting devices and sensors among others.

Along with the elaboration of new technological concepts comes the necessary development of new materials and processes. Although for a long time the microelectronic industry has been dominated by silicon-based technologies, new materials have been explored during the last 50 years to try to overcome certain impediments linked to these technologies. In addition, research has been motivated by the scientific interest to explore new fundamental aspects of the solid state properties of novel materials. In particular, organic semiconductor (OSC) materials have been extensively researched, boosted by the promises of lower production costs than their inorganic counterparts.

Nature shows many examples where the properties of a system are altered when a certain level of order is introduced in its structure. Ordering can occur at various length scales, from molecular building blocks to macroscopic dimensions. An interesting feature of OSCs is their ability to generate new physical properties when brought in close contact, while retaining some of their molecular attributes. Fine-tuning the morphology of OSC thin films can help engineer new functional properties in materials and therefore the study of property-

morphology relationships is particularly important.

This thesis focuses on the structure-property relationship in thin films of cyanine dyes. This specific class of OSCs is relevant for a number of applications such as organic solar cells and light-emitting devices because of their unique light absorption and emission properties. Specifically, two aspects will be addressed. The first aspect relates to the morphology control of cyanine dye films and the creation of assemblies at the microscopic and nanoscopic scales. The second aspect focuses on exploring and understanding the new properties arising from these assemblies.

Chapter 1 aims to motivate this work in the broader context of organic semiconductor materials for applications. After defining the general characteristics of OSCs, a brief overview of the main classes of materials that have been researched so far will be given, examining the place of cyanine dyes among them. After a discussion on the importance of morphology in molecular solids, a review of the recent methods developed to control OSCs' thin film morphology will be provided. Particular importance will be given to solution-deposition methods. This introduction is meant to be general and more specific background will be deepened at the beginning of each chapter.

In **chapter 2**, this work investigates the optical features arising from an ensemble of cyanine droplets deposited on a substrate, with dimensions in the range of visible light wavelength. Light-matter interactions can vary widely when a system is brought from randomness to order (or even partial order), in particular if the characteristic length-scale of the system matches that of the wavelength of light. The strong light-scattering efficiency resulting from sub-micrometer cyanine dye droplets was already pointed out in previous work. Here the focus lies on investigating the origin of the phenomenon and the relationship between droplets morphology and scattering efficiency. A detailed analysis of the observed effect is presented, based on experimental data and finite-difference time-domain simulations.

Earlier work had demonstrated the possibility to grow single crystals of cyanine dye by exposing dewetted droplet films to solvent vapor. In **chapter 3**, the morphological evolution of cyanine crystal during growth is investigated. Specifically, it is shown that the initial crystal morphology destabilizes and transition from a polyhedron to a dendritic crystal. By in-situ

microscopy observation during growth and atomic force microscopy of individual crystals, the link between changes in morphology and growth conditions is highlighted.

Organization of single crystalline objects on a substrate is particularly relevant for device applications. However, it also presents many challenges in terms of processing. **Chapter 4** aims to demonstrate the possibility to grow single crystals of cyanine dye at specific locations on a substrate. The approach developed involves surface patterning of substrates to induce preferential dewetting of the dye droplets.

The anisotropic nature of planar molecules such as cyanine dyes leads to the dependence of many physical properties, often critical to devices' performances, on the orientation of molecules within a thin film. The use of thin molecular crystals represents an interesting approach to enhance dyes' intrinsic optical properties. **Chapter 5** focuses on relating the structure of cyanine crystals to their optical properties. By means of x-ray analysis and local transmission microspectroscopy on individual crystals, this chapter aims to shed light on the photophysics of this system.

Finally, **chapter 6** will summarize the conclusions of this work and give a few perspectives for future research possibilities on this topic.

1 General introduction

1.1 Organic semiconductors for optoelectronic applications

In the last two decades, organic electronics and optoelectronics have generated tremendous interest across many fields of research from chemistry, to material science to applied physics and engineering. This enthusiasm has resulted from the perspective of potential low-cost high-tech applications^[1] such as light-emitting devices (OLEDs),^[2,3] organic field-effect transistors (OFETs)^[4,5] and organic photovoltaics (OPVs).^[6,7] On the other hand, the wide variety of materials available and the almost endless possibilities to tune their properties through chemistry routes have made these fields particularly attractive.^[8] This section first describes the key features characterizing materials used in organic optoelectronics. Then, a review of the most important classes of such materials is given with particular emphasis on cyanine dyes.

1.1.1 General characteristics of organic semiconductors

Organic optoelectronics are based on organic semiconductors (OSCs). These materials encompass many compounds, comprising small molecules and polymers, which contain conjugated chains of carbon atoms. OSCs have the ability to transport charges under certain conditions, however, they are intrinsically poor conductors and charge transport generally results from extrinsic factors such as charge injection, doping or dissociation of photo-generated

Chapter 1. General introduction

electron-hole pairs.^[9]

The possibility of OSCs to transport charges is the result of the hybridization of carbon atoms. In conjugated π -systems, the hybridized $2sp^2$ orbitals form σ -bonds while the remaining $2p_z$ orbitals of each carbon will overlap, forming a π -orbital above and below the plane of the π -system. The shared pair of electrons in π -orbitals of adjacent carbons constitutes a π -bond. Through the conjugation of neighboring π -orbitals, electrons can delocalize over the conjugated system.

A key feature characterizing organic semiconductor molecules is the energy gap ΔE between the highest occupied molecular orbital (HOMO) and the lowest unoccupied molecular orbital (LUMO). Because σ -orbitals between two carbon atoms exhibit a significant amount of electron density close to the nuclei, the splitting between bonding and anti-bonding states σ and σ^* of these orbitals is large. On the other hand, interactions between the $2p_z$ constituting the π -orbitals occur at some distance from the nuclei and therefore the splitting energy between bonding and anti-bonding states (π and π^*) is small. Therefore in organic semiconductors, HOMO and LUMO correspond to π and π^* -orbitals, respectively. It is clear that in molecules containing conjugated π -electrons, ΔE is related to the conjugation length of the system. A simple illustration of this relation can be given by considering a linear π -conjugated system as a 1-dimensional quantum box. The energy difference between HOMO and LUMO is given by^[10]

$$\Delta E = \frac{(2n + 1)h^2}{8mL^2} \quad (1.1)$$

where h is Planck's constant, m the mass of an electron, L represents the length of the conjugated system and n is number of electrons in the box. Since n and L are proportional to the number of carbon atoms N involved in the system, it is clear from Equation 1.1 that $\Delta E \sim 1/N$. Bandgaps in organic semiconductors are large, typically on the order of 2-4 eV. Such large bandgaps prevent the creation of intrinsic charge carriers at room temperature, as it is the case with most inorganic semiconductors. Nevertheless, this energy range corresponds to that of visible light, from wavelengths of 700 nm to 400 nm. Therefore, electrons in OSCs

1.1. Organic semiconductors for optoelectronic applications

can be promoted to an unoccupied orbital absorbing visible photons, provided their energy matches that of the bandgap: $\Delta E = \frac{hc}{\lambda}$. In practice, however, most conjugated systems cannot be well represented by the particle in a box model because π -electrons are usually not fully delocalized. Hence, increasing the conjugation length is not always sufficient to reduce the bandgap of OSCs and different approaches for bandgap control have been investigated.^[11-13]

Mainly composed of carbon atoms, molecular OSCs typically exhibit low dielectric constants ϵ , because carbon's valence electrons are more tightly bound to the nucleus than those of silicon, for instance. Therefore, most OSCs possess a dielectric constant in the range of $\epsilon = 3.5-5.5$ while for crystalline silicon $\epsilon = 11.5$.^[14] As a result, electrons and holes in OSCs are tightly bound by electrostatic interactions which has important implications on their electrical and optical properties.

The absorption of a photon by an organic semiconductor generates an excited state that can be described in the solid state by a neutral quasi-particle consisting of a tightly bound electron-hole pair called *Frenkel exciton*. These excitons have typical binding energies of 0.1-0.5 eV due to the low dielectric constant of OSCs.^[14] Excitons can also be generated in inorganic semiconductors at low temperature,^[15,16] however their binding energy is generally low, on the order of 0.01 eV, due to the Coulombic screening resulting from the high dielectric constants of inorganic semiconductors. This is a fundamental difference between organic and inorganic semiconductors. While excited states in inorganic semiconductors can dissociate readily (at room temperature) into free electrons and holes, *Frenkel excitons* remain as neutral quasi-particles, unaffected by electric fields, and diffuse from molecular sites to molecular sites until they recombine or find a suitable interface to dissociate into free electrons and holes. The concepts of generation and transport of excitons and charges are at the core of most applications where OSCs are used.

1.1.2 Organic semiconductor materials

Organic semiconductors can be classified in two types: *small molecules* and *polymers*. Small molecule is a broad term which regroup all classes of compounds with a well-defined, generally small molecular weight. On the other end, polymers are long chain-like macromolecules, constituted of a large number repeating units. Contrary to small molecules, the molecular

weight of polymers is not well-defined and generally presents a certain distribution.

These two classes present a number of similarities in their electronic and optical properties, in particular the fact that excitonic states govern their optical properties. However, small molecules and polymers each present their own advantages and shortcomings in terms of processing and integration into devices. In this section, a brief overview of the most representative compounds of each class is given. The emphasis is put on organic dyes, in particular cyanines, which are the focus of this work.

Semiconducting polymers

In 1976, Shirakawa, MacDiarmid and Heeger discovered conducting polymers by studying the conductivity of different halogen derivatives of *trans*-polyacetylene, one of the simplest π -conjugated polymers.^[17] This major discovery opened the way to new fields of research, enabling researchers to address a number of fundamental questions in the fields of quantum chemistry and condensed-matter physics.^[18] Perhaps most importantly, it opened novel perspectives for the fabrication of a new generation of materials, combining the optical and electrical properties of metals or semiconductors, while conserving the mechanical characteristics and processing benefits of polymers.^[18] Since the discovery of Shirakawa, MacDiarmid and Heeger, a large library of semiconducting polymers has been synthesized and investigated.^[8,19,20] Important classes of conjugated polymers include the highly luminescent poly(*para*-phenylenes) which have found applications in OLEDs,^[21,22] polythiophenes^[19,23] and poly(*para*-phenylenes)^[24] which have been used in OFETs^[25,26] and OPVs.^[26]

Most conjugated polymers possess a one-dimensional extended π -system which enables them to interact with visible light and transport electric charges along their backbone.^[19] Because of the inherent bond length alternation in their conjugated backbone, π -electrons are not fully delocalized and therefore most conjugated polymers present a bandgap between HOMO and LUMO levels. Moreover, because the chains are never ideal and always contain defects, chemical or structural, the effective conjugation length is typically smaller than the length of the polymer chain which tends to reduce the overall mobility of the polymers.

Because of the strong intermolecular interactions between their conjugated backbone, most

1.1. Organic semiconductors for optoelectronic applications

semiconducting polymers are rather insoluble. To be processed through solution routes, they need to be functionalized in order to become soluble in common organic solvents. This is generally achieved by adding alkyl or alkoxy side-chains to the backbone. While side-chains substantially improve polymers' solubility they may also induce some torsions between consecutive repeating units leading to interruption in the conjugation of the backbone.^[27] Moreover, introduction of alkyl side-chains generally increases polymers' sensitivity to atmospheric oxygen, by increasing their HOMO levels.^[28,29]

On the other hand, side-chains can influence the relative orientation of polymer chains upon deposition in the form of thin films.^[9] This is important because the microstructure of polymers in the solid state plays a key role in controlling the properties of the materials.^[30,31] The optoelectronic properties of polymer films do not only depend on intra-chain transport along the polymer backbone but inter-chain interactions are also a key feature playing an important role on luminescence efficiency,^[32] charge carriers generation,^[33,34] and charge carriers' mobility.^[35,36] However, polymer films most commonly consist of crystalline regions dispersed in an amorphous matrix^[37] therefore containing detrimental interfacial regions and grain boundaries.^[38] The fabrication of single crystalline or highly crystalline semiconducting polymer films remains challenging. This is in part due to the large free energy cost necessary to rearrange the many chain conformations, further accentuated by the various energy contributions arising from π - π stacking and the hydrophobic interactions between aliphatic side-chains.^[39] The use of polymeric OSCs generally requires to find a balance between convenient processing possibilities, morphology and properties.

Small molecule organic semiconductors

The interest for semiconducting small molecules emerged in part from early studies on conductivity, photoconductivity, fluorescence and the photoelectric effect of organic crystals.^[9] In the mid-1960's, the discovery of anthracene's electroluminescence^[40,41] boosted researchers' curiosity to synthesize and study the properties of molecular solids. In comparison to polymer semiconductors, small molecules are monodisperse and their synthesis is generally well reproducible.^[7] Until the mid-1990s, research on organic electronics was mostly focused on carbon-based skeleton materials, comprising polycyclic aromatic hydrocarbons (PAHs),^[42]

Chapter 1. General introduction

conjugated oligomers, such as phenylvinylene and oligothiophenes, and fullerenes.^[4,43] In particular, oligoacenes such as pentacene, anthracene and its derivative, rubrene, have attracted much attention.^[44,45] Although rather insoluble, these low molecular weight compounds can be deposited in the form of large single crystals of high purity through multiple sublimation steps.^[46,47] They therefore provide an excellent platform to study the fundamental structure-properties relationships^[48-50] and have been used to produce some of the highest mobility thin film organic transistors.^[51,52]

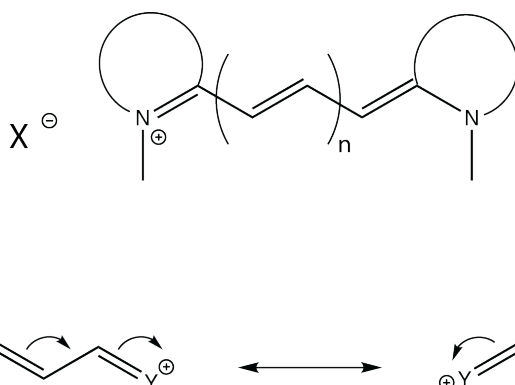
In parallel to the few compounds mentioned above, other classes of functional molecules emerged from various industries where they were already used as organic dyes and pigments^[53] or as active layers in photoconductor technology.^[54] Their potential was demonstrated in 1986, when C.W. Tang used copper phthalocyanine (one of the most widely used colorants) together with a perylene tetracarboxylic derivative to prove the concept of heterojunction photovoltaic cells.^[55] However, at the end of the 1990's the interest for organic colorants had faded and the demand from the fields in which they were still in use such as data storage, non-linear optics and impact printing remained relatively small.^[43] Nonetheless, in the last 15 years, the expanding field of organic electronics has given organic colorants a new lease of life and they are now applied in the various fields of organic electronics as demonstrated in a recent review by M. Gsänger *et al.*^[43]

Cyanine dyes form an important class of polymethine compounds, owing to their unique optical properties. The first cyanine dye was synthesized by Williams in 1856, who described a compound with "*a blue of great beauty and intensity*".^[56] Different dyes with the same basic structure were later synthesized showing a wide variety of colors but the term cyanine (from *cyanos*, blue) remained. Cyanine dyes generally exhibit pronounced absorption and fluorescence in the visible and near-infrared range. These features have made them particularly attractive, for example as labeling reagents for biological samples.^[57]

Cyanine dyes are organic salts, generally composed of a photoactive cation (the *chromophore*) and a non-photoactive anion (the *counterion*), although anionic chromophores can be synthesized and photoactive anions have also been used.^[58,59] Their general structure is presented in Scheme 1.1. The chromophores are composed of a π -conjugated polymethine chain, comprising an odd number of methine units ($-\text{CH}=\text{}$), appended on each side by N-heterocyclic rings.

1.1. Organic semiconductors for optoelectronic applications

It has been understood early on that the color of the compounds was mainly determined by the length of the polymethine chain.^[58] As visible from Scheme 1.1, the positive charge born by the nitrogen atom results in equal mesomeric resonance structures. This leads to the perfect delocalization of the π -electrons and very small bond length alternation, bringing cyanine dyes particularly close to the ideal polymethine state, which can be well described by the particle in a box model.^[60] This characteristic gives polymethine compounds especially small bandgaps compared to other small molecules with a similar number of carbon atoms involved in the conjugated system. By tuning the length of the polymethine chain, the maximum absorption of the dye can be shifted by approximately 100 nm for each additional methine unit. Monomethine ($n = 0$), trimethine ($n = 1$), pentamethine ($n = 2$) and heptamethine ($n = 3$) dyes have been reported in literature. Longer polymethine chains generally result in the loss of the ideal polymethine state, due to oxidation of the double bonds and breaking of the polymethine chain symmetry.^[61,62]



Scheme 1.1 – The general structure of cyanine dyes (top) and mesomeric resonance structure of polymethines flanked by nitrogen-containing end groups Y (bottom).

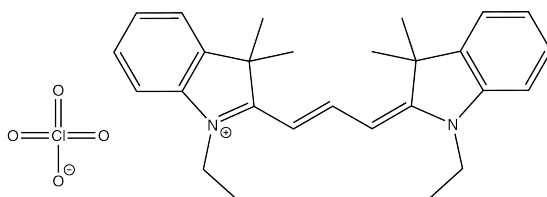
The ionic character of cyanines makes them well suited for solution processing since they are generally soluble in a range of common organic solvents. The nature of the counterion can be diverse, from halide ions to bulky anions such as Δ -TRISPHAT⁻.^[59] Although the influence of the counterion on the optical properties of the dye in solution has been shown to be limited, its influence on the solid state morphology and device performances is significant.^[59,63] Moreover, the nature of the counterion can also have an influence on the bond length alternation. Strongly coordinating anions have been shown to disturb the ideal polymethine state of the chromophores by distorting the electron cloud in the π -system resulting in the loss of cyanines'

Chapter 1. General introduction

absorption properties.^[62]

Substitution can be performed at various loci on the chromophore to fine tune its properties. For example, short alkyl chains are often substituted on the heterocycles' nitrogens in order to ensure the good solubility of the dye.^[64] In addition, different heterocycles can be used to extend the conjugation length of the dye, hence shifting the absorption to the near-infrared.^[62] Finally, substitutions along the polymethine chain with either electron-donating or -withdrawing substituents have been shown to alter the bandgap and modify the HOMO and LUMO levels of the chromophores.^[65] This chemical versatility makes cyanine dyes particularly attractive as organic semiconductor compounds for application in optoelectronics.

The structure of the cyanine dye studied in this work is shown in Scheme 1.2. It is composed of a trimethine cationic chromophore (Cy³⁺) associated to a perchlorate anion (ClO₄⁻). The structure's name is abbreviated "CyC" in the rest of this manuscript.



Scheme 1.2 – Chemical structure of CyC

This trimethine dye has been used as a standard dye for the study of organic solar cells^[66–69] and light emitting electrochemical cells.^[70] The study of its morphology-property relationship is therefore particularly relevant in this regard.

1.2 On the importance of OSC thin film morphology

The previous section mentioned at several occasions how the intrinsic properties of OSCs can depend on the specific arrangement of molecules in the solid state. Organisation of OSC materials at different length scales can influence the material's intrinsic properties or device performances. If the development of ever smaller and lighter devices has naturally promoted the processing of materials in the form of thin films,^[71] the morphological nature of the thin layers can vary depending on the intended application and has evolved over the year to optimize device performances. This section compares the different types of molecular solids,

1.2. On the importance of OSC thin film morphology

with particular emphasis on molecular crystals and their specific spectroscopic properties, which is the topic of this thesis.

1.2.1 Molecular solids

Molecular solids are held together by weak and short range van der Waals interactions. In comparison intramolecular binding is strong in organic solids and therefore most of their electronic and optical properties partly retain the attributes of their constituting individual molecules, as opposed to covalent or ionic crystals. Nonetheless, the characteristics of molecular solids are strongly related to the overlap of the frontier orbitals and therefore the collective arrangement of molecules in an organic solid has an important role to play on the electronic and optical processes in OSCs. In particular, charge transport,^[72,73] exciton diffusion,^[48,74,75] energy transfer, energy level alignments^[76] and absorption^[49,77] are properties playing a key role in the performance of organic optoelectronic devices and that are related to the molecular arrangement in the solid state.

One usually distinguishes two types of molecular solids: amorphous molecular films and molecular crystals. To a certain extent, polycrystalline films could also be considered as a type of molecular solid.^[14,78] Amorphous molecular films generally present a "glass-like" morphology where molecules are randomly oriented relative to each other, resulting in homogeneous and isotropic properties of the material.^[79,80] They have some advantages in terms of processing: they are easy to deposit on large area through vacuum or solution methods on a variety of substrates, compared to the delicate growth and handling of crystalline materials. On the other hand, amorphous states in semiconductor small molecules generally correspond to non-equilibrium states that can recrystallize above a certain temperature leading to polycrystalline films,^[81] which can eventually be detrimental to optoelectronic properties.^[82]

Molecular crystals are characterized by the ordered arrangement in space of repeating building units in a point lattice. The strong distance dependence of van der Waals forces ($F_{vdW} \propto r^{-7}$) generally leads to rather tightly packed structures. Therefore, the optical and electrical properties of molecular semiconductor crystals are usually highly anisotropic. In general molecular crystals are made up of individual molecules, they can also be made of pair of molecules

bound together more or less strongly. This is the case for example of pyrene, where two weakly bound identical pyrene molecules constitute the building units of pyrene crystals. Another example is that of crystals made of organic salts, such as cyanines, where the building units are composed of a chromophore and its counterion. Although the counterion does not have a direct influence on the optoelectronic properties, it can still affect the crystal packing which leads to variations of various solid state properties of the compound such as melting temperature and spectroscopic properties.^[63]

While the interest in molecular crystals mostly revolves around the field of organic field-effect transistors, due to the improved charge mobilities resulting from the higher degree of order, some studies have also been devoted to other applications where crystalline material could improve devices' performance.^[83] For example, Tseng *et al.* studied the anisotropic photovoltaic properties of a tetracene single crystal/ C_{60} bilayer solar cell.^[84] They showed that the anisotropic absorption of the tetracene crystal resulted in orientation-dependent photocurrent and photovoltaic efficiency in the solar cell. However, these efficiencies remained quite low (>0.1%), in part because of practical limitations on the thickness of the crystals (about 220 nm), which limits efficient charge collection and because of the relatively high transparency of tetracene crystals. From a more fundamental perspective, single crystals are also interesting because they present well defined structures which can be used as models to study a specific property of a compound. For example, the study of oligothiophene crystals' properties has served as a basis to understand conductivity of polythiophenes.^[78,85]

1.2.2 Spectroscopic properties of molecular crystals

An interesting characteristics of molecular solids is their capacity to transfer and transport optical excitation energy to another place in the solid where it can induce photophysical processes requiring energy such as the generation of charge carriers, sensitized luminescence or photochemical reactions.^[86] A number of important phenomena characteristic of molecular solids such as exciton formation, transition band splitting and energy transfer can be probed by means of spectroscopic methods and give precious information about the photophysical behavior of molecules and their interactions with their local environment.

1.2. On the importance of OSC thin film morphology

Molecular exciton formation

A good starting point to understand the specificity of molecular crystals' spectroscopic properties is to consider the case two identical molecules brought together to form a weakly interacting pair called a *physical dimer*. This type of structure occurs often in planar, linear π -conjugated chromophores that do not contain side-chains such as naphthalene, anthracene, tetracene and pentacene. The treatment of this problem was first considered by Alexander Davydov in 1948 and treated with a simple formalism by Michael Kasha in 1965.^[87,88] It is sometimes referred to as the *theory of molecular exciton*.

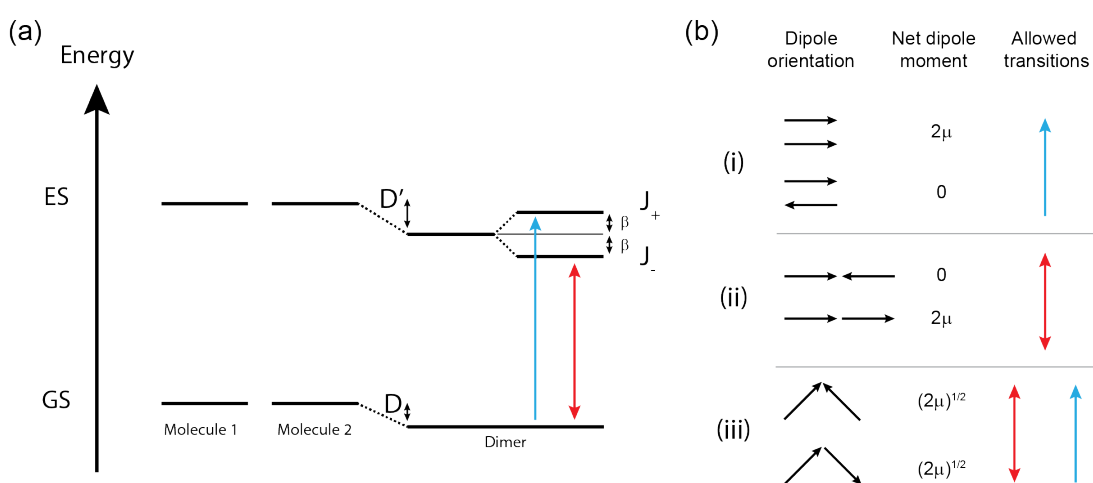


Figure 1.1 – (a) Schematic diagram of the energy level splitting resulting from the electronic coupling between two identical molecules. (b) Limiting cases of allowed transitions depending on the orientation of the molecules constituting the dimer.

The energy level situation resulting from the electronic coupling between two identical molecules is presented in Figure 1.1 (a). The formation of a physical dimer results from van der Waals interactions which reduce the energy of the ground state (GS) of the dimer compared to the individual molecules taken in the gas state. This polarization energy D depends of course on the intermolecular distance and orientation between the two molecules. One of the key assumptions here is that the overlap between molecular orbitals is small. Therefore, the perturbation problem can be treated to the first order only. When one of the two molecules is excited by the absorption of a photon, the excitation can resonantly oscillate between the molecules. Thus, the excited state (ES) splits into two levels J_+ and J_- separated by the resonance interaction energy β around an average level corresponding to the excited

Chapter 1. General introduction

state of the single molecules diminished by the van der Waals interaction energy of the excited state of one molecule with the ground state of the other, D' .

The probability of a dimer to go from its ground state to one or the other of the split energy levels (in other word the oscillator strength of the transitions) depends on the orientation of the transition dipole moments of the molecules. Three limiting cases are generally considered. They are presented in Figure 1.1 (b):

- (i) When the molecules stack on top of each other, only the transition to J_+ is allowed when transition dipole moments are parallel. In the anti-parallel configuration, the sum vector of the transition dipole moments is equal to 0 and the transition has no oscillator strength. This results in a blue-shift of the absorption spectrum with respect to that of the original molecule. The excited state will relax non-radiatively to the J_- state and finally to the ground state.
- (ii) When the molecules arrange in a sequential fashion, only the transition to J_- is allowed, corresponding to parallel arrangement of the transition dipole moments. This results in a red-shift of the absorption spectrum. In this case, the excited electron can relax to the ground state by emitting a photon.
- (iii) When the molecules are arranged in a arbitrary fashion, both transitions are allowed and the oscillator strength of each depends on the vector sum of the monomer transition dipole moments. In this case, the transitions are polarized in the directions of the resulting vector sums.

Configurations (i) and (ii) are found in *H-* and *J-aggregates*, respectively. In these structures, many molecules form supramolecular aggregates in either one or the other arrangement and an exciton band is formed over many chromophores. The formation of delocalized coherent exciton upon absorption results in a sharp red-shifted absorption band in the case of *J-aggregate* together with strong fluorescence. On the other hand, *H-aggregates* show blue-shifted absorption and no fluorescence. The study of *J-aggregates* is strongly linked to that of cyanine dyes, since their peculiar optical properties were first observed by Scheibe and Jelley in pseudoisocyanine (PIC). A comparison between the absorption spectra of PIC in its

1.2. On the importance of OSC thin film morphology

non-aggregated and J-aggregated form is reproduced in Figure 1.2. The scientific interest in cyanine J-aggregates has grown mainly during the silver halide photography era, when it was recognized that such structures could be used to sensitize photographic emulsions to specific wavelengths. Since then, many studies concerning their fabrication, structural characteristics, optical and photophysical properties have been conducted. A 2011 review by Frank Würthner and co-workers gives an excellent overview of the different aspects of dye aggregates.^[58]

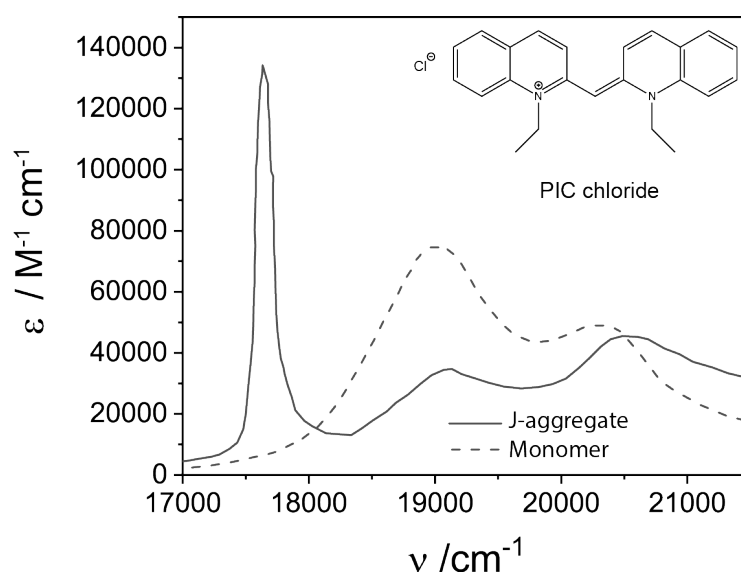


Figure 1.2 – Absorption spectra of PIC chloride J-aggregates in water solution (solid line) and its monomer in ethanol (dash line). The J-aggregated dye shows a characteristic narrow and intense absorption peak, red-shifted in comparison to the monomer species' spectrum. Adapted with permission from [89].

A simple model to estimate the excitonic splitting term J was developed by Hans Kuhn and co-workers.^[90] In this *extended dipole model*, the molecules are represented as dipoles with a positive and negative charge Q separated by a distance L . The value of Q is related to the transition dipole moment of the molecule by the relation $\mu = Q \cdot L$. The splitting term can therefore be expressed as

$$J = \frac{Q^2}{4\pi\epsilon\epsilon_0} \left(\frac{1}{R_1} + \frac{1}{R_2} - \frac{1}{R_3} - \frac{1}{R_4} \right) \quad (1.2)$$

where $R_i (i = 1...4)$ is the distance between the charges as presented in Figure 1.3, ϵ the di-

Chapter 1. General introduction

electric constant of the molecule and ϵ_0 the vacuum permittivity. This model gives very good approximation of the spectral shifts to expect for dimers with short distances (below 1 nanometers).

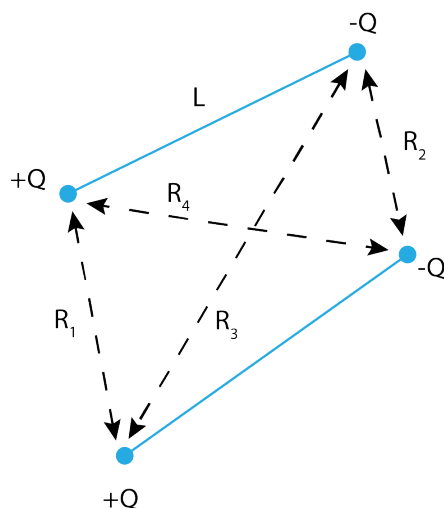


Figure 1.3 – Schematic representation of a dimer in the extended dipole model. Each molecule is represented by a dipole with positive and negative charge Q , separated by the distance L .

From molecular excitons to Frenkel excitons

So far, the result of electronic interactions between two molecules has been presented. In order to understand the nature of excitonic excitation in a molecular crystal, the concept of dimer coupling has to be extended to an infinitely large 3-dimensional crystal lattice. Such problem is conceptually similar to that of transitioning from the covalent bonding between two atoms to a valence/conduction band structure with delocalized states in metals and inorganic semiconductors. As represented in Figure 1.4 (a), the two well defined levels presented in Figure 1.1 for the dimer split into a manifold of levels to form a *excitonic band structure*, whose width depends on the overlap of molecular orbitals β in the lattice and the periodic lattice potential. The formal treatment of this problem exceeds the scope of this introduction, however it is presented in many reference textbooks.^[10,86] The concept can be further extended to a crystal in which the unit cell contains two molecules (Figure 1.4 (b)). In that case, the excitonic band splits to form two bands, the width of which is determined by the resonance interaction between translationally equivalent molecules in different unit cells. The

1.2. On the importance of OSC thin film morphology

magnitude of the splitting between the two bands (called *Davydov splitting*) is determined by the resonance interaction of non-translationally equivalent molecules within the unit cell. Davydov splitting has been clearly observed in tetracene and anthracene crystals.^[91,92] The number of Davydov components keeps increasing together with the number of non-equivalent molecules in the unit cell.

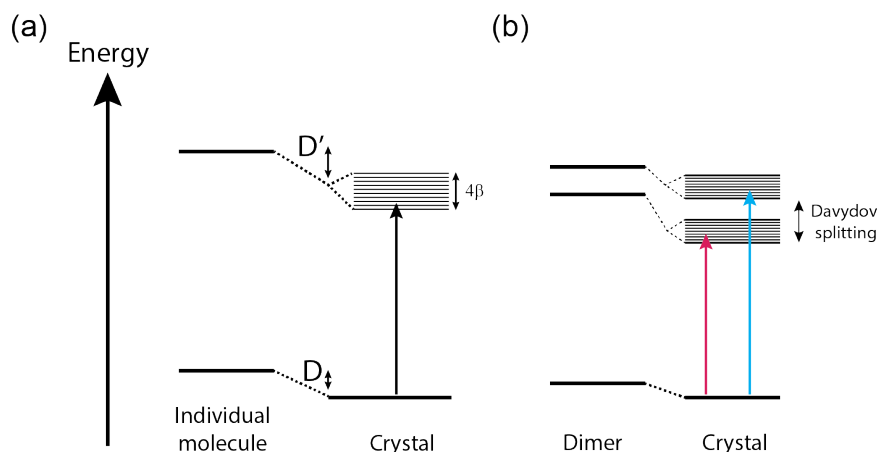


Figure 1.4 – Schematic representation of energy levels resulting from electronic coupling in a molecular crystal, (a) in the case of 1 molecule per unit cell and (b) 2 molecules per unit cell.

In this picture, an excited state initially arising on one molecule, can delocalize over the crystal lattice. This excited state can be seen as a quasi-particle of neutral charge and is called a *Frenkel exciton*. In principle, Frenkel excitons can travel coherently within a perfect crystal. However, static energetic disorder and vibrations of the crystal lattice (phonons) in most cases tend to scatter excitons and destroy the coherence of the exciton band. In that case, excitons travel by non-radiative energy transfer and thermal hopping between molecular sites of slightly different energies. In an absorption spectrum, the loss of coherency can be seen in the form of an inhomogeneous broadening of the excitonic transition bands, reflecting the energetic distribution of the individual molecules.^[93] An exceptional case is that of dye J-aggregates, for which the excitons have been shown to delocalize over 30-100 monomer units in the case of PIC chloride, depending on the experimental conditions and the methods used to calculate these number.^[58] Nonetheless, the extended coherence of excitons in J-aggregates accounts for the characteristic narrowness of their absorption and emission bands, as visible in Figure 1.2. One should note that the perfect excitonic band picture is hardly ever realized, since energetic disorder between molecular sites is always present even in single crystals, due

to slight conformation differences between molecular building units.

The solid state photophysics of cyanine dyes is relevant both from a fundamental and more applied point of view. As mentioned earlier, cyanine dyes have attracted much interest in the form of J- and H-aggregates. Their narrow absorption and emission bands and the tunability of their absorption maxima have made them particularly interesting for photodetection or lasing.^[94,95] However their use in functional devices remains scarce. One reason may be that, although their extinction coefficient is high, their absorption bandwidth is narrow which can be detrimental for certain applications. On the other hand, J-aggregates also have narrow emission which would make them interesting as monochromatic emitters, however their quantum yields are low due to re-absorption phenomena. This has prohibited their use in competitive light-emitting devices. On the other hand, cyanines have been well investigated in the form of amorphous thin film, for various optoelectronic applications, owing to their broad and strong absorption bands in the visible and near-infrared region. Examples include organic photovoltaic solar cells, light-emitting electrochemical cells and photodetectors.^[70,96,97] However, disorder and trap states limit the transport of exciton to a typical length of 5-10 nm, which limits the performances of photovoltaic devices. In this context, cyanine dye crystal appears as an interesting alternative. In particular, crystals having a broader absorption bandwidth than the aggregated species and lower static energetic disorder than the amorphous films might provide an interesting approach to improve OPV devices for example. From this perspective it is relevant to study the photophysical properties of cyanine dye crystals. While there are a large number of studies concerning J- and H-aggregates^[98] spectroscopic investigations of cyanine single crystals have been rather limited so far.^[99,100] In chapter 5 the structure and optical properties of CyC single crystals are investigated using crystal X-ray analysis and optical micro-spectrometry.

1.3 Fabrication and patterning of thin-film molecular crystals

The previous sections have stressed the importance of OSC single crystals to gain fundamental knowledge about a material's properties and in terms of device performances' improvement. As a consequence, the fabrication of single crystals has gained momentum and attracted researchers' interest. With some devices having entered the market already or being close

1.3. Fabrication and patterning of thin-film molecular crystals

to, the development of technologically relevant processing methods has become paramount. In particular, cost-efficiency, large area processing possibilities, high-throughput are important criteria to take into consideration. In order to meet these criteria, crystal fabrication processes should also allow controlling the location of single crystal growth as well as their crystallographic orientation. Two main routes to synthesize OSC single crystals are usually distinguished: vapor-based and solution-based methods, each presenting some advantages and drawbacks.

In this section, an overview of vapor and solution-based thin film crystal growth methods is given. Finally, a review of different techniques that have been developed to control the position and orientation of crystals on substrates is given. The emphasis will be put on small molecule materials, however, methods that have been applied to polymeric materials that might also be relevant for growth of small molecule crystals will be highlighted as well.

1.3.1 Vapor growth

Traditionally, vapor deposition methods have been the preferred method to fabricate organic molecular crystals owing to the high quality of the crystals and the high charge carrier mobility obtained.^[101] The deposition process in these methods is based on the evaporation (or sublimation) of the material by increasing its temperature, followed by its condensation on a substrate. These methods are sometimes grouped under the term *organic molecular beam deposition* (OMBD).^[46] Clearly, OMBD methods are only suitable for materials whose vaporization (or sublimation) temperature lies below their decomposition temperature. Therefore, high molecular weight molecules such as polymers can typically not be processed by such methods. OMBD has emerged in the 1980's and was further developed in the following decade, mostly by Stephen R. Forrest and co-workers, to become a standard route to grow organic thin films.^[46,102,103]

Thermal sublimation is one of the most common methods to evaporate organic small molecules. The source material is heated in a vacuum chamber where the substrate is placed at some distance, typically held upside-down, above the source. The material flux is controlled by adjusting the temperature of the source and mechanical shutters which can be switched between different materials if needed.^[46] This method has the advantage to be relatively

Chapter 1. General introduction

simple to handle and provide good control over the layer thickness. Moreover, many layers of different materials can be evaporated sequentially using several sources. On the other hand, this method is quite material-consuming. In addition, due to the thermally insulating nature of most organic materials, the evaporation rate can prove difficult to stabilize.^[104]

The second most widespread technique is organic vapor phase deposition. There, the chamber is typically an elongated cylindrical vessel, the wall of which is heated, and where an inert carrier gas flux is introduced. At one end of the vessel, the source material is vaporized, saturating the carrier gas which transports the material vapor to the other end of the vessel where it adsorbs on a cooled substrate. By controlling the temperature and gas pressure in the vessel, different growth modes can be achieved and hence different thin film morphologies, from amorphous to large crystalline domains.^[46,105] By setting a temperature gradient between the source and the substrate, high purity can be obtained: the heavier impurities contained in the source material have lower sublimation pressure and deposit close to the source, while the lighter ones (with higher sublimation pressure) are carried to the end of the tube. This method has enabled growing high quality single crystals of millimeter to centimeter size.^[106,107]

For both methods, a good fundamental understanding of nucleation and growth mechanisms is generally necessary to gain full control over the thin film morphology. These characteristics are typically influenced by many factors such as deposition rate, substrate temperature, substrate surface chemistry and substrate roughness.^[108] The growth of pentacene films has been particularly well studied.^[109–112] For example, Pratontep *et al.* have shown that the substrate temperature influences the nucleation of pentacene islands, which is related to the binding energy in the critical island and the desorption energy of pentacene from the substrate. The role of surface diffusion of pentacene on different substrates was also shown to be influencing the nucleation density.^[113–115]

1.3.2 Solution growth

Although vapor processing methods have originally been the methods of choice to grow high quality OSC thin films and single crystals, the preference has shifted towards solution-based processes in the last decade.^[116–118] The main arguments brought forward for the use of solution-based fabrication techniques are the more cost-effective, low temperature processing

1.3. Fabrication and patterning of thin-film molecular crystals

techniques, the industrially relevant potential for large-area and high-throughput fabrication and a more efficient material utilization.^[118] Another argument for the use of solution routes is the impossibility to use vapor-deposition techniques for certain classes of materials. As previously mentioned, polymers for instance are not suitable candidates to be deposited via vapor-based routes, because of their high molecular weight. Organic salts, such as cyanine dyes, are ionic species with also relatively high molecular weight. Due to their ionic character, salts exhibit important coulombic interactions which are more difficult to overcome by thermal energy than van der Waals forces. As a result, organic salts usually have a low vapor pressure compared to neutral small molecules. Therefore, their decomposition temperature usually lies below their sublimation temperature.^[119] So far, organic salts could not be processed by vapor-based methods and solution routes are therefore the only way to apply them.

Solution deposition methods

A large library of solution deposition methods exists, from the simplest methods such as drop casting, to more technically advanced printing techniques.^[120] This demonstrates the versatility of solution-based deposition and their potential for larger scale applications. In this section, an overview of the main methods found in literature is given.

One of the simplest ways of depositing OSC material from solution is *drop-casting*. The solution is directly applied on a substrate in the form of a drop and the solvent subsequently evaporates, resulting in the formation of a solid deposit. The nature of the deposit, crystalline or amorphous, can in principle be induced by controlling the evaporation of solvent. This has been achieved in different ways including the use of saturated solvent environment, surface treatments or sealed vessels.^[121,122] Another approach to drop-casting is to deposit OSC solutions already containing suspended crystallites grown from a previous step.^[123] However, one of the major drawback of drop-casting is the irregular and non-uniform deposition patterns arising from the stick-slip motion of the contact line during drying. Methods to regulate the recession motion of the triple line have been implemented based on droplet pinning, for example using a solid structure fabricated on the substrate. Using this method, Li *et al.* managed to radially grow ribbons and wires of C₆₀ following the stable recession of the contact line.^[124] However, it could be argued that the necessary fabrication of pinning structures on

the substrate counterbalance the simplicity of the drop-casting method.

Another widespread method to form OSC thin film is *spin-coating*. There, the solution is typically deposited on a substrate, which is spun at a certain angular velocity to spread the solution homogeneously over the surface and quickly evaporate the solvent. The thickness of the solution film depends on the angular velocity of the spinning process, the concentration and the viscosity of the solution. Because solvent evaporation occurs fast, the films usually dry in a frozen "metastable" state and may recrystallize over time. Nonetheless, spin-casting is commonly used to deposit active layers in many organic electronic devices because it is simple and usually yields rather uniform thicknesses. On the other hand, spin-casting has also been used to purposely create non-continuous films. In particular, Heier *et al.* have taken advantage of the film instabilities arising during the spinning process to induce phase separation in molecular blends by spinodal decomposition of the solutions for application in bulk heterojunction solar cells.^[125] The same principle was used by Tisserant and co-workers to fabricate dewetted films of cyanine dyes. The films formed by this method are composed of micro-sized dye droplets, which are frozen in a metastable state and are able to re-crystallize upon solvent vapor treatment.^[126] This method will be discussed in more detail throughout this thesis as it serves as a basis for this work.

Another ensemble of methods involves the spreading of the solution by linear motion of a coating tool. In these techniques, the solution meniscus plays an essential role as it acts as an interface for evaporation and crystallization. Diao and co-workers grouped these methods under the term *meniscus-guided coating*.^[120] They include: dip-coating, slot-die coating, solution shearing, blade-coating and so on. One of the main advantage of these techniques is that in many cases, growth of thin films can be oriented in the direction of spreading.^[127]

Finally, *printing* techniques such as inkjet printing, spray coating and stamping enable depositing material over large areas with control over the deposition location. However, fine-tuning of inks' parameters (such as concentration, boiling point, viscosity, surface tension) and accurate positioning of printing heads can prove to be difficult.^[120,128]

In chapter 2, the spectroscopic properties of cyanine droplets films deposited via the method of Tisserant *et al.*^[129] are investigated. It is shown that the strong scattering properties can be understood as an optical phenomenon arising from the particular morphology of the

1.3. Fabrication and patterning of thin-film molecular crystals

films. Possible electronic contributions arising from a particular aggregation of the cyanine molecules would play a minor role.

Morphology control of solution deposited thin-films

The reputation of solution-deposited thin films to yield "lower quality" solids than their vapor-deposited counterparts has been called into question over the years, with the development of better morphology control strategies. The wide variety of solution deposition methods leads to a variable amount of parameters that could influence thin films' morphology. However, as for vapor deposition techniques, this challenge mostly comes down to understanding and controlling nucleation and growth during the deposition process. This section reviews some of the strategies that have been successful in controlling these parameters.

Nucleation is the first step of crystallization and it is stochastic in nature. Therefore, uncontrolled nucleation leads to the random distribution of domains size and boundaries. The thermodynamics of the nucleation process will be detailed in chapter 4. In all solution deposition methods described in the previous paragraph, solvent evaporation, which leads to the increase of the solution's supersaturation, is the driving force for nucleation. Therefore regulating evaporation appears to be one of the keys to control nucleation. Different strategies to do so can be found in literature. An approach, for example, is to pre-pattern substrates such that the deposition volume varies along the substrate: smaller volumes evaporate faster, thus triggering nucleation events. Goto and co-workers succeeded in fabricating arrays of single crystals by inducing solution nucleation in micro-patterned rectangular regions of small area where evaporation occurs faster.^[122] Another example is that of Minemawari *et al.* who also made use of patterned substrates to create volume asymmetry during inkjet-printing deposition of material, and induce nucleation events in smaller solution volumes.^[130] They demonstrated that they could yield about 50% single-crystal formation compared with symmetric volume depositions which mostly resulted in polycrystalline films.

Another approach to control solvent evaporation is based on the mechanism behind the coffee ring effect:^[131] evaporation occurs faster where the curvature of the contact line at the interface between solution/air/substrate is highest. An example is that of Diao *et al.* who patterned substrates with solvent wetting and dewetting regions to modulate the shape of the

Chapter 1. General introduction

contact line.^[117] The nucleation events were triggered at the tip of triangle-shaped wetting regions and the solution was dragged linearly using a shearing method to yield aligned single crystalline domains of trisopropylsilylethynol-pentacene.

Post-deposition processing methods have also been developed to control the degree of nucleation, in particular in polymer films. Using well-controlled temperature annealing treatment followed by temperature quenching, Xu *et al.* managed to partially re-melt a single crystal and "cloning" it into several smaller crystallites of the same nature.^[132] This *self-seeding* approach is based on a special characteristic of polymers: contrary to small molecules, polymer crystals contain regions with different degrees of order and conformational entropy, and therefore a range of melting temperatures.^[133] By carefully choosing the annealing temperature, the authors managed to re-melt the initial crystal while keeping nanoscopic regions of chain order (seeds). The subsequent quenching step provided the driving force to trigger re-crystallization from the seeds. A similar approach has also been used to control the nucleation density (and eventually the domains' size) of Poly(3-hexylthiophene) (P3HT) films using post-deposition *solvent vapor annealing* (SVA) and quenching.^[134]

Crystal growth is also an important parameter to control since it influences the structural perfection of films, the domain size, substrate coverage and so on. Crystal growth can either be concomitant to solution deposition (the film nucleates and crystallizes during deposition) as it is the case with some examples already discussed above such as the inkjet method developed by Minemawari and co-workers^[130] or the shear-guided crystallization of Diao *et al.*^[117] On the other hand, crystal growth can be induced "post-deposition". This approach has the advantage to decouple nucleation from growth and therefore enables easier control over these individual steps. Post-deposition growth typically involves thermal or solvent annealing. Two examples have already been discussed in the case of polymers in the previous paragraph. Solvent vapor annealing has also been used to control the morphology of small molecule thin films. Mascaro *et al.* demonstrated the power of SVA techniques to improve the morphology of vapor-deposited or spin-coated tris(8-hydroxyquinoline)aluminium (Alq₃) films, changing their morphology from amorphous to centimeter long single-crystalline needles.^[135] Change of morphology during SVA can occur via two mechanisms: (i) if a solvent in which the film is poorly soluble is used, the solvent vapor triggers nucleation by adsorbing on molecules in the

1.3. Fabrication and patterning of thin-film molecular crystals

films and inducing a rearrangement in molecular packing; (ii) if a "good" solvent for the film is used, adsorption of solvent molecules may release thermodynamically metastable states in the film, enabling crystallization.^[135] The latter mechanism was also the one suggested by Tisserant *et al.* to explain the growth of cyanine dye crystals upon solvent vapor annealing of dewetted droplet films, as previously discussed.^[126] Other methods to control crystal growth and morphology also include substrate templating methods, using functionalized substrates interacting with the solution to be deposited. One example is that of the use of protonated *dendrimers* as scaffolds to induce nucleation and growth of cyanine J-aggregates through coulombic interactions between the chromophore and the dendrimer surface.^[136] More examples of the use of substrate templates will be discussed in section 1.3.3 and chapter 4.

Control of the in-plane alignment of crystalline domain is also important, given the anisotropic nature of OSCs crystalline materials' properties. In this regard, many strategies have also been implemented.^[101,137] They include methods relying on mechanical stretching of organic films,^[138] friction-transfer process,^[139] mechanical rubbing of a pre-deposited thin films,^[140] growth on pre-oriented polymeric substrates,^[141] the Langmuir-Blodgett technique,^[142] epitaxial growth on inorganic single crystals^[143] and magnetic/electric-field induced alignment. Tisserant and co-workers partially succeeded in aligning cyanine dye single crystals by templating gold substrates with stripes of self-assembled monolayers of hydrophobic alkanethiols.^[126] The crystals were shown to preferentially arrange with their side-faces parallel to the hydrophobic linear pattern, in order to reduce their interfacial energy with the substrate.

Chapters 3 and 4 deal with the control of nucleation and growth of single CyC crystals grown from dewetted droplet films. While in chapter 3 crystal growth on non-patterned substrates is shown to lead to un-controlled crystal morphology evolution, chapter 4 aims to demonstrate that the crystal morphology can be stabilized if nucleation and growth are performed on a patterned substrate. In addition, the method used in chapter 4 allows to shed light in the nucleation mechanism and to partially control the position of the single crystals on the substrate.

1.3.3 Patterning of functional material

The previous section demonstrated the wide variety of growth and solution deposition methods to fabricate crystalline thin films of OSCs with control over their morphology and in-plane orientation. However, integration of crystalline films, in particular single-crystalline ones, into devices remains challenging. On one hand, conventional methods in microtechnology, such as photolithography and sputtering are almost impossible to implement with OSC materials because of the harsh processes involved such as the use of solvents for lift-off, although a few photolithographic methods for organic materials have been developed.^[144,145] On the other hand, most of the early methods to fabricate single crystal devices such as OFETs, relied on the manual picking and placement of individual crystals on the device substrate. Besides the obvious prohibitive time-consuming aspect of this approach, the introduction of contaminant and defects induced by the manipulations of fragile molecular crystals often resulted in poor crystal quality. Therefore, large efforts have been put to directly grow single crystalline objects at specific locations.

Many methods to control location of OSC crystals have been developed, with different level of complexity in the preparation of the substrates and the crystallization processes. The majority of these methods necessitate pre-treatment of the substrate. One example was already discussed in section 1.3.2 with the work of Goto *et al.* who created areas of lyophilic and lyophobic nature to tune the solution volume and thus trigger nucleation on specific areas of the substrates.^[122] Besides this example, other methods in literature typically involve the functionalization of substrates with self-assembled monolayers (SAMs) deposited by microcontact printing. The use of SAMs to control nucleation location can be based on three mechanisms: (i) the induction of heterogeneous nucleation by selectively increase the surface roughness; (ii) the selective interaction with the deposited material; (iii) selective wetting of patterned areas. An example of (i) is given by Briseno *et al.*^[146,147] who patterned SiO₂/Si substrates with rough pillars of octadecyltriethoxysilane (OTS) by microcontact printing and managed to grow arrays of pentacene, rubrene and C₆₀ crystals by vapor deposition. The number of crystallites grown at each location could be tuned by varying the area of the OTS-patterned regions and the number of pillars. Briseno and co-workers have also used SAMs to grow large oriented single crystals of anthracene selectively interacting with substrates

1.3. Fabrication and patterning of thin-film molecular crystals

patterned with terphenylthiol.^[148] Finally, an example of crystal patterning by dewetting can be given with the work of Liu *et al.*^[149] There, the authors have patterned substrates with hydrophilic and hydrophobic features and selectively deposited crystals via two approaches. In the first approach a crystal suspension is deposited on the patterned substrates and selectively wets the hydrophilic areas, resulting in the settling of the suspended crystals on these areas only. In the second approach, the patterned substrate is covered uniformly with crystals. Subsequently, the substrates were rinsed with hydrophilic (hydrophobic) solvent to lift-off the crystals sitting on the hydrophilic (hydrophobic) areas only. This method is attractive because of its simplicity, however it requires to use a suspension of crystals that have been pre-grown and therefore the crystals settle on the substrate with random in-plane and out-of-plane orientations. Moreover, this method yielded areas containing many single crystals rather than an array of single crystals.

Some methods not requiring any specific substrate preparation have also been reported, such as stamp-assisted crystallization techniques induced by means of solution confinement described by Gentili *et al.*^[150,151] Printing techniques can also yield patterned OSC films, as already discussed in section 1.3.2. However, in these methods, control over nucleation is limited and the resulting crystals are often polycrystalline.

In chapter 4, the selective wetting/dewetting approach will be used to try to selectively deposit droplets of cyanine dye on patterned substrates and from there grow single crystals of cyanine dye at specific location via solvent vapor annealing. More details about this strategy and the principles behind SAMs will be given.



Bibliography

- [1] J. R. Sheats, *Journal of Materials Research* **2004**, *19*, 1974–1989.
- [2] U. Mitschke, P. Bäuerle, *Journal of Materials Chemistry* **2000**, *10*, 1471–1507.
- [3] A. C. Grimsdale, K. Leok Chan, R. E. Martin, P. G. Jokisz, A. B. Holmes, *Chemical Reviews* **2009**, *109*, 897–1091.
- [4] A. R. Murphy, J. M. J. Fréchet, *Chemical Reviews* **2007**, *107*, 1066–1096.
- [5] X. Guo, Y. Xu, S. Ogier, T. N. Ng, M. Caironi, A. Perinot, L. Li, J. Zhao, W. Tang, R. A. Sporea, A. Nejim, J. Carrabina, P. Cain, F. Yan, *IEEE Transactions on Electron Devices* **2017**, *64*, 1906–1921.
- [6] B. Kippelen, J.-L. Brédas, *Energy & Environmental Science* **2009**, *2*, 251–261.
- [7] A. Mishra, P. Bäuerle, *Angewandte Chemie International Edition* **2012**, *51*, 2020–2067.
- [8] C. Wang, H. Dong, W. Hu, Y. Liu, D. Zhu, *Chemical Reviews* **2012**, *112*, 2208–2267.
- [9] A. Köhler, H. Bässler in *Electronic Processes in Organic Semiconductors*, Wiley-Blackwell, **2015**, pp. 1–86.
- [10] A. Köhler, H. Bässler in *Electronic Processes in Organic Semiconductors*, Wiley-Blackwell, **2015**, pp. 87–191.
- [11] J. Roncali, *Chemical Reviews* **1997**, *97*, 173–206.
- [12] J. Roncali, *Macromolecular Rapid Communications* **2007**, *28*, 1761–1775.
- [13] J.-H. Tsai, W.-R. Tu, C.-L. Liu, W.-C. Wu, W.-C. Chen, *Polymer Journal* **2009**, *41*, 363–369.
- [14] A. W. Hains, Z. Liang, M. A. Woodhouse, B. A. Gregg, *Chemical Reviews* **2010**, *110*, 6689–6735.

Bibliography

- [15] P. P. Debye, E. M. Conwell, *Physical Review* **1954**, *93*, 693–706.
- [16] G. L. Pearson, J. Bardeen, *Physical Review* **1949**, *75*, 865–883.
- [17] H. Shirakawa, E. J. Louis, A. G. MacDiarmid, C. K. Chiang, A. J. Heeger, *Journal of the Chemical Society Chemical Communications* **1977**, *0*, 578–580.
- [18] A. J. Heeger, *Angewandte Chemie International Edition* **2001**, *40*, 2591–2611.
- [19] X. Guo, M. Baumgarten, K. Müllen, *Progress in Polymer Science*, Topical issue on Conductive Polymers **2013**, *38*, 1832–1908.
- [20] L. Bian, E. Zhu, J. Tang, W. Tang, F. Zhang, *Progress in Polymer Science*, Topical Issue on Conducting Polymers **2012**, *37*, 1292–1331.
- [21] J. H. Burroughes, D. D. C. Bradley, A. R. Brown, R. N. Marks, K. Mackay, R. H. Friend, P. L. Burns, A. B. Holmes, *Nature* **1990**, *347*, 539–541.
- [22] D. Braun, A. J. Heeger, *Applied Physics Letters* **1991**, *58*, 1982–1984.
- [23] A. Tsumura, H. Koezuka, T. Ando, *Applied Physics Letters* **1986**, *49*, 1210–1212.
- [24] A. C. Grimsdale, K. Müllen, *Macromolecular Rapid Communications* **2007**, *28*, 1676–1702.
- [25] B. S. Ong, Y. Wu, P. Liu, S. Gardner, *Journal of the American Chemical Society* **2004**, *126*, 3378–3379.
- [26] S. Ko, E. Verploegen, S. Hong, R. Mondal, E. T. Hoke, M. F. Toney, M. D. McGehee, Z. Bao, *Journal of the American Chemical Society* **2011**, *133*, 16722–16725.
- [27] Y. Yang, Q. Pei, A. J. Heeger, *Journal of Applied Physics* **1996**, *79*, 934–939.
- [28] X. Zhao, X. Zhan, *Chemical Society Reviews* **2011**, *40*, 3728–3743.
- [29] D. S. Chung, J. W. Park, S.-O. Kim, K. Heo, C. E. Park, M. Ree, Y.-H. Kim, S.-K. Kwon, *Chemistry of Materials* **2009**, *21*, 5499–5507.
- [30] A. Salleo, R. J. Kline, D. M. DeLongchamp, M. L. Chabinyc, *Advanced Materials* **2010**, *22*, 3812–3838.
- [31] H. Sirringhaus, P. J. Brown, R. H. Friend, M. M. Nielsen, K. Bechgaard, B. M. W. Langeveld-Voss, A. J. H. Spiering, R. a. J. Janssen, E. W. Meijer, P. Herwig, D. M. d. Leeuw, *Nature* **1999**, *401*, 685–688.

- [32] M. Ariu, D. G. Lidzey, M. Sims, A. J. Cadby, P. A. Lane, D. D. C. Bradley, *Journal of Physics: Condensed Matter* **2002**, *14*, 9975.
- [33] C. Silva, D. M. Russell, A. S. Dhoot, L. M. Herz, C. Daniel, N. C. Greenham, A. C. Arias, S. Setayesh, K. Müllen, R. H. Friend, *Journal of Physics: Condensed Matter* **2002**, *14*, 9803.
- [34] A. Hayer, A. L. T. Khan, R. H. Friend, A. Köhler, *Physical Review B* **2005**, *71*, 241302.
- [35] R. Mauer, M. Kastler, F. Laquai, *Advanced Functional Materials* **2010**, *20*, 2085–2092.
- [36] E. J. W. Crossland, K. Tremel, F. Fischer, K. Rahimi, G. Reiter, U. Steiner, S. Ludwigs, *Advanced Materials* **2012**, *24*, 839–844.
- [37] A. Salleo, *Materials Today* **2007**, *10*, 38–45.
- [38] K. Rahimi, I. Botiz, N. Stingelin, N. Kayunkid, M. Sommer, F. P. V. Koch, H. Nguyen, O. Coulembier, P. Dubois, M. Brinkmann, G. Reiter, *Angewandte Chemie International Edition* **2012**, *51*, 11131–11135.
- [39] J. A. Lim, F. Liu, S. Ferdous, M. Muthukumar, A. L. Briseno, *Materials Today* **2010**, *13*, 14–24.
- [40] M. Pope, H. P. Kallmann, P. Magnante, *The Journal of Chemical Physics* **1963**, *38*, 2042–2043.
- [41] W. Helfrich, W. G. Schneider, *Physical Review Letters* **1965**, *14*, 229–231.
- [42] J. E. Anthony, *Chemical Reviews* **2006**, *106*, 5028–5048.
- [43] M. Gsänger, D. Bialas, L. Huang, M. Stolte, F. Würthner, *Advanced Materials* **2016**, *28*, 3615–3645.
- [44] R. W. I. de Boer, M. E. Gershenson, A. F. Morpurgo, V. Podzorov, *physica status solidi (a)* **2004**, *201*, 1302–1331.
- [45] R. Zeis, C. Besnard, T. Siegrist, C. Schlockermann, X. Chi, C. Kloc, *Chemistry of Materials* **2006**, *18*, 244–248.
- [46] S. R. Forrest, *Chemical Reviews* **1997**, *97*, 1793–1896.
- [47] O. D. Jurchescu, J. Baas, T. T. M. Palstra, *Applied Physics Letters* **2004**, *84*, 3061–3063.
- [48] P. Irkhin, I. Biaggio, *Physical Review Letters* **2011**, *107*, 017402.

Bibliography

- [49] P. Irkhin, A. Ryasnyanskiy, M. Koehler, I. Biaggio, *Physical Review B* **2012**, *86*, 085143.
- [50] C. Sutton, C. Risko, J.-L. Brédas, *Chemistry of Materials* **2016**, *28*, 3–16.
- [51] H. Klauk, M. Halik, U. Zschieschang, G. Schmid, W. Radlik, W. Weber, *Journal of Applied Physics* **2002**, *92*, 5259–5263.
- [52] C. Reese, Z. Bao, *Materials Today* **2007**, *10*, 20–27.
- [53] W. Herbst, K. Hunger, *Industrial organic pigments: production, properties, applications*, John Wiley & Sons, **2006**.
- [54] D. S. Weiss, M. Abkowitz, *Chemical Reviews* **2010**, *110*, 479–526.
- [55] C. W. Tang, *Applied Physics Letters* **1986**, *48*, 183–185.
- [56] C. G. Williams, *Earth and Environmental Science Transactions of The Royal Society of Edinburgh* **1857**, *21*, 377–401.
- [57] R. B. Mujumdar, L. A. Ernst, S. R. Mujumdar, C. J. Lewis, A. S. Waggoner, *Bioconjugate Chemistry* **1993**, *4*, 105–111.
- [58] F. Würthner, T. E. Kaiser, C. R. Saha-Möller, *Angewandte Chemie International Edition* **2011**, *50*, 3376–3410.
- [59] M. Bates, R. R. Lunt, *Sustainable Energy & Fuels* **2017**.
- [60] S. Dähne, *Science* **1978**, *199*, 1163–1167.
- [61] R. S. Lepkowicz, O. V. Przhonska, J. M. Hales, J. Fu, D. J. Hagan, E. W. Van Stryland, M. V. Bondar, Y. L. Slominsky, A. D. Kachkovski, *Chemical Physics* **2004**, *305*, 259–270.
- [62] P.-A. Bouit, C. Aronica, L. Toupet, B. Le Guennic, C. Andraud, O. Maury, *Journal of the American Chemical Society* **2010**, *132*, 4328–4335.
- [63] A. C. Véron, H. Zhang, A. Linden, F. Nüesch, J. Heier, R. Hany, T. Geiger, *Organic Letters* **2014**, *16*, 1044–1047.
- [64] G. Chapman, M. Henary, G. Patonay, *Analytical Chemistry Insights* **2011**, *6*, ACI.S6568.
- [65] S. Pascal, A. Haefele, C. Monnereau, A. Charaf-Eddin, D. Jacquemin, B. Le Guennic, C. Andraud, O. Maury, *The Journal of Physical Chemistry A* **2014**, *118*, 4038–4047.
- [66] B. Fan, R. Hany, J.-E. Moser, F. Nüesch, *Organic Electronics* **2008**, *9*, 85–94.

- [67] B. Fan, F. A. de Castro, J. Heier, R. Hany, F. Nüesch, *Organic Electronics* **2010**, *11*, 583–588.
- [68] H. Zhang, B. Niesen, E. Hack, S. Jenatsch, L. Wang, A. C. Véron, M. Makha, R. Schneider, Y. Arroyo, R. Hany, F. Nüesch, *Organic Electronics* **2016**, *30*, 191–199.
- [69] S. Jenatsch, R. Hany, A. C. Véron, M. Neukom, S. Züfle, A. Borgschulte, B. Ruhstaller, F. Nüesch, *The Journal of Physical Chemistry C* **2014**, *118*, 17036–17045.
- [70] S. Jenatsch, L. Wang, N. Leclaire, E. Hack, R. Steim, S. B. Anantharaman, J. Heier, B. Ruhstaller, L. Penninck, F. Nüesch, R. Hany, *Organic Electronics* **2017**, *48*, 77–84.
- [71] M. Eslamian, *Nano-Micro Letters* **2017**, *9*, 3.
- [72] V. Coropceanu, J. Cornil, D. A. da Silva Filho, Y. Olivier, R. Silbey, J.-L. Brédas, *Chemical Reviews* **2007**, *107*, 926–952.
- [73] V. C. Sundar, J. Zaumseil, V. Podzorov, E. Menard, R. L. Willett, T. Someya, M. E. Gershenson, J. A. Rogers, *Science* **2004**, *303*, 1644–1646.
- [74] G. M. Akselrod, P. B. Deotare, N. J. Thompson, J. Lee, W. A. Tisdale, M. A. Baldo, V. M. Menon, V. Bulović, *Nature Communications* **2014**, *5*, 3646.
- [75] O. V. Mikhnenko, P. W. M. Blom, T.-Q. Nguyen, *Energy & Environmental Science* **2015**, *8*, 1867–1888.
- [76] B. P. Rand, D. Cheyns, K. Vasseur, N. C. Giebink, S. Mothy, Y. Yi, V. Coropceanu, D. Beljonne, J. Cornil, J.-L. Brédas, J. Genoe, *Advanced Functional Materials* **2012**, *22*, 2987–2995.
- [77] M. Brinkmann, G. Gadret, M. Muccini, C. Taliani, N. Masciocchi, A. Sironi, *Journal of the American Chemical Society* **2000**, *122*, 5147–5157.
- [78] Y. Shirota, H. Kageyama, *Chemical Reviews* **2007**, *107*, 953–1010.
- [79] Y. Shirota, *Journal of Materials Chemistry* **2000**, *10*, 1–25.
- [80] Y. Shirota, *Journal of Materials Chemistry* **2005**, *15*, 75–93.
- [81] D. J. Mascaró, M. E. Thompson, H. I. Smith, V. Bulović, *Organic Electronics* **2005**, *6*, 211–220.
- [82] B. A. Gregg, *The Journal of Physical Chemistry* **1996**, *100*, 852–859.

Bibliography

- [83] T. Saito, C.-y. Liu, V. M. Lynch, A. J. Bard, *Chemistry of Materials* **1997**, *9*, 1318–1327.
- [84] R. J. Tseng, R. Chan, V. C. Tung, Y. Yang, *Advanced Materials* **2008**, *20*, 435–438.
- [85] P. Bäuerle, T. Fischer, B. Bidlingmeier, J. P. Rabe, A. Stabel, *Angewandte Chemie International Edition in English* **1995**, *34*, 303–307.
- [86] M. Schwoerer, H. C. Wolf in *Organic Molecular Solids*, Wiley-VCH Verlag GmbH, **2006**, pp. 125–175.
- [87] M. Kasha, H. R. Rawls, E.-B. M. Ashraf, *Pure and Applied Chemistry* **1965**, *11*, 371–392.
- [88] A. S. Davydov, *Theory of Molecular Excitons*.
- [89] G. Scheibe, *Kolloid-Zeitschrift* **1938**, *82*, 1–14.
- [90] V. Czikkely, H. D. Forsterling, H. Kuhn, *Chemical Physics Letters* **1970**, *6*, 207–210.
- [91] A. Bree, L. E. Lyons, *Journal of the Chemical Society (Resumed)* **1960**, *0*, 5206–5212.
- [92] H. C. Wolf, *Zeitschrift für Naturforschung A* **2014**, *13*, 414–419.
- [93] H. Port, D. Rund, G. J. Small, V. Yakhot, *Chemical Physics* **1979**, *39*, 175–188.
- [94] T. P. Osedach, A. Iacchetti, R. R. Lunt, T. L. Andrew, P. R. Brown, G. M. Akselrod, V. Bulović, *Applied Physics Letters* **2012**, *101*, 113303.
- [95] M. S. Bradley, V. Bulović, *Physical Review B* **2010**, *82*.
- [96] H. Zhang, G. Wicht, C. Gretener, M. Nagel, F. Nüesch, Y. Romanyuk, J.-N. Tisserant, R. Hany, *Solar Energy Materials and Solar Cells* **2013**, *118*, 157–164.
- [97] H. Zhang, S. Jenatsch, J. D. Jonghe, F. Nüesch, R. Steim, A. C. Véron, R. Hany, *Scientific Reports* **2015**, *5*, srep09439.
- [98] M. Ramanathan, K. Hong, Q. Ji, Y. Yonamine, J. P. Hill, K. Ariga, **2014**, *14*, 1–14.
- [99] A. P. Marchetti, C. D. Salzberg, E. I. P. Walker, *The Journal of Chemical Physics* **1976**, *64*, 4693–4698.
- [100] H. von Berlepsch, S. Möller, L. Dähne, *The Journal of Physical Chemistry B* **2001**, *105*, 5689–5699.
- [101] S. Liu, W. M. Wang, A. L. Briseno, S. C. B. Mannsfeld, Z. Bao, *Advanced Materials* **2009**, *21*, 1217–1232.

- [102] M. Hara, H. Sasabe, A. Yamada, A. F. Garito, *Japanese Journal of Applied Physics* **1989**, 28, L306.
- [103] N. Karl, *Journal of Crystal Growth* **1990**, 99, 1009–1016.
- [104] S. R. Forrest, *Nature* **2004**, 428, 911–918.
- [105] M. Shtein, J. Mapel, J. B. Benziger, S. R. Forrest, *Applied Physics Letters* **2002**, 81, 268–270.
- [106] C. Kloc, P. G. Simpkins, T. Siegrist, R. A. Laudise, *Journal of Crystal Growth* **1997**, 182, 416–427.
- [107] R. A. Laudise, C. Kloc, P. G. Simpkins, T. Siegrist, *Journal of Crystal Growth* **1998**, 187, 449–454.
- [108] A. A. Virkar, S. Mannsfeld, Z. Bao, N. Stingelin, *Advanced Materials* **2010**, 22, 3857–3875.
- [109] F.-J. M. z. Heringdorf, M. C. Reuter, R. M. Tromp, *Nature* **2001**, 412, 517–520.
- [110] S. E. Fritz, T. W. Kelley, C. D. Frisbie, *The Journal of Physical Chemistry B* **2005**, 109, 10574–10577.
- [111] D. Knipp, R. A. Street, A. Völkel, J. Ho, *Journal of Applied Physics* **2002**, 93, 347–355.
- [112] D. Choudhary, P. Clancy, R. Shetty, F. Escobedo, *Advanced Functional Materials* **2006**, 16, 1768–1775.
- [113] S. Pratontep, M. Brinkmann, F. Nüesch, L. Zuppiroli, *Synthetic Metals, Organic Field-Effect Transistors: Towards Molecular Scale. Proceedings of Symposium E. E-MRS Spring Meeting*. **2004**, 146, 387–391.
- [114] S. Pratontep, M. Brinkmann, F. Nüesch, L. Zuppiroli, *Physical Review B* **2004**, 69, 165201.
- [115] S. Pratontep, F. Nüesch, L. Zuppiroli, M. Brinkmann, *Physical Review B* **2005**, 72.
- [116] A. C. Arias, J. D. MacKenzie, I. McCulloch, J. Rivnay, A. Salleo, *Chemical Reviews* **2010**, 110, 3–24.
- [117] Y. Diao, B. C.-K. Tee, G. Giri, J. Xu, D. H. Kim, H. A. Becerril, R. M. Stoltenberg, T. H. Lee, G. Xue, S. C. B. Mannsfeld, Z. Bao, *Nature Materials* **2013**, 12, 665–671.
- [118] L. Shaw, Z. Bao, *Israel Journal of Chemistry* **2014**, 54, 496–512.

Bibliography

- [119] V. E. Shershov, M. A. Spitsyn, V. E. Kuznetsova, E. N. Timofeev, O. A. Ivashkina, I. S. Abramov, T. V. Nasedkina, A. S. Zasedatelev, A. V. Chudinov, *Dyes and Pigments* **2013**, *97*, 353–360.
- [120] Y. Diao, L. Shaw, Z. Bao, S. C. B. Mannsfeld, *Energy & Environmental Science* **2014**, *7*, 2145–2159.
- [121] S. Wang, M. Kappl, I. Liebewirth, M. Müller, K. Kirchhoff, W. Pisula, K. Müllen, *Advanced Materials* **2012**, *24*, 417–420.
- [122] O. Goto, S. Tomiya, Y. Murakami, A. Shinozaki, A. Toda, J. Kasahara, D. Hobara, *Advanced Materials* **2012**, *24*, 1117–1122.
- [123] C.-T. Chien, C.-C. Lin, M. Watanabe, Y.-D. Lin, T.-H. Chao, T.-c. Chiang, X.-H. Huang, Y.-S. Wen, C.-H. Tu, C.-H. Sun, T. J. Chow, *Journal of Materials Chemistry* **2012**, *22*, 13070–13075.
- [124] H. Li, B. C.-K. Tee, J. J. Cha, Y. Cui, J. W. Chung, S. Y. Lee, Z. Bao, *Journal of the American Chemical Society* **2012**, *134*, 2760–2765.
- [125] J. Heier, J. Groenewold, S. Huber, F. Nüesch, R. Hany, *Langmuir* **2008**, *24*, 7316–7322.
- [126] J.-N. Tisserant, G. Wicht, O. F. Göbel, E. Bocek, G.-L. Bona, T. Geiger, R. Hany, R. Mezzenga, S. Partel, P. Schmid, W. B. Schweizer, J. Heier, *ACS Nano* **2013**, *7*, 5506–5513.
- [127] J. Soeda, T. Uemura, T. Okamoto, C. Mitsui, M. Yamagishi, J. Takeya, *Applied Physics Express* **2013**, *6*, 076503.
- [128] B.-J. de Gans, U. S. Schubert, *Langmuir* **2004**, *20*, 7789–7793.
- [129] J.-N. Tisserant, R. Hany, S. Partel, G.-L. Bona, R. Mezzenga, J. Heier, *Soft Matter* **2012**, *8*, 5804–5810.
- [130] H. Minemawari, T. Yamada, H. Matsui, J. Tsutsumi, S. Haas, R. Chiba, R. Kumai, T. Hasegawa, *Nature* **2011**, *475*, 364–367.
- [131] R. D. Deegan, O. Bakajin, T. F. Dupont, G. Huber, S. R. Nagel, T. A. Witten, *Nature* **1997**, *389*, 827–829.
- [132] J. Xu, Y. Ma, W. Hu, M. Rehahn, G. Reiter, *Nature Materials* **2009**, *8*, 348.

- [133] G. Reiter, *Chemical Society Reviews* **2014**, *43*, 2055–2065.
- [134] E. J. W. Crossland, K. Rahimi, G. Reiter, U. Steiner, S. Ludwigs, *Advanced Functional Materials* **2011**, *21*, 518–524.
- [135] D. J. L. Mascaro, Thesis, Massachusetts Institute of Technology, **2004**.
- [136] R. Steiger, R. Pugin, J. Heier, *Colloids and Surfaces B: Biointerfaces*, From manipulation in two dimensions to attempt to understand the origin of life - in honour of the 90th birthday of Hans Kuhn **2009**, *74*, 484–491.
- [137] M. Brinkmann, L. Hartmann, L. Biniek, K. Tremel, N. Kayunkid, *Macromolecular Rapid Communications* **2014**, *35*, 9–26.
- [138] P. Dyreklev, G. Gustafsson, O. Inganäs, H. Stubb, *Synthetic Metals*, Proceedings of the International Conference on Science and Technology of Synthetic Metals **1993**, *57*, 4093–4098.
- [139] S. Nagamatsu, W. Takashima, K. Kaneto, Y. Yoshida, N. Tanigaki, K. Yase, *Applied Physics Letters* **2004**, *84*, 4608–4610.
- [140] H. Sirringhaus, R. J. Wilson, R. H. Friend, M. Inbasekaran, W. Wu, E. P. Woo, M. Grell, D. D. C. Bradley, *Applied Physics Letters* **2000**, *77*, 406–408.
- [141] M. Brinkmann, S. Pratontep, C. Chaumont, J.-C. Wittmann, *Macromolecules* **2007**, *40*, 9420–9426.
- [142] G. Xu, Z. Bao, J. T. Groves, *Langmuir* **2000**, *16*, 1834–1841.
- [143] T. Dienel, C. Loppacher, S. C. B. Mannsfeld, R. Forker, T. Fritz, *Advanced Materials* **2008**, *20*, 959–963.
- [144] J. A. DeFranco, B. S. Schmidt, M. Lipson, G. G. Malliaras, *Organic Electronics* **2006**, *7*, 22–28.
- [145] H. S. Hwang, A. A. Zakhidov, J.-K. Lee, X. André, J. A. DeFranco, H. H. Fong, A. B. Holmes, G. G. Malliaras, C. K. Ober, *Journal of Materials Chemistry* **2008**, *18*, 3087–3090.
- [146] A. L. Briseno, S. C. B. Mannsfeld, M. M. Ling, S. Liu, R. J. Tseng, C. Reese, M. E. Roberts, Y. Yang, F. Wudl, Z. Bao, *Nature* **2006**, *444*, 913–917.
- [147] S. C. B. Mannsfeld, A. L. Briseno, S. Liu, C. Reese, M. E. Roberts, Z. Bao, *Advanced Functional Materials* **2007**, *17*, 3545–3553.

Bibliography

- [148] A. L. Briseno, J. Aizenberg, Y.-J. Han, R. A. Penkala, H. Moon, A. J. Lovinger, C. Kloc, Z. Bao, *Journal of the American Chemical Society* **2005**, *127*, 12164–12165.
- [149] S. Liu, W. M. Wang, S. C. B. Mannsfeld, J. Locklin, P. Erk, M. Gomez, F. Richter, Z. Bao, *Langmuir* **2007**, *23*, 7428–7432.
- [150] D. Gentili, F. Valle, C. Albonetti, F. Liscio, M. Cavallini, *Accounts of Chemical Research* **2014**, *47*, 2692–2699.
- [151] D. Gentili, F. Liscio, L. Mariucci, L. Beverina, M. Melucci, S. Toffanin, S. Milita, M. Cavallini, *Advanced Functional Materials* **2016**, *26*, 2387–2393.

2 Structuring amorphous thin films of cyanine dyes

Light Scattering Enhancement at the Absorption Edge in Dewetting Droplets of Cyanine Dyes

Nicolas A. Leclaire,^{1,2} Florent Boudoire,¹ Erwin Hack,³ Rolf Brönnimann,³ Frank A. Nüesch,^{1,2} and Jakob Heier¹

¹Laboratory for Functional Polymers, Swiss Federal Laboratories for Materials Science and Technology, EMPA, Überlandstrasse 129, 8600 Dübendorf, Switzerland

²Institut des Matériaux, Ecole Polytechnique Fédérale de Lausanne, EPFL, Station 12, 1015 Lausanne, Switzerland

³Reliability Science and Technology, Swiss Federal Laboratories for Materials Science and Technology, EMPA, Überlandstrasse 129, 8600 Dübendorf, Switzerland

Adapted with permission from Advanced Optical Materials.
©2017 WILEY-VCH Verlag GmbH & Co. KGaA, Weinheim.

Adv. Opt. Mat., **2017**, 5 (5), 1600903, DOI: 10.1002/adom.201600903
<http://onlinelibrary.wiley.com/doi/10.1002/adom.201600903/abstract>

Declaration of Contribution N.A.L fabricated all samples, performed diffraction experiments as well as atomic force microscopy and absorption measurements, carried out FDTD simulations, analysed the data and contributed to manuscript preparation. Theoretical calculations were carried out by E.H..

2.1 Introduction and aims

Electromagnetic scattering by particles is a universal phenomenon that manifests itself in a large number of everyday-life visual effects such as rainbows or clouds. From a technological standpoint, light scattering has attracted much attention in the last decades in the fields of nano-optics and nanophotonics because light–matter interactions with structures of subwavelength dimensions allows overcoming limitations of conventional optical elements at these scales.^[1] Numbers of devices allowing to control light at the nanoscale such as nanoantennas^[2,3] or light trapping structures in photovoltaic devices make use of plasmonic effects in metallic nanostructures.^[4–6] Large efforts have also been put in the study of high refractive index dielectric cavities^[7,8] for they allow overcoming intrinsic optical losses associated with plasmonic structures in the visible range^[9] and are compatible with conventional semiconductor processing techniques.^[10–12]

Mie theory, in its original form, gives an analytical solution to Maxwell's equations in the case of a plane electromagnetic wave interacting with a spherical particle of arbitrary size.^[13,14] The theory is particularly useful for particles which dimensions are similar to that of the wavelength of the incident light, where neither ray optics nor Rayleigh's approximation apply. In this case, light scattering (often called “Mie scattering”) results from the confinement of strong electromagnetic modes (Mie modes) in the volume of the particle. However, in low refractive-index structures, light scattering can be considerably different from classical resonant mechanisms and has been described as weak (lossy) Mie resonances or as nonresonant Mie scattering.^[15] Although Mie theory was originally derived for homogenous spherical particles, a number of extensions to the theory have been analytically or experimentally demonstrated, highlighting the effect of changes on the particle geometry^[16] and composition on the optical properties of the structure. Various photonic devices with selective spectral properties can thus be obtained by tuning the morphology (and in turn the optical properties)

of such scattering nanostructures.^[17]

While most photonic nanostructures, such as optical microcavities, plasmonic metal nanostructures, and photonic crystals, make use of either metallic or inorganic materials with high dielectric constants, only little effort has been devoted to study subwavelength scattering effects from organic material systems.^[15,18] Yet organic materials are attractive in terms of the versatility of their fabrication processes and low cost compared to metallic and inorganic dielectric materials, allowing fabrication of large-area devices.

Organic chromophores, such as cyanine dyes, show interesting intrinsic electro-optical properties. Mostly known for their role as sensitizers in photographic films,^[19] this class of organic semiconductors has recently been investigated as amorphous active layers in organic solar cells^[20–22] and light emitting electrochemical cells.^[23] The high oscillator strength of cyanine dyes accounts for their pronounced light absorption in the visible wavelength range. Together with strong absorption bands, cyanine dyes also exhibit significant variations in their refractive index that can be described by the Lorentz oscillator model.^[24] Few studies have reported on the effect of variations in refractive index in absorbing materials on the scattering from particles.^[25,26]

In this work, we fabricated droplets of 1-ethyl-2-[3-(1-ethyl-1,3-dihydro-3,3-dimethyl-2H-indol-2-ylidene)-1-propen-1-yl]-3,3-dimethyl-3H-indolium perchlorate (CyC) of different shape on glass substrates by dewetting during spin-coating.^[27,28] The droplet ensemble gives rise to diffraction. Diffraction depends on the scattering properties of the individual scatterers, as well as on the nearest neighbor arrangement of the scattering elements. Only first-order diffraction is notable and shows an unusual wavelength dependence with high intensity near the absorbance edge of the dye. In 2.2.1, we describe the dye droplet ensemble. In section 2.2.2, we show the results of experimentally recorded diffraction efficiencies for different samples. Depending on droplet size, a very different behavior is found. In 2.2.3, we demonstrate that the diffraction is complementary to transmission measured by UV-vis. These measurements allow defining three distinguishable scattering regimes. In section 2.2.4, we introduce an analytical solution that connects the arrangement of the scattering elements with the scattering properties of the individual scatterers (dye droplets). While we find an amazing consistency between

theory and experimental data, reproducing three different scattering regimes, the analytical solution hardly illustrates the reason for the scattering behavior. For this purpose we present finite-difference timedomain (FDTD) simulations of the system (sections 2.2.5, 2.2.6 and 2.2.7). Again, the simulations reproduce the experiment, and also bring an intuitive understanding of how anomalous dispersion of the refractive index at the absorption edge of the dye causes the narrowing down of the extinction peak compared to Mie scattering. From the simulations, electrical field distributions can be extracted that reveal the origin of the scattering contrast: the interaction between the dye droplets and light can be best described as a nonresonant form of Mie scattering whereby the droplets act as microlenses defocusing the light.

While in earlier publications we attributed the apparition of the new spectral feature solely to the formation of aggregates and resonantly enhanced scattering,^[29–31] we here decipher to what extent the unusual scattering phenomena can be attributed to the droplet morphology alone.

2.2 Results and discussion

2.2.1 Droplet film formation

Films consisting of microdroplets of CyC dye were fabricated by spin-casting the dye from saturated ethanol solutions. The liquid dewets from the glass substrate and self-assembles into droplets upon solvent evaporation. The processes leading to droplet formation are complex and involve the formation of film instabilities due to temperature and concentration gradients (Marangoni instability), Van der Waals interactions, and solvent evaporation.^[32,33] Droplets of different size were obtained by varying the rotational speed from 300 to 2500 rpm during spin-casting (scanning probe microscopy (SPM) images in Figure 2.1 (a)). Figure 2.1 (b) shows profiles of droplets cast at different rotational speeds. While the smaller droplets take the form of almost spherical caps (some are almost hemispherical), larger droplets take the shape of an oblate spherical cap. Figure 2.1 (c) shows mean droplet radius and height as function of casting velocity for the images shown in Figure 2.1a. As already obvious from the profiles shown in Figure 2.1 (b), the droplet form varies with different spin speeds, coming closest to hemispherical for a casting velocity between 1000 and 1500 rpm. Nevertheless, in a first

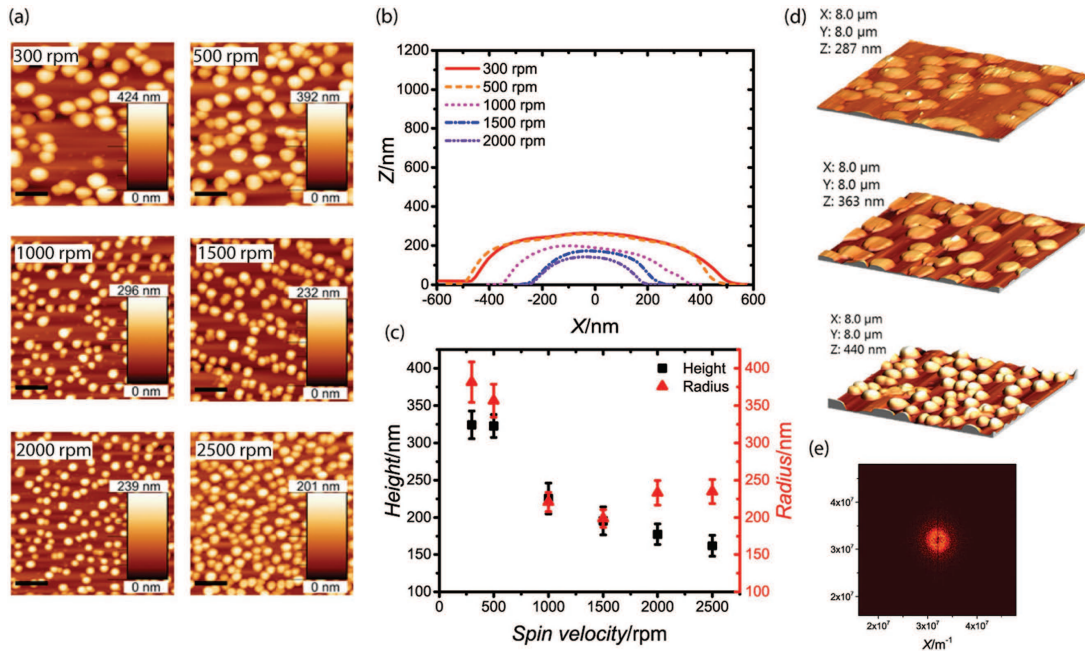


Figure 2.1 – (a) Scanning probe microscopy images of CyC droplets samples cast at different velocities. (b) Representative SPM profiles and (c) mean droplet height and radius as a function of casting velocity. Error bars on the droplets radius and height represent the standard deviation within the sample measured for each velocity. (d) 3D view of the effect of water added to the precursor CyC solution on the morphology of the drops (0, 4, and 10 vol% from top to bottom). (e) 2D-FFT of the SPM image of CyC droplets cast at 2500 rpm.

approximation, we describe the droplet morphology by two parameters: the droplet radius and their aspect ratio s , defined as the height/radius ratio. For a hemispherical droplet s would be 1. The droplet height and radius should be understood as mean value measured on a reasonable number of droplets by scanning probe microscopy. Parameters controlling the droplet shape are contact angle, surface tension, and droplet volume. Surface tension limits the minimum droplet size.^[34] More details on the control of droplet formation in the CyC system can be found in earlier work.^[35] Analysis of the height and size distribution of the droplet samples show the unimodal nature of the distribution for spin-coating speeds above 300 rpm (Figure S2.1, section 2.5). A strategy to control the droplet aspect ratio is to add water to the CyC initial ethanol solution in a controlled manner. Figure 2.1 (d) shows the 3D views of droplets cast at the same rotational speed but from initial solutions containing an increasing amount of water (0, 4, and 10 vol%). Addition of water to the initial dye solution results in an increase in the surface tension of the solution, leading to a change in the droplets' morphology

from spherical cap (dry ethanol solution) to almost hemispherical (10 vol% water).

2.2.2 Diffraction from droplet films

The characteristic droplet size and spacing resulting from the spinodal dewetting process gives rise to a characteristic ring pattern in the Fourier transform of the droplet arrangement (see Figure 2.1 (e)).^[31] We compare this to the Fraunhofer diffraction pattern of the sample. Also here we observe a ring pattern typical for a spinodal diffraction structure. To quantify the data, we record the intensity of the scattered light with a detector mounted to a goniometer that probes the polar angle. Diffraction intensities are then integrated over the azimuthal angle and are shown as a function of scattering (polar) angle and wavelength in Figure 2.2 for three different morphology regimes, characteristic for three different diffracting behaviors. The diffraction intensity depends strongly on wavelength and droplet dimensions. In a morphology regime 1 (height below 225 nm), diffraction is restricted to wavelengths below $\lambda = 600$ nm, in a morphology regime 3 (height above 350 nm) the main contribution to diffraction stems from wavelengths above $\lambda = 650$ nm, and in a morphology regime 2 (height between 225 and 350 nm) the main diffraction contribution is observed for wavelengths around $\lambda = 610$ nm. Here the diffraction intensity is higher than in the other regimes. The course of the diffraction angle with wavelength can be roughly estimated from Figure 2.2, it shows a rather linear dependence, which proves that light is indeed diffracted from the droplet ensemble and the individual droplets represent the scattering objects. Higher diffraction orders only become visible at very long integration times. What exactly provides the scattering contrast is the subject of the following sections, diffraction here obviously does not only depend on absorption and index of refraction of the droplets, but also on droplet dimensions.

2.2.3 Extinction and contribution of scattering

We continue our analysis by looking at the extinction properties of the films. Our diffraction and UV-vis measurements fully complement each other. UV-vis detects transmission of light that is scattered up to 5° and finally converted into extinction. All of our samples, on the other hand, scatter light into an angle larger than 5° (Figure 2.2). Absorbance can be measured with an integrating sphere. The diffraction component to extinction can thus be extracted from

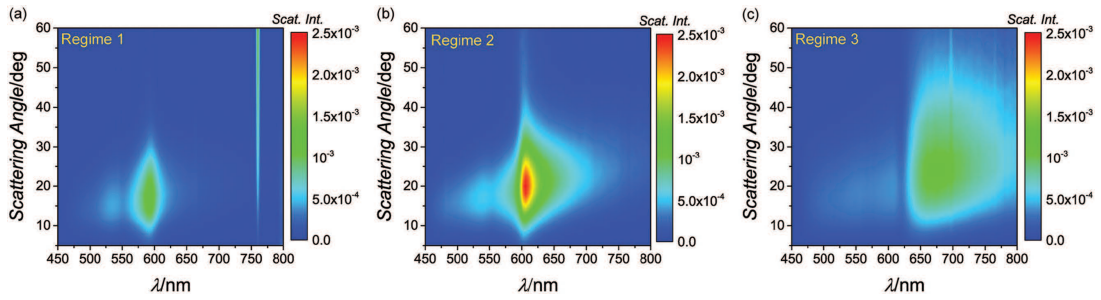


Figure 2.2 – Diffraction angles and wavelength dependence of diffraction intensity from samples of three different morphology types: (a) $r = 449$ nm, $h = 165$ nm; (b) $r = 647$ nm, $h = 279$ nm; and (c) $r = 483$ nm, $h = 543$ nm.

the UV–vis measurement. The data have to be analyzed carefully though because most of the droplets are thicker than 100 nm from whereon all incoming light is absorbed and coverage of the substrate with droplets greatly determines the absolute values. For a continuous CyC film and samples corresponding to the diffraction pattern shown in Figure 2.2, we show UV–vis extinction spectra as obtained from a transmission measurement and absorbance data as obtained from the integrating sphere (Figure 2.3 (a)). The thin film sample shows a spectrum that closely follows the imaginary part of the index of refraction (absorption coefficient k) as measured by ellipsometry (Figure 2.3 (b)). The two peaks at 575 and 525 nm correspond to the absorption of the monomer and dimer form of the dye, respectively.^[31]

The UV–vis extinction spectra of the droplet samples exhibit very different profiles. In particular, the three scattering regimes identified above also lead to three distinguishable extinction profiles (Figure 2.3 (a),(c)). The diffraction contribution in extinction is more or less represented by the difference between the extinction and absorbance profiles. As the samples also diffract light in the absorbance region (Figure 2.2), absorbance never reaches the values of extinction. In regime 2 the contribution to scattering in the absorption region is largest. The absorbance spectra from the integrating sphere exhibit flat profiles attributed to the strong absorption from the droplet samples.

The accuracy of UV–vis spectroscopy allows for a detailed analysis of all droplet samples. When plotting the extinction peak position as a function of the droplet height, we find that all data fall onto one master curve (Figure 2.3 (d)). Within the range in radii we find for a certain height we can thus also use the average droplet height to quantify the scattering behavior. Height and radius of all droplets investigated in Figure 2.3 are shown in the Supporting Information. To

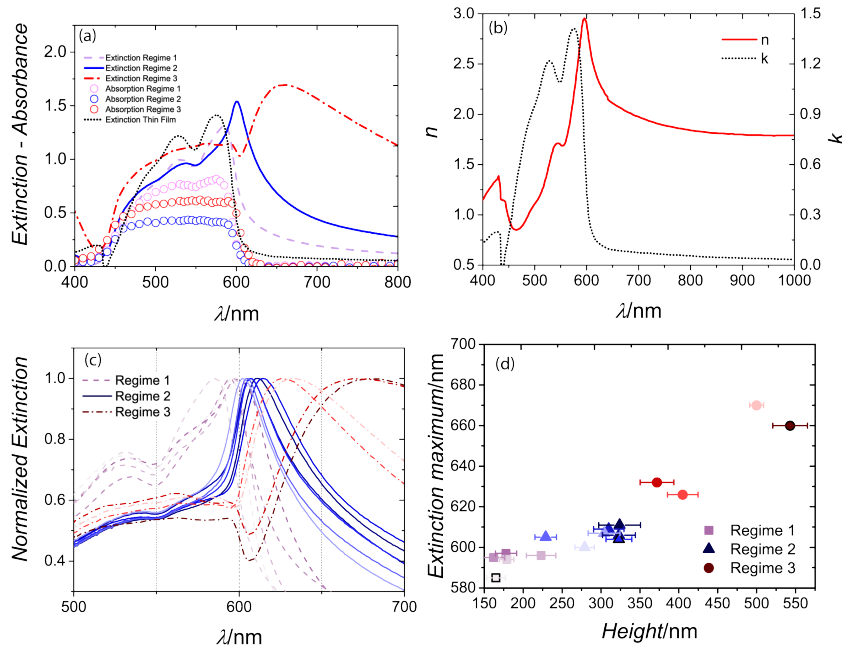


Figure 2.3 – (a) Extinction (lines) and absorbance (circles) spectra of droplet samples characteristic from regimes 1, 2, and 3 (pink dashed, blue full, and red dotted-dashed, respectively) compared to a thin film (black dotted line). Depending on the droplet morphology, extinction spectra exhibit different profiles attributed to different scattering regimes. Regimes 1, 2, and 3 correspond to pink dotted, blue full, and red dotted-dashed lines, respectively. (b) Optical constants of CyC in a continuous film measured by ellipsometry. n and k are the real and imaginary part of the refractive index, respectively. (c) Normalized extinction spectra of droplet samples in the height range from $h = 160$ to 550 nm, indicated by different color tones and line types specified in (d). The characteristic shape of the profiles allows assigning each spectrum indisputably to one of the three “regimes” indicated by different colors. (d) Wavelength of extinction maximum versus droplet height from the spectra shown in (c). Bordered symbols correspond to the samples presented in (a).

further justify this choice we performed FDTD simulations on the droplets (described in detail in 2.2.6) that confirm that height is the most sensitive parameter to describe optical behavior. In smaller droplets (droplet height $h < 225$ nm, regime 1) the extinction spectrum shows a profile close to that of a continuous film. However, an additional feature appears, red-shifted compared to the monomer peak, significantly broadening the extinction between $\lambda = 550$ and 600 nm.

Moreover, a small extinction tail characteristic of light scattering from the sample is visible in the nonabsorbing region of the dye, above 600 nm. For larger droplets (droplet height $h > 375$ nm, regime 3) the extinction deviates quite substantially from the thin film absorption profile.

It is characterized by a flat extinction profile in the absorbing region of the dye and a broad prominent feature at long wavelengths (regime 3). This long wavelength feature is reminiscent of Mie scattering observed in nonabsorbing particles of constant refractive index. Extinction in the absorption region of the dye remains featureless because the incoming light is fully absorbed within a droplet.

For samples in the intermediate regime 2 ($225\text{nm} < h < 350\text{nm}$), the extinction peak resembles an optical resonance. The peak narrows down and gains intensity. The peak lies between $\lambda = 600$ and 610 nm. The spectra also show an extended scattering tail into the long wavelength region. The peak maximum now is fully outside of the absorption band of the dye, but coincides with the region where the dye shows a strong variation in the refractive index (Figure 2.3 (b)). The strong variations of the refractive index near the absorption edges are a natural consequence of the oscillatory nature of the electronic absorption and are consistent with Kramers–Kronig relations.^[24,36] This observation suggests that the sharp scattering features are also related to the index of refraction n . This effect will be discussed in more details later.

Figure 2.3 (c) shows normalized extinction spectra of a set of samples with increasing droplet height (but varying aspect ratios). In this paper the similarity of the spectra of the different regimes becomes clear. Each regime can thus be assigned to a certain range of droplet height or to a range of extinction peak wavelengths. Droplets with a height below $h = 225$ nm can be assigned to regime 1 (peak wavelength between $\lambda = 595$ and 598 nm), droplets with a height between 225 and 350 nm can be assigned to regime 2 (peak wavelength between $\lambda = 600$ and 610 nm), while droplets higher than 350 nm are assigned to regime 3. Interestingly enough, the peak extinctions of regime 1 and 2 are all in a wavelength region where n is sharply increasing and decreasing, respectively.

2.2.4 Array of scatterers in a diffraction plane

To fully understand the optical behavior of the thin film we have to understand how the optical properties of the individual droplets generate an optical contrast leading to the observed diffraction pattern. In the following we perform an analytical study of the diffraction of an array of scatterers taking strong variations in n and k into account (Figure 2.3 (b)). The full

Chapter 2. Structuring amorphous thin films of cyanine dyes

derivation of the formulas can be found in section 2.4. The total diffracted field of an array of identical scatterers in the far field is given by the product of two terms: (i) the Fourier transform of the individual scatterer which gives rise to the envelope of the diffraction field and (ii) the sum of phase terms which incorporates the distribution of the scattering elements. While a completely random arrangement of scattering elements does not give rise to any preferred diffraction angles, the diffraction cone observed in our experiments can be explained by a distribution of scattering elements with a (quasi-)constant nearest neighbor distance $p = \lambda / \sin \theta_{\text{cone}}$, as suggested by the Fourier transform of the SPM images (Figure 2.1e). Higher diffraction orders are very weak in this example.

We define the efficiency of scattering M as the ratio of the first and zeroth order (forward scattering) signal. M is given by the Fourier transform of a single scatterer alone, as the sum of phase terms is equal for all orders of the diffraction signal:

$$M = \frac{I(m=1)}{I(m=0)} = \frac{|\Psi_p(k=k_1)|^2}{|\Psi_p(k=0)|^2} = \left| \frac{N \times FT[\tilde{d}(x)](k=k_1)}{A + N \times FT[\tilde{d}(x)](k=0)} \right|^2 \quad (2.1)$$

where N is the number of scatterers on an area A , k_1 the direction of first-order scattering, while $\tilde{d}(x)$ describes the transmission behavior of the individual element, which represents a material with a complex refractive index $\tilde{n} = n + ik$. The real part n leads to a phase shift of the transmitted light, while k describes absorption. For simplicity, we describe the scatterers as cylinders with radius r and height h . We then arrive at the following expression:

$$M = \frac{\left| N \times [\exp(i\Phi) \times t - 1] \pi r^2 \frac{2J_1\left(2\pi \frac{r}{p}\right)}{2\pi \frac{r}{p}} \right|^2}{\left| A + N \times [\exp(i\Phi) \times t - 1] \pi r^2 \right|^2} \quad (2.2)$$

where t is the amplitude transmission coefficient of the diffraction element, while Φ is the phase change. As the distance p between neighboring scatterers is larger than their diameter, $p > 2r$, the argument of the Bessel function J_1 is smaller than π . Introducing the fill factor:

$$F = \frac{N \times \pi r^2}{A} \quad (2.3)$$

i.e., the ratio of the area occupied by the scatterers divided by the total area, we find

$$M = F^2 \left| \frac{2J_1\left(2\pi\frac{r}{p}\right)}{2\pi\frac{r}{p}} \right|^2 \frac{|\exp(i\Phi) \times t - 1|^2}{|1 + F \times [\exp(i\Phi) \times t - 1]|^2} \quad (2.4)$$

In the general case, the phase shift and transmission through a thin film are related to the complex refractive indices according to^[37]

$$t \times \exp(i\Phi) = \frac{t_{01} t_{12} \exp(-i\beta_1)}{1 + r_{01} r_{12} \exp(-2i\beta_1)} \times \exp(i\beta_0) \quad (2.5)$$

where

$$\beta_1 = \frac{2\pi}{\lambda} h \tilde{n}_i, \quad t_{ij} = \frac{2\tilde{n}_i}{\tilde{n}_i + \tilde{n}_j}, \quad r_{ij} = \frac{\tilde{n}_i - \tilde{n}_j}{\tilde{n}_i + \tilde{n}_j} \quad (2.6)$$

\tilde{n}_j is the complex refractive index of air ($j = 0$), of the scatterer ($j = 1$) and the substrate ($j = 2$), respectively.

Figure 2.4 shows the first-order diffraction efficiency, Equation 2.4 with the optical parameters of CyC on a BK7 glass substrate, a fill factor of $F = 0.25$, and different radii r and height h of the individual scattering element according to the three regimes. The average nearest neighbor distance p was estimated from $F = \pi r^2 / p^2$. The analysis shows that close to the absorption band diffraction can be enhanced. The analysis also qualitatively reproduces the different scattering plots given in Figure 2.2. For larger droplets a strong dependence of the scattering spectra on droplet size is observed. The broad scattering feature indicates a nonresonant Mie-type phenomenon at the individual droplets and is addressed in the next section.

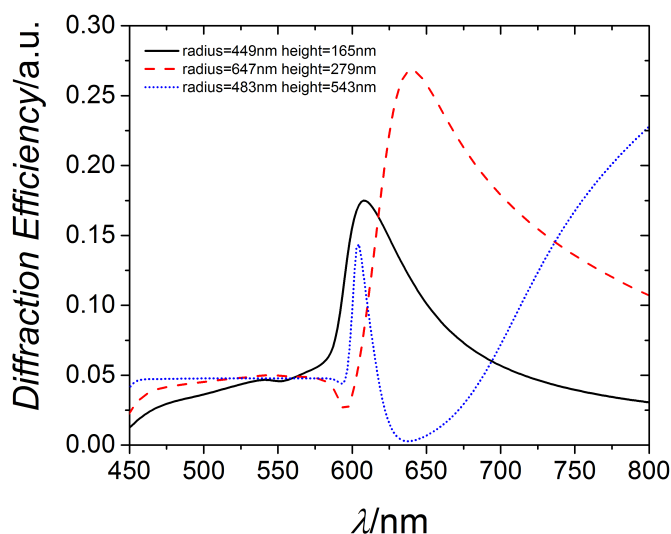


Figure 2.4 – Simulated diffraction efficiencies for the three regimes.

2.2.5 Anomalous dispersion effect

For a further understanding we performed FDTD simulations for assemblies of droplets of different diameters. The intermediate droplet size regime is of prime interest because in this case the scattering contribution is close to the absorption edge of the dye. The scattered electric field distribution around the individual droplets was simulated. The transmitted power through a randomly distributed grating of dye droplets was calculated for the (0,0) grating order. The near-field solution was propagated into the far-field and extinction spectra were calculated. For a meaningful analysis, the experimental values for the optical constants of the dye were used in the simulations. For the sake of clarity, in a first set of simulations droplets were taken to be hemispherical (height = radius).

Figure 2.5 (a) shows the simulated extinction spectra of samples with heights ranging from 50 to 470 nm. Along general lines, the simulations follow the experimentally observed trends, but show differences in some details. In the experiment, sharp transitions can be identified between three different extinction profiles with characteristic features when increasing the droplet height (Figure 2.5 (b)). In the simulations, the spectral changes can be best described by a smooth transition of the main extinction peak from an absorption peak with maximum at $\lambda = 585$ nm into a broad scattering feature reminiscent of Mie scattering at longer wavelengths.

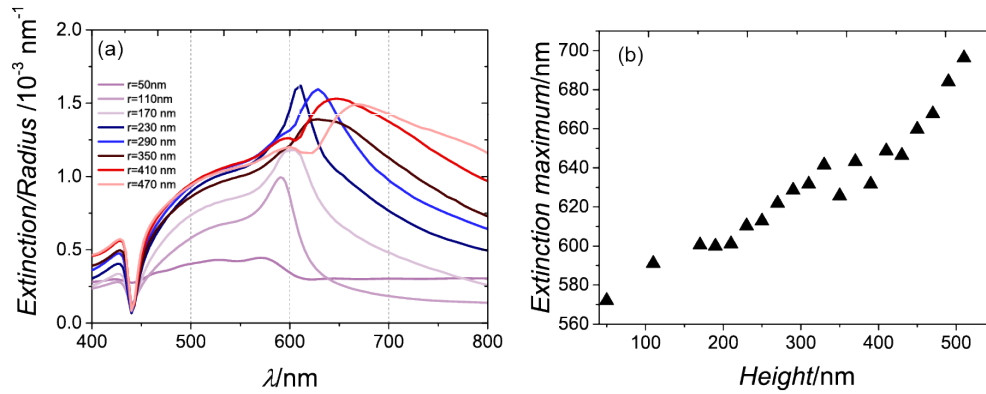


Figure 2.5 – (a) Simulated extinction spectra of hemispherical droplets of varying radius. (b) Simulated extinction maxima as a function of droplet height (here height=radius). The values are comparable to the experimental data (Figure 2.3d)

In between, for a droplet height of $h = 230$ nm extinction reaches a maximum while the FWHM is smallest. Intuitively, it can be understood that the Mie peak is never observed in wavelength regions where the dye absorbs since only little light is transmitted through the droplets.

Now that we validated the FDTD simulations, through the comparison of simulated and experimental extinction spectra, we can rationalize the resonance peak character of scattering from samples of regime 2. For that we look at the dependence of the scattering efficiency on the optical constants n and k of a particle of given size.^[14] If n is rapidly changing across the spectrum (as it is the case at an absorption edge) the scattering efficiency will also vary rapidly. In Figure 2.6 the extinction efficiencies of a hemispherical droplet of $h = 375$ nm with different constant values of n and k (taken from the dispersion relation of the dye) are shown. The extinction features of these artificial droplets are rather broad but show large variations when varying the n and corresponding k values. The extinction spectrum of a dye droplet is then constructed by picking for each λ the extinction value of the corresponding pair of n and k (Figure 2.6, solid red line). More details on that procedure are found in [25]. Even though this approach does not represent a real physical situation, it is useful to understand the effect of a strongly varying n index, sometimes called anomalous dispersion artifact,^[25] on extinction spectra.

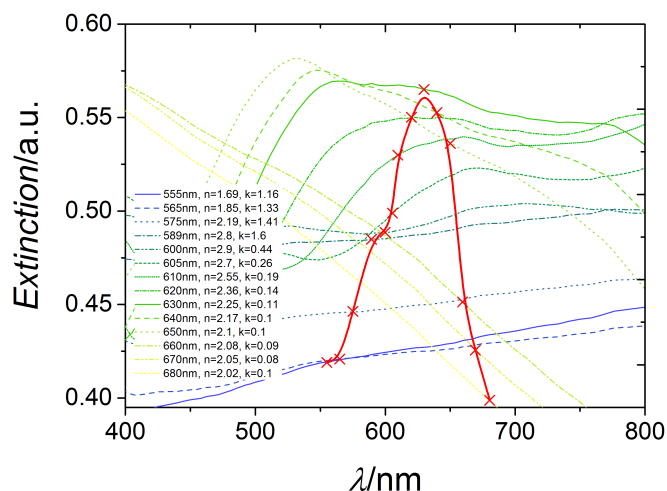


Figure 2.6 – Extinction spectra simulated for an ensemble of hemispheres with radius $r = 375$ nm and fixed optical constants taken from the dispersion relation of the dye (thin blue, green and yellow lines). From these curves the effective extinction of the droplet ensemble with varying k and n is constructed (thick red solid line).

2.2.6 Droplet height and size distribution

In section 2.2.1 describing droplet formation we had pointed out that in the standard dye solution the aspect ratio decreased with increasing droplet radius. We also pointed to the possibility to adjust the aspect ratio by adding water to the solution. In the experiments we were analyzing samples with different aspect ratios and came to conclude that only the droplet height h determines the optical response. We here consolidate this observation with a FDTD simulation. In a first step, we keep the radius constant and vary the height (Figure S2.4 (a), section 2.5). Varying the height alone can cause transitions from one regime to another. In the second case, we keep the height constant and vary the radius (Figure S2.4 (b), section 2.5). As expected in this case, only small spectral changes are observed, while the scattering efficiency increases with increasing radius. Along the same lines, the effect of a more realistic droplet size distribution versus monodisperse droplets was also evaluated. As visible from Figure S2.4 (c) and (d) (section 2.5), the presence of droplets of smaller size significantly broadens the main extinction peak, while the effect of a radius size distribution at constant height on the spectral features is limited. The thickness dependency of the extinction behavior as well as the scattering peaks can be compared to thin-film interferences in low-index layers. In

this case, scattering results from reflection or refraction effects at the boundaries between the different media that are involved. Thin film interference phenomena typically show a thickness dependency and high damping due to the fact that light is not resonantly oscillating within the film. The dye droplet indeed cannot confine light and the scattering behavior results from an interference-like phenomenon, as described in the next section. This again speaks for droplet height as the most relevant parameter to describe the optical phenomena.

2.2.7 Non-resonant Mie scattering

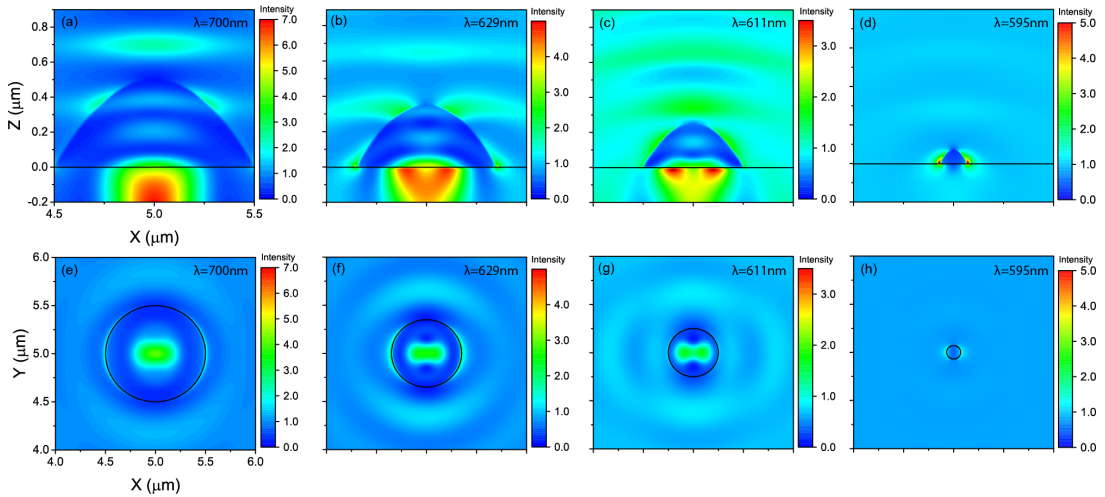


Figure 2.7 – Cross sections (top row) and top view (bottom row) of the simulated near-field intensity within CyC droplets of height (a,e) 500, (b,f) 350, (c,g) 250 and (d,h) 70 nm on a glass substrate. For each droplet radius simulation is performed at the wavelength of maximum extinction.

So far we attributed the long wavelength extinction feature to Mie scattering, whereby Mie scattering refers to a situation where the size of the scattering particles is comparable to the wavelength of the incoming light. We already suspected that the low index nature of our material is not able to confine electrical modes within the droplet. In order to better understand the exact nature of the scattering process, we simulate the electrical near-field intensities by the FDTD method. Figure 2.7 shows the intensity of the electromagnetic wave for cross sections along the propagation direction and top views at the interface between the droplet and the glass substrate at the extinction maximum for CyC spherical caps on a glass substrate for heights $h = 500, 350, 250,$ and 70 nm, representing regimes 3, 2, 2, and 1, respectively. While

the height/radius ratios in these samples are 1, the shape is not strictly hemispherical to better represent the experimental situation. Droplets are illuminated from top by a linearly polarized plane wave light source. Each droplet is illuminated at the maximum extinction wavelength ((a) and (e) $\lambda = 700$ nm, (b) and (f) $\lambda = 629$ nm, (c) and (g) $\lambda = 611$ nm, (d) and (h) $\lambda = 595$ nm), where the contribution from scattering is maximum.

The non-resonant nature of the scattering can also be seen from the time sequence of a wave packet traveling through the droplet (see section 2.5). Generally speaking, the spherical caps act as a microlens due to the phase difference the light wave experiences when traveling through the droplet with respect to vacuum. Assuming a thin structure this phase difference can be expressed as $\Delta\phi = z(n - 1)$, where z is the distance traveled through the drop and n the real part of the refractive index. It is clear from the previous expression that the accumulated phase difference depends on the point of entry and the total distance traveled through the droplet and that it is maximum for light traveling through the center of the droplet.^[38] The accumulated phase difference results in the formation of constructive/destructive interferences in the near field around and beyond the droplet and leads to a complex E-field pattern. Depending on height, radius, and wavelength, the incoming plane wave traveling through a droplet will eventually bend. For droplets of 500 (corresponding to regime 3), 350, and 250 nm (corresponding to regime 2) height, at the wavelength of maximum extinction, the incoming wave is focused behind the droplet forming a source of scattered light.

We now describe the optical characteristic when decreasing the droplet size, focusing especially on the resonant-type regime 2. We note that the field intensity inside a droplet is generally lower than in the surrounding vacuum, and is lowest for the peak wavelength in regime 2. Second, a stationary interference pattern is observed in front of the droplet, which can be a rough indication of the scattering cross section of the individual droplet. This modulation of field intensity is also largest for the peak wavelength in regime 2. For larger droplets, light is focused onto one point well below the substrate plane. As one decreases the droplet size, the focal point moves closer to the interface between droplet and substrate, where it splits into two points (for non-polarized light a ring would be observed). For 70 nm droplets (regime 1) in the absorption range, most of the light is absorbed by the droplets and the focal points are guided to the contact line of the droplet above the substrate.

Similar to regime 1, the far-field optical response is dominated by diffraction of the droplet

array. The diffraction contrast in regimes 2 and 3 is a result of defocusing the incoming wave behind the focal points.

2.2.8 Towards sensor applications

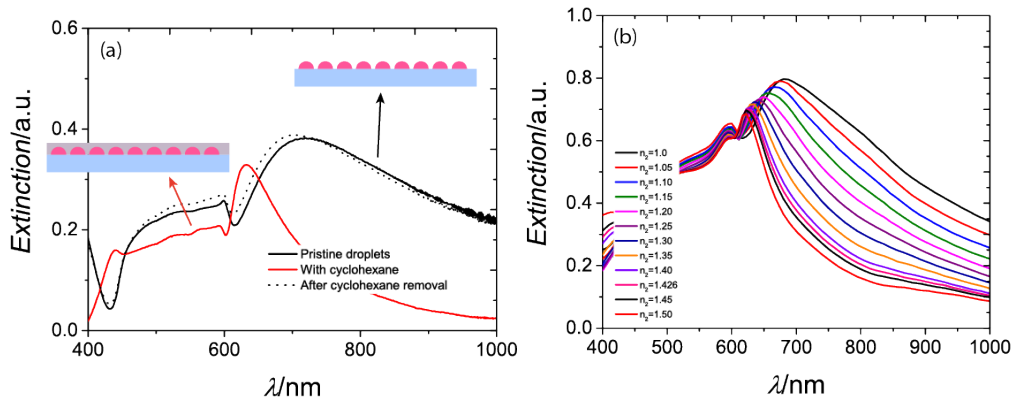


Figure 2.8 – (a) Significant changes in the extinction profile of an array of CyC droplets is measured when the surrounding index of refraction is changed from 1.0 (air) to 1.43 (cyclohexane). (b) Simulated changes in the extinction profiles of 500 nm droplets sample for incremental variations in the refractive index surrounding the structure.

Generally speaking, dielectric materials find a wide range of applications in optical sensing based on resonant structures such as nanofibers, photonic crystals, and diffraction gratings. In this section, we demonstrate the potential of our cyanine droplet system for refractive index-based sensor applications. Changes in the refractive index surrounding a classical resonant Mie scattering structure induce only limited spectral changes. However, in the case of non-resonant structures like ours, the extinction response shows high sensitivity to variations in the refractive index of the medium surrounding the droplets.

Figure 2.8 (a) shows the variation in the spectral response when droplets showing a regime 3 type extinction are immersed in cyclohexane ($n_{\text{cyclohexane}} = 1.426$). In this case, a large spectral shift is observed from 710 nm for the pristine structure to 610 nm for the structure immersed in cyclohexane. After removal and drying from cyclohexane, the original extinction profile is recovered.

Figure 2.8 (b) shows the simulated spectral changes obtained for incremental variations of the refractive index surrounding the structure from 1.0 to 1.5. The broad extinction peak observed

for the droplets in air narrows down and blue-shifts proportionally to the changes in refractive index. Such sensitivity to small incremental changes is extremely promising for the design of refractive index-based sensors.

2.3 Conclusion

We have demonstrated an easy fabrication method for diffracting arrays of cyanine dye droplets with very specific optical properties. The arrays diffract light in different wavelength ranges depending on the thickness of the individual droplets. In particular, for droplets with thicknesses in the range of 225–350 nm, diffraction occurs mainly within a narrow wavelength window. Strong wavelength selectivity occurs when a nonresonant form of Mie scattering interferes with a strong variation of the index of refraction at the absorption edge of the dye. In that scattering regime, the droplet acts as a wavelength selective diffracting microlens. Strong, resonance-type features in extinction are here a pure effect of the droplet geometry and the index of refraction variation. We are confident that the droplet fabrication process can be applied to dyes with absorption bands at different wavelengths hence allowing tuning the diffraction selectivity to different colors.

A proof-of-concept for the application of these arrays as refractive index-based sensor has been presented. The sensing mechanism is based on the variation of the scattering efficiency when the array is exposed to environmental media of different refractive indices.

The strong wavelength dependence of scattering in regime 2 is particularly interesting as it can find applications in wavelength selective diffraction and in wavelength selective switches. Finally, microlens arrays as such find numerous applications,^[39] miniaturization of lenses with small focal spot size and depth of focus are a key factor for subdiffraction optics.^[40]

2.4 Experimental details

Dye preparation

CyC was synthesized in laboratory.^[41] A saturated solution of CyC was prepared by dissolving 10.2 mg mL⁻¹^[31] of the dye in ethanol (puriss., over molecular sieve (H₂O ≤ 0.01%), Sigma-Aldrich). In order to obtain larger hemispherical droplets, deionized water was intentionally added to the saturated ethanolic solution (up to 10 vol%). Solutions were stirred for at least 24 hours before use.

Droplets formation

2.5 × 2.5 cm² microscopy glass slides were used as substrates. The slides were cleaned by ultrasonication in an acetone bath for 5 min followed by an ethanol bath for another 5 min. Substrates were then blow-dried with nitrogen. CyC droplets were obtained by spincoating the dye saturated solution on glass substrates. 0.3 mL of dye solution was first filtered and distributed on the substrates, followed by a slow rotation at 200 rpm for 3 s. The rotational speed was then increased to the desired value (ranging from 300 to 2500 rpm) at a rate of 3000 rpm s⁻¹ and the samples were spun for 60 s.

Scanning probe microscopy

The samples' morphology was evaluated by SPM using a NanoSurfMobile S (Nanosurf AG, Switzerland) in tapping mode at 170 kHz with rectangular silicon cantilevers (Nanosensors: MikroMasch, Lady's Island, SC) with a force constant of ≈40 N m⁻¹ and a tip radius of 10 nm. The droplet thickness was measured with WsXM software.^[42] Droplet radii were measured using ImageJ software, by fitting a circle.

Extinction measurements

Extinction spectra of the samples were measured using a Varian Cary 50 UV-vis spectrophotometer. Absorbance was measured with the Horiba Jobin Yvon Fluorolog FL-3 equipped with an integrating sphere (Horiba Jobin Yvon F-3018).

Angle resolved scattering

Light diffraction was measured with a photodiode mounted to a motorized goniometer. The light source was a Xenon lamp (LOT-Oriel, UK) coupled to a monochromator (Omni- λ 300, Zolix, China). The beam was optically focused on the sample surface, with a focal length of 175 mm and a spot size of 1 mm². The angle of incidence was 90°. The increment in wavelength was 4 nm, the goniometer angle steps were 2°. The mechanical scanning range of the monochromator is 0–1200 nm.

FDTD simulations

FDTD simulations were performed using Lumerical FDTD Solution software (Lumerical Inc., Canada). Perfectly matched boundary conditions on all the sides of the simulation box were used for single droplet simulations, whereas periodic conditions were used for the simulation of a droplet ensemble. The wavelength range of the simulation was 400–800 or 400–1000 nm. The arrangement of droplets for the simulations was adapted from experimental data and is shown in the Supporting Information. Optical constant values (n,k) of CyC were obtained by ellipsometry on a continuous dye film.

Ellipsometry

Values of the optical constants (n,k) of CyC were obtained on a continuous dye film, using a spectroscopic ellipsometer M2000VI (J.A. Woollam, USA).

2.5 Supporting Information

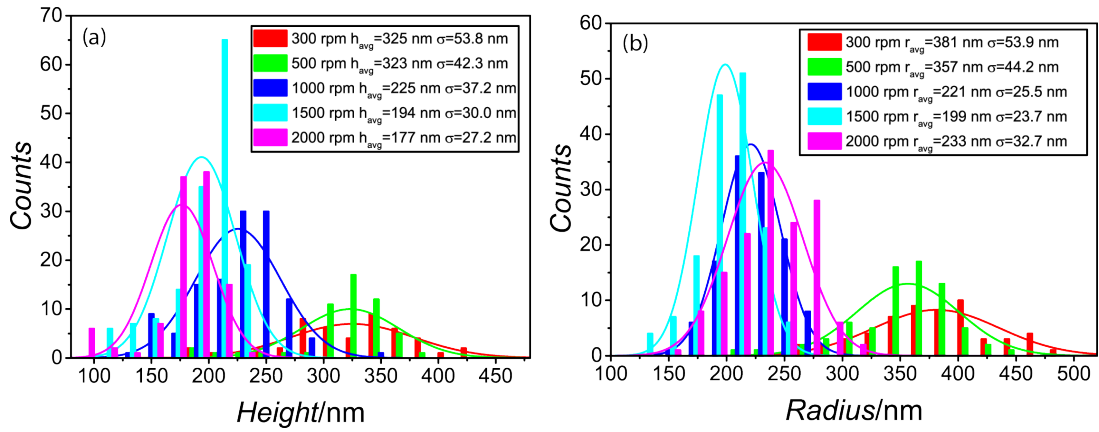


Figure S2.1 – Droplets height and radius distribution as a function of spin-coating velocities. Normal distribution curves are superimposed to the histograms. Dimensions average and standard deviation are indicated in the legend.

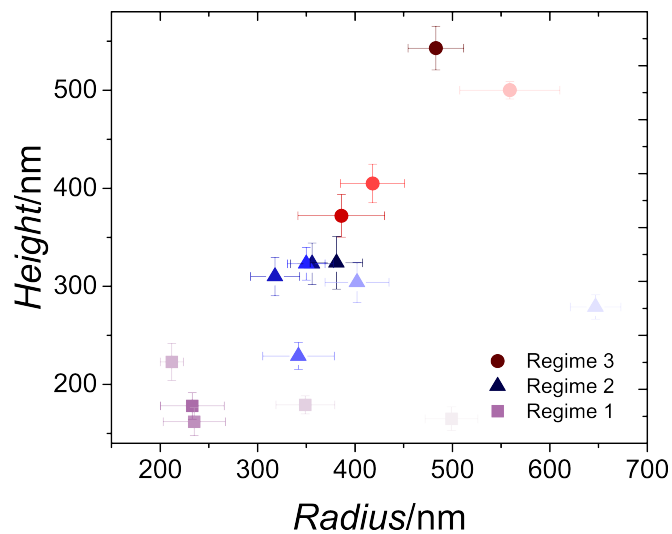


Figure S2.2 – Height and radius of droplets from samples described in section 2.2.3.

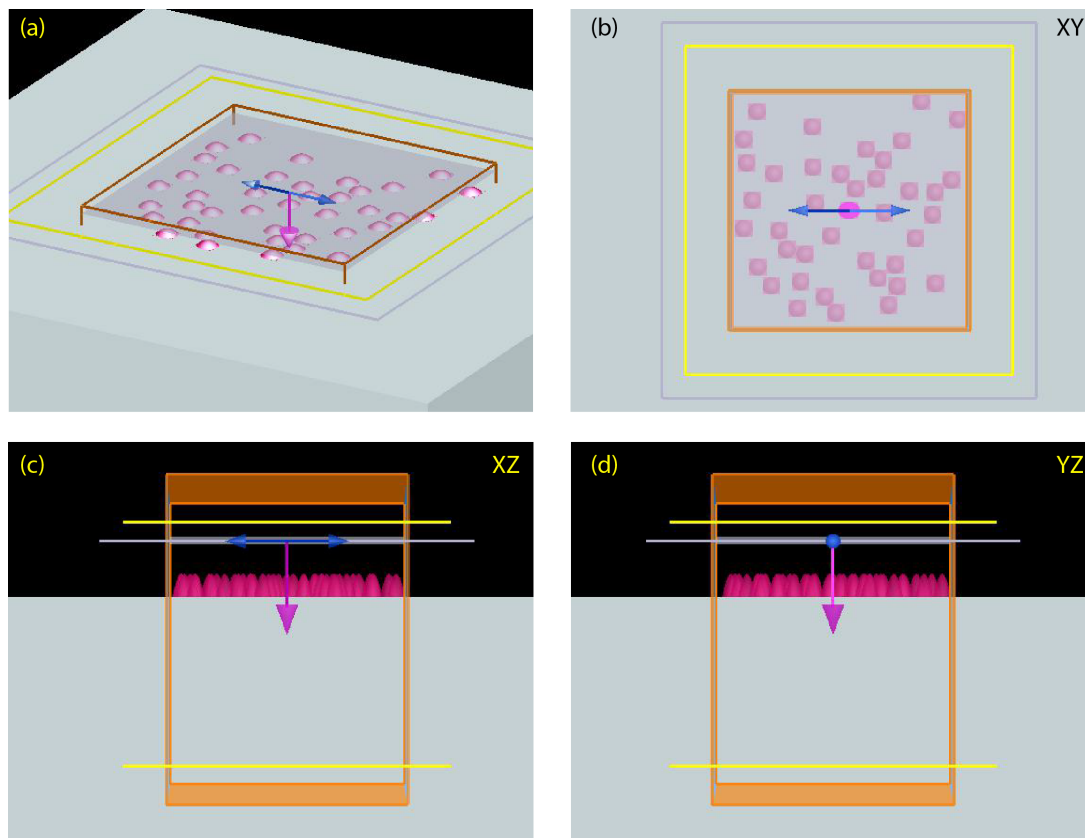


Figure S2.3 – Arrangement of droplets used in the FDTD simulations.

A plane wave light source is placed above the droplets. The propagation direction is along the z axis, as shown by the pink arrow. The electric field is polarized parallel to the substrate in the X direction as shown by the blue double arrow. The orange box represents the simulation area. The boundary conditions along the z-axis are taken to be perfect matched layers (PML). The boundary conditions in the x-y plane are taken periodic to reduce the calculation time. A reflection and a transmission monitor are placed above and below the droplets respectively to calculate reflected and transmitted power. The raw results are used to calculate the number of grating order in the structure and then extract the power transmitted (or reflected) at each order. To simulate the extinction measured in a UV-vis experiment, only the transmitted power at the (0,0) grating order was taken. The script used to perform the calculations was adapted from.^[43]

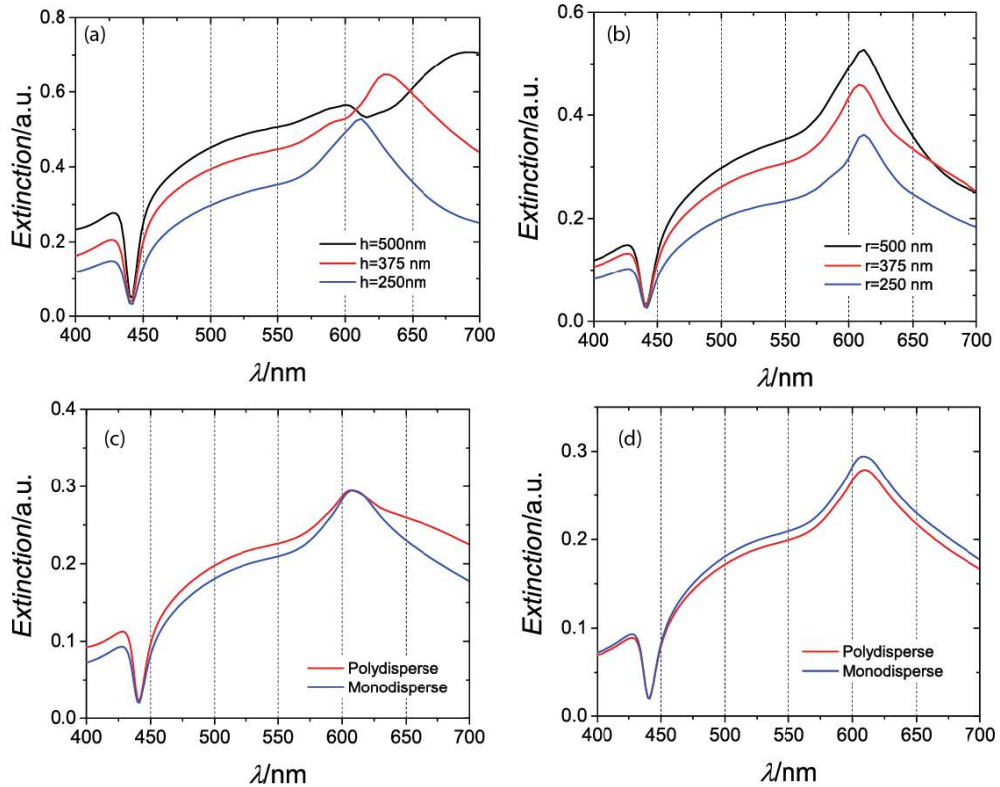


Figure S2.4 – FDTD simulations of extinction spectra of different droplet ensembles.

(a) The effect of height variations (for a constant radius of 500 nm) and (b) the effect of radius variation (for a constant height of 250 nm) shows the important influence of the droplet height on the extinction spectra CyC droplet samples. (c) Changing the droplet ensemble from “all equal” (monodisperse) with $h = 281\text{ nm}$ and $r = 500\text{ nm}$ to droplets with a thickness distribution as specified (17% $h = 125\text{ nm}$, 17% $h = 250\text{ nm}$, 66% $h = 281\text{ nm}$; $r = 500\text{ nm}$) leads to broadening of the extinction peak. (d) Changing the droplet ensemble from monodisperse ($h = 250\text{ nm}$, $r = 325\text{ nm}$) to droplets with different radii (17% $r = 250\text{ nm}$, 66% $r = 325\text{ nm}$, 17% $r = 500\text{ nm}$; $h = 250\text{ nm}$) shows almost no effect on extinction.

Theoretical Analysis

Array of scatterers in a diffraction plane The diffraction mask on a plane G containing a set of N identical scatterers or diffraction elements, such as an array of droplets, is written^[44]

$$D(\mathbf{x}) = 1 + \sum_{n=0}^N \delta(\mathbf{x}_n - \mathbf{x}_0) \tilde{d}(\mathbf{x}, \mathbf{x}_0) \quad (\text{S2.1})$$

where \mathbf{x}_n are the positions of the diffracting elements, while $\tilde{d}(\mathbf{x}, \mathbf{x}_0)$ describes the transmission behavior of the individual element. A value of $\tilde{d} = -1$ corresponds to complete blocking. If the diffracted light is collected in direction $\hat{\mathbf{k}}$ under the angle $\cos(\theta_{out}) = \hat{\mathbf{k}} \cdot \hat{\mathbf{z}}$ in the far field using a lens (Fraunhofer diffraction), the total diffracted field is proportional to

$$\Psi_P \propto \iint_G D(\mathbf{x}) \exp[-i\mathbf{k} \cdot \mathbf{x}] dx dy \quad (\text{S2.2})$$

which is the Fourier transform of the diffraction mask.^[45] Inserting the array of scatterers, Equation S2.1 we obtain

$$\Psi_P \propto \delta(\mathbf{k}) \times A + \sum_n \iint_G \delta(\mathbf{x}_n - \mathbf{x}_0) \tilde{d}(\mathbf{x}, \mathbf{x}_0) \exp[-i\mathbf{k} \cdot \mathbf{x}] dx dy \quad (\text{S2.3})$$

where A is the illuminated area. The only effect of the delta-distribution is to shift the element to a different place on the plane. According to the Fourier shift theorem and selecting $\mathbf{x}_0 = 0$ the transform is

$$\Psi_P(\mathbf{k}) \propto \delta(\mathbf{k}) \times A + \sum_n \exp(-i\mathbf{k} \cdot \mathbf{x}_n) \times FT[\tilde{d}(\mathbf{x})](\mathbf{k}) \quad (\text{S2.4})$$

The total diffracted field of an array of identical scatterers is given by the product of two terms: (i) the Fourier transform of the individual scatterer which gives rise to the envelope of the

diffraction field; and (ii) the sum of phase terms which incorporates the distribution of the scattering elements. The field in forward direction $\mathbf{k} = 0$ is

$$\Psi_p(\mathbf{k} = 0) \propto A + N \times FT[\tilde{d}(\mathbf{x})](\mathbf{k} = 0) \quad (\text{S2.5})$$

which includes N times the forward signal of an individual scatterer. Assuming a regular 2-dimensional array of scatterers, the positions \mathbf{x}_n can be written

$$\mathbf{x}_n = n_x \mathbf{p}_x + n_y \mathbf{p}_y \quad \text{with} \quad n_x \in [1, N_x], \quad n_y \in [1, N_y] \quad (\text{S2.6})$$

In this case, the sum of phase terms in Equation S2.4 represents a geometric sum which is^[44]

$$\sum_n \exp(-i\mathbf{k} \cdot \mathbf{x}_n) = \frac{1 - \exp(-iN_x \mathbf{k} \cdot \mathbf{p}_x)}{1 - \exp(-i\mathbf{k} \cdot \mathbf{p}_x)} \times \frac{1 - \exp(-iN_y \mathbf{k} \cdot \mathbf{p}_y)}{1 - \exp(-i\mathbf{k} \cdot \mathbf{p}_y)} \quad (\text{S2.7})$$

The largest signals are obtained if the denominator vanishes, i.e. if

$$\mathbf{k} \cdot \mathbf{p}_x = m_x \times 2\pi \quad \text{and} \quad \mathbf{k} \cdot \mathbf{p}_y = m_y \times 2\pi \quad (\text{S2.8})$$

for which the sum equals, $N = N_x \times N_y$. Introducing the scattering angle explicitly

$$\frac{2\pi}{\lambda} \sin\theta_{x,y} p_{x,y} = m_{x,y} \times 2\pi \quad \text{or} \quad \sin\theta_{x,y} = m_{x,y} \frac{\lambda}{p_{x,y}} \quad (\text{S2.9})$$

The diffraction condition obtained from simple geometric arguments, Figure S2.5, is reproduced.

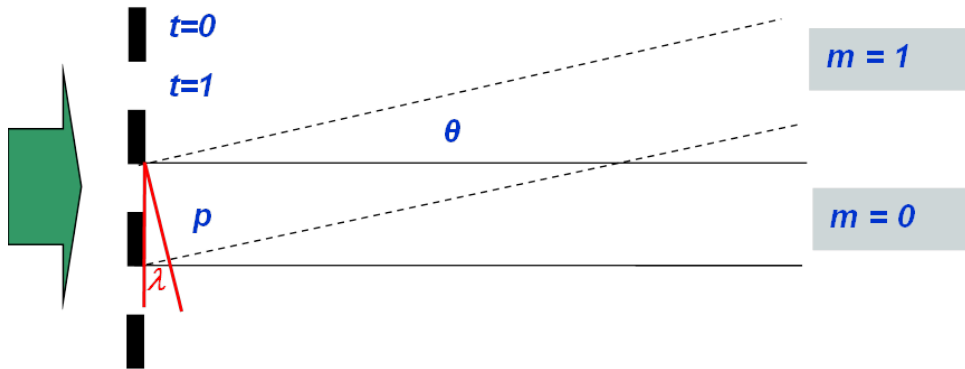


Figure S2.5 – Simple geometric argument to explain the origin of diffraction orders.

For a transmission grating the black lines in Figure S2.5 block the light coming from left, $t = 0$, and the diffraction orders are determined by the condition that the rays from neighbouring grating lines are shifted by m times the wavelength and hence interfere constructively. This is equivalent to $\sin \theta = m\lambda/p$, Equation S2.9. The sine of the diffraction angle increases linearly with the wavelength.

Let's turn now to the efficiency of scattering given by the ratio of the first and zeroth order signal. According to Equation S2.4 the ratio is given by the Fourier transform of a single scatterer alone, as the sum of phase terms is equal for all orders of the diffraction signal.

$$M = \frac{I(m=1)}{I(m=0)} = \frac{|\Psi_P(\mathbf{k} = \mathbf{k}_1)|^2}{|\Psi_P(\mathbf{k} = \mathbf{0})|^2} = \left| \frac{N \times FT[\tilde{d}(\mathbf{x})](\mathbf{k} = \mathbf{k}_1)}{A + N \times FT[\tilde{d}(\mathbf{x})](\mathbf{k} = \mathbf{0})} \right|^2 \quad (\text{S2.10})$$

The individual scattering element represents a material with a complex refractive index $\tilde{n} = n + ik$. The real part n leads to a phase shift of the transmitted light, while k describes absorption. A scatterer of cylindrical shape with radius r and height h is described by

$$\tilde{d}(\mathbf{x}) = \text{circ}(\mathbf{x}, r) \times [\exp(i\Phi) \times t - 1] \quad (\text{S2.11})$$

where we introduced a transmission coefficient t and a phase shift Φ . The only \mathbf{x} -dependence is found in the circ function, the Fourier transform of which is given by^[45]

$$FT[\text{circ}(\mathbf{x}, r)](\mathbf{k}) = \pi r^2 \frac{2J_1(k_{\parallel} r)}{k_{\parallel} r} \quad (\text{S2.12})$$

Inserting into Equation S2.10

$$M = \left| \frac{N \times [\exp(i\Phi) \times t - 1] \pi r^2 \frac{2J_1(k_{1\parallel} r)}{k_{1\parallel} r}}{A + N \times [\exp(i\Phi) \times t - 1] \pi r^2 \frac{2J_1(k_{0\parallel} r)}{k_{0\parallel} r}} \right|^2 = \frac{\left| N \times [\exp(i\Phi) \times t - 1] \pi r^2 \frac{2J_1\left(2\pi \frac{r}{p}\right)}{2\pi \frac{r}{p}} \right|^2}{|A + N \times [\exp(i\Phi) \times t - 1] \pi r^2|^2} \quad (\text{S2.13})$$

As the distance p between neighbouring scatterers is larger than their diameter, $p > 2r$, the argument of the Bessel function J_1 is smaller than π and always positive. Introducing the fill factor

$$F = \frac{N \times \pi r^2}{A} \quad (\text{S2.14})$$

i.e. the ratio of the area occupied by the scatterers divided by the total area, we have

$$M = F^2 \left| \frac{2J_1\left(2\pi \frac{r}{p}\right)}{2\pi \frac{r}{p}} \right|^2 \frac{|[\exp(i\Phi) \times t - 1]|^2}{|1 + F \times [\exp(i\Phi) \times t - 1]|^2} \quad (\text{S2.15})$$

For our samples the fill factor is between 0.20 and 0.35. The expression

$$|\exp(i\Phi) \times t - 1|^2 = 1 + t^2 - 2t \cos(\Phi) \quad (\text{S2.16})$$

equals 1 for a pure transmission grating with $t = 0$, while for a pure phase $\lambda/2$ grating with

Chapter 2. Structuring amorphous thin films of cyanine dyes

$t = 1$ and $\Phi = \pi$ leads to a factor of 4. Hence

$$M = F^2 \left| \frac{2J_1\left(2\pi\frac{r}{p}\right)}{2\pi\frac{r}{p}} \right|^2 \times \begin{cases} \frac{1}{(1-F)^2} & \text{pure transmission grating} \\ \frac{4}{|1-2F|^2} & \text{pure } \lambda/2 \text{ phase grating} \end{cases} \quad (\text{S2.17})$$

Note that for a $\lambda/2$ phase grating with $F = 0.5$ the zeroth diffraction order vanishes and the ratio M is meaningless. In the general case, the phase shift and transmission through a thin film are related to the complex refractive indices according to^[37]

$$t \times \exp(i\Phi) = \frac{t_{01} t_{12} \exp(-i\beta_1)}{1 + r_{01} r_{12} \exp(-2i\beta_1)} \times (i\beta_0) \quad (\text{S2.18})$$

where

$$\beta_i = \frac{2\pi}{\lambda} h \tilde{n}_i, \quad t_{ij} = \frac{2\tilde{n}_i}{\tilde{n}_i + \tilde{n}_j}, \quad r_{ij} = \frac{\tilde{n}_i - \tilde{n}_j}{\tilde{n}_i + \tilde{n}_j} \quad (\text{S2.19})$$

\tilde{n}_j is the complex refractive index of air ($j = 0$), of the scatterer ($j = 1$) and the substrate ($j = 2$), respectively. For a weak phase grating we assume $\beta_i \ll 1$ and obtain from Equation S2.16 and Equation S2.18

$$\begin{aligned} |t \times \exp(i\Phi) - 1|^2 &\approx |\exp(-i\beta_1) \times \exp(i\beta_0) - 1|^2 \approx |\beta_0 - \beta_1|^2 \\ &= \left(\frac{2\pi}{\lambda} h\right)^2 |1 - n_1 - i\kappa_1|^2 = \left(\frac{2\pi}{\lambda} h\right)^2 |(1 - n_1)^2 + \kappa_1^2| \end{aligned} \quad (\text{S2.20})$$

Close to an absorption band, however, the diffraction can be much stronger and the full expression Equation S2.18 must be taken into account.

While a regular array of scatterers would lead to distinct diffraction orders, and a completely irregular distribution of scattering elements would not give rise to any preferred diffraction angle, the broad diffraction cone observed in our experiments (Figure 2.1(e)) can be explained

by a distribution of scattering elements with a quasi-constant nearest neighbour distance as exemplified in Figure S2.6 for an array with a scatterer distance distribution of $1.3 \pm 0.6 \mu\text{m}$. Higher order diffraction is very weak in this case.

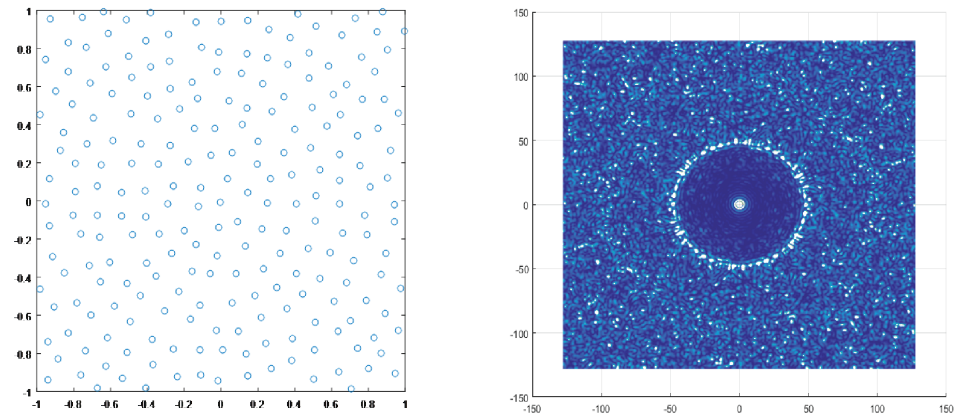


Figure S2.6 – Distribution of scattering elements with average nearest neighbour distance of $1.3 \mu\text{m}$ (left) and its Fraunhofer diffraction pattern (right).



Bibliography

- [1] Y. H. Fu, A. I. Kuznetsov, A. E. Miroshnichenko, Y. F. Yu, B. Luk'yanchuk, *Nature Communications* **2013**, *4*, 1527.
- [2] V. Giannini, A. I. Fernández-Domínguez, S. C. Heck, S. A. Maier, *Chemical Reviews* **2011**, *111*, 3888–3912.
- [3] X. Ni, N. K. Emani, A. V. Kildishev, A. Boltasseva, V. M. Shalaev, *Science* **2012**, *335*, 427–427.
- [4] K. R. Catchpole, A. Polman, *Optics Express* **2008**, *16*, 21793–21800.
- [5] H. A. Atwater, A. Polman, *Nature Materials* **2010**, *9*, 205–213.
- [6] K. Jung, H.-J. Song, G. Lee, Y. Ko, K. Ahn, H. Choi, J. Y. Kim, K. Ha, J. Song, J.-K. Lee, C. Lee, M. Choi, *ACS Nano* **2014**, *8*, 2590–2601.
- [7] F. J. Bezares, J. P. Long, O. J. Glembocki, J. Guo, R. W. Rendell, R. Kasica, L. Shirey, J. C. Owrutsky, J. D. Caldwell, *Optics Express* **2013**, *21*, 27587.
- [8] M. L. Brongersma, Y. Cui, S. Fan, *Nature Materials* **2014**, *13*, 451–460.
- [9] A. A. Maradudin, J. R. Sambles, W. L. Barnes, *Modern Plasmonics*, 1st ed., Elsevier.
- [10] J. A. Schuller, M. L. Brongersma, *Optics Express* **2009**, *17*, 24084.
- [11] P. Spinelli, M. A. Verschuuren, A. Polman, *Nature Communications* **2012**, *3*, 692.
- [12] S. A. Mann, R. R. Grote, R. M. Osgood, J. A. Schuller, *Optics Express* **2011**, *19*, 25729.
- [13] G. Mie, *Annalen der Physik* **1908**, *330*, 377–445.
- [14] C. F. Bohren, D. R. Huffman, *Absorption and Scattering of Light by Small Particles*, Wiley-VCH Verlag GmbH.

Bibliography

- [15] T. Khudiyev, E. Huseyinoglu, M. Bayindir, *Scientific Reports* **2014**, *4*.
- [16] S. Asano, *Applied Optics* **1979**, *18*, 712.
- [17] S. J. Oldenburg, R. D. Averitt, S. L. Westcott, N. J. Halas, *Chemical Physics Letters* **1998**, *288*, 243–247.
- [18] T. Khudiyev, M. Bayindir, *Scientific Reports* **2014**, *4*, 7505.
- [19] W. West, P. Gilman, T. James, *The Theory of the Photographic Process*, Macmillan Pub. Co., New York, **1977**.
- [20] B. Fan, R. Hany, J.-E. Moser, F. Nüesch, *Organic Electronics* **2008**, *9*, 85–94.
- [21] B. Fan, F. A. de Castro, J. Heier, R. Hany, F. Nüesch, *Organic Electronics* **2010**, *11*, 583–588.
- [22] L. Wang, C. Hinderling, S. Jenatsch, F. Nüesch, D. Rentsch, R. Steim, H. Zhang, R. Hany, *Polymer* **2014**, *55*, 3195–3201.
- [23] A. Pertegás, D. Tordera, J. J. Serrano-Pérez, E. Ortí, H. J. Bolink, *Journal of the American Chemical Society* **2013**, *135*, 18008–18011.
- [24] H. G. Tompkins, E. A. Irene in *Handbook of Ellipsometry*, William Andrew Publishing/Noyes, **2005**, pp. 159–163.
- [25] P. Bassan, H. J. Byrne, F. Bonnier, J. Lee, P. Dumas, P. Gardner, *Analyst* **2009**, *134*, 1586–1593.
- [26] P. Bassan, A. Kohler, H. Martens, J. Lee, H. J. Byrne, P. Dumas, E. Gazi, M. Brown, N. Clarke, P. Gardner, *Analyst* **2010**, *135*, 268–277.
- [27] R. Seemann, S. Herminghaus, K. Jacobs, *Journal of Physics: Condensed Matter* **2001**, *13*, 4925.
- [28] Y. Hashimoto, O. Karthaus, *Journal of Colloid and Interface Science* **2007**, *311*, 289–295.
- [29] J. Heier, R. Steiger, F. Nüesch, R. Hany, *Langmuir* **2010**, *26*, 3955–3961.
- [30] J. Heier, R. Steiger, R. Hany, F. Nüesch, *Physical Chemistry Chemical Physics* **2011**, *13*, 15714–15722.
- [31] J.-N. Tisserant, R. Brönnimann, R. Hany, S. Jenatsch, F. A. Nüesch, R. Mezzenga, G.-L. Bona, J. Heier, *ACS Nano* **2014**, *8*, 10057–10065.

- [32] P. G. de Gennes, *Reviews of Modern Physics* **1985**, 57, 827–863.
- [33] J. N. Israelachvili in *Intermolecular and Surface Forces (Third Edition)*, (Ed.: J. N. Israelachvili), Academic Press, San Diego, **2011**, pp. 253–289.
- [34] J. Berthier, *Micro-drops and digital microfluidics*, William Andrew Publishing/Noyes, **2012**.
- [35] J.-N. Tisserant, G. Wicht, O. F. Göbel, E. Bocek, G.-L. Bona, T. Geiger, R. Hany, R. Mezzenga, S. Partel, P. Schmid, W. B. Schweizer, J. Heier, *ACS Nano* **2013**, 7, 5506–5513.
- [36] D. C. Hutchings, M. Sheik-Bahae, D. J. Hagan, E. W. V. Stryland, *Optical and Quantum Electronics* **1992**, 24, 1–30.
- [37] H. Fujiwara, *Spectroscopic Ellipsometry: Principles and Applications*, John Wiley and Sons, Ltd, Chichester, **2007**.
- [38] M. Jonasz, G. R. Fournier in *Light Scattering by Particles in Water*, (Ed.: M. J. R. Fournier), Academic Press, Amsterdam, **2007**, pp. 87–143.
- [39] S. C. Shen, J. C. Huang, *Optics Express* **2009**, 17, 13122.
- [40] S. Saxena, R. P. Chaudhary, A. Singh, S. Awasthi, S. Shukla, *Scientific Reports* **2014**, 4.
- [41] L. A. Ernst, R. K. Gupta, R. B. Mujumdar, A. S. Waggoner, *Cytometry* **1989**, 10, 3–10.
- [42] I. Horcas, R. Fernández, J. M. Gómez-Rodríguez, J. Colchero, J. Gómez-Herrero, A. M. Baro, *Review of Scientific Instruments* **2007**, 78, 013705.
- [43] I. Lumerical Solution, Grating order transmission | Lumerical Knowledge Base, https://kb.lumerical.com/en/diffractive_optics_gratings_order_transmission.html.
- [44] A. Lipson, S. G. Lipson, H. Lipson, *Optical Physics*, 3rd, Cambridge University Press, **1995**.
- [45] J. W. Goodman, *Introduction to Fourier Optics*, 2nd, McGraw-Hill, **1996**.

3 Dye crystal stability

3.1 Introduction and aims

Engineering of crystal morphologies is a topic of significant importance in many fields where crystalline materials are applied: pharmaceuticals, food industry, semi-conductor electronics or photovoltaics.^[1] Crystal morphology can have a great influence on the suitability of a compound for a specific application, and it is therefore important to understand and control the parameters governing a crystal's morphology.

Molecular crystals grown from vapor or *via* sublimation^[2,3] processes present the advantage to yield large dimensions, high purity and good quality crystalline materials.^[4] This is due in part to the fact that vapor deposition techniques enable good control over the critical growth parameters (mainly temperature and vapor pressure) helping to keep growth conditions stable.^[5] Moreover, some vapor growth methods such as the gradient sublimation technique are directly related to purification methods.^[4] On the other hand, growth from solution presents some advantages compared to vapor growth methods. The possibility to use low temperatures enables avoiding decomposition of the material and limits built-in stresses and structural defects often associated with high temperature growth. Moreover, they allow in principle for large area deposition and higher fabrication throughput. However, solution routes for crystal growth pose other issues, which can mostly be interpreted under the light of crystal interfaces' interaction with the surrounding environment. In solution growth, interfacial interactions are multiple (solvent, impurities, and supersaturation) and can vary with time if

the system is not fully under control. The growth rate of crystal faces are determined by such interfacial interactions. In addition other external factors, such as hydrodynamic convection can play a significant role in the growth shape of crystals.^[6,7] Even for a given crystalline packing (a given polymorph), in solution, crystals very often show the tendency to crystallize in many different crystal shapes depending on the growth conditions. In addition, growth instabilities can occur, leading to the formation of defects both on the macroscopic and microscopic scales. Thus, it is important to understand crystal evolution pathways during growth to fabricate high quality molecular single crystals from solution.

A method to crystallize CyC directly on substrate was developed by Tisserant and co-workers.^[8] The method involved casting a solution of the dye on a substrate to form a dewetted film of randomly distributed dye droplets. The dewetted film was subsequently exposed to chlorobenzene vapor for several hours, resulting in the growth of micrometer-sized rhomb-shaped single crystals on the substrate. The author pointed out that nucleation likely occurs during the dewetting step, resulting in mostly amorphous droplets containing metastable nuclei. Their subsequent growth by solvent vapor annealing was described to result from the absorption of solvent molecules by the droplets, and the growth of the metastable nuclei by incorporation of surrounding solute. After outgrowing their parent droplet, single crystals were shown to grow by transport of solute to the growing crystal from the surrounding amorphous droplets. Two growth rate regimes were highlighted, depending on the availability of solute around a growing crystal.

This chapter builds on the results from Tisserant *et al.* and investigates the later stage of crystal growth. While seemingly keeping the growth conditions (temperature, solvent vapor pressure) constant, the firstly grown polyhedral single crystals lose their stability and undergo a catastrophic transformation to a branched form after extended solvent vapor annealing periods. By investigating the crystal transformation process, this chapter aims to shed light on the important conditions to guarantee the stability of single crystals during growth.

Growth morphology Crystals of a same compound can take a wide variety of forms. In addition to morphological variations resulting from polymorphism^[9,10] and polytypism,^[11,12] even crystals of a single phase may have different macroscopic appearance. The equilibrium

form of a crystal is the expected crystal shape under given thermodynamic conditions.^[13] Gibbs showed that the equilibrium shape of a solid crystal is that which minimizes its total surface free energy $\sum \gamma_i A_i$ (γ_i and A_i are the surface free energy and the relative area of the crystallographic face i , respectively) for a given crystal volume.^[1] While for isotropic materials (liquids for instance) this condition leads to a sphere, for anisotropic material (which have different surface energies in different directions) the thermodynamic requirements results in a crystal bounded by flat faces. A geometric approach was developed by Wulff to determine the equilibrium shape of crystals.^[14] However this approach does not take into account the growth rate of different faces.

The prominence of a particular face indeed depends on its rate of growth: fast growing faces tend to disappear and the crystal shape will therefore be defined by the slowest growing faces. Equivalent observations were reported for dissolving crystals where the fast-dissolving faces tend to disappear over time. The *structural form*^[13] of a crystal can be evaluated based on crystallographic considerations, giving the relative growth rates of different faces. The Bravais-Friedel-Donnay-Harker model (BFDH)^[15] states that the growth rate of a face is inversely proportional to its reticular distance. Therefore low index faces are favored compared to higher index faces. Another model was developed by Hartman and co-workers^[16-18] taking the energetic interactions within the crystal into account in addition to the crystal geometry. Rather than using surface energy considerations, they define the attachment energy as the bond energy released when a building unit attaches to the surface of a face. Moreover, they assume the time necessary to the formation of a bond is inversely proportional to the bond energy. With this approach the fast growing faces will be the ones with high attachment energies.

While these methods give relatively simple approaches to predict the form of a crystal, they are only based on crystal structure considerations and often fail to picture the reality of crystal growth. In general, crystal morphology results from both internal and external factors. The nature of the ambient phase (liquid, vapor, solid), growth conditions (temperature, concentration, pressure, diffusion, convection), the presence of solvents, impurities and dislocations are many external parameters that influence the crystal morphology. The *growth form*^[13] is the crystal shape that occurs due to specific growth environment and processes. Information extracted from variations in crystal morphologies can be particularly useful to understand the

Chapter 3. Dye crystal stability

growth mechanisms at play and uncover fluctuations in the conditions throughout the growth history. This understanding may help in designing specific processes to better control growth conditions and synthesize crystals of desired morphology through solution-based methods for particular applications.

Growth mechanisms To be able to extract information out of the crystal growth forms it is necessary to understand how growth proceeds at the microscopic level. The growth of a crystal face in solution occurs through a sequence of events which will determine the kinetics of face growth:^[1]

1. Building units are transported from the bulk solution to the crystal face by diffusion and/or convection.
2. Building units diffuse on the terrace of a the crystal face.
3. Kinks and building units separate from their environment (solvent molecules).
4. Building units are integrated to kink sites.
5. Latent heat of crystallization is released to the crystal and to the solution.

In solution, the growth of crystals takes place at the liquid-solid interface only. Therefore, the growth mechanism and rate of displacement of an interface is define by the interface roughness at the atomic level.^[19] The growth rates are determined by the roughness of the interfaces, the growth mechanism and the driving force.^[20] Sunagawa has represented the relation between growth rate R and chemical potential difference (driving force) in the schematic diagram Figure 3.1.^[13] Above $\star\star$ the crystal interface is rough and growth is expected to occur through adhesive mechanism, controlled by bulk diffusion. The crystal will be bounded by rounded interfaces. The crystal will tend to protrude into high supersaturation regions leading to rapid growth with elongated morphologies such as dendrites, spherulites or fractals.^[19] Below $\star\star$, interfaces are smooth. The growth of crystal faces with smooth interfaces occurs layer by layer, either by 2-dimensional nucleation or by spiral growth.^[21] In the region below \star , spiral growth is the dominant mechanism: layers originate from screw dislocations

emerging at the surface of a smooth interface and advance outward by propagation of trains of steps, leading to *polyhedral* crystal bounded by flat faces. Between \star and $\star\star$, 2D nucleation dominates the growth of interfaces. To form, a 2D nucleus needs to overcome the energy barrier associated with the formation of a new interface. In solution, the supersaturation is not homogeneous over the crystal surface due to the Berg effect: it is higher at corner and edges of the crystal.^[22] Therefore, 2D nucleation tends to take place near the edges and growth layers advance inward to the middle of a face, leading to *hopper* or *skeletal* crystals.

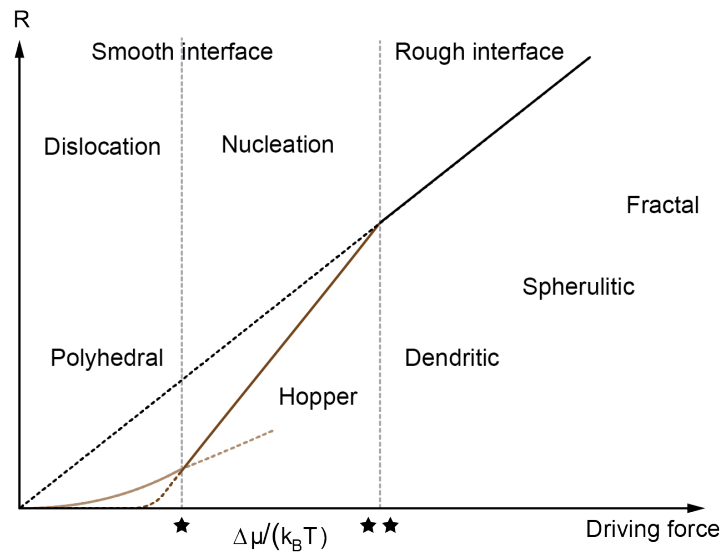


Figure 3.1 – Normal growth rate R as a function of the driving force for crystal growth. Adapted with permission from [13].

The exact values of \star and $\star\star$ depend on many factors such as the nature of the solute-solvent interaction, the diffusion rate or the crystal size. Most importantly, \star and $\star\star$ are different depending on the crystallographic directions on a crystal. It is then likely that some faces will grow below \star while others will evolve above \star or $\star\star$.^[19] Finally, it is also possible that a crystal undergoes one or several transitions between \star and $\star\star$ during its growth history. All these variations are lead to different crystal growth forms.

Stability of polyhedral crystals The integrity of a growing crystal’s morphology under diffusion limited conditions is the result of competition between shape stabilizing and destabilizing factors.^[23] The main destabilizing factor has been shown to be the uneven concentration distribution around the surface of the crystal growing under diffusion limitation, due to the Berg

effect.^[24,25] To counter-balance the effect of non-homogeneous concentration distribution the existence of a stabilizing factor has been proposed by Chernov.^[24] To compensate for the uneven concentration profile along a crystal face, anisotropy in the surface growth kinetics of the face will develop such that the crystal changes its microscopic profile by creating steps to increase the number of possible attachment sites for solute building units. The works of Chernov^[24] and Nanev^[23,26] concluded the slope of the train of steps at the face center coupled with the crystal size were the critical parameters governing the stability of a polyhedral crystal.

Under diffusion limited conditions, the Berg effect results in higher concentration at the edges than at the center of the face. Since the rate of growth of a face depends on the concentration, edges have a tendency to grow at a higher rate than the face's center. This effect is amplified with the increasing crystal size since the concentration difference between the center and the edges increases also. Chernov's theoretical compensation profile is sketched in Figure 3.2. As long as the slope of the train of steps $p(x)$ remains small, the rate of growth $R(x)$ at the center of the face is able to "catch up" with that of the corners. In this case the face will remain macroscopically flat (monoatomic steps and dislocation hillocks could in principle be observed at the nanometer scale). However, when the slope of the step profile overcomes a critical value, the rate of growth at the center of the face cannot compensate that of the edges and the face becomes unstable: a macroscopic depression appears at the face center.

Aims In this chapter, we take advantage of the catastrophic morphological changes occurring during growth of CyC crystal during solvent vapor annealing of a dewetted droplet film to better understand the mechanisms involved during CyC crystal growth. In a first part, the different stages of crystal shape transformation that can be observed during growth are described. X-ray crystal analysis is used to conclude the nature of the morphological change of the crystals. Then, a physical picture of the specific growth conditions over the crystallization process is given. In-situ measurement of growth kinetics and atomic force microscopy of unstable crystals underline the role of the local droplet distribution as a destabilizing parameter.

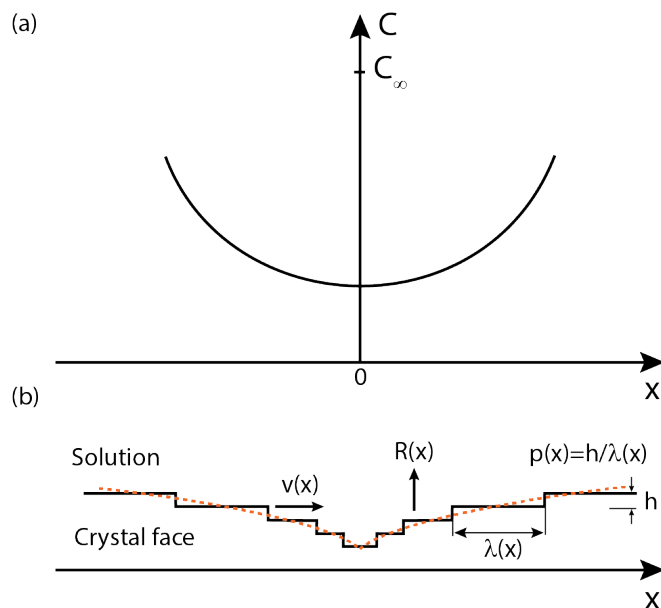


Figure 3.2 – (a) Schematic representation of the concentration distribution along a crystal face under diffusion limited conditions. The concentration C is lowest at the face centre and highest at the edges. (b) Chernov's compensation profile. $R(x)$ is the face's normal growth rate, $v(x)$ the velocity of a step, $\lambda(x)$ the length of a terrace and h the height of a step. The density of the steps increases at the face's center to compensate the lower concentration. Adapted from [19].

3.2 Results and discussion

3.2.1 Cyanine crystal morphology evolution: from polyhedral to hopper to dendritic crystals

Cyanine single crystals were produced following the established recipe by Tisserant *et al.*:^[8] droplets were spun-cast from 10 mg mL^{-1} dye solution in ethanol on a clean substrate. The films were subsequently exposed to chlorobenzene vapor at room temperature for up to 48 hours.

While in the first stages of crystal growth single crystals seem to maintain their polyhedral form, as was previously observed,^[8] prolonged exposure to chlorobenzene vapor leads to loss of polyhedral stability and morphological transformation of the crystal. Figure 3.3 shows electron microscopy images of crystals from different samples, representing the different transformation stages observed. Once the crystal has outgrown its parent droplet it exhibits a

Chapter 3. Dye crystal stability

characteristic rhombohedral shape (Figure 3.3 (a)). As the crystals increase in size, a depression appears in the center of the [100] singular face of the crystal (Figure 3.3 (b)). Sometimes, partial dissolution of the crystal may occur at the depression as visible from Figure 3.3 (c). Then the crystal's apices branch out radially from the initial crystal position (Figure 3.3 (d)). Finally, after extended annealing periods the crystal adopts a dendritic morphology extending on hundreds of micrometers (Figure 3.3 (e)). The strong similarity between diffractograms of polyhedral and dendritic crystals (Figure 3.3 (f)) suggests the two crystal forms are the same phase with similar crystallographic orientation (the diffractogram of polyhedral crystals will be discussed in more details in chapter 5). It can therefore be concluded that the transition from polyhedral to dendritic form results from a change in growth forms. The reasons for this change are detailed in the following sections.

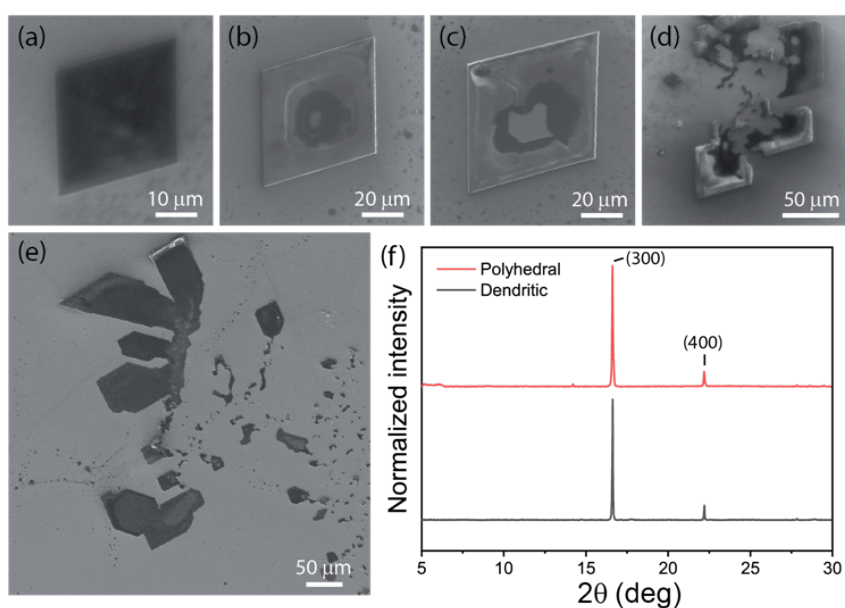


Figure 3.3 – Scanning electron microscopy images of distinct crystals illustrating the different stages of morphological transformation. (a) From an initial polyhedral rhomb-shaped crystal (b) a depression appears on the basal face. (c) Dissolution at the depression was sometimes observed. (d) The corner of the crystal start outgrowing the initial rhomb-shaped crystal in their respective directions. (e) After extended annealing periods, the crystal branches out while dissolution and recrystallization of the initial seed may happen, leading to dendritic like crystal extending on $100\ \mu\text{m}^2$ areas. (f) Comparison of diffractograms of polyhedral single and branched crystals reveals the two forms belong to the same phase. (SEM image acquired by J.-N. Tisserant)

3.2.2 Growth conditions

To understand the growth mechanism at play, it is essential to identify the specific growth conditions of the system. During the experiment, the SVA chamber is saturated with chlorobenzene vapor. Vaporized chlorobenzene molecules interact with the amorphous dye droplets, reducing their glass transition temperature to room temperature and making them somewhat liquid.^[27] The minimum volume fraction of chlorobenzene in dye droplets necessary for them to become liquid was estimated to be at least 27%.^[8]

For the following discussion three assumptions are made. First, once a sufficient volume fraction of solvent is absorbed by the dye droplets to increase dye mobility, it is assumed that a thin liquid layer wets the substrate, linking the droplets between each other, and provides a pathway for the transport of solute to the growing crystal. In that case, the evolution of the dye-chlorobenzene system is controlled by the dynamics of liquid thin films. This assumption is based on the model developed by Yu *et al.* to describe the growth of Alq3 needles from dewetted films by SVA.^[28] Second, also based on the model by Yu, it is assumed that the liquid layer forms a concave meniscus at the crystal front.^[28] Finally, to simplify the discussion, it is assumed that the liquid and solid phases in the SVA chamber are in equilibrium with the vapor phase, such that evaporation and condensation can be neglected.

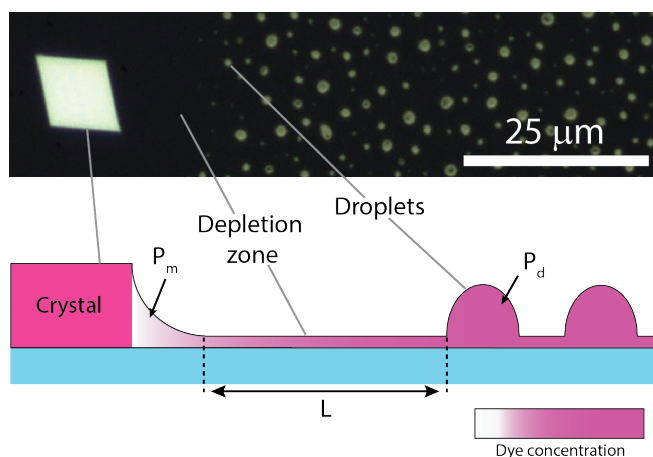


Figure 3.4 – Configuration of crystal growth conditions. Top: optical microscopy image (top view) of a CyC crystal on substrate. The crystal is separated from the solute droplets by a depletion zone. Bottom: sketch (cross-sectional view) of the growth configuration.

In a first stage, the dye crystal grows by consuming the solute of its parent droplet.^[8] When the

parent droplet is completely consumed, the crystal grows at the expense of the surrounding amorphous droplets such that three different regions coexist: (i) the growing crystal, (ii) a depletion zone devoid of droplets and (iii) a collection of amorphous dye droplets surrounding the crystal. Such configuration is illustrated in Figure 3.4.

Once the crystal has outgrown its parent droplet, the specific arrangement of the system allows only for a 2-dimensional transport of the solute (in the substrate's plane) to the crystal's lateral faces, as can be seen from the sketch in Figure 3.4. Solute transport in the direction normal to the substrate is limited, assuming that the gas phase does not carry solute.

The concentration profile through the sample is sketched in Figure 3.4. Far from the crystal, the droplet concentration is assumed to be maximum and homogeneous. Close to the growing crystal face, crystal growth locally consumes solute from the surrounding liquid, such that a concentration gradient forms driving the diffusion of solute to the crystal face. Calculation of the concentration field around the growing crystal amounts to solving a diffusion problem with moving boundaries. The general solution of this problem is time dependent.^[29,30] Therefore, it is expected that the diffusion boundary thickness varies with time, leading to variations in the rate of growth of the crystal front. However, when the depletion zone is large, variation of the boundary layer's thickness can be considered negligible compared to the diffusion distance. The form of the gradient beyond the crystal front is a function of (1) the diffusion of solute through the liquid layer and (2) the advection flux of liquid driven by the pressure difference between droplets and the meniscus formed at the crystal/liquid interface (see Figure 3.4).^[28] Indeed, the concave curvature of the meniscus creates a region of negative pressure while the convex shape of the droplets results in a positive pressure ($P_m < P_d$).^[31]

The configuration presented in Figure 3.4 is not static during the course of the SVA experiment. As previously shown, both crystal size and depleted area increase with time.^[8] In addition, the droplet arrangement far from the growth front also changes during SVA: while droplets closest to the crystal are consumed to feed the crystal, those farther from the crystal front coalesce such that the average droplet size increases with time. Figure 3.5 summarizes the evolution of droplet number and area over the annealing experiment. The number of droplets and the contact area of the 10% largest drops have been measured by image analysis of in-situ time-lapse pictures of a growing crystal (see supporting information, Figure S3.2).

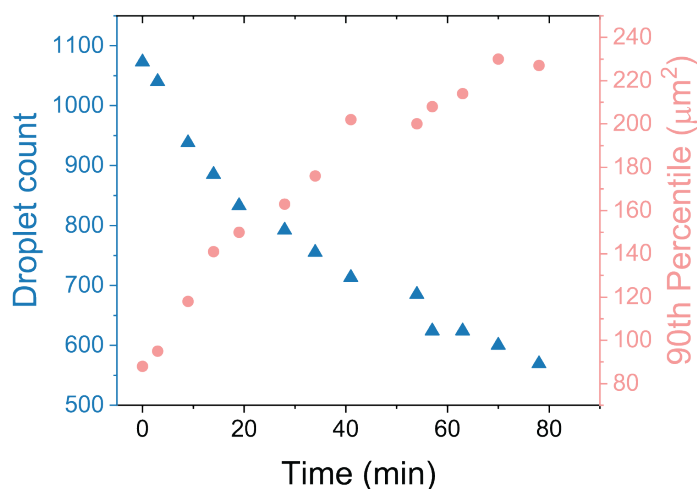


Figure 3.5 – Evolution of droplet number and area of droplets during crystal growth. Only the evolution of the area of the 10% largest droplets is shown.

The minimum contact area of the 10% largest drops increases more than 150% over the course of the experiment (about 80 minutes). Close observation of *in-situ* microscopy images (Figure S3.1) shows that while some droplets seem to coalesce by local displacement and collision with close neighboring drops, there is no large-scale displacement of drops. Instead, coalescence appears to be mostly occurring by collapse of droplets. Such behavior occurs due to pressure differences in neighboring drops of different size such that smaller ones (where the pressure is high) collapse in favor of larger ones (where the pressure is lower), due to Ostwald ripening.^[31–33]

3.2.3 Stable growth of polyhedral crystals

In section 3.2.1 it was shown that the morphological stability of CyC single crystals is compromised under prolonged annealing times. Such dramatic transformations of the crystal morphology result directly from changes in the growth conditions which have been detailed in the previous paragraphs. This section and the following ones describe how the specific growth conditions affect the crystal morphology leading to a transition from a polyhedral to hopper crystals first, then to a dendritic growth form.

The first step of crystal growth after nucleation occurs within a single droplet. At this stage,

Chapter 3. Dye crystal stability

solute is readily available all around the growing crystal and growth occurs fast (on the order of $0.25 \mu\text{m} \cdot \text{min}^{-1}$), as was shown by Tisserant *et al.*^[8] Crystals resulting from this first growth stage exhibit a rhombohedral morphology with macroscopically flat, low index faces (see chapter 4 and 5): the stability of the polyhedral shape is conserved during this stage. These characteristics are typical of crystals formed mainly by a spiral growth mechanism around one or several screw dislocations.^[13,21] The following paragraphs only discuss the growth kinetics after the crystals have outgrown their parent droplets.

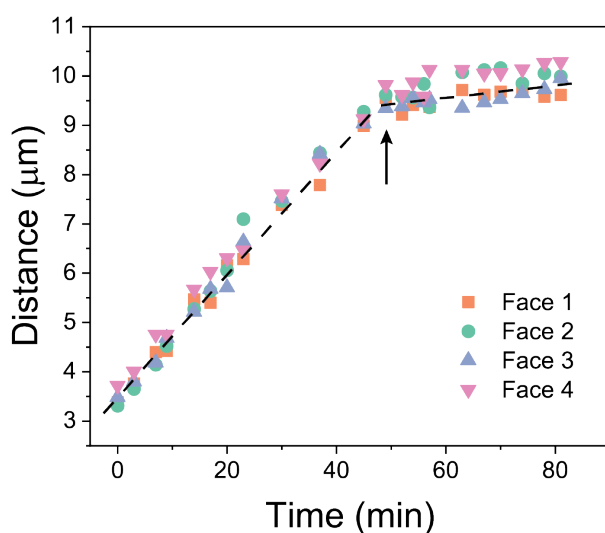


Figure 3.6 – Positions of the 4 faces to the center of a polyhedral crystal over annealing time. The first points ($t = 0 \text{ min}$) correspond to the moment where the single crystal has visibly outgrown its parent droplet. After about 50 minutes of lateral growth, the rate of advance of the crystal faces drops of about 1 order of magnitude.

In a second step, the single crystal has outgrown its initial droplet and starts integrating solute from surrounding droplets (Figure 3.4). Small droplets surround the crystal's close vicinity and a diffusion gradient forms in the plane around the crystal. There, the growth is slowed down compared to the first step of growth within a droplet, due to the increased distance between solute source and crystal front: the solute has now to diffuse through the depletion zone to reach the growth front. Figure 3.6 shows the linear growth of each face of a CyC rhomb-shaped crystal. The growth is measured as the distance of each lateral faces from the center of the rhombohedron (intersection of the diagonals) over time. The initial time $t = 0$ corresponds to the moment where the single crystal has visibly outgrown its parent droplet (the full time-lapse

is shown in Figure S3.4). Figure 3.6 shows that for about 45 minutes the growth of the crystal occurs at constant rate and similar for all lateral faces. The linear growth rate, given by the slope of the plot, is in average $0.131 \pm 0.008 \mu\text{m min}^{-1}$, i.e. about two times slower than during growth in the parent droplet. On the other hand, the normal growth of the basal face is limited since the solute is only provided to the side faces of the crystal and incorporated to the train of steps created by dislocation mechanism .

3.2.4 Transition from stable growth to polyhedral instability

The stability of the polyhedral crystals is compromised when the solute transport conditions suddenly change. Figure 3.6 shows that after about 45 minutes, the linear growth rate of the crystal drops significantly for all side faces to about $0.018 \pm 0.004 \mu\text{m min}^{-1}$, i.e. about one order of magnitude slower than the previous growth stage. Figure 3.7 (a) shows the local droplet evolution around and far from the growing crystal. The microscopy image is that of the initial situation ($t = 0$). The droplets are colored according to the time interval during which they disappear measured by *in situ* time-lapse (SI). Groups of droplets circled by a black line correspond to droplets that coalesce together during the time of the experiment. During the first 45 minutes, droplets located close to the crystal front gradually disappear, being integrated into the growing crystal front.

At 52 minutes the simultaneous disappearance of the "purple droplets" is clearly visible. This event correspond to the decrease of growth rate observed in Figure 3.6, marked by the arrow. Although the reasons are not exactly clear, this collapse may results from a concomitant change in pressure equilibrium between the crystal front, the purple droplets and droplets further away from the crystal front. Indeed, as visible from Figure 3.7 (a), droplets far from the growth front coalesce by Ostwald ripening (circled in black). This is believed to result in a decrease of the capillary pressure in these droplets, therefore creating a pressure difference between the "small" purple droplets (where the pressure is high), the crystal front and the coalesced droplets (where the pressure is low). Therefore the purple droplets collapse together in the same time period to re-establish the pressure equilibrium. These collapsing droplets push a large quantity of concentrated solution at the edge of the crystal by advection, leading to a sudden increase of solute concentration at the growth front. From Figure 3.7 (b) it is clear

Chapter 3. Dye crystal stability

that from 52 minutes on the lateral expansion of the crystal almost stops, while its thickness increases. This thickness increase can be seen from the change of color of the crystal, propagating from the edges towards the center between 52 minutes and 63 minutes. Simultaneously, instability appears in the form of a depression surrounded by a macroscopically flat periphery (visible from 56 minutes on, Figure 3.7 (b)). From there on the crystal lateral dimensions do not change until the end of the experiment (see supporting information, Figure S3.4). However large droplets still disappear around the crystal, suggesting that the crystal thickness probably keeps increasing.

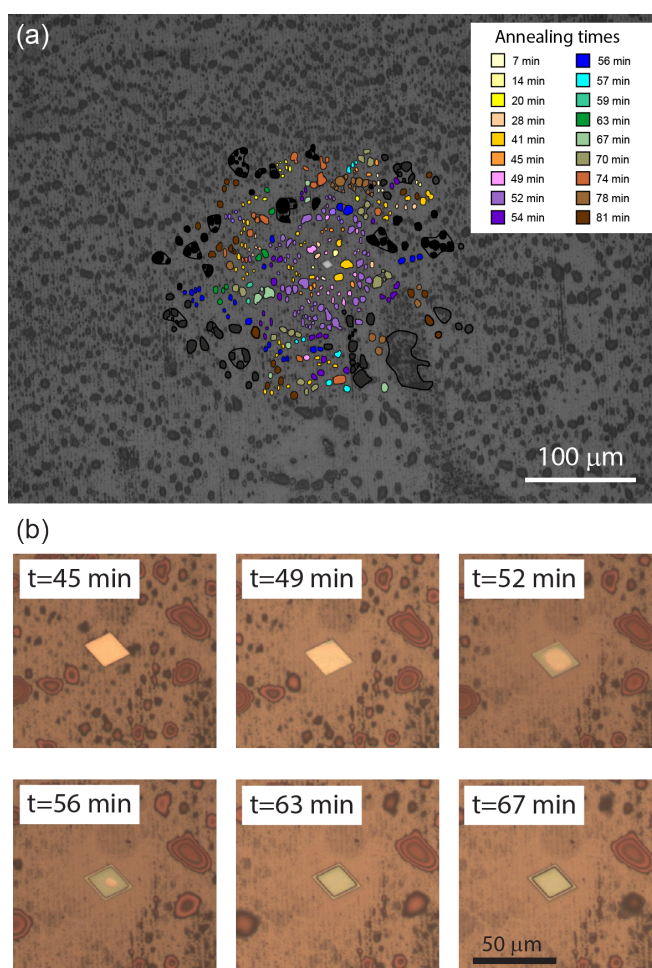


Figure 3.7 – (a) Optical microscopy image of the initial distribution of droplets around the growing CyC crystal. Droplets are colorized as a function of their disappearing time (indicated in the legend): a group of droplets of the same color disappear during the same time period. (b) *In situ* optical microscopy image of the growing crystal from 45 minutes to 67 minutes of annealing.

The influence of the growth rate variations on the crystals' morphological stability is reflected by the topography of unstable crystals. Figure 3.8 (a) and (c) shows an AFM topographic image of such a destabilized crystal. The presence of steps on the inner side of the depression (vicinal surface) confirms that the instability occurs due to the creation of new layers at the edges of the polyhedral crystal. Given the asymmetry of the solute distribution around the crystal (only available to the outer edges but not to the top of the singular face), advance of new steps occurs mostly outwards, creating an apparent depression at the center of the face. In addition to spiral growth mechanism, the presence of flat polyhedral layers at the corners or edges of a destabilized crystals indicates that 2D nucleation mechanism may also occur, as visible in Figure S3.3.

A deeper AFM analysis of the steps appearing in the center of the basal face shown in Figure 3.8, provides insight on the changes in growth rates and directions. It is clear from the topographic images in Figure 3.8 (a) that the density of steps varies along a vicinal surface. Such variations are sometimes called “kinematic shock waves” or simply “kinematic waves” and their properties have been described in detail elsewhere.^[34,35] It is sufficient to say that under diffusion limited conditions, variations in the rate of growth of a crystal face (that is, in the direction normal to the face) is proportional to the density of steps, or the “slope” of the vicinal face, $p = \frac{h}{\lambda}$, where h is the step height and λ is the mean step distance (see Figure 3.2).^[34] In addition, the step velocity v (rate of advance of a step in a train of steps, in a direction parallel to itself) decreases with increasing step density.^[34]

Figure 3.8 (b) shows the local step slope p as a function of the position along the depression, extracted from three line profiles of the same face (face 1), indicated in Figure 3.8 (a). All line profiles start from the lowest level measured by AFM and the first step length corresponds to the distance between the first and second steps. It can be seen from 3.8 (a) and (b) that even though local variations in the slope occur along a same face, the general trend is similar for profiles 1a-c: the rate generally increases, with a strong spike in growth after the 3-4 first steps. On the other hand, the rate of growth may vary substantially between different faces. Figure 3.8 (c) and (d) show the local slope variations of three different faces. Increase in growth rate is much slower for face 2 than faces 3 and 4. The growth of face 3 clearly accelerates faster and earlier than the others. It is therefore expected that the flat periphery surrounding vicinal face

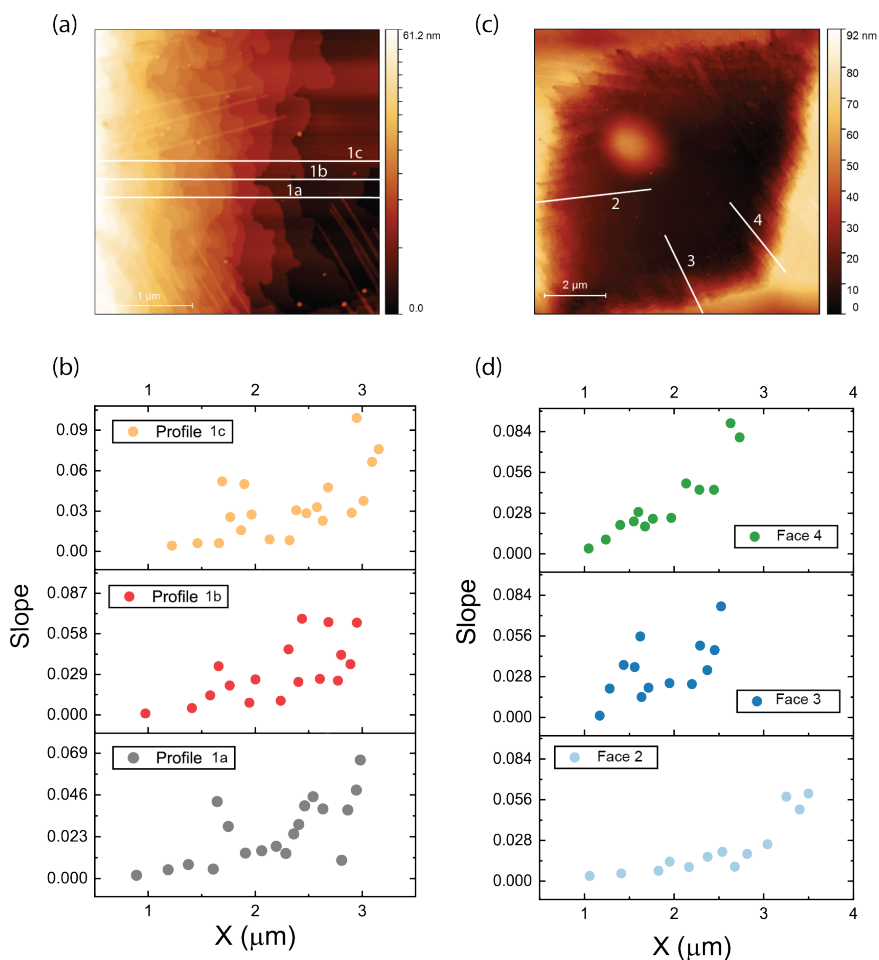


Figure 3.8 – (a) AFM observation of the basal face depression reveals the macrosteps formed. (b) Variations in the steps' local slope (corresponding to profiles marked in (a)) as a function of the distance from the depression base shows that the growth rate varies during crystal growth. (c) Analysis of the slopes of different faces shows (d) that the rate of growth varies on different faces. In figure (a) the color scale is non-linear, in order to highlight the step topography.

2 is larger (faster lateral growth due to lower step density) but thinner (slower normal growth due to larger steps) than surrounding faces 3 and 4. This is indeed observed, as visible on the full crystal topography in Figure S3.3.

3.2.5 Dendritic branching

Subsequently to the destabilization of the crystal's basal face, dendritic branching is observed (Figure 3.9 (a)), due to an instability occurring on the side faces. Fractal dimension analysis of a large number of crystals at different stages of growth reveals that branching of the crystal

only occurs when a critical crystal size has been reached. Figure 3.9 (b) shows that up to crystal sizes in the range of 70-90 μm , the fractal dimension of the crystals is close to 2 (which corresponds to the fractal dimension of a square). Above 90 μm , the fractal dimension of the crystals gradually drops towards a value of 1, which correspond to the fractal dimension of a 1-dimensional object.

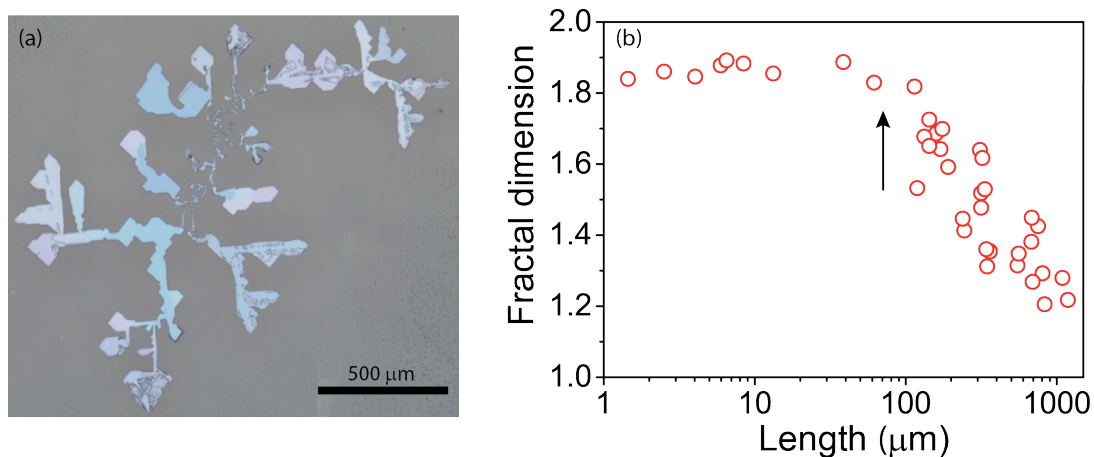


Figure 3.9 – (a) Optical microscopy image (reflection mode) of a large dendritic crystal. (b) Fractal dimension of crystal ensembles as a function of their maximum lateral extension. The arrow marks the onset of the dendritic branching.

As discussed previously, the polyhedral instability of the basal face is believed to occur due to the concomitant collapse of the surrounding droplets. With each wave of collapsing droplets, highly concentrated liquid is pushed to the crystal edge. The corresponding increase in solute concentration leads to additional layers being added at the edges and the appearance of a depression at the center of the basal face.

To understand the branching mechanism, it is necessary to take into consideration the diffusion field in substrate's plane, i.e. in the thin liquid layer. It is well established that under diffusion limited conditions, the concentration profile is inhomogeneous around a polyhedral crystal. The phenomenon, called Berg effect,^[22] has been described in the 2-dimensional case by Seeger^[36] as follows: in the case of dilute solutions, when the surface mobility of solute on a crystal face is small and the diffusion coefficient does not depend on concentration, the concentration gradient normal to a crystal face has to be homogeneous all along that face. However, this means concentration itself is not homogeneous along the face: it is larger at corner and edges. In that case, the growth of the crystal apices occurs faster than that of the

middle of a face.

As visible from Figure 3.9 (b), the difference in growth rates between apices and face center is not visible macroscopically, as long as the crystal remains small. However, as the crystal grows larger, the concentration difference between apex and center increases. Instability on the lateral faces may then appear, in the form of kinematic waves, similar to that observed on the basal face discussed in 3.2.4. The apices of the polyhedral crystal therefore move faster than the center of the adjacent faces, leading to the branching out of crystal.^[37] In some cases, a kinematic wave may abruptly form a new facet, branching the crystal into a new direction with respect to the original face.^[38] The exact branching pathway depends, however, on the local droplet distribution which drives the growth.

3.3 Conclusion

The morphological stability of CyC rhombohedral crystals is limited. Over extended periods of solvent annealing, crystals tend to destabilize and transition from polyhedral, to hopper, to branched crystals. The destabilization finds its origin in the variations of growth conditions such as the increase of the droplets' size and that of the depletion zone.

The stability of a crystal seems to be guaranteed in the first steps of growth, when the crystal grows in direct contact with its parent droplet. While growing from its parent droplet, the crystal is fed in an isotropic manner: both the basal and side-faces are provided with solute. If any inhomogeneity in concentration exists during this step (Berg effect) it is likely compensated by anisotropy of surface growth kinetics as proposed by Chernov.

When the parent droplet is consumed, the feeding pathway is not isotropic anymore: solute is only brought to the crystal's side faces, from the surrounding droplets, probably through a thin liquid layer. Nonetheless, crystal stability is ensured through the short diffusion distances, the solute being readily available in the surroundings. When the distance between crystal front and the droplets increases, the diffusion distance increases too. Therefore, growth occurs mostly laterally, by advancement of the existing train of steps.

Droplets' dimensions are not constant during solvent annealing and coalescence was shown to occur. The number of droplets contributing to crystal growth and their distance to the

crystal front was shown to be irregular over time. It is presumably resulting from variations in the pressure equilibrium between the droplets, the crystal front and other surrounding droplets. This irregular transport of solute results in waves of concentrated liquid reaching the crystal front. At this point, the crystal's lateral growth slows down of about one order of magnitude, while the crystal's thickness increases as was showed by in-situ optical microscopy of a growing crystal, leading to the formation of an apparent depression in the basal face.

Transition to dendritic branching occurs because of destabilization of the side faces. Transport of solute by long-range diffusion inevitably leads to even concentration distribution about the crystal side faces: the crystal's corners are better supplied than the center of the faces. This results in faster growth of the apices, eventually leading to the formation of kinematic waves on the side faces and branching out of the crystal in a dendritic manner.

In conclusion, the main factors leading to CyC single crystal destabilization have been identified to be the anisotropic solute distribution around a growing crystal, droplets coalescence and the uneven concentration distribution at the a crystal's faces. The exact growth form of a particular crystal will result from a complex interplay of these three factors, and it is hard to predict exactly how the crystal will evolve. Moreover, additional effects may occur (and have occasionally been observed) such as partial dissolution and/or recrystallization of certain faces, formation of defects such as solvent inclusions, dislocations or even twins.

Using the current approach, droplet coalescence and uneven concentration distribution inevitably appear, meaning that it is likely that most crystals will eventually destabilize and branch out. In the next chapter, an alternative approach is discussed in which the droplets' formation are restricted to certain areas by substrate functionalization with hydrophilic/hydrophobic patterns. Using this method the coalescence phenomena could be avoided and the crystal growth restricted to polyhedral forms only.

3.4 Experimental details

Droplet film formation and crystallization

The cyanine dye 1,1'-diethyl-3,3,3',3'-tetramethylcarbocyanine perchlorate (CyC) was synthesized in our laboratory. All films were spin-coated at 500 rpm from saturated (10.2 mg/mL) solutions in ethanol and solvent annealed under saturated chlorobenzene atmosphere at room temperature, in a sealed stainless steel container allowing in-situ optical microscopy.

Characterization

Optical microscopy was performed on a polarizing microscope equipped with a universal stage (Leitz-Orthoplan-Pol with Leitz universal stage).

SEM images were taken measuring the secondary electrons (SE mode) with a Philips XL30 ESEM, operated typically at 5 kV. The samples were coated with 2 nm platinum before examination.

Atomic force microscopy images were acquired with a Bruker ICON3 in soft tapping mode. Antimony-doped silicon tips (Bruker, RTE SP-300) were used at a resonance frequency of 300 kHz. The acquired images were treated with Gwyddion 2.47.

Image analysis of droplets and crystals was performed with Image J. The fractal dimension was measured using the box counting method. The SEM images were binarised with a threshold value to differentiate the islands from the background before the fractal analysis was performed.

3.5 Supporting Information

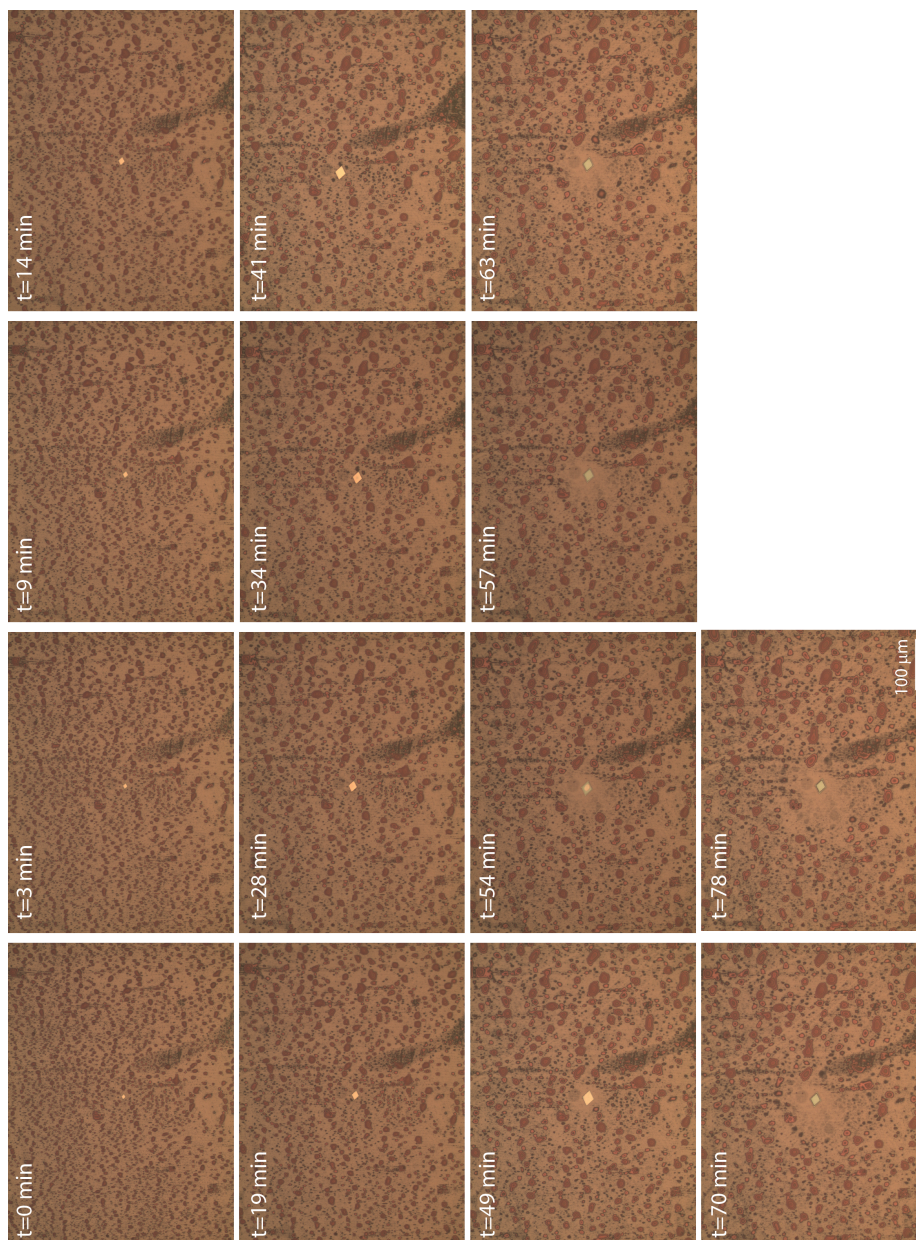


Figure S3.1 – *In-situ* microscopy time-lapse of droplets size evolution around a growing crystal. (Microscopy images acquired by J.-N. Tisserant)

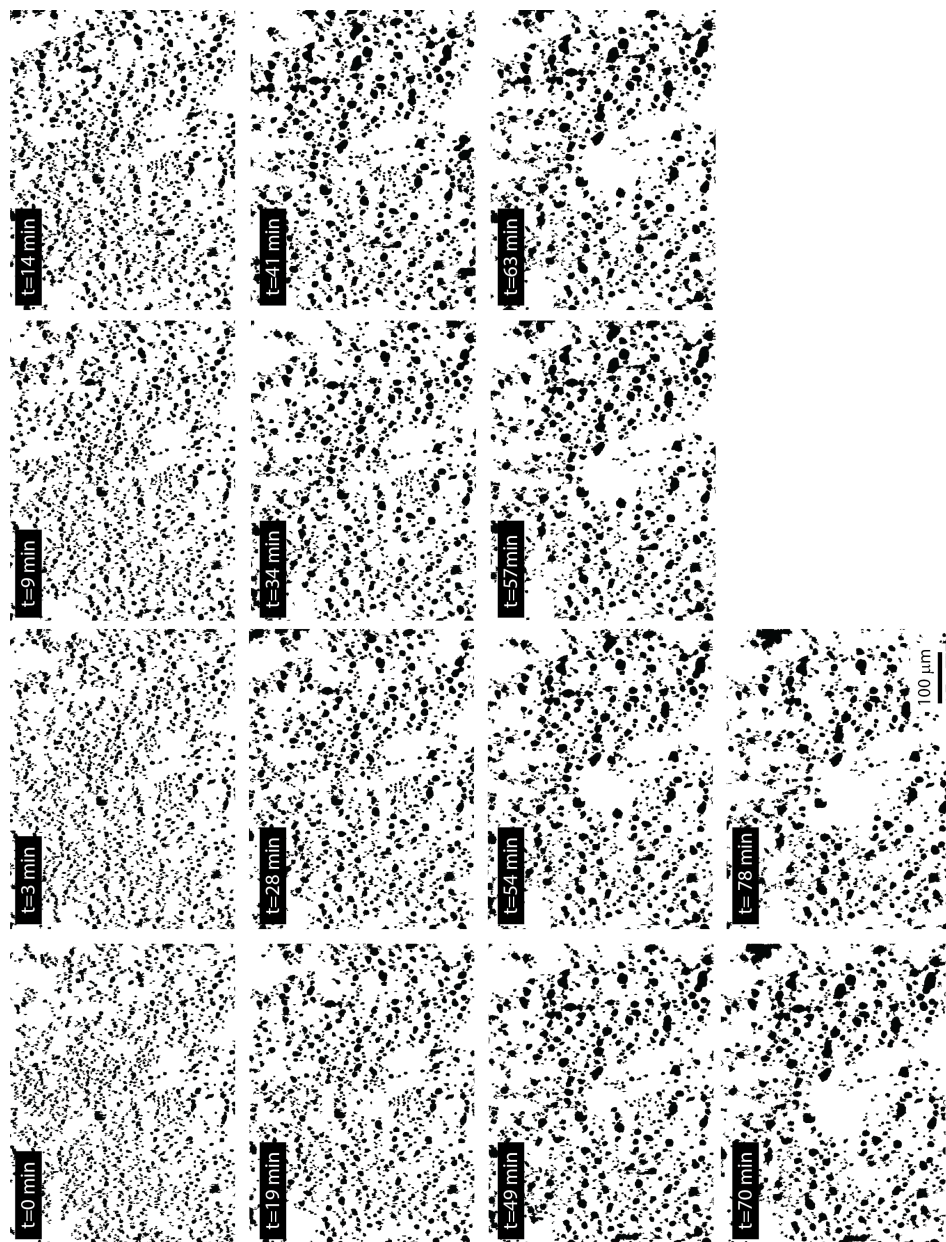


Figure S3.2 – Binarized *in-situ* microscopy time-lapse of droplet size evolution around a growing crystal. The black areas correspond to droplets and were used to extract the evolution of the droplet coverage over annealing time.

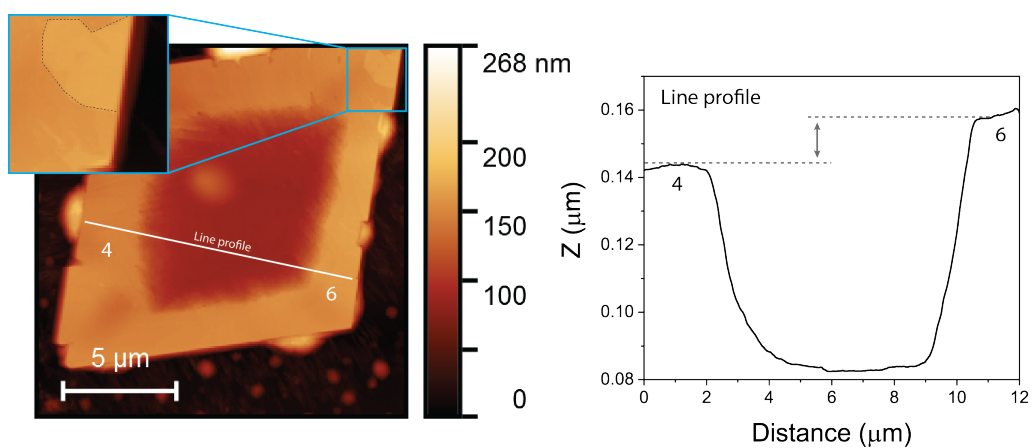


Figure S3.3 – (a) AFM topographic image of a CyC hopper crystal. The inset shows the presence of a new layer forming at the corner of the crystal. (b) The height and wideness differences between the left and right part of the crystal results from the difference in growth rates and velocities of the two faces.

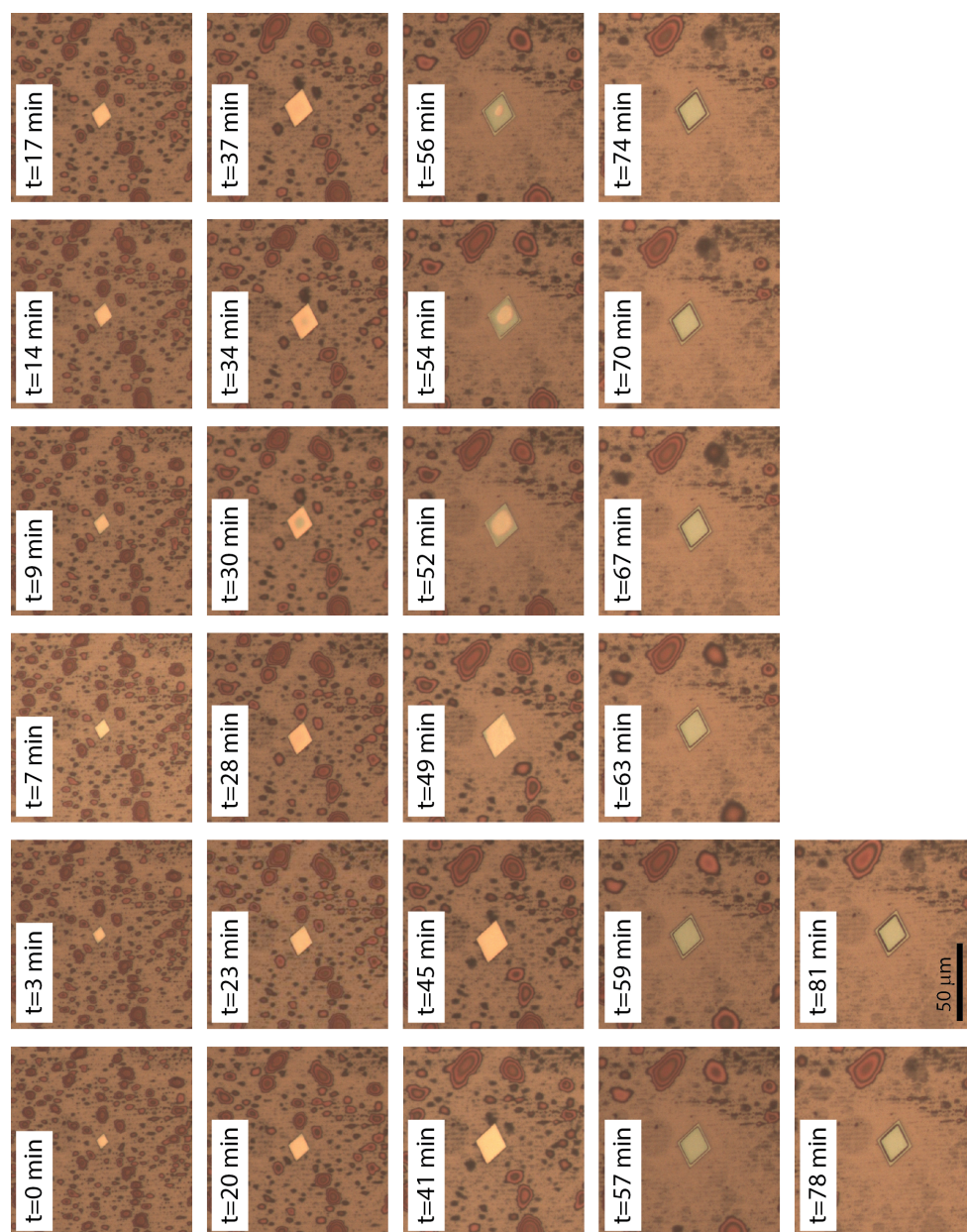


Figure S3.4 – Full *in-situ* time-lapse of CyC crystal growth. (Microscopy images acquired by J.-N. Tisserant)

Bibliography

- [1] P. Dandekar, Z. B. Kuvadia, M. F. Doherty, *Annual Review of Materials Research* **2013**, *43*, 359–386.
- [2] C. Kloc, P. G. Simpkins, T. Siegrist, R. A. Laudise, *Journal of Crystal Growth* **1997**, *182*, 416–427.
- [3] R. A. Laudise, C. Kloc, P. G. Simpkins, T. Siegrist, *Journal of Crystal Growth* **1998**, *187*, 449–454.
- [4] M. Schwoerer, H. C. Wolf in *Organic Molecular Solids*, Wiley-VCH Verlag GmbH, **2006**, pp. 57–73.
- [5] S. R. Forrest, *Nature* **2004**, *428*, 911–918.
- [6] K. Onuma, K. Tsukamoto, I. Sunagawa, *Journal of Crystal Growth* **1988**, *89*, 177–188.
- [7] K. Onuma, K. Tsukamoto, I. Sunagawa, *Journal of Crystal Growth* **1989**, *98*, 384–390.
- [8] J.-N. Tisserant, G. Wicht, O. F. Göbel, E. Bocek, G.-L. Bona, T. Geiger, R. Hany, R. Mezzenga, S. Partel, P. Schmid, W. B. Schweizer, J. Heier, *ACS Nano* **2013**, *7*, 5506–5513.
- [9] D. Braga, F. Grepioni, L. Maini, *Chemical Communications* **2010**, *46*, 6232–6242.
- [10] A. Y. Lee, D. Erdemir, A. S. Myerson, *Annual Review of Chemical and Biomolecular Engineering* **2011**, *2*, 259–280.
- [11] H. Baumhauer, *Zeitschrift für Kristallographie - Crystalline Materials* **1915**, *55*, 249–259.
- [12] K. Fichtner in *X-Ray and Neutron Structure Analysis in Materials Science*, (Ed.: J. Hašek), Springer US, **1989**, pp. 341–351.

Bibliography

- [13] I. Sunagawa in *Springer Handbook of Crystal Growth*, (Eds.: D. G. D. Dr, P. K. Byrappa, D. V. P. Dr, P. M. D. Dr), Springer Berlin Heidelberg, **2010**, pp. 133–157.
- [14] G. Wulff, *Zeitschrift für Kristallographie - Crystalline Materials* **1901**, 34, 449–530.
- [15] J. D. H. Donnay, D. Harker, *Am. Mineral* **1937**, 22, 446–467.
- [16] P. Hartman, W. G. Perdok, On the relations between structure and morphology of crystals. I, *Acta Crystallographica*, **1955**, <http://scripts.iucr.org/cgi-bin/paper?S0365110X55000121> (visited on 12/01/2017).
- [17] P. Hartman, W. G. Perdok, *Acta Crystallographica* **1955**, 8, 521–524.
- [18] P. Hartman, P. Bennema, *Journal of Crystal Growth* **1980**, 49, 145–156.
- [19] I. Sunagawa, *Morphology of Crystals: Part B*, Terra Scientific Publishing Company, Tokyo, **1987**.
- [20] I. Sunagawa, *Forma* **1999**, 14, 147–166.
- [21] K. W. Burton, N. Cabrera, F. C. Frank, *Phil. Trans. R. Soc. Lond. A* **1951**, 243, 299–358.
- [22] W. F. Berg, P. D. (Berlin), P. D. (Manchester), *Proc. R. Soc. Lond. A* **1938**, 164, 79–95.
- [23] C. N. Nanév, *Progress in Crystal Growth and Characterization of Materials* **1997**, 35, 1–26.
- [24] A. A. Chernov, *Journal of Crystal Growth* **1974**, 24-25, 11–31.
- [25] T. Kuroda, T. Irisawa, A. Ookawa, *Journal of Crystal Growth* **1977**, 42, 41–46.
- [26] C. N. Nanév, *Journal of Crystal Growth* **2000**, 212, 516–521.
- [27] D. J. Mascaró, M. E. Thompson, H. I. Smith, V. Bulović, *Organic Electronics* **2005**, 6, 211–220.
- [28] T. S. Yu, V. Bulović, A. E. Hosoi, *Journal of Fluid Mechanics* **2013**, 723, 69–90.
- [29] K. Jackson, A. in *Kinetic Processes*, Wiley Online Books, WILEY, Weinheim, Germany, **2005**.
- [30] K. Jackson, A. in *Kinetic Processes*, Wiley Online Books, WILEY, Weinheim, Germany, **2005**.
- [31] P.-G. de Gennes, F. Brochard-Wyart, D. Quéré in *Capillarity and Wetting Phenomena*, Springer, New York, NY, **2004**, pp. 1–31.

- [32] K. B. Glasner, T. P. Witelski, *Physical Review E* **2003**, 67.
- [33] K. B. Glasner, T. P. Witelski, *Physica D: Nonlinear Phenomena*, Non-linear Dynamics of Thin Films and Fluid Interfaces **2005**, 209, 80–104.
- [34] I. V. Markov in *Crystal Growth for Beginners*, 0 vols., WORLD SCIENTIFIC, **2003**, pp. 181–351.
- [35] J. W. Mullin in *Crystallization (Fourth Edition)*, Butterworth-Heinemann, Oxford, **2001**, pp. 216–288.
- [36] A. Seeger, *The London Edinburgh and Dublin Philosophical Magazine and Journal of Science* **1953**, 44, 1–13.
- [37] C. N. Nanev, R. St. Rashkov, *Journal of Crystal Growth* **1996**, 158, 136–143.
- [38] W. R. Wilcox, *Journal of Crystal Growth* **1977**, 38, 73–81.

4 Local droplet deposition, nucleation and growth of cyanine thin film crystals

4.1 Introduction and aims

Mastering the crystallization process of OSCs is an essential step towards the fabrication of better performing optoelectronic devices. For example, this has been of pivotal importance throughout the development of organic transistors^[1] based on both small molecules^[2] and polymers.^[3,4] In addition to the intrinsic quality of the crystalline material, which for most applications means low defect density and few grain boundaries, it is also highly desirable to be able to control the location, orientation and size of crystals. Large-scale fabrication of devices would benefit from robust and reproducible methods to control nucleation and growth of molecular crystals on substrates. The development of such methods has remained a practical challenge so far.

A method to crystallize CyC directly on substrate was developed by Tisserant *et al.*^[5] The method involved casting a solution of the dye on a substrate to form a dewetted film of randomly distributed dye droplets. The dewetted film was subsequently exposed to chlorobenzene vapor for several hours, resulting in the growth of micrometer-sized rhomb-shaped single crystals on the substrate. The authors identified the dewetting step as the nucleation stage, while growth took place during the solvent vapor annealing step. Two growth rate regimes were highlighted, depending on the availability of solute around a growing crystal. Moreover, by patterning the substrate with self-assembled monolayers (SAMs) stripes of alkanethiols, Tisserant *et al.* were able to orient the crystals along the stripes direction, owing to

Chapter 4. Local droplet deposition, nucleation and growth of cyanine thin film crystals

the necessity for crystals to minimize their interfacial energy with the substrate. While this work provides a good basis to understand the growth mechanism of CyC it does not give a strategy to control the location and number of nucleation events which are key parameters to allow a reproducible crystallization process. Specifically, the coalescence of droplets on non-patterned substrates leads to many changes in the crystal growth conditions, as was shown in chapter 3. Moreover, the randomness of the droplets distribution did not allow a clear quantification of the crystallization density.

Building up on these results, this chapter proposes a method to grow arrays of CyC single crystals. More specifically, the goal is to control the deposition of dye droplets from which single crystals are grown. Nucleation was identified as the critical step defining where a crystal will grow. Assuming that nucleation occurs during the solution dewetting stage, as proposed by Tisserant *et al.*, the method developed here focuses on controlling the dewetting process by means of surface patterning and from there to shed light on the nucleation mechanism and gain control on the distribution of crystals on the surface.

Local crystal growth by surface patterning As discussed in section 1.3.3 surface patterning has been widely researched as a main route to organize crystalline objects on substrates, regardless of the crystal fabrication media (solution or vapor).^[6] Classical techniques mostly make use of photolithographic methods which are not always compatible with the use of organic materials due to the harsh processes involved for lift off. Moreover, photolithographic techniques are arguably limited in terms of large area coating potential. On the other hand, alternative methods such as inkjet printing,^[7] soft-lithography methods or shadow masking allow for higher throughput but often necessitate expensive equipment and suffer from restrictions on feature size, alignment accuracy and on the type of material that can be deposited.^[8] In this regard, using SAMs as a patterning route presents many advantages.

The idea to use SAMs as patterning tool for etching of metallic films has emerged in the 1990s from the work of G. M. Whitesides^[9-11] and has been brought back into focus with the necessity to find new patterning routes compatible with OSC device processing.^[8,12] One of the main advantages of SAMs is the facility of their deposition into patterns by various high-throughput methods. The most common technique to deposit SAMs on substrates is

microcontact printing (μ CP) which is also the method used in this work. The procedure involves soaking an elastomeric stamp (typically poly(dimethylsiloxane), PDMS) of the desired pattern with an ink containing an organic surfactant generally composed of an anchor group, an alkyl chain and a functional end group. After soaking, the stamp is put into conformal contact with the substrate on which the surfactant is allowed to specifically bind *via* its anchor group. This method allows for large area patterning with resolutions approaching the sub-100nm range.^[13] Microcontact printing of SAMs has been largely exploited for many applications and procedures are now well established,^[14–18] although their reproducibility in continuous processes still needs to be demonstrated.^[8] Different types of surfactant exist depending on the targeted substrates, however the use of thiolate SAMs on gold surfaces is by far the most widely used system.^[19] Another advantage of SAMs is the broad variety of functional end groups that can be used to tune the topography, chemistry^[20] or surface energy^[21] of an interface.

Local crystallization based on surface patterning by SAMs can be implemented following two different approaches: (i) selective interaction of the deposited material with the functionalized surface and/or (ii) selective wetting of a precursor solution on an energetically patterned substrate. The former approach can be used both with vapor-deposition methods^[22] and solution-based routes.^[23,24] In this work, the latter method is chosen. SAMs of alkanethiols are used to pattern substrates with hydrophilic and hydrophobic areas via μ CP. The aim is to use these energetically-patterned substrates to induce selective wetting of a dye solution, hence restraining nucleation events to specific locations.

Nucleation theory Once droplet formation has been mastered, the second challenge is to understand and control the nucleation and growth of single crystals. Nucleation represents a main challenge in crystal technology in part because of the process' stochastic nature. Classical nucleation theory (CNT) has been developed in the last century and is useful to understand the key parameters governing nucleation. This part briefly reviews concepts of the CNT relevant to this work.

The formation of a solid cluster in its parent solution is associated with a change in the free energy of the system, which can be understood as the difference in thermodynamic potentials

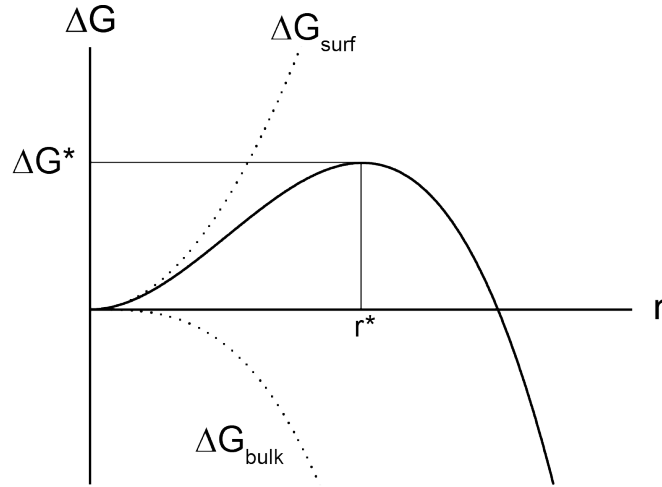


Figure 4.1 – Excess Gibbs free energy as a function of cluster size

between the solid and the liquid phase. The overall change in free energy ΔG_{homo} can be expressed as the sum of the surface excess free energy ΔG_{surf} (which is a positive value, i.e. work to supply) and the volume excess free energy ΔG_{bulk} (which is a negative value, i.e. an energy loss for the system):

$$\Delta G_{\text{homo}} = \Delta G_{\text{bulk}} + \Delta G_{\text{surf}} = \frac{4}{3}\pi r^3 \Delta g_{\text{bulk}} + 4\pi r^2 \gamma \quad (4.1)$$

where Δg_{bulk} is the free energy change of the transformation per unit volume and is proportional to the supersaturation $\Delta\mu = \mu_l - \mu_s$ (i.e. the difference between chemical potentials of two phases); γ is the interfacial energy between liquid and solid. Figure 4.1 shows the typical plot of $\Delta G(r)$: an energy barrier ΔG^* exist for the formation of a stable nucleus which is crossed when a cluster reaches the critical size r^* . If $r < r^*$ any cluster will re-dissolve in the solution, while for $r \geq r^*$ the cluster will spontaneously grow to reduce the free energy of the system. Equation 4.1 shows that the main driving force for crossing the nucleation barrier is the supersaturation $\Delta\mu$: at high supersaturation, the energy barrier is low and the critical size smaller; at low supersaturation the energy barrier is high and critical size larger. The presence of foreign bodies or surface defects on the container of the solution (or on a substrate on which the solution is applied) generally favors nucleation events. Such nucleation mechanism

is called *heterogeneous* nucleation. The presence of a foreign particle or defective surface reduces the energy barrier for nucleation such that:

$$\Delta G_{\text{hetero}} = \phi \Delta G_{\text{homo}} \quad (4.2)$$

where ΔG_{homo} is the nucleation energy barrier for the case of homogeneous nucleation, as expressed by Equation 4.1. ϕ is a factor ($0 < \phi \leq 1$) related to the interfacial tension at the boundaries between three phases (for instance a solide substrate, a solid cluster and the liquid phase). It was first expressed by Volmer^[25] as a function of the contact angle θ at the boundary between the three phases:

$$\phi = \frac{(2 + \cos\theta)(1 - \cos\theta)^2}{4} \quad (4.3)$$

Except for surfaces with complete aversion for the crystalline phase ($\theta = 180^\circ$), most surfaces generally reduce the energy barrier for nucleation. Although heterogeneous nucleation is very likely to occur in real systems (where avoiding the presence of any defect is virtually impossible), it has been often observed that large volumes of a given system spontaneously nucleates at lower supersaturation than smaller volumes.^[26] One explanation can be that smaller volumes have lesser chance of containing impurities.

A saturated solution corresponds to a solution in thermodynamic equilibrium with its solid phase. A supersaturated solution contains more dissolved solid than allowed by the saturation condition. The supersolubility limit can be sketched in a concentration-temperature phase diagram.^[27] Three different regions of importance are visible:

1. Stable region: under the solubility limit (undersaturated) crystallization is impossible.
2. Metastable region: the solution is supersaturated, however spontaneous nucleation is impossible but the growth of pre-existing crystal seeds will happen.
3. Labile region: spontaneous nucleation may occur.

Chapter 4. Local droplet deposition, nucleation and growth of cyanine thin film crystals

As visible from Figure 4.2 supersaturation can be obtained by either cooling down a solution of given concentration or evaporating the solvent to increase the concentration at constant temperature. This work involves the latter mechanism.

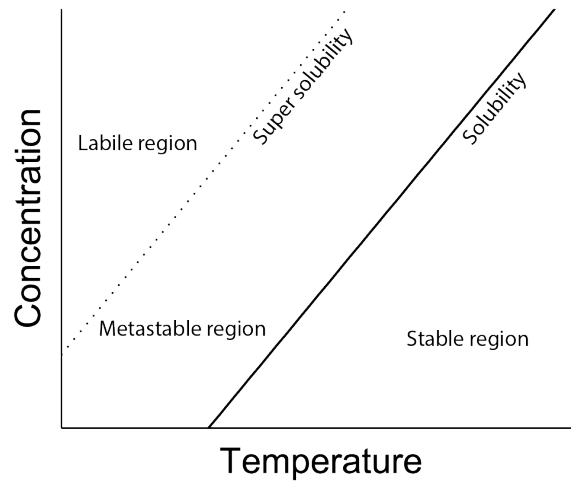


Figure 4.2 – Schematic solubility-supersolubility phase diagram

The average number of nuclei N formed in the time interval τ is related to the nucleation rate J and the volume V of the system such that:

$$N = \tau J V \quad (4.4)$$

As mentioned earlier, nucleation is an intrinsically random process. At constant supersaturation and for an time interval τ the probability to form m critical nuclei can be described with a Poisson distribution:^[28]

$$P_m = \frac{N^m}{m!} \exp(-N) \quad (4.5)$$

τ is the induction time and corresponds to the period between achievement of supersaturation and the detection of a first nucleus.^[29] Direct measurement of nucleation rates and induction

times is a difficult task, owing to the limitation in resolution to detect a first nucleus and the stochastic nature of its spatial occurrence.^[28,30,31]

The validity of CNT has been extensively discussed and its main shortcomings have been reviewed elsewhere.^[32] The general consensus is that under certain conditions (namely, at low constant supersaturations) CNT enables a good qualitative understanding of nucleation phenomena.^[32,33] With the improvement of computer-aided simulations other alternative nucleation pathways have been developed to try giving a better quantitative picture of nucleation kinetics^[32] and predict the preferred morphology of nucleating clusters.^[34–36]

Aims This chapter aims to clarify how the droplet dewetting and resulting morphology influences crystal nucleation. First, the process of dye deposition on patterned substrates and the effect of initial solution concentration on droplet morphology is described. In a second step, these observations are used to clarify the droplet drying mechanism which is essential to understand how and where nucleation occurs. Third, after exposure of the samples to solvent vapor in order to promote crystal growth, the location and density of nucleation events are evaluated by optical and atomic force microscopy. A qualitative explanation of the nucleation mechanism is outlined, stressing the importance of the droplet volume on the nucleation process. Finally the possibility to control crystal size is assessed by comparing the average droplet volume to the crystal volume.

4.2 Results and discussion

4.2.1 Droplets deposition and dimensions

In a first stage the goal is to selectively deposit droplets of cyanine dye at specific loci on a substrate. For this purpose, SAMs of alkanethiols were used to pattern the surface energy of substrates. Hexagonal patterns of hydrophilic disks of 16-mercaptohexadecanoic acid (MHDA) were deposited on gold substrates by μ CP. The remaining gold regions were then rendered hydrophobic by immersing the substrate in 1-octadecanethiol (ODT) solution. The resulting pattern geometry is shown in Figure 4.3 (a): hydrophilic disk of 1 μ m radius are arranged in a hexagonal pattern of characteristic distance $a = 10 \mu$ m. Dye solutions of different

Chapter 4. Local droplet deposition, nucleation and growth of cyanine thin film crystals

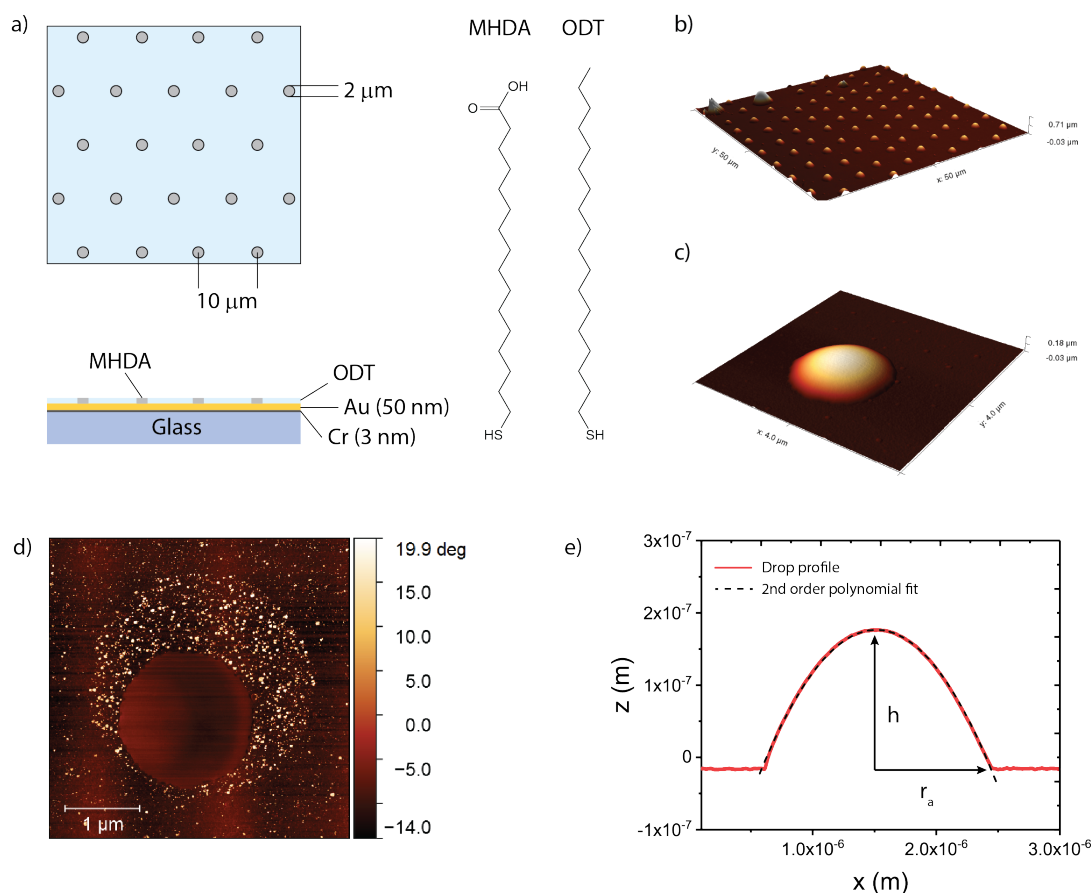


Figure 4.3 – (a) SAMs pattern geometry and structures of the thiols used. (b),(c) Topographic AFM examination shows that after deposition the dye film dewets the substrate following the printed pattern, forming an hexagonal array of dye droplets. (d) Phase contrast imaging in AFM reveals that the droplets do not fully cover the hydrophilic area. (e) Single droplets exhibit a paraboloid profile.

concentrations in chloroform were deposited on the functionalized substrates by rolling a drop of solution over the patterned substrates. To do so, the substrate was tilted back and forth at low angle such that the dye droplet rolls over the whole patterned area 5 times.^[37] After deposition on the patterned substrate, dye droplets laid on hydrophilic areas only, forming hexagonal arrays of drops (Figure 4.3 (b)). AFM examination of the samples shows that the droplets take the form of paraboloids of radius r_a and thickness h . The droplets were homogeneous and showed no visible nuclei or precipitates in topography or phase-contrast imaging modes (Figure 4.3 (c) and (d)). Figure 4.3 (e) shows that the profile of a typical droplet

can be fitted with a parabolic curve. Phase contrast imaging (Figure 4.3 (d)) reveals the dye droplet covers the hydrophilic area only partially.

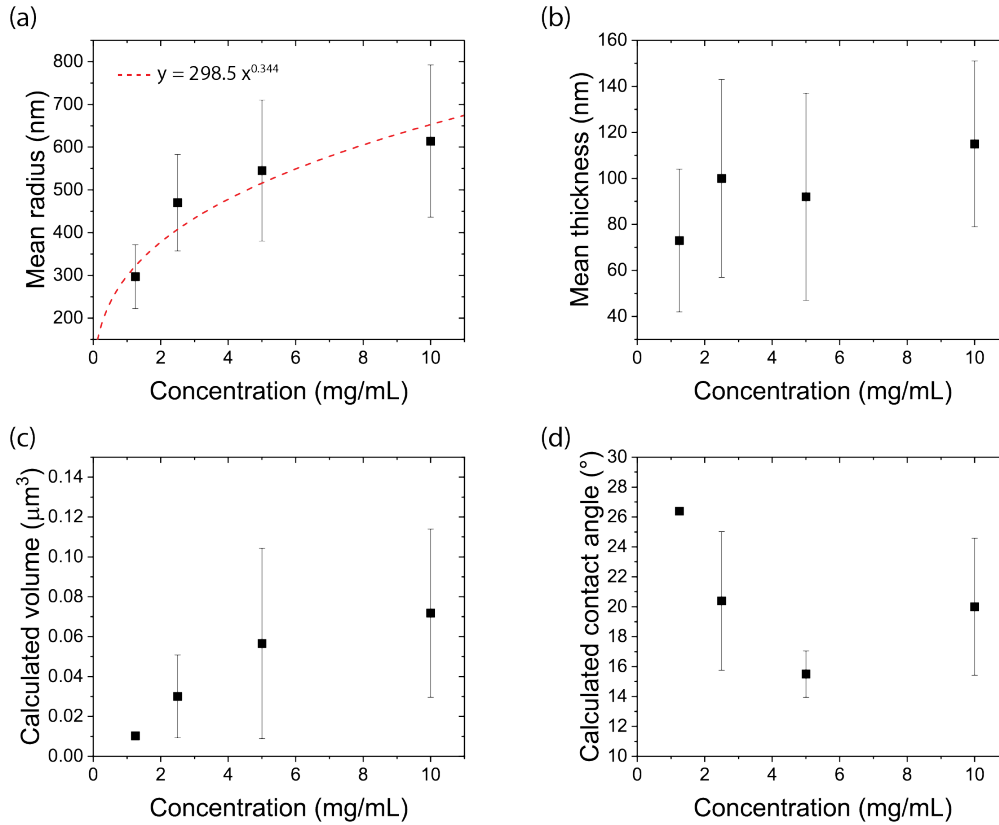


Figure 4.4 – (a) Mean droplet radius and (b) mean droplet thickness measured by AFM image analysis, as a function of dye solution concentration. (c) The droplet volume and (d) contact angles were calculated assuming a paraboloid profile. The mean droplet radius (a) varies as a cubic root of the concentration (red dashed line)

The effect of dye solution concentration on the droplets dimension was evaluated by a statistical analysis on a large number of droplets (200-500) from different samples. The mean radius and thickness were measured by image analysis of AFM images. From the droplet profiles the microscopic droplet volume and contact angle were estimated, assuming an axisymmetric paraboloid geometry and using the relations:

$$V = \frac{\pi}{2} h r_a^2 \quad (4.6)$$

Chapter 4. Local droplet deposition, nucleation and growth of cyanine thin film crystals

$$\theta_c = \tan^{-1} \left(\frac{2h}{r} \right) \quad (4.7)$$

As visible from Figure 4.4 (a) and (b), the mean radius and mean thickness of the drop increases together with the increasing dye concentration. The droplet volume also increases correspondingly. The equilibrium contact angle of chloroform on MHDA substrates was measured to be $\theta_{\text{CHCl}_3/\text{MHDA}} = 5.76^\circ \pm 0.72^\circ$, while it was measured to $\theta_{\text{CHCl}_3/\text{ODT}} = 31.3 \pm 1.4^\circ$ on ODT surface. Comparison with the estimation of the droplets final contact angle reveals that at all concentrations the droplets wet the hydrophilic areas with higher values than that of chloroform on MHDA surface. The values of contact angle calculated indicate that if the wetting behavior is controlled by that of chloroform during deposition, the final contact angle is defined by the surface tension of the dye, measured to be 34.3 mN m^{-1} .^[38]

The droplet drying process can be outlined based on the previous observations which suggest that the dye droplets dry on the patterned substrate without being pinned at the interface between hydrophilic and hydrophobic areas. Moreover, observation of droplet topography and profiles (Figure 4.3 (c) and (e)) do not reveal any characteristic signs of coffee ring formation, which often occurs in drying liquid droplets systems.^[39] The drying process steps can be qualitatively described as follow:

1. Dye droplets deposit on hydrophilic domains and form a thin spherical cap of solution, which diameter is that of the hydrophilic area with a contact angle between that of chloroform on ODT ($\sim 30^\circ$) and on MHDA ($\sim 6^\circ$).^[40] The volume of the initial liquid droplet is only defined by the surface tension of the solution on the hydrophilic area and thus should be the same at all concentrations (assuming the dye concentration does not influence the surface tension of the solution too much). The initial droplet volume $V_{\text{ini}} = \frac{V_{\text{final}} \rho_{\text{film}}}{C}$ was estimated using the final droplet volumes V_{final} shown in Figure 4.4 (c), the amorphous film density ρ_{film} (see supporting information) and the initial solution concentration C to $V_{\text{ini}} = 11.3 \pm 2.3 \mu\text{m}^3$
2. In the early stage of drying the contact angle decreases and droplets de-pin from the

hydrophilic pattern edge.

3. Given that no ring pattern is observed after drying, it can be concluded that during the evaporation droplets are free to reduce their diameter without being pinned to the substrate.
4. During evaporation, the concentration in the droplets increases. When it crosses critical supersaturation limit, the first nuclei start to form and the droplets are pinned again.
5. As evaporation proceeds further, the molar ratio dye/solvent increases: when the ratio becomes >1 the contact angle of the droplets start to increase again to reach that prescribed by the surface tension of the dye (Figure 4.4 (d)). The increase of contact angle reduces the evaporation rate towards the end of the drying process.

It is important to note that during evaporation the viscosity of the droplet increases, which tends to reduce the diffusion coefficient^[41]

$$D_s = \frac{kT}{6\pi\eta r} \quad (4.8)$$

with k the Boltzmann constant, T the temperature, η the viscosity of the solvent and r the radius of the dye cation. When the D_s approaches 0 the system becomes kinetically frozen^[42] and the fraction of solute which has not yet nucleated remains amorphous.

Assuming that the initial droplet radius is the same at every concentration level (that of the patterned area) and that the evaporation rate is similar for all samples over most of the evaporation process, then it becomes clear that the final droplet radius is governed by the intermolecular distance $L_m = \sqrt[3]{\frac{V_{ini}}{n}}$, where V_{ini} is the initial droplet volume and n is the number of molecules in the drop. Therefore, the radius is expected to vary as a cubic root of concentration, which is verified in Figure 4.4 (a).

Chapter 4. Local droplet deposition, nucleation and growth of cyanine thin film crystals

4.2.2 Nucleation mechanism

The previous section outlined how the droplet drying process takes place and showed how evaporation and dye solution concentration govern the droplets' morphology. However, at this stage no exterior signs of nucleation (such as coffee ring structures) could be observed and the exact nature of the droplets after deposition is not clear. Tisserant *et al.* already showed that dewetting was the main nucleation step and observed that almost no new nuclei were formed during solvent vapor annealing.^[5] This section attempts to further clarify (i) if crystals can indeed be grown at loci defined by the substrate pattern by solvent annealing of deposited droplets, (ii) how nucleation occurs within a single droplet and (iii) what is the influence of the droplets dimensions on nucleation.

Types of droplets features after annealing

In order to be able to observe nucleation events, growth of crystals was induced by solvent vapor annealing. Arrays of deposited droplets were exposed to a continuous flow of chlorobenzene vapor at room temperature for 7 hours to promote growth of single crystals.^[5] Observation of samples after annealing under the optical microscope, Figure 4.5, shows that single crystals grow at locations defined by the droplets' position. It should also be noted that, contrary to droplets deposited on non-structured substrates like presented in chapter 3, here droplets remain within their defined area and no apparent coalescence occurs. This is an advantage as the crystal volume is in principle bound to the volume of dye available within a single drop. Moreover, even after extended annealing periods, rhomb-shaped crystals remained stable and transition to dendritic forms was never observed.

It is clear from microscopy observations that not every single droplet lead to a single crystal. When observed under crossed polarizers (Figure 4.5 (b)), samples show three distinct types of features:

- (i) Rhomb-shaped single crystals of micrometer dimensions that are either extinct or visible depending on their relative orientation to the polarizer.
- (ii) Scattering droplets which color does not appear to depend on the polarizer's orientation and are attributed to polycrystalline aggregates.

- (iii) Extinct droplets, that never scatter light, no matter their relative orientation to the polarizer, which are attributed to amorphous dye.

All fully grown crystals seem to adopt the same rhomb-shaped morphology, characteristic of a preferential crystallographic out-of-plane orientation, as will be shown in chapter 5.

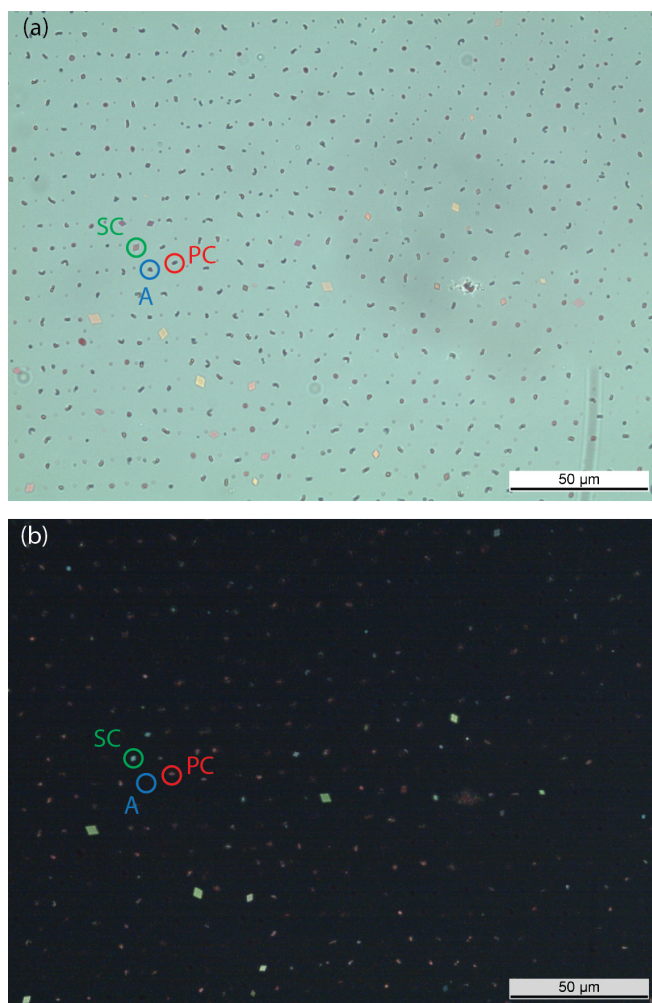


Figure 4.5 – Array of annealed CyC droplets cast from 10 mg/mL solution, observed under (a) non-polarized and (b) cross-polarized optical microscope. Three different types of features can be seen: fully grown single crystals (SC, circled in green), polycrystalline aggregates (PC, circled in red) and amorphous droplets (A, circled in blue).

Closer observation with AFM confirms the nature of the different features after annealing. However, their precise character appears to vary with the initial solution concentration. Figure 4.6 shows AFM topography scans of annealed samples cast from 10 mg mL^{-1} (top row) and

Chapter 4. Local droplet deposition, nucleation and growth of cyanine thin film crystals

5 mgmL⁻¹ (bottom row) dye solutions. For each type of sample the inset shows the most common types of features occurring on samples. After annealing, droplets cast from higher concentration yield large rhomb-shaped crystals (Figure 4.6, top-leftmost inset), polycrystalline aggregates (Figure 4.6, top-rightmost inset) and droplets which appear to contain a large number of clusters (Figure 4.6, top-middle inset). In comparison, droplets cast from less concentrated solution yield smaller rhomb-shaped crystals (Figure 4.6, bottom-leftmost inset) and droplets containing a small number of clusters at their rim, while larger crystallites are found in their center (Figure 4.6, bottom-middle and -rightmost insets).

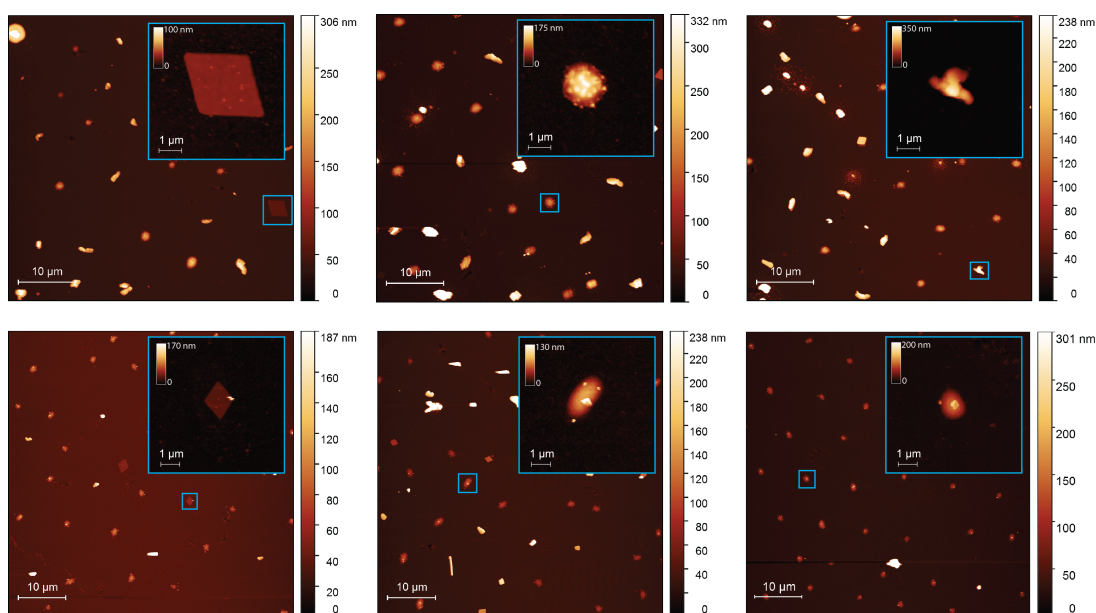


Figure 4.6 – AFM topography images of CyC droplets after 7 hrs annealing in chlorobenzene vapor at 25 °C. Top row: droplets cast from 10 mgmL⁻¹ dye solution. Bottom row: droplets cast from 5 mgmL⁻¹ solution. The insets show most common types of features found on the samples.

These observations suggest that droplets cast from higher concentration solutions tend to form a greater number of critical nuclei per droplet after deposition, which have to compete for solute during the growth step. Droplets containing several large clusters are likely to lead to polycrystalline aggregates while droplets containing a large cluster and several smaller ones are likely to result in the formation of single crystals due Ostwald ripening mechanism.

In droplet samples cast from less concentrated dye solutions, the number of clusters per droplet appears to be lower, which in principle should result in a smaller number of poly-

crystalline aggregates. Qualitative observation under cross-polarized microscope tend to confirm this hypothesis as visible from Figure 4.7. Droplets cast at lower concentration appear to form fewer light scattering objects than those formed from more concentrated solutions. Unfortunately a quantitative estimation of the exact number of polycrystalline aggregates formed after annealing by either AFM or optical microscopy is difficult. One reason is that the resolution of the optical microscope hardly allows distinguishing between polycrystals, small single crystals and droplets containing a single nucleus not yet fully grown (such as the one shown in Figure 4.6, bottom-leftmost inset). In addition, the exact effect of the solvent vapor step on pre-existing metastable clusters is not clear. It is likely that absorption of chlorobenzene molecules in dye droplets (up to 27%) leads to the re-dissolution of smaller metastable clusters and small nuclei which have a higher solubility than larger ones. Finally, at the end of the SVA step, chlorobenzene evaporates from the droplets when they are taken out of the SVA chamber. It is possible that this second evaporation leads to additional nuclei forming in droplets which have not fully transformed.

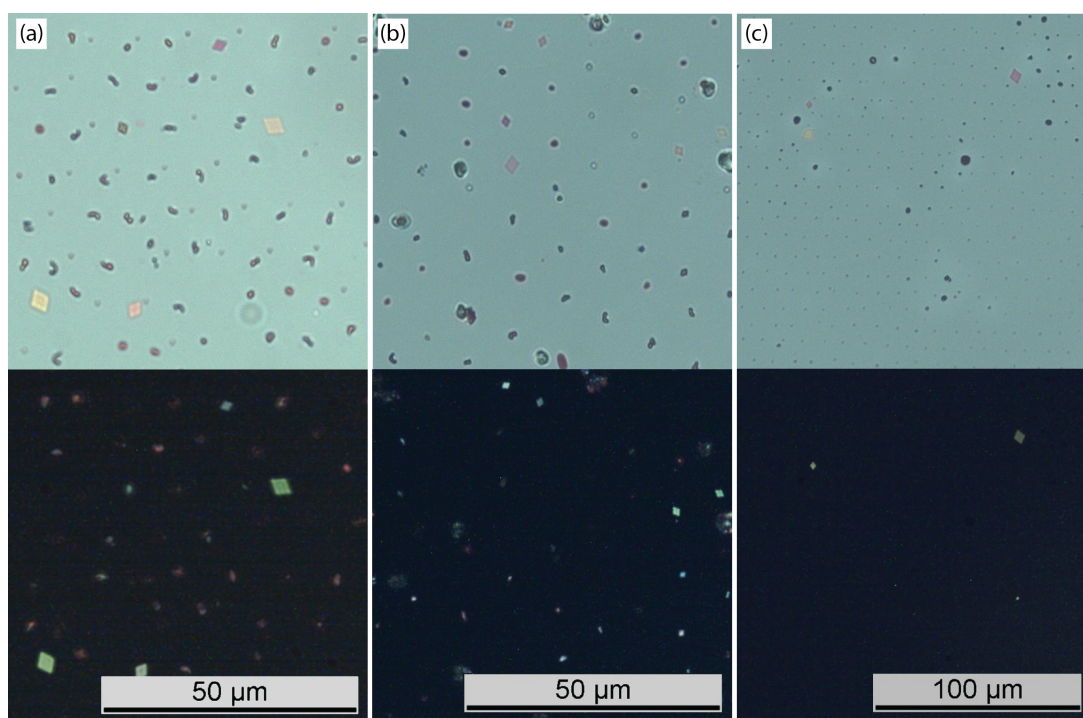


Figure 4.7 – Optical microscopy images of (a) 10 mg/mL, (b) 5 mg/mL and (c) 1.25 mg/mL droplets after annealing under non-polarized (top row) and cross-polarized light (bottom row).

Chapter 4. Local droplet deposition, nucleation and growth of cyanine thin film crystals

Nucleation location

The absence of coffee ring residue after droplet deposition indicates that nucleation does not occur at the liquid/substrate interface but rather somewhere in the bulk of droplets or at the air/liquid interface. On the other hand, observation of droplets after annealing has revealed that the small clusters are found preferentially at the rim of drops while crystallites showing a more advanced state of growth are found in the middle of droplets.

The slow diffusion of the salt compared to solvent evaporation can lead to concentration gradients within the droplet, with higher concentrations near the edge of the droplet where evaporation occurs faster.^[43] In order to evaluate the importance of the concentration gradient within a droplet, the Péclet number is calculated. It represents the ratio between advection and diffusion rates within an evaporating droplet and can be expressed as $Pe = \frac{uR}{D_s}$, where u is the flow velocity within the drop, R the radius of a drop and D_s the diffusion coefficient of the ionic species in solution, as expressed by Equation 4.8. $Pe \gg 1$ is characteristic of heterogeneous distribution of ions while $Pe \ll 1$ implies that diffusion compensates for advection mass flow and the ion distribution can be considered homogeneous throughout the droplet volume. Pe was calculated by estimating the radial flow rate with $u = \frac{j}{\rho_L}$ where ρ_L is the solvent density and j the evaporation rate expressed by:^[42,44]

$$j(r) = \frac{2D_v(c_0 - c_\infty)}{\pi\sqrt{R^2 - r^2}} \quad (4.9)$$

where D_v is the molecular diffusion coefficient of chloroform in air, c_∞ and c_0 the densities of the saturated vapor pressure in the ambient atmosphere and just above the drop (respectively), R and r the droplet radius and the distance from the center of the drop, respectively. Here it is assumed that the ambient atmosphere does not contain any chloroform vapor and that $c_\infty = 0$. The value of c_0 can be evaluated by:

$$c_0 = \frac{M_w P_{vs}}{RT} \quad (4.10)$$

M_w is the molar mass of chloroform and P_{vs} the saturated vapor pressure of the solvent at ambient conditions. The radial flow rate is found to be $u \approx 5 \text{ mms}^{-1}$ near the center of the droplet. The diffusion coefficient of CyC in chloroform was calculated to be $D_s = 2.7 \cdot 10^{-10} \text{ m}^2 \text{ s}^{-1}$ at 25 °C. This leads to $Pe \approx 18$ for the system considered here. It can therefore be concluded that nucleation occurs preferentially at the rim of the drop, above the solid/liquid interface, likely due to a higher concentration of solute near the edge as indicated by the value of Pe .

In the case of droplets cast from 5 mg mL^{-1} and less, there is a consistent presence of larger crystallites in the middle of the droplet while smaller clusters seem to stay at the rim. Similar observation was made by Shahidzadeh *et al.* for the case of NaCl crystals growing from evaporating water droplets.^[45] The presence of large crystals at the middle of the drop was explained to result from the a capillary force occurring at the edge of the droplet during evaporation, pushing the growing nuclei towards the center of the droplet. Such effect has also been described as "reverse coffee ring effect" and was shown to segregate particles of different sizes in evaporating drops.^[46,47] This interpretation would also be consistent with previous observations that crystals are rotating on a liquid layer during growth.^[5]

Effect of droplet volume on crystal density

As previously mentioned, direct observation of nucleation is a difficult task due to practical limitations arising from the size of critical clusters as well as their stochastic occurrence in space and time. With the goal to gain insights on the effect of droplet size on nucleation events, nucleation density was evaluated as a function of the droplet's final volume by counting the number of fully grown single crystals visible under optical microscopy after annealing. For all samples the annealing conditions were kept constant (50 sccm for 7 hours at 25 °C). The number of crystals was then normalized to the size of the total investigated area to give the crystal density.

As visible from Figure 4.8 the crystal density is directly proportional to the average drop volume after deposition. The correlation between droplet volume and nucleation density originates from the confinement of nucleation events to very small volumes. A kinetic limitation indeed

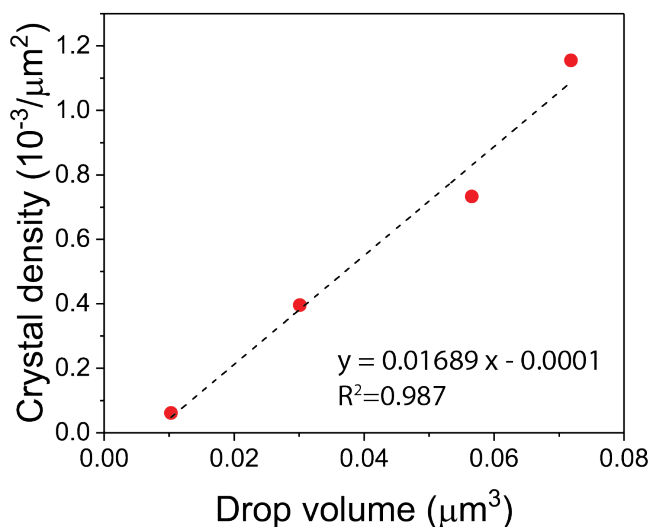


Figure 4.8 – Crystal density as a function of droplet volume

arises from the rate of nucleation J (number of nucleation event per second and by unit volume). Although J does not vary with volume (it is an intensive property of the system), it is inversely proportional to it, as expressed by Equation 4.4. On the other hand, the induction time varies linearly with the volume (Equation 4.4): the smaller the volume the longer the induction time. Thus, over the same time period less nucleation events are expected in smaller droplet samples than in larger ones. In the present case, it is assumed that the solution concentration does not influence the evaporation rate $j = -\frac{dV}{dt}$. Therefore, the evaporation time is proportional to the difference between the initial and final droplet volumes $t_{\text{evap}} \propto V_{\text{ini}} - V_{\text{final}}$. Considering the initial and final volumes measured in subsection 4.2.1 it is clear that the volume variation is over 99% at every concentrations. Therefore, the difference in evaporation times between droplets deposited from solutions of different concentrations is negligible and the evaporation time can be considered equal at all concentrations. Thus, the number of nucleation events is indeed expected to be proportional to the droplet volume, as shown in Figure 4.8.

4.2.3 Influence of solution concentration on crystal mass

The average mass of a single crystal as a function of the initial dye concentration is compared to the average mass of deposited drops. The crystal volume was calculated using:

$$V_{\text{crystal}} = \frac{d_1 d_2 h}{2} \quad (4.11)$$

where d_1 , d_2 and h are the long diagonal, short diagonal and thickness of the rhombic crystal respectively, as measured by AFM. The values were averaged over 15-25 crystals per sample. In order to account for the different densities between crystals and droplets, masses are compared rather than volumes. The droplets' density is assumed to be similar to that of an amorphous thin film and was measured to be $\rho_{\text{film}} = 1.17 \pm 0.04 \text{ g cm}^{-3}$ (see SI). The density of the crystalline phase is $\rho_{\text{crystal}} = 1.254 \text{ g cm}^{-3}$, as measured by X-ray single crystal analysis (see chapter 5).

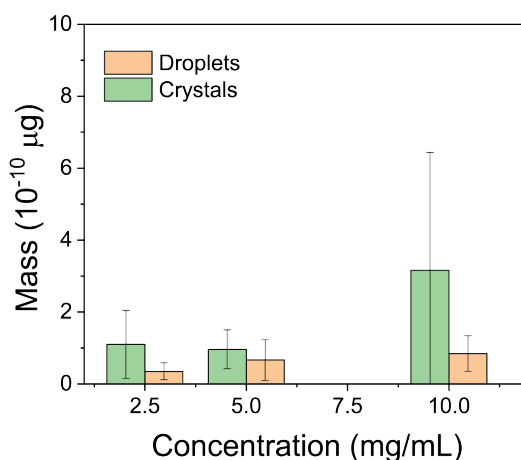


Figure 4.9 – Crystal mass and droplet mass as a function of CyC solution concentration.

Figure 4.9 shows that the crystals' mass increases together with initial solution concentration, as it is also the case for the droplets' mass. However, large differences can be seen between the crystal mass and droplet mass of same concentration and overall, the mass of the crystals always appear to be larger than that of the droplets. In addition, the deviations associated with crystal mass are large, mostly for crystals grown from 10 mg mL^{-1} solutions. This reveals

Chapter 4. Local droplet deposition, nucleation and growth of cyanine thin film crystals

heterogeneities between the crystals grown from a same solution concentration.

Several explanations could be given here to explain such differences. First, the statistical values are not performed on the same population size: about 10 times more droplets were measured than crystals. As seen previously, the number of fully grown crystals per sample is rather limited (in the order of 10^{-3} crystals/ μm^2) and measuring a representative amount of crystals is a difficult task. Therefore, on a limited population of crystals, volume variations resulting from initial droplet to droplets variations might be high, while they are averaged when measuring the droplet volumes. Another potential explanation could be that the exact volume deposited at each position will depend on the contact angle of the liquid droplet. As mentioned earlier, this contact angle can take in principle any value between $\theta_{\text{CHCl}_3/\text{MHDA}} = 5.76^\circ \pm 0.72^\circ$ and $\theta_{\text{CHCl}_3/\text{ODT}} = 31.3 \pm 1.4^\circ$. Therefore, there might be important droplet-to-droplet volume variations, leading to a large distribution of crystal volumes. Finally, it is possible that some crystals nucleate at different moments *during* SVA such that the effective growth time during the 7 hours of annealing might vary between crystals. This would also yield a broad distribution in the crystal volume, most pronounced for droplets cast at higher concentration. Finally, mass transport between droplets could also occur during solvent vapor annealing. However, if it were the case, a zone of depleted droplets would be visible around single crystals. This is not observed in the samples analyzed here, likely due to the presence of hydrophobic surfaces separating the individual droplets.

4.3 Conclusion

In this chapter the possibility to locally grow single crystals of CyC was demonstrated. By rolling a macroscopic drop of CyC solution over substrates patterned with SAMs of hydrophilic and hydrophobic nature, local deposition of a dye droplet on hydrophilic areas was achieved. It was shown that the volume of the deposited droplets can be controlled by varying the initial solution concentration. Observation of the droplets' morphology after deposition revealed that the droplets dry without being pinned to the substrate.

The location and number of nucleation events was evaluated by observing the morphology of the samples after a solvent vapor annealing step. It was shown that due to the fast evaporation of solvent, the crystal nuclei are forming at the rim of the drops, above the solid/liquid

interface.

The number of nucleation events was qualitatively shown to be dependent on the droplet volume. However, it is difficult to really assess the exact number of nucleation events per droplet due to resolution limitation of the imaging techniques, but also because additional nucleation may also occur during SVA, mostly in larger droplets. A tentative to detect nuclei by probing dye droplets *before* annealing (right after casting on the substrate) with confocal fluorescence microscopy has proven unsuccessful due again to optical resolution limitations. Finally, evaluation of the average crystal mass after solvent annealing revealed that more concentrated initial solution leads to larger crystals. However, large variations of crystal size were observed that could be attributed to a statistical artefact, or delayed nucleation events occurring during SVA.

To conclude, the method proposed here appears to be a promising way to easily form arrays of dye single crystals from a simple preparation method, adaptable to large area processing. The droplet volume could be used to tune the number of nucleation events. However, better control over the time given for evaporation would be beneficial to avoid nucleation of polycrystals and instead promote single crystal nucleation. This could be achieved for example by using different solvents than chloroform, with higher boiling points. However, the wetting properties of the solvent should also enable local droplet deposition on the patterned substrates. Another approach would be to use a controlled solvent atmosphere or variations in the substrate temperature during solution deposition to tune the evaporation rate. In addition, a better control over the solvent vapor environment during SVA would also be beneficial. The use of solvent atmosphere with controlled partial pressure would for example allow to tune the supersaturation level in the droplets to promote growth of crystals and avoid unwanted nucleation.

4.4 Experimental details

Substrates preparation

Gold substrates were prepared by physical vapor deposition (PVD) on microscope glass slides. The glass slides were cleaned by consecutive sonicating baths of acetone, isopropanol and

Chapter 4. Local droplet deposition, nucleation and growth of cyanine thin film crystals

deionized water and dried under nitrogen flow. A 3 nm chromium adhesion layer followed by 50 nm of gold were evaporated by PVD on the glass substrates at a typical deposition rate of 0.5 \AA s^{-1} and a pressure of $4 \cdot 10^{-6}$ mbar. Poly(dimethylsiloxane) (PDMS) stamps were prepared by using a degassed polymer:curing agent mixture of 10:1 (wt) (Sylgard 184, Dow Corning) which was poured over a silicon pattern template. The stamps were cured at $100 \text{ }^\circ\text{C}$ for 2 hours. The PDMS stamps were swelled for 30 s with 0.5 mM solution of 16-mercaptohexadecanoic acid (Sigma Aldrich) in ethanol, dried with nitrogen for 30 s and put in conformal contact with the gold substrate for 15 s. The substrates were then thoroughly rinsed with ethanol and dried. To render the remaining gold areas of the substrate hydrophobic, the samples were then covered with a 0.25 mM solution of 1-octadecanethiol (Sigma Aldrich) in ethanol for 60 s, then thoroughly rinsed with ethanol and dried.

Dye solution preparation and deposition

The cyanine dye 1-ethyl-2-[3-(1-ethyl-1,3-dihydro-3,3-dimethyl-2H-indol-2-ylidene)-1-propen-1-yl]-3,3-dimethyl-3H-indolium perchlorate (CyC) was synthesized in the laboratory. Solutions of 1.25 mg mL^{-1} , 2.5 mg mL^{-1} , 5 mg mL^{-1} and 10 mg mL^{-1} in chloroform (Sigma Aldrich, Chloroform ReagentPlus, >99.8%) were prepared.

A $50 \mu\text{L}$ drop of dye solution was deposited on the substrate. The substrate was then tilted back and forth with low angle such that the dye droplet rolls over the whole patterned area 5 times.^[37] The excess solution was removed by capillary suction of a paper tissue.

Crystal growth

Droplet samples were put in a self-built chamber connected to a stream of chlorobenzene vapor. The solvent vapor was carried by a stream of dry nitrogen controlled by a mass-flow controller (Vögtlin, Red-y Smart MFC) passing through a chlorobenzene bubbler. The stream was kept constant at 50 ± 0.01 sccm. The bubbler was immersed in a silicon oil bath to be kept at room temperature ($25 \text{ }^\circ\text{C}$). Droplet samples were exposed to a continuous chlorobenzene flow for 7 hours.

Contact angle measurements

Contact angle of chloroform on MHDA, ODT was measured on a Drop shape analyzer DSA30 (Krüss GmbH, Hamburg, Germany). MHDA and ODT substrates were prepared by immersing 50 nm thick gold surfaces in the 0.5 mM thiol solutions (in ethanol) for 60 s. The substrates were subsequently rinsed in pure ethanol and dried under N₂ flow. For contact angle measurements, microliter drops of chloroform were deposited at ambient conditions on the different substrates. Contact angles were measured on 10-20 drops using the Krüss ADVANCE software, using the circle fitting method.

Atomic force microscopy characterization

Samples were analyzed with a Bruker ICON3 atomic force microscope in soft tapping mode. Antimony-doped silicon tips (Bruker, RTESP-300) were used at a resonance frequency of 300 kHz. The acquired images were treated with Gwyddion 2.47.

Optical microscopy

Optical microscopy was performed on a polarizing microscope equipped with a universal stage (Leitz-Orthoplan-Pol with Leitz universal stage). Images were analyzed with ImageJ software.

4.5 Supporting Information

CyC amorphous film density measurement

Films of different thicknesses were prepared by spin-casting dye solutions of different concentration (10 mgmL⁻¹, 5 mgmL⁻¹ and 2.5 mgmL⁻¹) on 25 × 25 mm² glass substrates at 2000 rpm. To avoid heterogeneity in the film thickness, only a small, homogeneous area of each film was kept for measurement, while the rest of the film was carefully washed away with ethanol. The film's thickness was measured by spectroscopic ellipsometry on a M2000VI ellipsometer (J.A. Woollam, USA). The film's total area was estimated from optical microscopy images with an image analysis software. Finally, to estimate the mass of the films, each of

Chapter 4. Local droplet deposition, nucleation and growth of cyanine thin film crystals

them was dissolved in 10 mL ethanol. The resulting concentration was measured by UV-vis spectroscopy using Beer-Lambert's law. The mass was extracted from the solution concentration using the relation

$$m_{\text{CyC film}} = C \times M_{\text{CyC}} \times V_{\text{solvent}} \quad (\text{S4.1})$$

where C is the solution concentration, $M_{\text{CyC}} = 485.01 \text{ g mol}^{-1}$ is the dye molecular weight and V_{solvent} the solvent volume. The average density of the films was measured to be $\rho_{\text{film}} = 1.17 \pm 0.04$. All measured values are summarized in Table S4.1

Table S4.1 – Values measured for CyC amorphous film density evaluation

Film thickness / nm	Film area / mm ²	Film volume / mm ³	A ₅₄₈	Concentration / M	Film mass / g	Density
58.9	199	$1.17 \cdot 10^{-2}$	0.37	$2.96 \cdot 10^{-6}$	$1.42 \cdot 10^{-5}$	1.21
32.1	198	$6.36 \cdot 10^{-3}$	0.20	$1.58 \cdot 10^{-6}$	$1.65 \cdot 10^{-5}$	1.20
15.4	182	$2.80 \cdot 10^{-3}$	0.082	$6.47 \cdot 10^{-7}$	$3.14 \cdot 10^{-6}$	1.12

Physical values used for calculations of the Péclet number

Table S4.2 – Physical values used for calculations of the Péclet number

Symbol	Value	Units / SI base units
R_i	$1 \cdot 10^{-6}$	m
ρ_{CHCl_3}	$1.47 \cdot 10^3$	kgm ⁻³
D_v	$9.0 \cdot 10^{-6}$	m ² s ⁻¹
R	8.3144	J mol ⁻¹ K ⁻¹ / kgm ² s ⁻² mol ⁻¹ K ⁻¹
T	298.15	K
M_{CHCl_3}	0.11938	kgmol ⁻¹
P_{vs}	26236	Pa/kgm ² s ⁻¹
k_b	$1.3806 \cdot 10^{-23}$	m ² kgs ⁻² K ⁻¹
η_{CHCl_3}	$5.42 \cdot 10^{-4}$	Pa s ⁻¹ / kgm ² s ⁻²
r_{CyC}	$1.5 \cdot 10^{-9}$	m



Bibliography

- [1] X. Guo, Y. Xu, S. Ogier, T. N. Ng, M. Caironi, A. Perinot, L. Li, J. Zhao, W. Tang, R. A. Sporea, A. Nejim, J. Carrabina, P. Cain, F. Yan, *IEEE Transactions on Electron Devices* **2017**, *64*, 1906–1921.
- [2] J. Mei, Y. Diao, A. L. Appleton, L. Fang, Z. Bao, *Journal of the American Chemical Society* **2013**, *135*, 6724–6746.
- [3] J. Y. Kim, D. S. Yang, J. Shin, D. Bilby, K. Chung, H. A. Um, J. Chun, S. Pyo, M. J. Cho, J. Kim, D. H. Choi, *ACS Applied Materials & Interfaces* **2015**, *7*, 13431–13439.
- [4] G. Qu, X. Zhao, G. M. Newbloom, F. Zhang, E. Mohammadi, J. W. Strzalka, L. D. Pozzo, J. Mei, Y. Diao, *ACS Applied Materials & Interfaces* **2017**, *9*, 27863–27874.
- [5] J.-N. Tisserant, G. Wicht, O. F. Göbel, E. Bocek, G.-L. Bona, T. Geiger, R. Hany, R. Mezzenga, S. Partel, P. Schmid, W. B. Schweizer, J. Heier, *ACS Nano* **2013**, *7*, 5506–5513.
- [6] S. Liu, W. M. Wang, A. L. Briseno, S. C. B. Mannsfeld, Z. Bao, *Advanced Materials* **2009**, *21*, 1217–1232.
- [7] H. Minemawari, T. Yamada, H. Matsui, J. Tsutsumi, S. Haas, R. Chiba, R. Kumai, T. Hasegawa, *Nature* **2011**, *475*, 364–367.
- [8] T. Schmaltz, G. Sforazzini, T. Reichert, H. Frauenrath, *Advanced Materials* **2017**, *29*, 1605286.
- [9] A. Kumar, H. A. Biebuyck, N. L. Abbott, G. M. Whitesides, *Journal of the American Chemical Society* **1992**, *114*, 9188–9189.
- [10] A. Kumar, G. M. Whitesides, *Applied Physics Letters* **1993**, *63*, 2002–2004.

Bibliography

- [11] J. L. Wilbur, A. Kumar, E. Kim, G. M. Whitesides, *Advanced Materials* **1994**, *6*, 600–604.
- [12] S. Casalini, C. A. Bortolotti, F. Leonardi, F. Biscarini, *Chemical Society Reviews* **2017**, *46*, 40–71.
- [13] A. Perl, D. N. Reinhoudt, J. Huskens, *Advanced Materials* **2009**, *21*, 2257–2268.
- [14] N. B. Larsen, H. Biebuyck, E. Delamarche, B. Michel, *Journal of the American Chemical Society* **1997**, *119*, 3017–3026.
- [15] E. Delamarche, H. Schmid, B. Michel, H. Biebuyck, *Advanced Materials* **1997**, *9*, 741–746.
- [16] E. Delamarche, H. Schmid, A. Bietsch, N. B. Larsen, H. Rothuizen, B. Michel, H. Biebuyck, *The Journal of Physical Chemistry B* **1998**, *102*, 3324–3334.
- [17] A. Kumar, N. L. Abbott, H. A. Biebuyck, E. Kim, G. M. Whitesides, *Accounts of Chemical Research* **1995**, *28*, 219–226.
- [18] Y. Xia, G. M. Whitesides, *Annual Review of Materials Science* **1998**, *28*, 153–184.
- [19] J. C. Love, L. A. Estroff, J. K. Kriebel, R. G. Nuzzo, G. M. Whitesides, *Chemical Reviews* **2005**, *105*, 1103–1170.
- [20] C. D. Bain, G. M. Whitesides, *Journal of the American Chemical Society* **1989**, *111*, 7164–7175.
- [21] T. R. Lee, R. I. Carey, H. A. Biebuyck, G. M. Whitesides, *Langmuir* **1994**, *10*, 741–749.
- [22] A. L. Briseno, J. Aizenberg, Y.-J. Han, R. A. Penkala, H. Moon, A. J. Lovinger, C. Kloc, Z. Bao, *Journal of the American Chemical Society* **2005**, *127*, 12164–12165.
- [23] J. Aizenberg, A. J. Black, G. M. Whitesides, *Nature* **1999**, *398*, 495–498.
- [24] J. Aizenberg, A. J. Black, G. M. Whitesides, *Journal of the American Chemical Society* **1999**, *121*, 4500–4509.
- [25] M. Volmer, *Kinetik der phasenbildung*, T. Steinkopff, Leipzig, **1939**.
- [26] J. W. Mullin in *Crystallization (Fourth Edition)*, Butterworth-Heinemann, Oxford, **2001**, pp. 181–215.
- [27] J. W. Mullin in *Crystallization (Fourth Edition)*, Butterworth-Heinemann, Oxford, **2001**, pp. 86–134.

- [28] S. Jiang, J. H. ter Horst, *Crystal Growth & Design* **2011**, *11*, 256–261.
- [29] J. W. Mullin in *Ullmann's Encyclopedia of Industrial Chemistry*, Wiley-VCH Verlag GmbH & Co. KGaA, **2000**.
- [30] D. Kashchiev in *Nucleation: Basic Theory with Applications*, Butterworth-Heinemann, Oxford, **2000**, pp. 373–390.
- [31] N. Candoni, Z. Hammadi, R. Grossier, M. Ildefonso, S. Zhang, R. Morin, S. Veessler in *Advances in Organic Crystal Chemistry*, Springer, Tokyo, **2015**, pp. 95–113.
- [32] D. Erdemir, A. Y. Lee, A. S. Myerson, *Accounts of Chemical Research* **2009**, *42*, 621–629.
- [33] D. Gebauer, H. Cölfen, *Nano Today* **2011**, *6*, 564–584.
- [34] R. J. Davey, S. L. M. Schroeder, J. H. ter Horst, *Angewandte Chemie International Edition* **2013**, *52*, 2166–2179.
- [35] S. Lee, H. S. Wi, W. Jo, Y. C. Cho, H. H. Lee, S.-Y. Jeong, Y.-I. Kim, G. W. Lee, *Proceedings of the National Academy of Sciences* **2016**, *113*, 13618–13623.
- [36] D. Bonn, N. Shahidzadeh, *Proceedings of the National Academy of Sciences* **2016**, *113*, 13551–13553.
- [37] Y. Wang, D. Maspoch, S. Zou, G. C. Schatz, R. E. Smalley, C. A. Mirkin, *Proceedings of the National Academy of Sciences of the United States of America* **2006**, *103*, 2026–2031.
- [38] J. Heier, J. Groenewold, S. Huber, F. Nüesch, R. Hany, *Langmuir* **2008**, *24*, 7316–7322.
- [39] R. D. Deegan, O. Bakajin, T. F. Dupont, G. Huber, S. R. Nagel, T. A. Witten, *Nature* **1997**, *389*, 827–829.
- [40] T.-S. Wong, A. P.-H. Huang, C.-M. Ho, *Langmuir* **2009**, *25*, 6599–6603.
- [41] A. Einstein, *Investigations on the Theory of the Brownian Movement*, **1956**.
- [42] H. M. Gorr, J. M. Zueger, J. A. Barnard, *The Journal of Physical Chemistry B* **2012**, *116*, 12213–12220.
- [43] J. Desarnaud, H. Derluyn, J. Carmeliet, D. Bonn, N. Shahidzadeh, *The Journal of Physical Chemistry Letters* **2014**, *5*, 890–895.
- [44] H. Hu, R. G. Larson, *Langmuir* **2005**, *21*, 3963–3971.

Bibliography

- [45] N. Shahidzadeh, M. F. L. Schut, J. Desarnaud, M. Prat, D. Bonn, *Scientific Reports* **2015**, 5, 10335.
- [46] A. S. Sangani, C. Lu, K. Su, J. A. Schwarz, *Physical Review E* **2009**, 80, 011603.
- [47] B. M. Weon, J. H. Je, *Physical Review E* **2010**, 82, 015305.

5 Structure and optical properties of cyanine thin film single crystals

5.1 Introduction and aims

Although held together by weak van der Waals forces, the anisotropic structure of many planar organic π -conjugated molecules largely determines the physical properties of the solid by the orientation of its composing molecules. In particular the characteristics of semiconductor molecular solids are strongly related to the intermolecular overlap of the frontier orbitals. Charge transport,^[1,2] exciton diffusion,^[3,4] absorption,^[5] charge transfer or energy level alignment^[6] are typical orientation-dependent attributes. These properties are essential to the performances of optoelectronic devices based on OSCs such as OLEDs,^[7] OFETs^[8,9] and OPV devices.^[10–12]

An approach to optimize OSC devices' performances is to control the molecular orientation in the active layers together with smart device design. The fabrication of crystalline films provides long range order and defined molecular orientation. Due to technological limitations in the fabrication processes of organic crystalline films from semiconducting small molecules, the field of organic optoelectronics has for a long time mainly focused on the use of amorphous layers.^[13] To be relevant in most device applications, crystalline active layers should be (i) thin (typically smaller than ~ 100 nm due to the short diffusion length of charges and excitons), (ii) free from defects (mechanical and chemical) and (iii) free from grain boundaries which are detrimental to transport properties. The choice of materials and fabrication methods has therefore been mostly limited to that enabling to meet these requirements. There are however

Chapter 5. Structure and optical properties of cyanine thin film single crystals

only few systematic investigations correlating the molecular packing of thin crystalline organic semiconductors to their corresponding optical and electronic properties.^[14,15] An exception is the field of OFETs where single crystal and device fabrication methods^[16] have now been optimized with performances competing with their inorganic amorphous counterparts.^[17] In this context it is interesting to explore the morphology-properties relationship of thin single crystals of OSC materials.

Due to the very intense first optical absorption transition in cyanine chromophores, exciton couplings may dominate the optical properties of the solid.^[18] While this phenomenon has been extensively studied in J- and H-aggregates,^[19,20] spectroscopic investigations of bulk single crystals have been rather limited so far.^[21,22]

Aims In this chapter, the crystal structure and the anisotropic absorption properties of the CyC rhomb-shaped single crystal presented in chapter 4 are investigated. The crystal was grown by solvent-vapor annealing of a dewetted film of the dye solution directly on a solid substrate. The structure of the thin crystal was elucidated by X-ray crystal structure analysis. The orientation-dependent optical properties were measured by optical spectroscopy on individual crystals.

5.2 Results and discussion

5.2.1 Crystal morphology and structure

Single crystals of CyC were grown by solvent vapor annealing of dye droplets on glass substrates. For this study, only crystals showing a characteristic rhombic shape were investigated: destabilized crystals and the dendritic growth form were excluded. Rhomb-shape crystals grown by this method typically exhibit an aspect ratio which can exceed three orders of magnitude. Figure 5.1 (a) shows an atomic force microscopy image of a typical CyC single crystal grown on glass. A few droplets of cyanine dye surrounding the crystal are also visible. The crystal shows a characteristic rhombic shape, with in this case the longest diagonal measuring about 2.7 μm . Profile analysis (Figure 5.1 (b)) of the crystal reveals a thickness of 50-60 nm. The

origin of this particular morphology can be understood from the crystal growth mechanisms described in chapter 3.

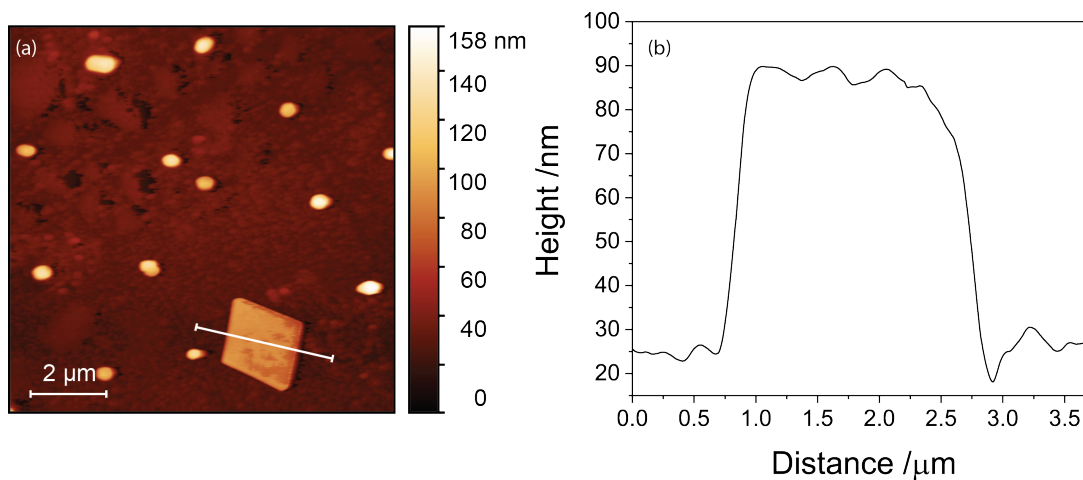


Figure 5.1 – (a) AFM topographic image of a CyC platelet single crystal surrounded by amorphous dye droplets. (b) Profile analysis of the crystal reveals a typical thickness of 50-60 nm.

Due to their reduced size and fragility, single crystal X-ray analysis could not be directly performed on platelet crystals. The crystal structure determination was therefore performed on a bulk crystal grown by vapor diffusion (see section 5.4). The correspondence between the structures is discussed in the next section. Single crystal analysis reveals that the dye crystallizes as a monoclinic crystal in the space group $P2_1/c$. The unit cell contains two asymmetric units consisting of two cations Cy^{3+} and two perchlorate anions ClO_4^- with molecular formula $[(\text{C}_{27}\text{H}_{33}\text{N}_2)\text{ClO}_4]$, shown in Figure 5.2 (a). Cations in the asymmetric units lay in planes forming 83.9° with respect to each other.

The packing of the crystal structure along the c-axis is shown in Figure 5.2 (b). Cyanine cations pack in a layered arrangement, with three different layers in the unit cell indicated by numbers 1, 2 and 3. Layers 1 and 3 are equivalent by symmetry (2-fold screw axis).

In layer 2, chromophores arrange in a rather closely packed herringbone fashion (Figure 5.2 (c)), with a stacking angle of $74.4(6)^\circ$. The shortest distance between molecular planes is 4.162 \AA which is quite close to the van der Waals distance of carbon. The distances between the central carbon atoms of the polymethine chain of parallel neighbors are 5.551 \AA and 11.422 \AA , respectively.

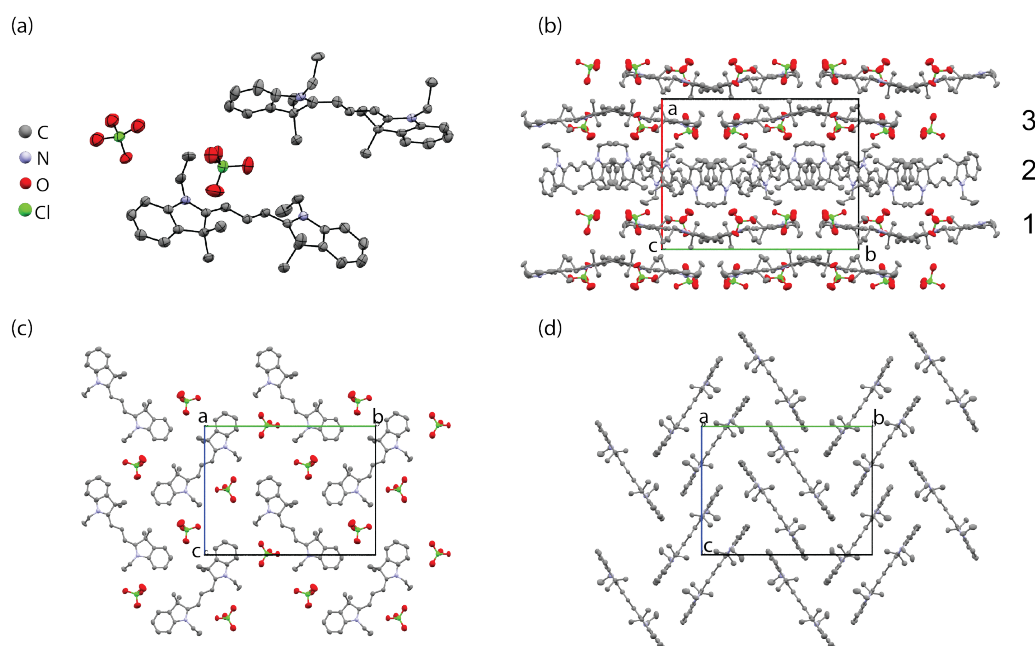


Figure 5.2 – (a) Asymmetric unit of the CyC crystal structure and (b) crystal packing viewed along the *c*-axis. The interlayer arrangement of (c) layers 1 (and 3, by symmetry) and (d) layer 2 reveals the herringbone structure between chromophores. Hydrogen atoms are omitted for clarity.

In layer 1 and 3 the molecular planes of the chromophores have a slight tilt angle of 6.31° with respect to the (100) plane (Figure 5.2 (b)). There, the chromophores also arrange in a herringbone fashion, however the shortest intermolecular distance is considerably larger than in layer 2 with 15.652 \AA . Interestingly, interlayer distances are rather short in the crystal structure: the shortest center to center distance between cations in layer 1 and 2 is 6.719 \AA , while it is 7.242 \AA for cations in layer 3 and the consecutive layer 1. Accordingly, excitonic couplings are expected to comprise intralayer and interlayer components. In other words, excitons may not only diffuse inside a particular layer but also across layers. The short intermolecular distances in the crystal suggest that electronic couplings might also be important. However, transfer integrals calculation would be necessary to confirm this hypothesis.

5.2.2 Out-of-plane orientation of the thin film crystal

Based on the single crystal analysis, the structural form of the crystal was calculated according to the Bravais-Friedel Donnay-Harker (BFDH) method (cf. chapter 3, section 3.1).^[23] The equilibrium faces, their multiplicity and relative area are summarized in Table 5.1 and the full structure is shown in the supporting information, section 5.5. However, as discussed in chapter 3, platelet crystals do not represent the equilibrium morphology but rather one of the growth forms of the phase. Based on the knowledge of the crystal growth conditions and the relative importance of each faces calculated by the BFDH model (Table 5.1), it is assumed the platelet crystals are predominantly bound by the faces {100}, {011} and {0-11}.

Table 5.1 – Calculated equilibrium BFDH morphology of CyC crystals

BFDH Faces	Multiplicity	Relative area /%
{100}	2	13.3
{011}	4	11.0
{110}	4	4.9
{020}	2	2.6
{-111}	4	1.1

Comparison of the BFDH-derived morphology with that of thin platelet crystals in Figure 5.3 (a) and (b) points towards a preference for crystals to grow with the {h00} planes parallel to the substrate. The angles formed between the edges of the crystals were measured from optical microscopy images to be $73.5 \pm 1.7^\circ$ and $106.1 \pm 1.1^\circ$ and agree well with the angles formed by the {011} and {0-11} faces predicted by the BFDH model of 73.8° and 106.2° , respectively. The BFDH model also reveals that the c-axis is oriented along the short diagonal axis of the crystal, while the b-axis is oriented along the long diagonal axis.

X-ray diffraction measurements in θ - 2θ further supports the nature of the platelet crystals as well as their out-of-plane orientation. In Figure 5.4 the diffraction pattern measured on hundreds of platelet crystals is compared to that calculated from the single crystal structure, assuming the (h00) planes to be parallel to the substrate surface.^[24] The measured diffractogram shows three main reflexes at $2\theta = 5.96^\circ$, $2\theta = 16.6^\circ$ and $2\theta = 22.2^\circ$, which can be attributed to d_{100} , d_{300} and d_{400} respectively, based on the simulated pattern. Although the d_{200} reflex does

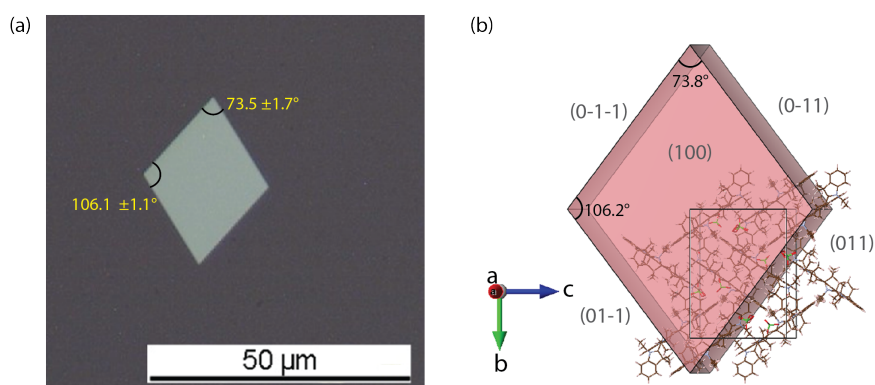


Figure 5.3 – Comparison between (a) the experimental crystal morphology observed by optical microscopy (reflection mode) and (b) the BFDH-derived morphology. The angles formed by the side faces of the crystal correspond well with those predicted by the BFDH model, suggesting the crystals align with the {h00} faces parallel to the substrate.

not correspond to a systematic extinction for this point group, its relative intensity is predicted to be low compared to the other reflexes of the {100} family. It therefore appears to be absent from both experimental and calculated diffractograms. The experimental diffractogram shows an additional reflex of small intensity at $\theta = 14.21^\circ$ which could be attributed to d_{022} according to the simulated powder pattern (assuming no preferential orientation). The occurrence of this peak with such low relative intensity may be attributed to the presence of mis-oriented platelet crystals on the sample.

The BFDH model and the crystal diffraction study strongly suggest that the single crystal structure is the same than that of the platelet crystals. In addition, these results further point toward a preferential out-of-plane orientation of the crystals, with the {h00} faces parallel to the substrate, which is consistent with a layer-by-layer growth mechanism (cf. chapter 3).

5.2.3 Optical transmission of CyC platelet crystals

The low thickness of the platelet crystals (50-100 nm) enables directly measuring their transmission spectra using a micro-spectrophotometer. Figure 5.5 compares the absorption spectra of the dye solution in chloroform, that of the amorphous thin film and of a single crystal.

The absorption spectrum of the dye in solution exhibits two absorption peaks at 18000 cm^{-1} and 19100 cm^{-1} corresponding to the 0-0 absorption and the 0-1 vibronic transition of the isolated chromophore, respectively.^[25] The amorphous thin film also shows two bands, red-

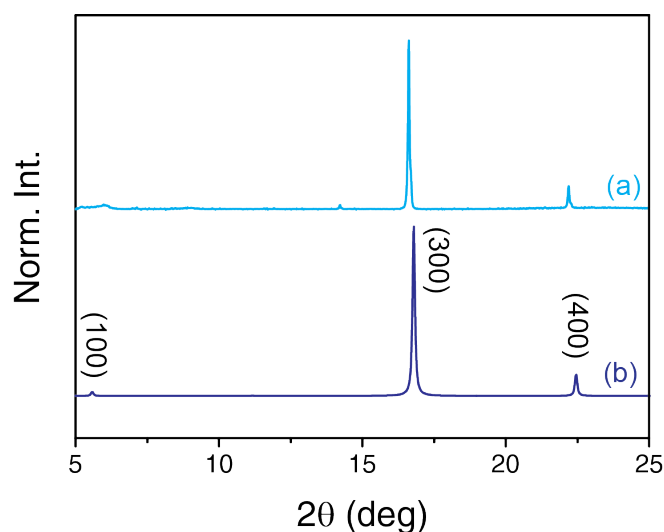


Figure 5.4 – Comparison of θ - 2θ diffractogram of (a) platelet crystals with (b) that simulated from the single crystal analysis supports the similarity between the structure and the preferred orientation of the crystals.

shifted compared to the solution spectrum, at 17280 cm^{-1} and 18790 cm^{-1} generally attributed to the monomer and dimer absorptions, respectively. The faint shoulder around 20300 cm^{-1} is attributed to H-aggregates forming in the film. In comparison, the single crystal exhibits a larger absorption bandwidth which can be decomposed into 4 peaks at about 16700 cm^{-1} , 17200 cm^{-1} , 18000 cm^{-1} and 19100 cm^{-1} . The peak at 15500 cm^{-1} did not appear consistently in every crystals and is attributed to thin film interference induced by the interfaces at the crystal's surfaces. This artefact is difficult to avoid, however it is reasonable to neglect it in the strongly absorbing region of the spectrum, i.e. $16000\text{--}22000\text{ cm}^{-1}$. Measurement of excitation spectra in Figure S5.2 confirmed the presence of peaks corresponding to the 19100 cm^{-1} and 17200 cm^{-1} bands, with however a larger bandwidth at high energies. This could be explained by the fact that excitation spectra were measured on a large number of small crystals and the resulting spectra are therefore an average of the slightly different contributions from different crystals.

At this stage it is difficult to determine which effects are responsible for the broadening of the crystal absorbance spectrum. Vibronic and excitonic coupling, as well as site effects and Stark effects, can influence the spectral envelope substantially. An attempt to fit the crystal

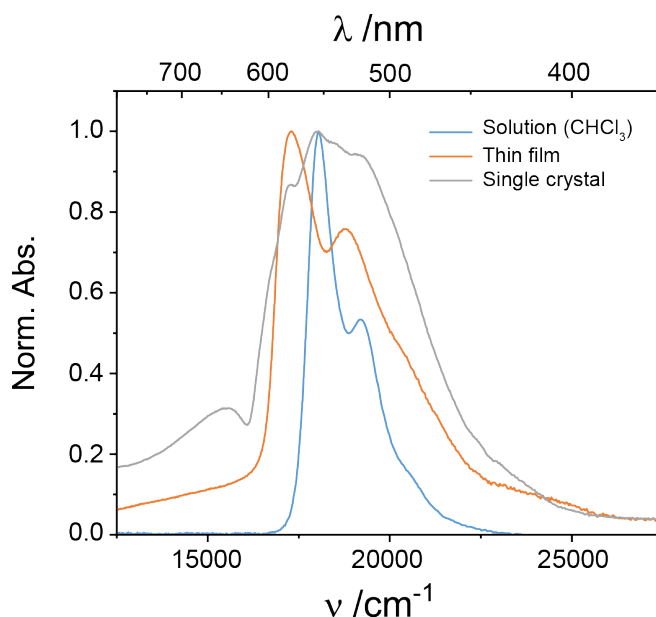


Figure 5.5 – Comparison between the absorbance spectra of CyC in chloroform solution, in the form of an amorphous thin film and platelet crystal.

spectrum assuming only vibronic contributions (see Figure S5.3), however, did not provide a satisfactory match to the observed spectrum. It therefore appears that excitonic effects are crucial to interpret the spectrum.

To get an estimation of the exciton coupling strength in the layered crystal structure, the transition dipole moment of the chromophore was calculated according to

$$|\mu|^2 = \frac{f}{4.702 \cdot 10^{-7} \bar{\nu}_{\max}} \quad (5.1)$$

where μ is the transition dipole moment in Debye, $\bar{\nu}_{\max}$ is the maximum absorption wavenumber, f is the oscillator strength measured in chloroform solution and $4.702 \cdot 10^{-7} \text{ D}^{-2} \text{ cm}$ is a collection of physical constants. This yields a transition dipole moment of $\mu = 10.9 \text{ D}$ for the Cy3^+ cation which can be used to calculate the exciton coupling energy J_D of selected chromophore pairs according to the extended dipole model presented in section 1.2.2.^[26] Using the relationship between the charge and the transition dipole moment $Q = \frac{\mu}{L}$ in Equation 1.2, the coupling energy can be expressed as

$$J_D = \frac{1}{4\pi\epsilon\epsilon_0} \left(\frac{\mu}{L}\right)^2 \left(\frac{1}{R_1} + \frac{1}{R_2} - \frac{1}{R_3} - \frac{1}{R_4}\right) \quad (5.2)$$

where $R_i (i = 1...4)$ are the intermolecular distances between the dipoles in a pair of molecules, L is the dipole length taken to be $9.5 \text{ \AA}^{[27-29]}$ and $\epsilon_0 = 8.85 \cdot 10^{-12} \text{ Fm}^{-1}$ is the vacuum permittivity. The relative permittivity of the dye was taken to be $\epsilon=4$ according to ellipsometry measurement presented in chapter 2 (Figure 2.3) and similar trimethine dyes.^[30,31]

The absolute values of coupling energies were calculated between pairs of chromophores in individual layers (*intralayer coupling*) and between consecutive layers (*interlayer coupling*). The full set of coupling energies is given in Table S5.1. In layer 2, couplings of 263 cm^{-1} and 219 cm^{-1} were obtained for parallel cations, while the strongest coupling between cations in a chevron arrangement is 128 cm^{-1} . Intralayer coupling energies in layers 1 and 3 were significantly lower with 12 cm^{-1} .

On the other hand, strong interlayer couplings between layers 1 and 2 (or 2 and 3) are found with 172 cm^{-1} and 107 cm^{-1} . The strongest interlayer coupling between layer 3 and the layer 1' of the consecutive unit cell is found to be 138 cm^{-1} .

Altogether the exciton coupling energies are important and excitonic contribution to the absorption spectrum of the crystal is expected. Moreover, given that the orientations of cations in layers 1 and 3 are similar to those of layer 2, only two excitonic bands polarized perpendicularly to each other are expected.

Analysis of the polarization dependence of the crystals' absorbance further strengthens this hypothesis. Figure 5.6(a) shows absorption spectra taken at various polarization angles with respect to the b-axis of a thin CyC crystal. A clear band structure is visible from the spectra. The intensity of the absorption band at 16700 cm^{-1} is maximum when light is polarized along the b-axis ($\theta = 0^\circ$) of the crystal while the 19100 cm^{-1} band is not visible. When polarized along the c-axis ($\theta = 90^\circ$), the 16700 cm^{-1} band vanishes. In between these two orientations the spectral features can be interpreted in terms of sinusoidally varying components of each components. Defining spectrum S_0 as the one obtained with polarization parallel to c ($\theta = 0^\circ$) and S_{90} the spectrum obtained with a polarization parallel to b ($\theta = 90^\circ$) the spectra reasonably

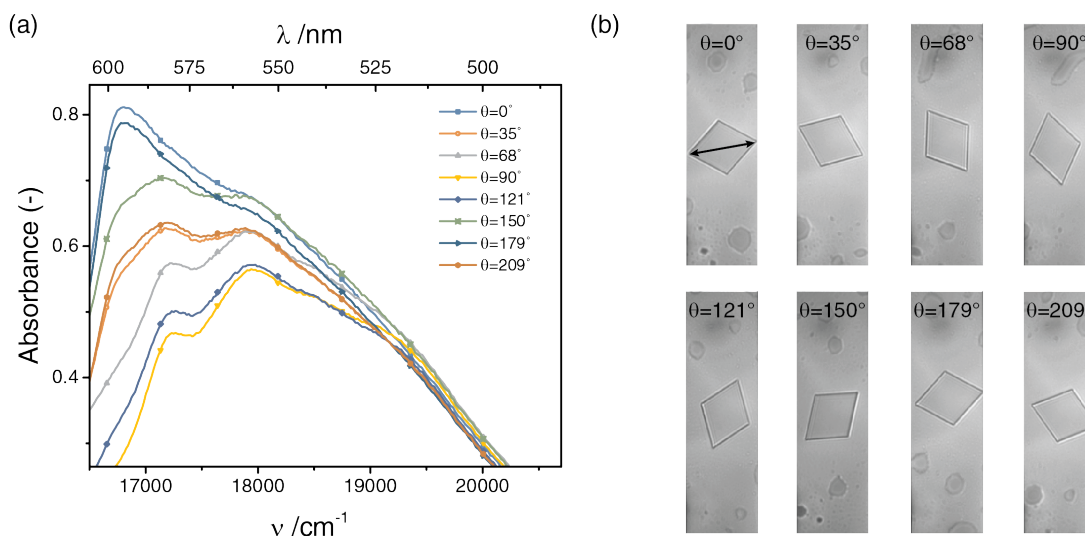


Figure 5.6 – (a) Under linearly polarized light, the absorbance of the crystal varies as a function of the crystal orientation. (b) Relative position of the crystal and light polarization direction (double arrow) at all angles presented in (a).

follow the relationship $S_{\theta} = S_0 \cos^2 \theta + S_{90} \sin^2 \theta$, which correspond to the expected variations of the electric-field intensity.

It has to be underlined that reflection and interference features complicate the interpretation of the transmission spectra. As visible from the crystal spectrum in Figure 5.5 an important interference feature is found, which could modulate the spectral features also at higher energies, with the effect possibly being largest for the spectra taken at angles of 0° and 180° . Moreover, reflection is important and can reach up to 38% for strong resonances (see Figure S5.8). This results in an increase and slight broadening of the spectral features of strong absorption bands with respect to weaker ones. The importance of this reflection seemed to vary from samples to samples, probably due to variations in the crystals thickness (see Figure S5.7). Unfortunately, the exact contribution of the reflection at different orientations could not be directly measured due to the small size of the crystals. Although a clear polarization dependence with two main axis along b and c reveals the excitonic nature of certain spectral features, many bands cannot be completely extinguished at 90° polarization. It can therefore be concluded that a combination of excitonic and vibronic coupling may be necessary to account for the spectral features.

5.3 Conclusion

The crystal structure of CyC was determined by single crystal X-ray analysis and revealed that the chromophores pack in a layered arrangement. The structure determined on bulk crystals from solution was demonstrated to correspond to that of the platelet crystals by comparison of morphology features and X-ray diffraction patterns. The excitonic couplings resulting from the crystal structure were estimated using the extended dipole model and based on the molecular packing. Due to the herringbone arrangement of the chromophores, significant intralayer coupling energies were found with components along the b and c axis of the crystals. Significant interlayer coupling energies were also found which could potentially improve exciton and charge transport between the crystal layers. The polarized absorbance spectra of the crystal were measured and confirmed the importance of the excitonic contribution to the crystal absorption. In particular, the intensity variations of the main absorption bands corresponded with orientations along the main axis of the crystal, where the coupling is the strongest.

While the approach used here gives good qualitative arguments to link the crystal structure and the absorption properties, it does unfortunately not allow describing all spectral features. The presence of experimental artifacts, difficult to avoid with the current equipment, complicates the full interpretation of the spectra. It is believed that first principle calculations taking vibronic coupling into account could be used to further enhance the experimental interpretation and unravel the key properties of CyC platelet crystals.

5.4 Experimental details

CyC single crystals growth

The dye 1-ethyl-2-[3-(1-ethyl-1,3-dihydro-3,3-dimethyl-2H-indol-2-ylidene)-1-propen-1-yl]-3,3-dimethyl-3H-indolium perchlorate (CyC) was synthesized in our laboratory. Platelet crystals were fabricated from a saturated solution of the dye (2.47 mM) in isopropyl alcohol solution (anhydrous, 99.5%, Sigma-Aldrich). CyC droplets were obtained by spin casting the dye saturated solution on glass substrates. 0.3 mL of dye solution was first filtered and distributed on the substrates, followed by a slow rotation at 200 rpm for 3 s. The rotational speed was then increased to 1000 rpm at a rate of 3000 rpm s⁻¹ and the samples were spun for 60 s. Subsequently, droplet films were annealed in chlorobenzene vapor overnight in a closed chamber (Sigma-Aldrich) at room temperature.

X-ray diffraction

The dimensions of platelet crystals made it impossible to directly measure single crystal X-ray diffraction (SC-XRD) with a conventional instrument. Therefore, single crystal X-ray analysis was performed on large single crystals grown by vapor diffusion method. A concentrated solution of the dye in chlorobenzene (44.3 mM) was filtered and exposed to isopropyl alcohol vapor in a closed vial. Rhomb-shaped single crystals of few millimeters in size grew after about 4 weeks.

A red block-like shaped crystal of CyC was mounted on a Stoe Mark II-Imaging Plate Diffractometer System (Stoe & Cie, 2015) equipped with a graphite-monochromator. Data collection was performed at -100 °C using Mo-K α radiation ($\lambda = 0.71073 \text{ \AA}$). 180 exposures (2 minutes per exposure) were obtained at an image plate distance of 135 mm, $\phi = 0^\circ$ and $0^\circ < \omega < 180^\circ$ with the crystal oscillating through 1° in ω . The resolution was $D_{\min} - D_{\max} 24.0-0.84 \text{ \AA}$.

The structure was solved by direct methods using the program SHELXS^[32] and refined by full matrix least squares on F^[33] with SHELXL.^[32] The hydrogen atoms were included in calculated positions and treated as riding atoms using SHELXL-97 default parameters. All non-hydrogen atoms were refined anisotropically.

Crystallographic details are given in the supplementary data file. The drawings carried out with PLATON.

X-ray diffraction (XRD) patterns of platelet samples were obtained from samples containing a large number of platelet crystals, as a $\theta - 2\theta$ scan in reflection mode on a PANalytical X'Pert PRO instrument equipped with a germanium monochromator selecting Cu-K α 1 radiation, $\lambda = 1.5406 \text{ \AA}$. The scattered intensities were recorded using a position-sensitive 1D detector (PANalytical X'Celerator). The detected count rate stayed in the linearity range of the detector. Diffraction patterns were recorded between 3° and 40° .

Spectroscopic measurement on platelet crystals

The transmission spectra of platelet crystals were acquired using a self-built micro-spectrophotometer. For the absorption measurements, a halogen light source was focused on the crystal sample using a condenser lens and the transmitted light was collected through an Olympus IX-81 microscope connected to an Andor Shamrock 301i spectrometer equipped with an iDUS DV420A camera. When needed, the light was polarized using a polarizing filter placed between the light source and the condenser lens.

For photoluminescence measurement a green laser (529 nm) was coupled to a single mode optical fiber focused on the crystal sample. For collection of emitted light a 532 nm band pass filter was inserted at the spectrometer's entrance slit.

Fluorescence spectroscopy (Horiba Jobin Yvon Fluorolog) was used to obtain the excitation spectra of a large number of platelet crystals. The measured spectra were corrected to take into account the excitation intensity.

5.5 Supporting Information

BFDH morphology prediction

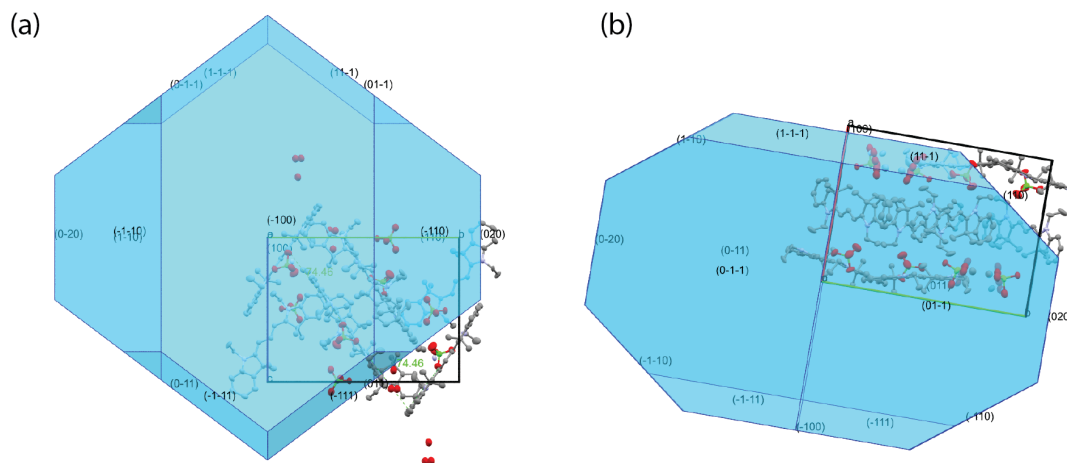


Figure S5.1 – Crystal equilibrium morphology using the BFDH model implemented in the Mercury 3.8 software. (a) View along the [100] direction (b) view along the [001] direction. While the BFDH morphology gives the equilibrium form of the crystal, the final growth form depends on growth conditions. In the present case, growth conditions give rise to crystals composed mainly of {100}, {011} and {0-11} faces.

Photoluminescence and excitation spectra

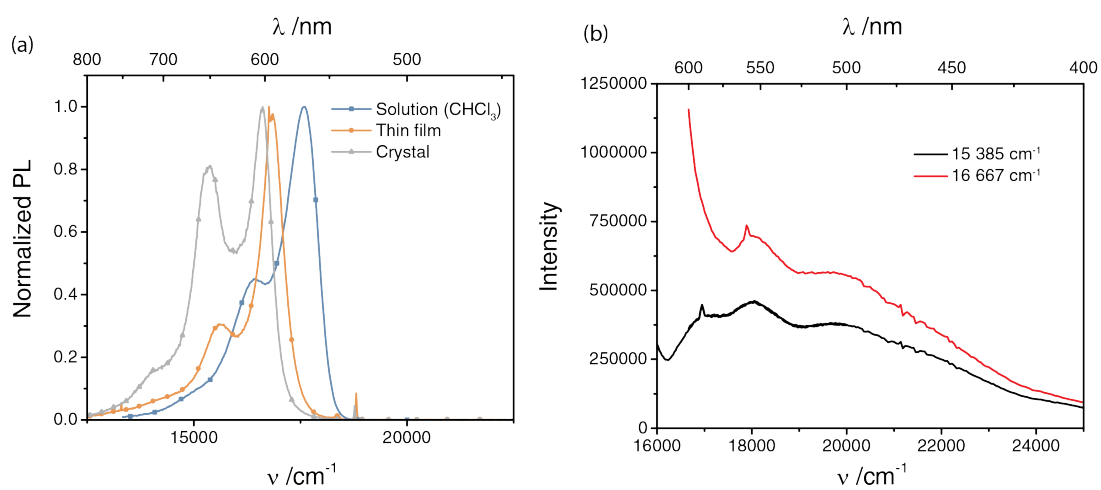


Figure S5.2 – (a) Compared emission of CyC solution, thin film and single crystal. (b) Excitation scan of a collection of single crystals grown on a substrate for emission at $16\,667\text{ cm}^{-1}$ and $15\,385\text{ cm}^{-1}$.

Calculated absorption spectra neglecting excitonic couplings¹

In Figure S5.3, the main components of the experimentally observed absorption (b-polarized in dotted red and c-polarized in dotted blue) are compared to spectra calculated with the CAM-B3LYP density functional.^[34] The spectra were calculated neglecting exciton couplings and therefore represent the transitions from the isolated monomers, taking into account the difference in energy of each monomer at different positions in the crystal (*site effect*) and the influence of the local electric fields in the crystal structure on the absorption energies of cations (*Stark effect*). The bandwidths of the monomer transition is determined by the reorganization energy.

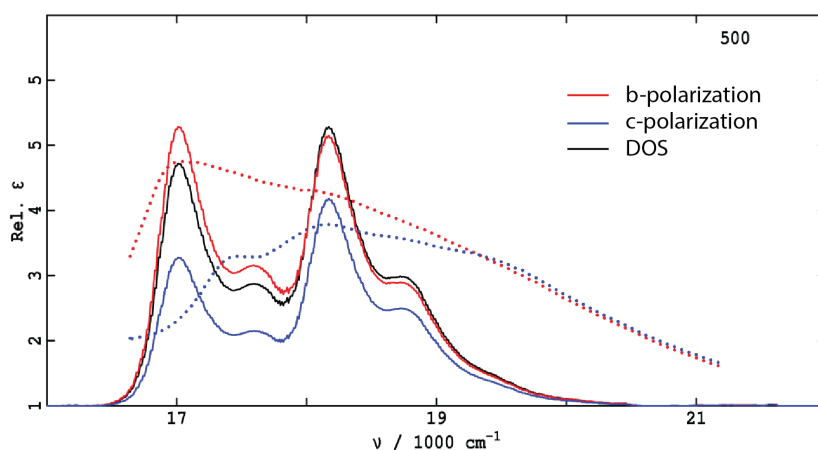


Figure S5.3 – Comparison of spectra calculated ignoring all exciton couplings with the observed crystal polarized spectral components.

The calculated spectra confirm the preference for the c-polarized absorption at lower wavenumbers. Moreover, the bandwidth of the spectra are comparable between experiment and calculations. However, the calculated bands have too much structure and the intensity variations between b- and c-polarization is not well reproduced.

¹These calculations were performed by M. Li and J.R. Reimers, ICQMS, University of Shanghai

Exciton coupling energies

The strongest excitonic couplings calculated from the extended dipole model (Equation 5.2) are summarized in Table S5.1.

Table S5.1 – Strongest excitonic couplings between pairs of chromophores calculated from the extended dipole model

$R_1 / \text{\AA}$	$R_2 / \text{\AA}$	$R_3 / \text{\AA}$	$R_4 / \text{\AA}$	J_D / cm^{-1}	Identifier
5.784	5.784	12.799	9.209	263.2	J_1
11.361	11.361	3.849	20.617	-218.9	J_2
8.046	14.902	7.312	17.265	-5.4	J_3
5.923	16.107	11.417	15.13	127.8	J_4
10.59	10.59	7.91	18.47	13.7	J_5
7.242	7.242	14.849	7.99	138.4	J_6
6.024	17.334	14	12.571	120.3	J_7
8.419	17.666	17.576	9.556	22.9	J_8
15.652	15.652	23.501	10.82	-11.9	J_9
7.056	6.822	8.866	14.021	172.4	J_{10}
6.252	15.23	13.249	11.69	106.9	J_{11}

The various exciton coupling energies J_1 to J_{11} are identified with the help of the crystal structure projection in Figure S5.4.

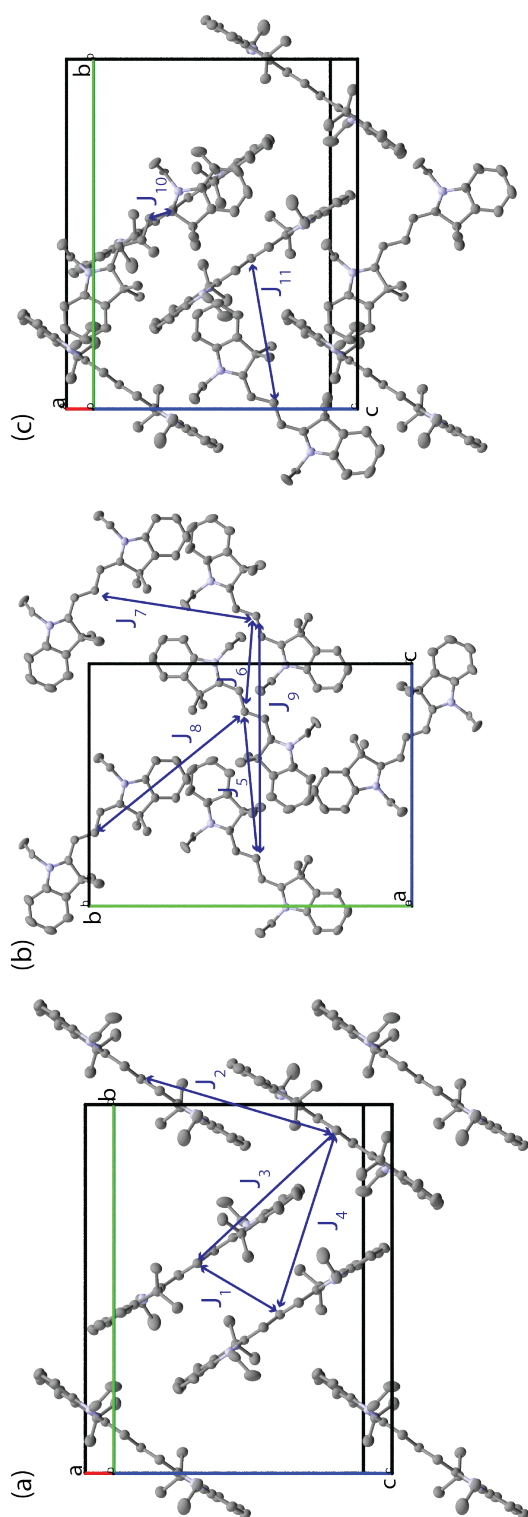


Figure S5.4 – Identification of exciton coupling terms J_1 to J_{11} viewed at different projections. (a) Intralayer couplings in layer 2 (b) Interlayer (J_5 to J_8) and intralayer (J_9) couplings between layers 3 and 3' (c) interlayer couplings between layers 1 and 2.

Single crystal spectroscopic measurements

Spectroscopic measurements on single crystals were performed on a self-built instrument, composed of a halogen light source, a rotating sample stage and a conventional microscope coupled to a spectrometer. The setup is sketched in Figure S5.5 A linear polarizer could be inserted between the light source and the condenser lens focusing light on the sample. Using the optical microscope equipped with a 60x objective, individual crystals were selected and illuminated with a focused light beam. The transmitted signal was collected through a slit at the entrance of the spectrometer, in the form of a spatially resolved transmission map: the slit is decomposed in 255 lines along its largest dimension, a spectrum being measured for each of these lines. The directly transmitted signal was converted to absorption using the following relation

$$\text{Abs} = -\log\left(\frac{I_{\text{sample}}}{I_0}\right) + \log\left(\frac{I_{\text{substrate}}}{I_0}\right) \quad (\text{S5.1})$$

where I_{sample} and $I_{\text{substrate}}$ are the transmitted intensity of the sample and the substrate, respectively. I_0 is the intensity of the illumination beam (with or without polarizing filter depending on the experiment) measured in the same conditions as the sample.

An example of the raw data is presented in Figure S5.6. The spatially resolved absorbance spectra of the same crystal are given for c- and b-polarization. The images correspond to the position of the crystal between the slit, as seen by the spectrometer. To achieve good spectral resolution, the slit opening was set to 3 nm.

As visible from Figure S5.6, the spatially resolved spectra present some artefacts, mostly at the edges of the crystals where diffraction occurs, resulting in absorbance extending to the infrared. In order to get representative spectra of the crystal absorbance, spectra were averaged over 15-20 lines in the center of the crystal where absorbance is homogeneous.

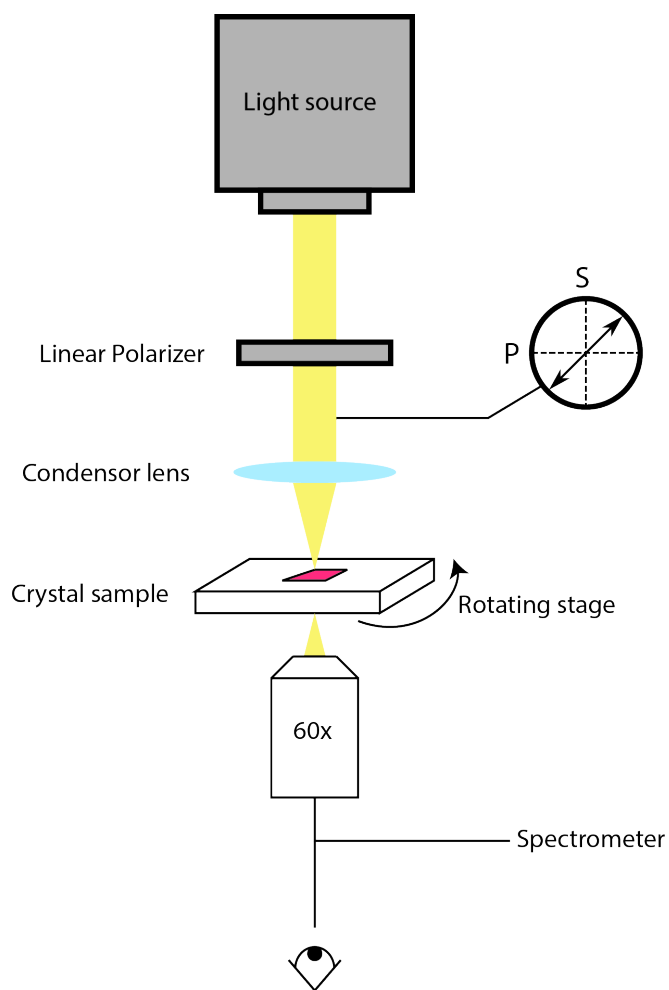


Figure S5.5 – Sketch of the micro-spectrometer setup

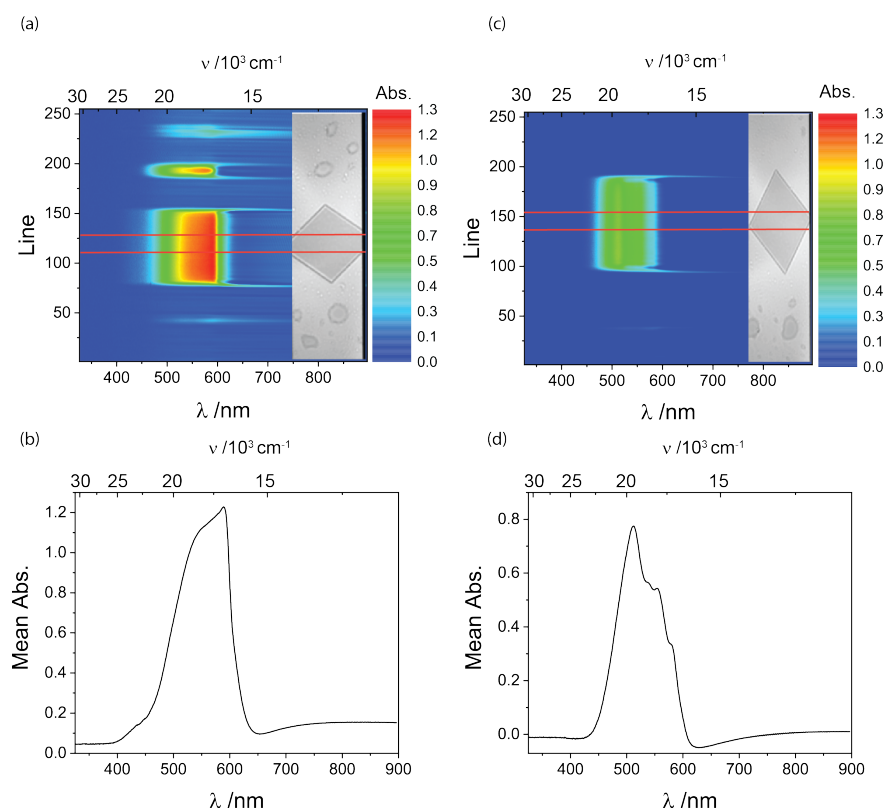


Figure S5.6 – Spatially resolved absorption spectra of a (a) b-polarized and (c) c-polarized CyC crystal. The area between the red lines was used to average the absorption spectra of each polarization. The resulting mean absorbance spectra visible in (b) and (d) for b-polarization and c-polarization, respectively.

Additional polarized transmission spectra of CyC platelet crystals

Transmission microscopy of rhombic CyC crystal platelets did not show identical spectral shapes. As mentioned in section 5.2.3, reflectance and interference severely affect the transmission signal and depend strongly on crystal thickness. In the measurement presented in Figure S5.7 (a) and (b) it is apparent that the intensity of the absorption band at 16700 cm^{-1} is maximum when light is polarized along the b-axis of the crystal while the 19100 cm^{-1} band is not visible. When polarized along the c-axis, the 16700 cm^{-1} band vanishes, while the 19100 cm^{-1} becomes maximum. At polarization angles between c- and b-polarization, the intensity of the 16700 cm^{-1} decreases to the benefit of the 19100 cm^{-1} band which increases correspondingly. However, in this case, contrary to that presented in Figure 5.6, the dependency of the absorption intensity with the electric-field orientation is not well represented, probably due to the effect of reflection on the spectral features.

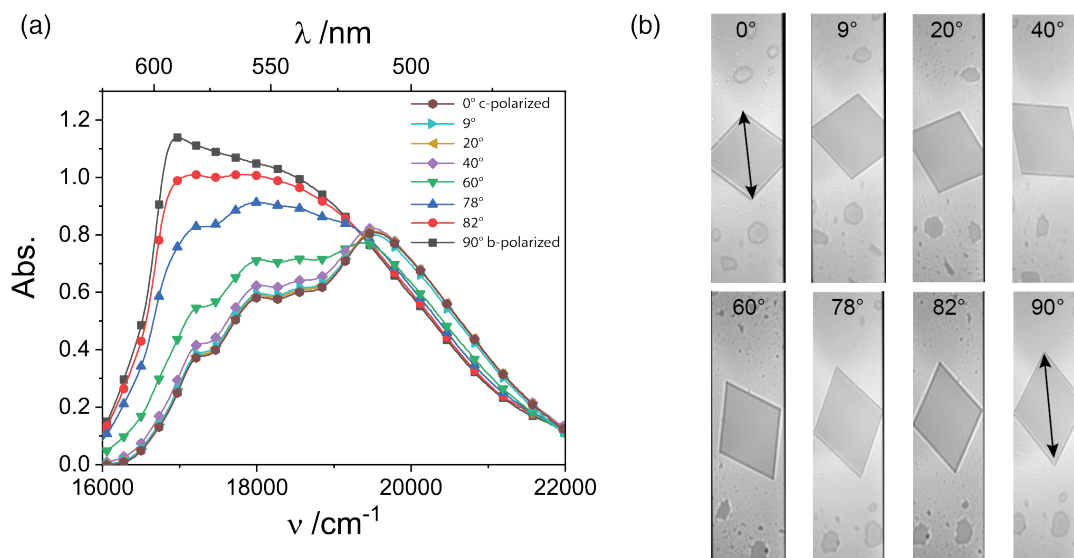


Figure S5.7 – (a) Transmission spectra of CyC single crystals under linearly polarized light, the absorbance of the crystal varies as a function of the crystal orientation (b) Relative position of the crystal and light polarization direction (double arrows) at all angles presented in (a).

Reflection from CyC thin films

The reflection resulting from a CyC amorphous thin film of about 50 nm was evaluated by comparing the absorbance of the film as measured in a UV-vis spectrometer to that measured in an integrating sphere. While the UV-vis measurement gives the transmission of the film ($T = 1 - A - R$), the integrating sphere measurement give the “true” absorption of the film.^[35] The two spectra are compared in Figure S5.8 below. At the main resonances, a difference of 28-38% is found and attributed to reflection from the film surface.

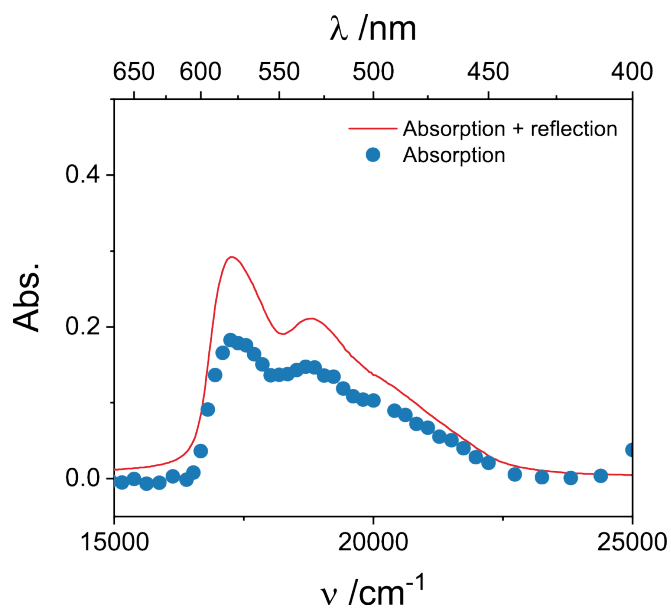


Figure S5.8 – Compared spectra of a 50 nm CyC film measured with a UV-vis spectrometer (red line) and in an integrating sphere (blue dots).

Table 1. Crystal data table for Batch-3.

Identification code	Batch-3
Crystal shape	block
Crystal colour	red
Crystal size	0.500 x 0.450 x 0.400 mm
Empirical formula	C ₂₇ H ₃₃ Cl N ₂ O ₄
Formula weight	485.00
Crystal system	Monoclinic
Space group	P2(1)/c
Unit cell dimensions	a = 15.9071(6) Å alpha = 90 deg. b = 20.7468(6) Å beta = 95.797(3) deg. c = 15.6519(6) Å gamma = 90 deg.
Volume	5139.0(3) Å ³
Cell refinement parameters	
Reflections	54601
Angle range	1.62 < theta < 29.54
Z	8
Density (calculated)	1.254 g/cm ³
Radiation used	MoK α
Wavelength	0.71073 Å
Linear absorption coefficient	0.183 mm ⁻¹
Temperature	173(2) K

Table 2. Data Collection Details for Batch-3.

Diffractometer	STOE IPDS 2
Scan method	rotation method
Number of Reflections measured	45791
Number of Independent reflections	9033
Number of observed reflections	7552
Criterion for recognizing	$I > 2\sigma(I)$
R(int) =	0.1641
Theta range for data collection	1.618 to 25.000 deg.
Index ranges	$-18 \leq h \leq 18$, $-24 \leq k \leq 24$, $-18 \leq l \leq 18$
F(000)	2064
H-locating and refining Method	constr
Number of reflections used	9033
Number of L.S. restraints	0
Number of refined Parameters	651
Goodness-of-fit on F^2	1.067
$S = \{[\text{SUM } w(F_o^2 - F_c^2)^2] / (n-p)^{1/2}\}$, n= number of reflections, p= Parameters used. $w = 1 / [\sigma^2(F_o^2) + (0.1337P)^2 + 2.1603P]$ where $P = (F_o^2 + 2F_c^2) / 3$	
Maximum delta/sigma	0.000
Maximum e-density	1.174 e.A ⁻³
Minimum e-density	-0.962 e.A ⁻³

Table 3. Computer Programs used for Batch-3.

Data collection program	STOE X-AREA
Cell refinement program	STOE X-AREA
Data reduction program	STOE X-RED
Structure Solving Program	?
Structure Refinement Program	SHELXL-2014/7 (Sheldrick, 2014)
Pictures drawn with	?
Tables made with	?
Extinction coefficient	0.0029(8)

Table 4. Atomic coordinates ($\times 10^4$) and equivalent isotropic displacement parameters ($\text{\AA}^2 \times 10^3$) for Batch-3. $U(\text{eq})$ is defined as one third of the trace of the orthogonalized U_{ij} tensor.

	x	y	z	$U(\text{eq})$
C (1)	996 (2)	3248 (1)	-228 (2)	30 (1)
C (2)	937 (2)	2930 (1)	-1006 (2)	40 (1)
C (3)	703 (2)	2284 (2)	-991 (2)	47 (1)
C (4)	541 (2)	1982 (1)	-243 (2)	45 (1)
C (5)	605 (2)	2313 (1)	533 (2)	38 (1)
C (6)	838 (2)	2954 (1)	530 (2)	31 (1)
C (7)	972 (2)	3433 (1)	1260 (2)	28 (1)
C (8)	1213 (1)	4039 (1)	785 (2)	28 (1)
C (9)	1375 (2)	4653 (1)	1116 (2)	30 (1)
C (10)	1378 (2)	4820 (1)	1973 (2)	31 (1)
C (11)	1501 (2)	5450 (1)	2269 (2)	36 (1)
C (12)	1498 (2)	5637 (1)	3121 (2)	37 (1)
C (13)	1389 (2)	5222 (1)	3907 (2)	31 (1)
C (14)	1474 (2)	5715 (1)	4618 (2)	34 (1)
C (15)	1462 (2)	5648 (2)	5492 (2)	41 (1)
C (16)	1548 (2)	6199 (2)	6001 (2)	50 (1)
C (17)	1640 (2)	6799 (2)	5639 (2)	55 (1)
C (18)	1661 (2)	6869 (2)	4764 (2)	57 (1)
C (19)	1579 (2)	6317 (1)	4274 (2)	44 (1)
C (20)	1439 (2)	4349 (1)	-720 (2)	33 (1)
C (21)	666 (2)	4703 (2)	-1110 (2)	49 (1)
C (22)	1702 (2)	3206 (1)	1915 (2)	38 (1)
C (23)	144 (2)	3524 (1)	1681 (2)	36 (1)
C (24)	2060 (2)	4695 (2)	4074 (2)	50 (1)
C (25)	496 (2)	4928 (1)	3845 (2)	42 (1)
C (26)	1843 (5)	6776 (3)	2857 (4)	31 (1)
C (27)	969 (5)	7023 (3)	2421 (5)	54 (2)
C (26A)	1374 (7)	6863 (4)	2748 (5)	48 (2)
C (27A)	2240 (5)	7103 (4)	2674 (5)	63 (2)
C (28)	4436 (2)	2950 (1)	3970 (2)	34 (1)
C (29)	4125 (2)	2566 (1)	3294 (2)	45 (1)
C (30)	4704 (2)	2302 (2)	2789 (2)	55 (1)
C (31)	5563 (2)	2417 (2)	2967 (2)	61 (1)
C (32)	5868 (2)	2803 (2)	3653 (2)	52 (1)
C (33)	5292 (2)	3076 (1)	4154 (2)	37 (1)
C (34)	5427 (2)	3494 (1)	4946 (2)	35 (1)
C (35)	4518 (2)	3608 (1)	5151 (2)	30 (1)
C (36)	4223 (2)	3958 (1)	5814 (2)	33 (1)
C (37)	4703 (2)	4302 (1)	6453 (2)	33 (1)
C (38)	4336 (2)	4628 (1)	7088 (2)	33 (1)
C (39)	4756 (2)	4967 (1)	7776 (2)	29 (1)
C (40)	5708 (2)	5069 (1)	7991 (2)	31 (1)
C (41)	5733 (2)	5431 (1)	8829 (2)	31 (1)
C (42)	6395 (2)	5644 (1)	9392 (2)	39 (1)
C (43)	6224 (2)	5981 (1)	10122 (2)	42 (1)
C (44)	5398 (2)	6114 (1)	10278 (2)	42 (1)
C (45)	4716 (2)	5901 (1)	9719 (2)	37 (1)
C (46)	4905 (2)	5556 (1)	9011 (2)	31 (1)
C (47)	3093 (2)	3173 (1)	4647 (2)	42 (1)
C (48)	2953 (2)	2650 (2)	5287 (3)	63 (1)
C (49)	5890 (2)	4120 (2)	4757 (2)	49 (1)
C (50)	5920 (2)	3113 (2)	5673 (2)	48 (1)
C (51)	6049 (2)	5512 (2)	7309 (2)	43 (1)
C (52)	6212 (2)	4438 (1)	8093 (2)	40 (1)
C (53)	3424 (2)	5331 (2)	8359 (2)	42 (1)
C (54)	3106 (2)	5900 (2)	7843 (2)	70 (1)
N (1)	1238 (1)	3898 (1)	-48 (1)	29 (1)
N (2)	1752 (4)	6221 (5)	3414 (7)	31 (2)
N (2A)	1440 (5)	6283 (5)	3345 (7)	35 (2)
N (3)	3993 (1)	3278 (1)	4577 (1)	33 (1)
N (4)	4349 (1)	5266 (1)	8366 (1)	31 (1)
O (1)	1975 (2)	3921 (1)	6057 (2)	70 (1)
O (2)	2482 (2)	3609 (2)	7445 (2)	95 (1)
O (3)	1932 (2)	4626 (1)	7194 (2)	65 (1)
O (4)	1040 (2)	3739 (1)	7091 (2)	64 (1)
O (5)	2469 (1)	5727 (1)	10068 (1)	49 (1)
O (6)	2140 (5)	6677 (4)	9301 (6)	72 (1)
O (7)	2406 (4)	6695 (3)	10842 (4)	72 (1)

O(8)	1196(4)	6202(3)	10224(4)	72(1)
O(6A)	1892(5)	6584(4)	9194(6)	72(1)
O(7A)	2784(4)	6758(3)	10499(4)	72(1)
O(8A)	1413(4)	6458(3)	10477(4)	72(1)
Cl(1)	1858(1)	3968(1)	6936(1)	42(1)
Cl(2)	2128(1)	6363(1)	10072(1)	46(1)

Table 5. Bond lengths [Å] and angles [deg] for Batch-3.

C(1)-C(6)	1.378(4)
C(1)-C(2)	1.379(4)
C(1)-N(1)	1.423(3)
C(2)-C(3)	1.392(4)
C(2)-H(2A)	0.9500
C(3)-C(4)	1.374(4)
C(3)-H(3A)	0.9500
C(4)-C(5)	1.390(4)
C(4)-H(4A)	0.9500
C(5)-C(6)	1.381(4)
C(5)-H(5A)	0.9500
C(6)-C(7)	1.512(3)
C(7)-C(8)	1.529(3)
C(7)-C(23)	1.543(3)
C(7)-C(22)	1.543(3)
C(8)-N(1)	1.340(3)
C(8)-C(9)	1.390(3)
C(9)-C(10)	1.386(3)
C(9)-H(9A)	0.9500
C(10)-C(11)	1.392(4)
C(10)-H(10A)	0.9500
C(11)-C(12)	1.389(4)
C(11)-H(11A)	0.9500
C(12)-N(2)	1.343(11)
C(12)-N(2A)	1.390(11)
C(12)-C(13)	1.527(3)
C(13)-C(14)	1.508(3)
C(13)-C(24)	1.532(4)
C(13)-C(25)	1.540(3)
C(14)-C(15)	1.377(4)
C(14)-C(19)	1.378(4)
C(15)-C(16)	1.391(4)
C(15)-H(15A)	0.9500
C(16)-C(17)	1.381(5)
C(16)-H(16A)	0.9500
C(17)-C(18)	1.381(5)
C(17)-H(17A)	0.9500
C(18)-C(19)	1.378(4)
C(18)-H(18A)	0.9500
C(19)-N(2)	1.414(11)
C(19)-N(2A)	1.449(12)
C(20)-N(1)	1.465(3)
C(20)-C(21)	1.508(4)
C(20)-H(20A)	0.9900
C(20)-H(20B)	0.9900
C(21)-H(21C)	0.9800
C(21)-H(21B)	0.9800
C(21)-H(21A)	0.9800
C(22)-H(22A)	0.9800
C(22)-H(22B)	0.9800
C(22)-H(22C)	0.9800
C(23)-H(23A)	0.9800
C(23)-H(23B)	0.9800
C(23)-H(23C)	0.9800
C(24)-H(24A)	0.9800
C(24)-H(24B)	0.9800
C(24)-H(24C)	0.9800
C(25)-H(25C)	0.9800
C(25)-H(25B)	0.9800
C(25)-H(25A)	0.9800
C(26)-N(2)	1.461(12)
C(26)-C(27)	1.572(10)
C(26)-H(26A)	0.9900
C(26)-H(26B)	0.9900
C(27)-H(27C)	0.9800

C (27) -H (27B)	0.9800
C (27) -H (27A)	0.9800
C (26A) -C (27A)	1.481 (11)
C (26A) -N (2A)	1.520 (14)
C (26A) -H (26C)	0.9900
C (26A) -H (26D)	0.9900
C (27A) -H (27D)	0.9800
C (27A) -H (27E)	0.9800
C (27A) -H (27F)	0.9800
C (28) -C (29)	1.375 (4)
C (28) -C (33)	1.388 (4)
C (28) -N (3)	1.413 (3)
C (29) -C (30)	1.386 (5)
C (29) -H (29A)	0.9500
C (30) -C (31)	1.386 (5)
C (30) -H (30A)	0.9500
C (31) -C (32)	1.386 (5)
C (31) -H (31A)	0.9500
C (32) -C (33)	1.386 (4)
C (32) -H (32A)	0.9500
C (33) -C (34)	1.509 (4)
C (34) -C (35)	1.532 (3)
C (34) -C (50)	1.534 (4)
C (34) -C (49)	1.536 (4)
C (35) -N (3)	1.350 (3)
C (35) -C (36)	1.387 (4)
C (36) -C (37)	1.392 (4)
C (36) -H (36A)	0.9500
C (37) -C (38)	1.380 (4)
C (37) -H (37A)	0.9500
C (38) -C (39)	1.399 (3)
C (38) -H (38A)	0.9500
C (39) -N (4)	1.334 (3)
C (39) -C (40)	1.531 (3)
C (40) -C (41)	1.508 (3)
C (40) -C (52)	1.536 (4)
C (40) -C (51)	1.547 (4)
C (41) -C (42)	1.376 (4)
C (41) -C (46)	1.399 (3)
C (42) -C (43)	1.390 (4)
C (42) -H (42A)	0.9500
C (43) -C (44)	1.389 (4)
C (43) -H (43A)	0.9500
C (44) -C (45)	1.395 (4)
C (44) -H (44A)	0.9500
C (45) -C (46)	1.378 (4)
C (45) -H (45A)	0.9500
C (46) -N (4)	1.408 (3)
C (47) -N (3)	1.464 (3)
C (47) -C (48)	1.508 (5)
C (47) -H (47A)	0.9900
C (47) -H (47B)	0.9900
C (48) -H (48A)	0.9800
C (48) -H (48B)	0.9800
C (48) -H (48C)	0.9800
C (49) -H (49A)	0.9800
C (49) -H (49B)	0.9800
C (49) -H (49C)	0.9800
C (50) -H (50A)	0.9800
C (50) -H (50B)	0.9800
C (50) -H (50C)	0.9800
C (51) -H (51A)	0.9800
C (51) -H (51B)	0.9800
C (51) -H (51C)	0.9800
C (52) -H (52C)	0.9800
C (52) -H (52B)	0.9800
C (52) -H (52A)	0.9800
C (53) -N (4)	1.476 (3)
C (53) -C (54)	1.490 (5)
C (53) -H (53A)	0.9900
C (53) -H (53B)	0.9900
C (54) -H (54A)	0.9800
C (54) -H (54B)	0.9800
C (54) -H (54C)	0.9800
O (1) -C1 (1)	1.411 (2)
O (2) -C1 (1)	1.419 (3)
O (3) -C1 (1)	1.425 (2)
O (4) -C1 (1)	1.428 (2)

O (5) -C1 (2)	1.426 (2)
O (6) -C1 (2)	1.374 (10)
O (7) -C1 (2)	1.419 (6)
O (8) -C1 (2)	1.561 (7)
O (6A) -C1 (2)	1.463 (10)
O (7A) -C1 (2)	1.438 (7)
O (8A) -C1 (2)	1.371 (7)
C (6) -C (1) -C (2)	123.1 (2)
C (6) -C (1) -N (1)	108.5 (2)
C (2) -C (1) -N (1)	128.3 (2)
C (1) -C (2) -C (3)	116.1 (3)
C (1) -C (2) -H (2A)	122.0
C (3) -C (2) -H (2A)	122.0
C (4) -C (3) -C (2)	121.8 (3)
C (4) -C (3) -H (3A)	119.1
C (2) -C (3) -H (3A)	119.1
C (3) -C (4) -C (5)	121.0 (3)
C (3) -C (4) -H (4A)	119.5
C (5) -C (4) -H (4A)	119.5
C (6) -C (5) -C (4)	118.0 (3)
C (6) -C (5) -H (5A)	121.0
C (4) -C (5) -H (5A)	121.0
C (1) -C (6) -C (5)	120.0 (2)
C (1) -C (6) -C (7)	109.6 (2)
C (5) -C (6) -C (7)	130.3 (2)
C (6) -C (7) -C (8)	101.28 (19)
C (6) -C (7) -C (23)	110.0 (2)
C (8) -C (7) -C (23)	111.97 (19)
C (6) -C (7) -C (22)	109.96 (19)
C (8) -C (7) -C (22)	111.4 (2)
C (23) -C (7) -C (22)	111.7 (2)
N (1) -C (8) -C (9)	122.6 (2)
N (1) -C (8) -C (7)	109.1 (2)
C (9) -C (8) -C (7)	128.3 (2)
C (10) -C (9) -C (8)	124.9 (2)
C (10) -C (9) -H (9A)	117.6
C (8) -C (9) -H (9A)	117.6
C (9) -C (10) -C (11)	122.9 (2)
C (9) -C (10) -H (10A)	118.5
C (11) -C (10) -H (10A)	118.5
C (12) -C (11) -C (10)	124.6 (2)
C (12) -C (11) -H (11A)	117.7
C (10) -C (11) -H (11A)	117.7
N (2) -C (12) -C (11)	123.4 (5)
C (11) -C (12) -N (2A)	121.3 (5)
N (2) -C (12) -C (13)	106.8 (5)
C (11) -C (12) -C (13)	128.8 (2)
N (2A) -C (12) -C (13)	108.9 (5)
C (14) -C (13) -C (12)	101.7 (2)
C (14) -C (13) -C (24)	110.4 (2)
C (12) -C (13) -C (24)	113.9 (2)
C (14) -C (13) -C (25)	109.2 (2)
C (12) -C (13) -C (25)	110.6 (2)
C (24) -C (13) -C (25)	110.6 (2)
C (15) -C (14) -C (19)	119.6 (3)
C (15) -C (14) -C (13)	131.0 (2)
C (19) -C (14) -C (13)	109.4 (2)
C (14) -C (15) -C (16)	118.4 (3)
C (14) -C (15) -H (15A)	120.8
C (16) -C (15) -H (15A)	120.8
C (17) -C (16) -C (15)	120.9 (3)
C (17) -C (16) -H (16A)	119.5
C (15) -C (16) -H (16A)	119.5
C (16) -C (17) -C (18)	121.1 (3)
C (16) -C (17) -H (17A)	119.5
C (18) -C (17) -H (17A)	119.5
C (19) -C (18) -C (17)	117.0 (3)
C (19) -C (18) -H (18A)	121.5
C (17) -C (18) -H (18A)	121.5
C (18) -C (19) -C (14)	123.0 (3)
C (18) -C (19) -N (2)	129.1 (5)
C (14) -C (19) -N (2)	106.7 (5)
C (18) -C (19) -N (2A)	126.5 (5)
C (14) -C (19) -N (2A)	109.6 (5)
N (1) -C (20) -C (21)	111.9 (2)
N (1) -C (20) -H (20A)	109.2
C (21) -C (20) -H (20A)	109.2

N (1) -C (20) -H (20B)	109.2
C (21) -C (20) -H (20B)	109.2
H (20A) -C (20) -H (20B)	107.9
C (20) -C (21) -H (21C)	109.5
C (20) -C (21) -H (21B)	109.5
H (21C) -C (21) -H (21B)	109.5
C (20) -C (21) -H (21A)	109.5
H (21C) -C (21) -H (21A)	109.5
H (21B) -C (21) -H (21A)	109.5
C (7) -C (22) -H (22A)	109.5
C (7) -C (22) -H (22B)	109.5
H (22A) -C (22) -H (22B)	109.5
C (7) -C (22) -H (22C)	109.5
H (22A) -C (22) -H (22C)	109.5
H (22B) -C (22) -H (22C)	109.5
C (7) -C (23) -H (23A)	109.5
C (7) -C (23) -H (23B)	109.5
H (23A) -C (23) -H (23B)	109.5
C (7) -C (23) -H (23C)	109.5
H (23A) -C (23) -H (23C)	109.5
H (23B) -C (23) -H (23C)	109.5
C (13) -C (24) -H (24A)	109.5
C (13) -C (24) -H (24B)	109.5
H (24A) -C (24) -H (24B)	109.5
C (13) -C (24) -H (24C)	109.5
H (24A) -C (24) -H (24C)	109.5
H (24B) -C (24) -H (24C)	109.5
C (13) -C (25) -H (25C)	109.5
C (13) -C (25) -H (25B)	109.5
H (25C) -C (25) -H (25B)	109.5
C (13) -C (25) -H (25A)	109.5
H (25C) -C (25) -H (25A)	109.5
H (25B) -C (25) -H (25A)	109.5
N (2) -C (26) -C (27)	112.3 (6)
N (2) -C (26) -H (26A)	109.1
C (27) -C (26) -H (26A)	109.1
N (2) -C (26) -H (26B)	109.1
C (27) -C (26) -H (26B)	109.1
H (26A) -C (26) -H (26B)	107.9
C (26) -C (27) -H (27C)	109.5
C (26) -C (27) -H (27B)	109.5
H (27C) -C (27) -H (27B)	109.5
C (26) -C (27) -H (27A)	109.5
H (27C) -C (27) -H (27A)	109.5
H (27B) -C (27) -H (27A)	109.5
C (27A) -C (26A) -N (2A)	108.0 (9)
C (27A) -C (26A) -H (26C)	110.1
N (2A) -C (26A) -H (26C)	110.1
C (27A) -C (26A) -H (26D)	110.1
N (2A) -C (26A) -H (26D)	110.1
H (26C) -C (26A) -H (26D)	108.4
C (26A) -C (27A) -H (27D)	109.5
C (26A) -C (27A) -H (27E)	109.5
H (27D) -C (27A) -H (27E)	109.5
C (26A) -C (27A) -H (27F)	109.5
H (27D) -C (27A) -H (27F)	109.5
H (27E) -C (27A) -H (27F)	109.5
C (29) -C (28) -C (33)	122.5 (3)
C (29) -C (28) -N (3)	129.2 (3)
C (33) -C (28) -N (3)	108.3 (2)
C (28) -C (29) -C (30)	117.4 (3)
C (28) -C (29) -H (29A)	121.3
C (30) -C (29) -H (29A)	121.3
C (29) -C (30) -C (31)	121.0 (3)
C (29) -C (30) -H (30A)	119.5
C (31) -C (30) -H (30A)	119.5
C (30) -C (31) -C (32)	121.1 (3)
C (30) -C (31) -H (31A)	119.5
C (32) -C (31) -H (31A)	119.5
C (33) -C (32) -C (31)	118.3 (3)
C (33) -C (32) -H (32A)	120.8
C (31) -C (32) -H (32A)	120.8
C (32) -C (33) -C (28)	119.7 (3)
C (32) -C (33) -C (34)	130.6 (3)
C (28) -C (33) -C (34)	109.5 (2)
C (33) -C (34) -C (35)	101.6 (2)
C (33) -C (34) -C (50)	109.5 (2)
C (35) -C (34) -C (50)	110.3 (2)

C (33) -C (34) -C (49)	111.0 (2)
C (35) -C (34) -C (49)	113.0 (2)
C (50) -C (34) -C (49)	111.1 (2)
N (3) -C (35) -C (36)	122.1 (2)
N (3) -C (35) -C (34)	108.4 (2)
C (36) -C (35) -C (34)	129.5 (2)
C (35) -C (36) -C (37)	127.1 (2)
C (35) -C (36) -H (36A)	116.5
C (37) -C (36) -H (36A)	116.5
C (38) -C (37) -C (36)	121.8 (2)
C (38) -C (37) -H (37A)	119.1
C (36) -C (37) -H (37A)	119.1
C (37) -C (38) -C (39)	126.6 (2)
C (37) -C (38) -H (38A)	116.7
C (39) -C (38) -H (38A)	116.7
N (4) -C (39) -C (38)	122.6 (2)
N (4) -C (39) -C (40)	108.8 (2)
C (38) -C (39) -C (40)	128.6 (2)
C (41) -C (40) -C (39)	101.47 (18)
C (41) -C (40) -C (52)	111.5 (2)
C (39) -C (40) -C (52)	113.5 (2)
C (41) -C (40) -C (51)	109.0 (2)
C (39) -C (40) -C (51)	109.8 (2)
C (52) -C (40) -C (51)	111.2 (2)
C (42) -C (41) -C (46)	119.0 (2)
C (42) -C (41) -C (40)	131.9 (2)
C (46) -C (41) -C (40)	109.1 (2)
C (41) -C (42) -C (43)	119.2 (3)
C (41) -C (42) -H (42A)	120.4
C (43) -C (42) -H (42A)	120.4
C (44) -C (43) -C (42)	120.7 (3)
C (44) -C (43) -H (43A)	119.6
C (42) -C (43) -H (43A)	119.6
C (43) -C (44) -C (45)	121.1 (3)
C (43) -C (44) -H (44A)	119.4
C (45) -C (44) -H (44A)	119.4
C (46) -C (45) -C (44)	116.7 (2)
C (46) -C (45) -H (45A)	121.6
C (44) -C (45) -H (45A)	121.6
C (45) -C (46) -C (41)	123.2 (2)
C (45) -C (46) -N (4)	128.7 (2)
C (41) -C (46) -N (4)	108.1 (2)
N (3) -C (47) -C (48)	111.5 (2)
N (3) -C (47) -H (47A)	109.3
C (48) -C (47) -H (47A)	109.3
N (3) -C (47) -H (47B)	109.3
C (48) -C (47) -H (47B)	109.3
H (47A) -C (47) -H (47B)	108.0
C (47) -C (48) -H (48A)	109.5
C (47) -C (48) -H (48B)	109.5
H (48A) -C (48) -H (48B)	109.5
C (47) -C (48) -H (48C)	109.5
H (48A) -C (48) -H (48C)	109.5
H (48B) -C (48) -H (48C)	109.5
C (34) -C (49) -H (49A)	109.5
C (34) -C (49) -H (49B)	109.5
H (49A) -C (49) -H (49B)	109.5
C (34) -C (49) -H (49C)	109.5
H (49A) -C (49) -H (49C)	109.5
H (49B) -C (49) -H (49C)	109.5
C (34) -C (50) -H (50A)	109.5
C (34) -C (50) -H (50B)	109.5
H (50A) -C (50) -H (50B)	109.5
C (34) -C (50) -H (50C)	109.5
H (50A) -C (50) -H (50C)	109.5
H (50B) -C (50) -H (50C)	109.5
C (40) -C (51) -H (51A)	109.5
C (40) -C (51) -H (51B)	109.5
H (51A) -C (51) -H (51B)	109.5
C (40) -C (51) -H (51C)	109.5
H (51A) -C (51) -H (51C)	109.5
H (51B) -C (51) -H (51C)	109.5
C (40) -C (52) -H (52C)	109.5
C (40) -C (52) -H (52B)	109.5
H (52C) -C (52) -H (52B)	109.5
C (40) -C (52) -H (52A)	109.5
H (52C) -C (52) -H (52A)	109.5
H (52B) -C (52) -H (52A)	109.5

N (4) -C (53) -C (54)	111.1 (3)
N (4) -C (53) -H (53A)	109.4
C (54) -C (53) -H (53A)	109.4
N (4) -C (53) -H (53B)	109.4
C (54) -C (53) -H (53B)	109.4
H (53A) -C (53) -H (53B)	108.0
C (53) -C (54) -H (54A)	109.5
C (53) -C (54) -H (54B)	109.5
H (54A) -C (54) -H (54B)	109.5
C (53) -C (54) -H (54C)	109.5
H (54A) -C (54) -H (54C)	109.5
H (54B) -C (54) -H (54C)	109.5
C (8) -N (1) -C (1)	111.4 (2)
C (8) -N (1) -C (20)	126.1 (2)
C (1) -N (1) -C (20)	122.5 (2)
C (12) -N (2) -C (19)	111.8 (8)
C (12) -N (2) -C (26)	123.5 (8)
C (19) -N (2) -C (26)	119.8 (8)
C (12) -N (2A) -C (19)	107.0 (7)
C (12) -N (2A) -C (26A)	127.6 (9)
C (19) -N (2A) -C (26A)	124.8 (8)
C (35) -N (3) -C (28)	112.0 (2)
C (35) -N (3) -C (47)	124.7 (2)
C (28) -N (3) -C (47)	122.5 (2)
C (39) -N (4) -C (46)	112.4 (2)
C (39) -N (4) -C (53)	126.2 (2)
C (46) -N (4) -C (53)	121.3 (2)
O (1) -Cl (1) -O (2)	111.0 (2)
O (1) -Cl (1) -O (3)	109.11 (16)
O (2) -Cl (1) -O (3)	108.1 (2)
O (1) -Cl (1) -O (4)	110.74 (16)
O (2) -Cl (1) -O (4)	109.20 (19)
O (3) -Cl (1) -O (4)	108.66 (16)
O (6) -Cl (2) -O (7)	119.0 (4)
O (8A) -Cl (2) -O (5)	118.0 (3)
O (6) -Cl (2) -O (5)	113.3 (4)
O (7) -Cl (2) -O (5)	111.6 (2)
O (8A) -Cl (2) -O (7A)	107.5 (4)
O (5) -Cl (2) -O (7A)	105.7 (3)
O (8A) -Cl (2) -O (6A)	104.0 (4)
O (5) -Cl (2) -O (6A)	110.3 (3)
O (7A) -Cl (2) -O (6A)	111.3 (4)
O (6) -Cl (2) -O (8)	109.4 (4)
O (7) -Cl (2) -O (8)	101.2 (4)
O (5) -Cl (2) -O (8)	99.9 (2)

Symmetry transformations used to generate equivalent atoms:

Table 6. Torsion-angles for Batch-3.

C (6) -C (1) -C (2) -C (3)	0.2 (4)
N (1) -C (1) -C (2) -C (3)	178.4 (2)
C (1) -C (2) -C (3) -C (4)	0.0 (4)
C (2) -C (3) -C (4) -C (5)	0.0 (5)
C (3) -C (4) -C (5) -C (6)	-0.2 (4)
C (2) -C (1) -C (6) -C (5)	-0.4 (4)
N (1) -C (1) -C (6) -C (5)	-178.9 (2)
C (2) -C (1) -C (6) -C (7)	179.1 (2)
N (1) -C (1) -C (6) -C (7)	0.6 (3)
C (4) -C (5) -C (6) -C (1)	0.3 (4)
C (4) -C (5) -C (6) -C (7)	-179.0 (2)
C (1) -C (6) -C (7) -C (8)	0.9 (2)
C (5) -C (6) -C (7) -C (8)	-179.7 (2)
C (1) -C (6) -C (7) -C (23)	119.5 (2)
C (5) -C (6) -C (7) -C (23)	-61.0 (3)
C (1) -C (6) -C (7) -C (22)	-117.0 (2)
C (5) -C (6) -C (7) -C (22)	62.4 (3)
C (6) -C (7) -C (8) -N (1)	-2.2 (2)
C (23) -C (7) -C (8) -N (1)	-119.4 (2)
C (22) -C (7) -C (8) -N (1)	114.7 (2)
C (6) -C (7) -C (8) -C (9)	176.8 (2)
C (23) -C (7) -C (8) -C (9)	59.6 (3)
C (22) -C (7) -C (8) -C (9)	-66.3 (3)
N (1) -C (8) -C (9) -C (10)	-178.4 (2)
C (7) -C (8) -C (9) -C (10)	2.7 (4)

C (8) -C (9) -C (10) -C (11)	-176.6 (2)
C (9) -C (10) -C (11) -C (12)	179.2 (3)
C (10) -C (11) -C (12) -N (2)	168.9 (4)
C (10) -C (11) -C (12) -N (2A)	-165.7 (4)
C (10) -C (11) -C (12) -C (13)	1.7 (5)
N (2) -C (12) -C (13) -C (14)	9.6 (4)
C (11) -C (12) -C (13) -C (14)	178.4 (3)
N (2A) -C (12) -C (13) -C (14)	-13.0 (4)
N (2) -C (12) -C (13) -C (24)	-109.2 (4)
C (11) -C (12) -C (13) -C (24)	59.7 (4)
N (2A) -C (12) -C (13) -C (24)	-131.7 (4)
N (2) -C (12) -C (13) -C (25)	125.5 (4)
C (11) -C (12) -C (13) -C (25)	-65.7 (4)
N (2A) -C (12) -C (13) -C (25)	102.9 (4)
C (12) -C (13) -C (14) -C (15)	-177.8 (3)
C (24) -C (13) -C (14) -C (15)	-56.5 (4)
C (25) -C (13) -C (14) -C (15)	65.3 (3)
C (12) -C (13) -C (14) -C (19)	2.2 (3)
C (24) -C (13) -C (14) -C (19)	123.5 (3)
C (25) -C (13) -C (14) -C (19)	-114.7 (3)
C (19) -C (14) -C (15) -C (16)	0.7 (4)
C (13) -C (14) -C (15) -C (16)	-179.3 (3)
C (14) -C (15) -C (16) -C (17)	0.2 (4)
C (15) -C (16) -C (17) -C (18)	-0.9 (5)
C (16) -C (17) -C (18) -C (19)	0.5 (5)
C (17) -C (18) -C (19) -C (14)	0.4 (5)
C (17) -C (18) -C (19) -N (2)	-165.2 (5)
C (17) -C (18) -C (19) -N (2A)	168.9 (5)
C (15) -C (14) -C (19) -C (18)	-1.0 (5)
C (13) -C (14) -C (19) -C (18)	179.0 (3)
C (15) -C (14) -C (19) -N (2)	167.4 (4)
C (13) -C (14) -C (19) -N (2)	-12.7 (4)
C (15) -C (14) -C (19) -N (2A)	-171.2 (4)
C (13) -C (14) -C (19) -N (2A)	8.8 (4)
C (33) -C (28) -C (29) -C (30)	0.1 (4)
N (3) -C (28) -C (29) -C (30)	179.8 (3)
C (28) -C (29) -C (30) -C (31)	0.5 (5)
C (29) -C (30) -C (31) -C (32)	-0.2 (5)
C (30) -C (31) -C (32) -C (33)	-0.6 (5)
C (31) -C (32) -C (33) -C (28)	1.2 (5)
C (31) -C (32) -C (33) -C (34)	177.9 (3)
C (29) -C (28) -C (33) -C (32)	-1.0 (4)
N (3) -C (28) -C (33) -C (32)	179.3 (3)
C (29) -C (28) -C (33) -C (34)	-178.3 (2)
N (3) -C (28) -C (33) -C (34)	1.9 (3)
C (32) -C (33) -C (34) -C (35)	-179.5 (3)
C (28) -C (33) -C (34) -C (35)	-2.6 (3)
C (32) -C (33) -C (34) -C (50)	-62.9 (4)
C (28) -C (33) -C (34) -C (50)	114.1 (3)
C (32) -C (33) -C (34) -C (49)	60.1 (4)
C (28) -C (33) -C (34) -C (49)	-123.0 (3)
C (33) -C (34) -C (35) -N (3)	2.3 (3)
C (50) -C (34) -C (35) -N (3)	-113.7 (2)
C (49) -C (34) -C (35) -N (3)	121.3 (2)
C (33) -C (34) -C (35) -C (36)	179.9 (3)
C (50) -C (34) -C (35) -C (36)	63.8 (3)
C (49) -C (34) -C (35) -C (36)	-61.1 (3)
N (3) -C (35) -C (36) -C (37)	178.3 (2)
C (34) -C (35) -C (36) -C (37)	1.0 (4)
C (35) -C (36) -C (37) -C (38)	-179.2 (2)
C (36) -C (37) -C (38) -C (39)	177.5 (2)
C (37) -C (38) -C (39) -N (4)	-179.6 (2)
C (37) -C (38) -C (39) -C (40)	0.7 (4)
N (4) -C (39) -C (40) -C (41)	4.0 (2)
C (38) -C (39) -C (40) -C (41)	-176.3 (2)
N (4) -C (39) -C (40) -C (52)	123.7 (2)
C (38) -C (39) -C (40) -C (52)	-56.6 (3)
N (4) -C (39) -C (40) -C (51)	-111.2 (2)
C (38) -C (39) -C (40) -C (51)	68.5 (3)
C (39) -C (40) -C (41) -C (42)	176.4 (3)
C (52) -C (40) -C (41) -C (42)	55.2 (4)
C (51) -C (40) -C (41) -C (42)	-67.9 (4)
C (39) -C (40) -C (41) -C (46)	-4.3 (3)
C (52) -C (40) -C (41) -C (46)	-125.4 (2)
C (51) -C (40) -C (41) -C (46)	111.5 (2)
C (46) -C (41) -C (42) -C (43)	-0.4 (4)
C (40) -C (41) -C (42) -C (43)	178.9 (3)
C (41) -C (42) -C (43) -C (44)	-1.3 (4)

C (42) -C (43) -C (44) -C (45)	1.6 (4)
C (43) -C (44) -C (45) -C (46)	-0.1 (4)
C (44) -C (45) -C (46) -C (41)	-1.6 (4)
C (44) -C (45) -C (46) -N (4)	177.4 (2)
C (42) -C (41) -C (46) -C (45)	1.9 (4)
C (40) -C (41) -C (46) -C (45)	-177.5 (2)
C (42) -C (41) -C (46) -N (4)	-177.3 (2)
C (40) -C (41) -C (46) -N (4)	3.2 (3)
C (9) -C (8) -N (1) -C (1)	-176.3 (2)
C (7) -C (8) -N (1) -C (1)	2.8 (3)
C (9) -C (8) -N (1) -C (20)	0.5 (4)
C (7) -C (8) -N (1) -C (20)	179.6 (2)
C (6) -C (1) -N (1) -C (8)	-2.2 (3)
C (2) -C (1) -N (1) -C (8)	179.4 (2)
C (6) -C (1) -N (1) -C (20)	-179.2 (2)
C (2) -C (1) -N (1) -C (20)	2.4 (4)
C (21) -C (20) -N (1) -C (8)	-87.4 (3)
C (21) -C (20) -N (1) -C (1)	89.2 (3)
C (11) -C (12) -N (2) -C (19)	172.0 (4)
C (13) -C (12) -N (2) -C (19)	-18.4 (5)
C (11) -C (12) -N (2) -C (26)	16.9 (8)
C (13) -C (12) -N (2) -C (26)	-173.5 (6)
C (18) -C (19) -N (2) -C (12)	-172.5 (4)
C (14) -C (19) -N (2) -C (12)	20.0 (6)
C (18) -C (19) -N (2) -C (26)	-16.4 (9)
C (14) -C (19) -N (2) -C (26)	176.2 (6)
C (27) -C (26) -N (2) -C (12)	68.4 (8)
C (27) -C (26) -N (2) -C (19)	-84.9 (8)
C (11) -C (12) -N (2A) -C (19)	-171.8 (3)
C (13) -C (12) -N (2A) -C (19)	18.6 (6)
C (11) -C (12) -N (2A) -C (26A)	-0.1 (10)
C (13) -C (12) -N (2A) -C (26A)	-169.7 (7)
C (18) -C (19) -N (2A) -C (12)	172.9 (4)
C (14) -C (19) -N (2A) -C (12)	-17.3 (6)
C (18) -C (19) -N (2A) -C (26A)	1.0 (10)
C (14) -C (19) -N (2A) -C (26A)	170.7 (7)
C (27A) -C (26A) -N (2A) -C (12)	-92.3 (8)
C (27A) -C (26A) -N (2A) -C (19)	78.0 (9)
C (36) -C (35) -N (3) -C (28)	-179.1 (2)
C (34) -C (35) -N (3) -C (28)	-1.3 (3)
C (36) -C (35) -N (3) -C (47)	-8.9 (4)
C (34) -C (35) -N (3) -C (47)	168.8 (2)
C (29) -C (28) -N (3) -C (35)	179.9 (3)
C (33) -C (28) -N (3) -C (35)	-0.4 (3)
C (29) -C (28) -N (3) -C (47)	9.5 (4)
C (33) -C (28) -N (3) -C (47)	-170.8 (2)
C (48) -C (47) -N (3) -C (35)	-77.7 (3)
C (48) -C (47) -N (3) -C (28)	91.4 (3)
C (38) -C (39) -N (4) -C (46)	178.0 (2)
C (40) -C (39) -N (4) -C (46)	-2.3 (3)
C (38) -C (39) -N (4) -C (53)	-4.9 (4)
C (40) -C (39) -N (4) -C (53)	174.8 (2)
C (45) -C (46) -N (4) -C (39)	-179.7 (3)
C (41) -C (46) -N (4) -C (39)	-0.5 (3)
C (45) -C (46) -N (4) -C (53)	2.9 (4)
C (41) -C (46) -N (4) -C (53)	-177.9 (2)
C (54) -C (53) -N (4) -C (39)	-85.7 (3)
C (54) -C (53) -N (4) -C (46)	91.3 (3)

Table 7. Anisotropic displacement parameters ($\text{\AA}^2 \times 10^3$) for Batch-3. The anisotropic displacement factor exponent takes the form: $-2 \pi^2 [h^2 a^{*2} U_{11} + \dots + 2 h k a^* b^* U_{12}]$

	U11	U22	U33	U23	U13	U12
C (1)	22 (1)	28 (1)	40 (1)	-3 (1)	0 (1)	4 (1)
C (2)	41 (1)	41 (1)	37 (1)	-5 (1)	6 (1)	2 (1)
C (3)	51 (2)	43 (2)	47 (2)	-15 (1)	1 (1)	-2 (1)
C (4)	43 (2)	34 (1)	59 (2)	-6 (1)	3 (1)	-3 (1)
C (5)	34 (1)	32 (1)	47 (2)	0 (1)	5 (1)	0 (1)
C (6)	22 (1)	31 (1)	39 (1)	-1 (1)	1 (1)	3 (1)

C(7)	24(1)	28(1)	34(1)	3(1)	5(1)	2(1)
C(8)	19(1)	31(1)	33(1)	1(1)	4(1)	3(1)
C(9)	25(1)	30(1)	35(1)	1(1)	7(1)	0(1)
C(10)	26(1)	32(1)	36(1)	1(1)	7(1)	-1(1)
C(11)	40(1)	32(1)	36(1)	2(1)	8(1)	-6(1)
C(12)	41(1)	31(1)	40(1)	-3(1)	10(1)	-10(1)
C(13)	27(1)	32(1)	36(1)	0(1)	9(1)	-2(1)
C(14)	24(1)	41(1)	39(1)	-1(1)	6(1)	-2(1)
C(15)	30(1)	54(2)	38(1)	2(1)	4(1)	2(1)
C(16)	37(2)	74(2)	37(1)	-12(1)	3(1)	0(1)
C(17)	50(2)	63(2)	53(2)	-27(2)	13(2)	-19(2)
C(18)	74(2)	46(2)	53(2)	-17(1)	22(2)	-25(2)
C(19)	53(2)	42(2)	40(1)	-8(1)	15(1)	-17(1)
C(20)	31(1)	35(1)	32(1)	1(1)	6(1)	4(1)
C(21)	47(2)	53(2)	48(2)	12(1)	5(1)	16(1)
C(22)	36(1)	36(1)	41(1)	3(1)	-4(1)	4(1)
C(23)	30(1)	38(1)	43(1)	-1(1)	13(1)	-4(1)
C(24)	48(2)	58(2)	45(2)	-1(1)	9(1)	19(1)
C(25)	38(2)	42(2)	48(2)	-6(1)	16(1)	-13(1)
C(26)	38(3)	18(3)	42(3)	1(2)	21(3)	-14(3)
C(27)	54(4)	51(4)	62(4)	32(3)	27(4)	30(3)
C(26A)	52(5)	48(5)	44(4)	-4(3)	9(4)	-14(4)
C(27A)	60(4)	63(5)	63(4)	7(4)	-2(4)	1(4)
C(28)	38(1)	30(1)	34(1)	3(1)	5(1)	7(1)
C(29)	55(2)	37(1)	41(1)	-2(1)	-3(1)	5(1)
C(30)	74(2)	48(2)	42(2)	-11(1)	4(2)	10(2)
C(31)	66(2)	69(2)	50(2)	-13(2)	19(2)	15(2)
C(32)	44(2)	66(2)	49(2)	-8(1)	16(1)	7(2)
C(33)	37(1)	39(1)	36(1)	1(1)	8(1)	4(1)
C(34)	29(1)	41(1)	36(1)	-1(1)	7(1)	2(1)
C(35)	28(1)	30(1)	33(1)	3(1)	4(1)	2(1)
C(36)	26(1)	37(1)	38(1)	-1(1)	7(1)	2(1)
C(37)	29(1)	34(1)	35(1)	1(1)	4(1)	1(1)
C(38)	25(1)	38(1)	38(1)	-2(1)	4(1)	-1(1)
C(39)	24(1)	31(1)	34(1)	1(1)	6(1)	-1(1)
C(40)	21(1)	36(1)	38(1)	0(1)	6(1)	-1(1)
C(41)	23(1)	32(1)	39(1)	3(1)	4(1)	-1(1)
C(42)	28(1)	38(1)	50(2)	-2(1)	2(1)	-5(1)
C(43)	36(1)	40(1)	49(2)	-3(1)	-2(1)	-8(1)
C(44)	43(2)	39(1)	42(1)	-9(1)	4(1)	-4(1)
C(45)	33(1)	38(1)	42(1)	-7(1)	6(1)	-1(1)
C(46)	25(1)	32(1)	35(1)	1(1)	2(1)	-2(1)
C(47)	24(1)	44(2)	56(2)	-15(1)	-2(1)	5(1)
C(48)	41(2)	45(2)	105(3)	-1(2)	22(2)	-9(1)
C(49)	45(2)	55(2)	50(2)	-5(1)	15(1)	-16(1)
C(50)	37(2)	63(2)	43(2)	0(1)	3(1)	15(1)
C(51)	33(1)	50(2)	48(2)	4(1)	11(1)	-8(1)
C(52)	29(1)	44(2)	48(2)	-4(1)	3(1)	8(1)
C(53)	19(1)	66(2)	43(1)	-14(1)	6(1)	2(1)
C(54)	45(2)	101(3)	62(2)	0(2)	0(2)	35(2)
N(1)	24(1)	28(1)	33(1)	0(1)	3(1)	4(1)
N(2)	23(4)	32(3)	36(3)	-1(2)	6(4)	-1(3)
N(2A)	36(5)	27(3)	42(3)	-2(2)	6(4)	-8(4)
N(3)	30(1)	32(1)	36(1)	-3(1)	2(1)	3(1)
N(4)	19(1)	38(1)	35(1)	-4(1)	4(1)	0(1)
O(1)	79(2)	82(2)	54(1)	-10(1)	29(1)	-19(1)
O(2)	76(2)	101(2)	107(2)	33(2)	5(2)	27(2)
O(3)	75(2)	51(1)	67(2)	-11(1)	7(1)	-23(1)
O(4)	50(1)	78(2)	66(2)	-16(1)	24(1)	-33(1)
O(5)	54(1)	33(1)	62(1)	1(1)	18(1)	7(1)
O(6)	85(2)	58(2)	76(2)	-3(1)	17(1)	10(2)
O(7)	85(2)	58(2)	76(2)	-3(1)	17(1)	10(2)
O(8)	85(2)	58(2)	76(2)	-3(1)	17(1)	10(2)
O(6A)	85(2)	58(2)	76(2)	-3(1)	17(1)	10(2)
O(7A)	85(2)	58(2)	76(2)	-3(1)	17(1)	10(2)
O(8A)	85(2)	58(2)	76(2)	-3(1)	17(1)	10(2)
Cl(1)	39(1)	45(1)	43(1)	-1(1)	11(1)	-9(1)
Cl(2)	58(1)	34(1)	46(1)	1(1)	10(1)	12(1)

Table 8. Hydrogen coordinates (x 10⁴) and isotropic

displacement parameters ($\text{Å}^2 \times 10^3$) for Batch-3.

	x	y	z	U (eq)
H (2A)	1050	3140	-1521	48
H (3A)	655	2046	-1511	57
H (4A)	383	1541	-257	54
H (5A)	491	2105	1049	45
H (9A)	1494	4983	724	36
H (10A)	1291	4491	2377	37
H (11A)	1594	5773	1860	43
H (15A)	1396	5236	5742	49
H (16A)	1543	6162	6605	59
H (17A)	1690	7169	5998	66
H (18A)	1729	7280	4511	68
H (20A)	1693	4107	-1175	39
H (20B)	1861	4665	-471	39
H (21C)	820	4979	-1578	59
H (21B)	439	4969	-670	59
H (21A)	238	4391	-1337	59
H (22A)	2231	3207	1644	46
H (22B)	1585	2769	2108	46
H (22C)	1753	3499	2409	46
H (23A)	-13	3116	1938	44
H (23B)	-307	3658	1245	44
H (23C)	226	3855	2129	44
H (24A)	2623	4886	4074	60
H (24B)	1979	4367	3623	60
H (24C)	2007	4495	4634	60
H (25C)	400	4731	4396	50
H (25B)	442	4599	3394	50
H (25A)	76	5267	3705	50
H (26A)	2206	6655	2405	38
H (26B)	2127	7129	3199	38
H (27C)	1046	7442	2149	65
H (27B)	572	7070	2858	65
H (27A)	742	6713	1986	65
H (26C)	1102	6737	2176	57
H (26D)	1029	7204	2984	57
H (27D)	2210	7515	2365	75
H (27E)	2550	6789	2360	75
H (27F)	2534	7166	3250	75
H (29A)	3537	2486	3178	54
H (30A)	4510	2038	2314	66
H (31A)	5948	2230	2614	73
H (32A)	6457	2877	3777	62
H (36A)	3628	3964	5834	40
H (37A)	5300	4313	6451	39
H (38A)	3736	4621	7056	40
H (42A)	6962	5562	9283	46
H (43A)	6678	6121	10520	50
H (44A)	5295	6354	10774	50
H (45A)	4149	5990	9821	45
H (47A)	2809	3052	4078	50
H (47B)	2836	3579	4828	50
H (48A)	3227	2771	5853	75
H (48B)	3196	2245	5103	75
H (48C)	2345	2593	5320	75
H (49A)	5560	4355	4295	59
H (49B)	6448	4015	4580	59
H (49C)	5957	4387	5275	59
H (50A)	6468	2981	5494	57
H (50B)	5597	2729	5803	57
H (50C)	6010	3384	6186	57
H (51A)	5716	5910	7257	52
H (51B)	6005	5289	6754	52
H (51C)	6642	5616	7484	52
H (52C)	6772	4524	8391	48
H (52B)	6272	4255	7525	48
H (52A)	5912	4131	8429	48
H (53A)	3277	5379	8956	51
H (53B)	3147	4936	8114	51
H (54A)	3193	5831	7239	84
H (54B)	3414	6287	8056	84
H (54C)	2502	5958	7895	84

Table 9. Hydrogen-bonds for Batch-3 [A and deg.].

D-H...A	d(D-H)	d(H...A)	d(D...A)	<(DHA)
C(2)-H(2A)...O(4)#1	0.95	2.50	3.438(4)	168.6
C(9)-H(9A)...O(5)#1	0.95	2.48	3.356(3)	152.5
C(11)-H(11A)...O(8A)#1	0.95	2.58	3.491(7)	160.6
C(18)-H(18A)...O(6)#2	0.95	2.29	3.212(9)	162.1
C(20)-H(20B)...O(5)#1	0.99	2.52	3.461(3)	159.1
C(26)-H(26A)...O(7)#1	0.99	2.50	3.369(8)	146.3
C(47)-H(47B)...O(1)	0.99	2.57	3.351(4)	135.6
C(53)-H(53A)...O(5)	0.99	2.38	3.309(3)	156.5
C(53)-H(53B)...O(3)	0.99	2.38	3.198(4)	139.6

Symmetry transformations used to generate equivalent atoms:

#1 $x, y, z-1$ #2 $x, -y+3/2, z-1/2$



Bibliography

- [1] V. Coropceanu, J. Cornil, D. A. da Silva Filho, Y. Olivier, R. Silbey, J.-L. Brédas, *Chemical Reviews* **2007**, *107*, 926–952.
- [2] V. C. Sundar, J. Zaumseil, V. Podzorov, E. Menard, R. L. Willett, T. Someya, M. E. Gershenson, J. A. Rogers, *Science* **2004**, *303*, 1644–1646.
- [3] G. M. Akselrod, P. B. Deotare, N. J. Thompson, J. Lee, W. A. Tisdale, M. A. Baldo, V. M. Menon, V. Bulović, *Nature Communications* **2014**, *5*, 3646.
- [4] P. Irkhin, I. Biaggio, *Physical Review Letters* **2011**, *107*, 017402.
- [5] P. Irkhin, A. Ryasnyanskiy, M. Koehler, I. Biaggio, *Physical Review B* **2012**, *86*, 085143.
- [6] B. P. Rand, D. Cheyns, K. Vasseur, N. C. Giebink, S. Mothy, Y. Yi, V. Coropceanu, D. Beljonne, J. Cornil, J.-L. Brédas, J. Genoe, *Advanced Functional Materials* **2012**, *22*, 2987–2995.
- [7] D. Yokoyama, *Journal of Materials Chemistry* **2011**, *21*, 19187–19202.
- [8] A. R. Murphy, J. M. J. Fréchet, *Chemical Reviews* **2007**, *107*, 1066–1096.
- [9] W. H. Lee, J. Park, S. H. Sim, S. Lim, K. S. Kim, B. H. Hong, K. Cho, *Journal of the American Chemical Society* **2011**, *133*, 4447–4454.
- [10] S. B. Jo, H. H. Kim, H. Lee, B. Kang, S. Lee, M. Sim, M. Kim, W. H. Lee, K. Cho, *ACS Nano* **2015**, *9*, 8206–8219.
- [11] C. Videlot, A. El Kassmi, D. Fichou, *Solar Energy Materials and Solar Cells* **2000**, *63*, 69–82.
- [12] R. J. Tseng, R. Chan, V. C. Tung, Y. Yang, *Advanced Materials* **2008**, *20*, 435–438.
- [13] S. Ahmad, *Journal of Polymer Engineering* **2014**, *34*, 279–338.

Bibliography

- [14] G. Lanzani, *Photophysics of molecular materials: from single molecules to single crystals*, John Wiley & Sons, **2006**.
- [15] M. Brinkmann, G. Gadret, M. Muccini, C. Taliani, N. Masciocchi, A. Sironi, *Journal of the American Chemical Society* **2000**, *122*, 5147–5157.
- [16] Y. Diao, L. Shaw, Z. Bao, S. C. B. Mannsfeld, *Energy & Environmental Science* **2014**, *7*, 2145–2159.
- [17] H. Sirringhaus, *Advanced Materials* **2014**, *26*, 1319–1335.
- [18] N. J. Hestand, F. C. Spano, *Accounts of Chemical Research* **2017**, *50*, 341–350.
- [19] M. Ramanathan, K. Hong, Q. Ji, Y. Yonamine, J. P. Hill, K. Ariga, **2014**, *14*, 1–14.
- [20] M. S. Bradley, J. R. Tischler, V. Bulović, *Advanced Materials* **2005**, *17*, 1881–1886.
- [21] A. P. Marchetti, C. D. Salzberg, E. I. P. Walker, *The Journal of Chemical Physics* **1976**, *64*, 4693–4698.
- [22] H. von Berlepsch, S. Möller, L. Dähne, *The Journal of Physical Chemistry B* **2001**, *105*, 5689–5699.
- [23] J. D. H. Donnay, D. Harker, *Am. Mineral* **1937**, *22*, 446–467.
- [24] W. A. Dollase, *Journal of Applied Crystallography* **1986**, *19*, 267–272.
- [25] S. B. Anantharaman, S. Yakunin, C. Peng, M. V. G. Vismara, C. F. O. Graeff, F. A. Nüesch, S. Jenatsch, R. Hany, M. V. Kovalenko, J. Heier, *The Journal of Physical Chemistry C* **2017**, *121*, 9587–9593.
- [26] V. Czikkely, H. D. Forsterling, H. Kuhn, *Chemical Physics Letters* **1970**, *6*, 207–210.
- [27] K. Saito, K. Ikegami, S. Kuroda, Y. Tabe, M. Sugi, *Journal of Applied Physics* **1992**, *71*, 1401–1406.
- [28] H. Yao, R. Kawabata, H. Ikeda, N. Kitamura, *Physical Chemistry Chemical Physics* **1999**, *1*, 4629–4633.
- [29] A. Gil, D. Möbius, I. Sánchez, A. Suárez, *Langmuir* **2003**, *19*, 6430–6435.
- [30] H. Zhang, B. Niesen, E. Hack, S. Jenatsch, L. Wang, A. C. Véron, M. Makha, R. Schneider, Y. Arroyo, R. Hany, F. Nüesch, *Organic Electronics* **2016**, *30*, 191–199.

- [31] S. Jenatsch, R. Hany, A. C. Véron, M. Neukom, S. Züfle, A. Borgschulte, B. Ruhstaller, F. Nüesch, *The Journal of Physical Chemistry C* **2014**, *118*, 17036–17045.
- [32] G. M. Sheldrick, *Acta Crystallographica Section A: Foundations of Crystallography* **2008**, *64*, 112–122.
- [33] A. L. Spek, *Journal of Applied Crystallography* **2003**, *36*, 7–13.
- [34] T. Yanai, D. P. Tew, N. C. Handy, *Chemical Physics Letters* **2004**, *393*, 51–57.
- [35] J. C. de Mello, H. F. Wittmann, R. H. Friend, *Advanced Materials* **1997**, *9*, 230–232.

6 Conclusions and outlook

The interest for cyanine dyes as active layers in organic optoelectronic applications has arisen from their unique photophysical properties and chemical versatility. As functional layers they have been mostly applied in the form of continuous amorphous thin films in OPVs and OLECs. It is believed that key properties of these layers could be improved by inducing order in the films at different length scales. Indeed, while individual molecules present a set of characteristics, these can be significantly altered when molecules are brought together with a certain degree of order.

The fabrication of different types of organized assemblies by solution-route presents advantages in terms of the versatility of the processes available. However, it is also challenging because of the high number of different parameters affecting the resulting morphology. Taking control of these parameters is therefore paramount to fully master the ordering process. In the light of these arguments, the goal of this work was twofold:

1. To take control of cyanine thin film morphology to create assemblies beyond continuous amorphous layers.
2. To explore and understand the origin the optical properties arising from these assemblies.

In chapter 2, films of cyanine droplets were formed by dewetting of dye solution during spin-coating. The spectroscopic properties of these films revealed intriguing features, which

Chapter 6. Conclusions and outlook

were originally thought to stem from clusters nucleating in the droplets. In fact they were demonstrated to arise primarily from the diffraction of visible light by the ensemble of sub-micrometer dye droplets, which act as individual scatterers. When probed with UV-vis spectroscopy, both the intrinsic absorption of the dye chromophores and the scattering efficiency of the droplets contributed to the attenuation spectra. By varying the droplets' dimensions through changes in the experimental procedure, three scattering regimes were found with different types of spectral features. These regimes could be analytically described to result from the array of scatterers in a diffraction plane formed by the dye droplets. Finite-difference time-domain simulations were used to further investigate the interaction of light with individual droplets of different dimensions. The results showed that, contrary to high refractive index structures, light does not resonate within the structure. It rather propagates through the droplets, focusing light intensity in the near-field beyond them, thus acting as secondary scattering sources.

A simple example was presented to show how these structures could potentially be used for sensing applications, since light scattering was shown to be sensitive to the refractive index of the medium surrounding the dye droplets. However, further work in this direction would necessitate better optimization of the structures, in particular with regards to their physical integrity when exposed to other substances. Other potential applications could include the fabrication of photonic crystals and wavelength-selective diffracting arrays.

In chapter 3, the morphological evolution of cyanine crystals during growth was investigated. The possibility to grow cyanine crystals from a dewetted film of dye droplets by exposing them to solvent vapor was demonstrated in previous work. Here, it was shown that the initial morphology of the crystals is not stable over extended annealing times: the initially polyhedral crystals destabilize and transform to a dendritic form. The destabilization was explained by changes in growth modes resulting from variations in the growth conditions. Although the specific growth conditions might change from one crystal to the other due to local variations in the droplet distribution, these results highlight the importance of the growth environment on the final morphology of the crystals.

The results presented in this chapter enabled to devise a strategy to avoid crystal destabilization by better controlling the droplets' distribution and prevent their coalescence. This

approach is used later on in the work. If the destabilization could be controlled, one could imagine taking advantage of the dendritic branching to grow linear dye crystals extending over long distance. While they could contain structural and chemical defects, the investigation of the branched crystals' properties would be of significant interest. So far, the optical properties of these crystals could not be investigated locally due to their important thickness, but methods such as local reflectometry measurements could be used to circumvent this issue.

Chapter 4 presented an approach to locally grow single crystals of cyanine dye. The method is based on the selective dewetting of dye droplets by surface patterning of a substrate with hydrophilic/hydrophobic self-assembled monolayers. This method was demonstrated to provide a few advantages. First, the approach was demonstrated to be successful in inducing nucleation at defined location on the substrate. Second, it gave better control over the growth conditions, hence preventing crystal destabilization. Finally, the localization of single droplets offered an ideal platform to evaluate nucleation events. The effect of initial solution concentration on crystal nucleation was evaluated. The study showed that higher solution concentration yielded more single crystals but also more polycrystals. In addition, the effect of droplet volume on the crystal volume was also evaluated. Although a close correlation was expected, the two parameters showed some discrepancies and control over the crystal size by this approach appeared to be limited.

Better control over nucleation should be possible by regulating the evaporation rate during deposition of droplets. In on-going work, a post-deposition approach has been implemented to be able to vary solvent vapor pressure during annealing, but yielded limited results so far. Another approach could be to improve the deposition process by using dip-coating under regulated environmental conditions for example. Improvement of the method could also enable in-plane alignment of the crystals. One way to implement crystal alignment would be to change the geometry of the patterned area. For instance, geometries containing flat edges such as squares or rectangle could help in aligning the crystal along these patterned edges by minimization of the interfacial energies.

Finally, the structure and spectroscopic properties of CyC single crystals were investigated in chapter 5. This study showed that the CyC crystals form a layered structure, with herringbone patterns between chromophores. The crystal structure exhibited substantial intra- and inter-

Chapter 6. Conclusions and outlook

layer electronic coupling based on calculation of the coupling energies using the extended dipole model. Optical absorption measurements on individual crystals confirmed the importance of the electronic coupling by revealing the presence of excitonic features. This could be of great interest for application in devices such as OPVs since the formation of excitonic bands should facilitate exciton transport in the crystalline thin film.

On-going work is focusing on performing first-principle calculations to enhance the experimental interpretation and further elucidate the key properties at play. In particular, the contribution of vibronic couplings to the absorption features should be clarified.

Future work could focus on the integration of the crystal in OPV devices and the measurement of orientation dependent photovoltaic properties. The strong absorption together with excitonic coupling and crystal thinness may help to improve the performance of cyanine dye solar cells. The methods elaborated in this thesis work also present a concept to grow platelet crystals at defined locations with high throughput. With additional control of the crystals in-plane orientation, this approach could be extremely valuable in the field of organic electronics. High performance and high throughput could be achieved at the same time.

Curriculum Vitae

Nicolas LECLAIRE

Mimosenstrasse 1, 8057 Zurich, Switzerland

+41 (0)78 956 64 79

nicolas.leclaire@epfl.ch

Personal	Birth date and location	28.05.1990, Clamart, France
	Nationality	French
	Languages	French (mother tongue), English (fluent), Spanish (basic knowledge), German (basic knowledge), Mandarin (basic knowledge)

Education	PhD Candidate	2014-present
	Swiss Federal Laboratories for Materials Science and Technology (EMPA), Dübendorf, Switzerland & École Polytechnique Fédérale de Lausanne (EPFL), Lausanne, Switzerland	
	Doctoral School of Materials Science (EDMX)	
	Master of Science (MSc) in Material Science and Engineering	2011-2014
	Ecole Polytechnique Fédérale de Lausanne (EPFL) Lausanne, Switzerland	
Bachelor of Science (BSc) in Material Science and Engineering	2009-2011	
Ecole Polytechnique Fédérale de Lausanne (EPFL) Lausanne, Switzerland		
Preparatory Classes	2008-2009	
for the French Grandes Ecoles entrance exams		
Lycée Lakanal		
Sceaux, France		
Baccalauréat in Science , obtained with highest honors	2008	
Ecole Alsacienne		
Paris, France		

Professional Experience	Ecole Polytechnique Fédérale de Lausanne (EPFL)	2011-2013
	Teaching assistant for “Introduction to Materials Sciences”	
	EPFL, Lausanne, Switzerland	
Swiss Center for Electronics and Microtechnology (CSEM)	2012-2013 (5 months)	
Intern in the Nanotechnology and Life Science Division		
Neuchâtel, Switzerland		
B.Braun Medical AG	2012 (2 months)	
Engineering Intern Packaging System Management		
Crissier, Switzerland		

Research Experience	PhD Thesis, Functional Polymers Laboratory	
	Swiss Federal Institute for Materials Science and Technology (EMPA), Switzerland	
	“Spatial and Morphological Control of Cyanine Dye Thin Films”	
	Thesis advisors: Prof. Frank A. Nüesch, Dr. Jakob Heier	

Master's Thesis, Biological and Biomimetic Materials Laboratory

Nanyang Technological University (NTU), Singapore

"Proof of concept for the use of Jumbo squid protein as a resist for plasmonic applications"

Thesis advisor: Prof. Ali Miserez

Semester Project, Powder Technology Laboratory,

EPFL, Switzerland

*"Synthesis and characterization of silica-coated superparamagnetic iron oxide nanoparticles (SPION) for biomedical applications"***Semester Project, Polymers and Composite Technology Laboratory,**

EPFL, Switzerland

"Evaluation of the barrier and piezoelectric properties of nanocomposites for high-pressure hydrogen storage in automobiles"

Contribution to scientific conferences	Oral presentations	EMPA PhD Students' Symposium, Dübendorf, Switzerland	2017
		FEMS Junior-Euromat, Lausanne, Switzerland	2016
	Poster contributions	MRS Spring Meeting Phoenix, AZ, USA	2018
		Soft Material Science (SoMaS) Mittelwihr, France	2017
		EDMX Research Day, Lausanne, Switzerland	2015, 2017
		EMPA PhD Students' Symposium Dübendorf, Switzerland	2014, 2016
		European Conference on Molecular Electronics (ECME) Strasbourg, France	2015
		Hierarchical Assembled Organic Materials for Electronics (HOMERIC), Bordeaux, France	2014

List of scientific publications:

- Leclaire, N. A., Li, M., Neels, A., Véron, A.C., Heier, J., Reimers, J.R., Nüesch, F.A., Cyanine Platelet Crystals: synthesis, crystal structure and optical spectra, *in preparation*
- Li, M., Leclaire, N.A., Heier, J., Nüesch, F.A., Reimers, J.R., Cyanine Platelet Crystals: excitonic and vibronic spectral simulations, *in preparation*
- Véron, A.C., Linden, A., Leclaire, N.A., Roedern, E., Hu, S., Ren, W., Rentsch, D., Nüesch, F.A., One-Dimensional Organic-Inorganic Hybrid Perovskite Incorporating Near-Infrared-Absorbing Cyanine Cations, *J. Phys. Chem. Lett.* **2018**, 9 (9), 2438–2442
- Leclaire, N.A., Boudoire, F., Hack, E., Brönnimann, R., Nüesch, F.A., Heier, J., Light Scattering Enhancement at the Absorption Edge in Dewetting Droplets of Cyanine Dyes. *Adv. Opt. Mat.* **2017**, 5 (5), 1600903.

- Jenatsch, S., Wang, L., Leclaire, N.A., Hack, E., Steim, R., Anantharaman, S.B., Heier, J., Ruhstaller, B., Penninck, L., Nüesch, F.A., Hany, R., Visible light-emitting host-guest electrochemical cells using cyanine dyes, *Organic Electronics* **2017**, *48*, 77-84
- Makha, M., Testa, P., Anantharaman, S.B., Heier, J., Jenatsch, S., Leclaire, N.A., Tisserant, J.-N., Véron, A.C., Wang, L., Nüesch, F.A., Hany, R., Ternary semitransparent organic solar cells with a laminated top electrode. *Sci. Technol. Adv. Mater.* **2017**, *18* (1), 68–75.
- Maurizi, L., Usawadee, S., Crowe, L.A., Dao, V.M., Leclaire, N.A., Vallée, J.-P., Hofmann, H., Syntheses of cross-linked polymeric superparamagnetic beads with tunable properties, *RSC Adv.* **2014**, *4*, 11142-11146

